`

Properties of coronavirus spike proteins and the antibody responses against them

Amin Addetia

A dissertation

submitted in partial fulfillment of the

requirements for the degree of

Doctor of Philosophy

University of Washington

2024

Reading Committee:

David J Veesler, Chair

Jesse D Bloom

Alex Greninger

Program Authorized to Offer Degree:

Molecular and Cellular Biology

©Copyright 2024

Amin Addetia

University of Washington

Abstract

Properties of coronavirus spike proteins and the antibody responses against them

Amin Addetia

Chair of the Supervisory Committee:

David Veesler

Biochemistry

Coronaviruses have a propensity to spillover from zoonotic reservoirs and cause significant morbidity and mortality in the human population. Three coronaviruses emerged and caused significant human outbreaks in recent history: severe acute respiratory syndrome coronavirus (SARS-CoV-1) in 2003, Middle East respiratory syndrome coronavirus (MERS-CoV) in 2012, and severe acute respiratory syndrome coronavirus 2 (SARS-CoV-2) in 2019. The coronavirus spike protein facilitates viral entry into target cells by engaging the host receptors and fusing the viral and host membrane together. As the primary determinant of viral entry into target cells, the coronavirus spike protein is the target of most vaccines and therapeutics. Antibodies induced by prior infection and vaccination and therapeutics may select for spike protein mutations that evade these antibodies without disrupting the spike protein's ability to

engage the host receptor and mediate membrane fusion. In the following dissertation, I detail a unique mechanism of antibody evasion induced by a mutation in the receptor binding domain of the SARS-CoV-2 spike protein. I additionally describe the impact of spike protein mutations observed in the SARS-CoV-2 Omicron variants on receptor engagement, fusogenicity, and evasion from infection- and vaccine-elicited antibodies. I further examine how updated SARS-CoV-2 vaccine formulations shape the humoral immune response. Finally, I detail the contribution of spike protein domains and epitopes to the neutralizing activity of convalescent plasma collected from individuals infected with MERS-CoV. Collectively, my work is informing the development of the next generation of coronavirus vaccines and therapeutics.

Table of Contents

List of Figures

List of Tables

Acknowledgments

Through my time in graduate school, I have been very fortunate to have an incredibly supportive community of mentors, colleagues, collaborators, and friends. These past few years would not have been nearly as enjoyable without all of you.

First, to all the previous and current members of the Veesler lab, I have really enjoyed working with all of you. I have learned so much from each of you and I cannot wait to see where we all end up in the future. To John and Matt in particular, I am so grateful for the all the time in and out of lab that we spent together. From our ridiculous camping trips to our nights out in Seattle, Portland, New York, and Vancouver, I have made so many memories with you guys and I cannot wait to make more memories with each of you. Next, to my many collaborators at Fred Hutch, University of Washington, Colorado State University, University of Utah, and Vir, you have been fantastic to work with and I am in awe of the incredible science we have done together. I hope to work with all of you in the future!

Next, I would like to thank my past and present scientific mentors. To Xuan, Anne Marie, Danielle, and Amanda, thank you for giving me my first post-college research position. Seattle Children's was a fantastic place to learn and grow and I would not have been able to accomplish all I have without your initial support and encouragement. To Alex, thank you for sparking my love for science and research. Finally, thank you David for your mentorship these past three years. I am so happy that I was able to participate in so much interesting and impactful research. I am incredibly excited to see what we achieve together in the future!

Karim and Robyn, thank you for supporting and encouraging my decisions from day one. To all of my friends who have been a part of my graduate school journey, our runs, ski trips, dodgeball games, climbing dates at SBP, backpacking trips, and so much more have made this time so fun and fulfilling. Lastly, to Zach, thank you for all the silliness – the last 40% of graduate school would not have been nearly as fun without my sister.

Chapter 1. Introduction

1.1 Viruses and the immune response against them

Viruses are obligate intracellular organisms that hijack the machinery within host cells to replicate and disseminate (Knipe & Howley, 2013). Viruses infect organisms belonging to all three domains of life and display remarkable diversity, ranging in everything from size to composition with some viruses nearly resembling prokaryotic cells and forming their own organelle-like structures (Chaikeeratisak et al., 2017; Devoto et al., 2019) to some viruses just consisting of a single strand of RNA that solely encodes an RNA-dependent RNA-polymerase (Rodriguez-Cousiño et al., 1991). Viruses infecting human cells form infectious particles, known as virions, that consist of genetic material, either RNA or DNA, bundled into capsids composed of proteins (Knipe & Howley, 2013). Some viruses will further surround their capsids with a lipid membrane snatched from their host cell. The surfaces of these enveloped viruses are generally decorated with glycoproteins that facilitate release from the current host cell and entry into the next cell. Once inside a cell, viruses will produce a number of other proteins that antagonize the defenses and function of the host cell and that promote the production of more viral nucleic acid and protein. Alternatively, some human viruses hide within host cells, remaining dormant until external factors promote re-activation and replication.

In the arms race between viruses and their hosts, host species have evolved to produce defenses that limit the replication and spread of viruses. In humans, both the innate and adaptive immune response act to counter viral infection (Knipe & Howley, 2013; Murphy & Weaver, 2016). Innate immunity is non-specific for pathogens and consists of barriers, such as skin, that prevent viruses from reaching target cells, and

innate immune cells, such as macrophages, that signal upon encountering pathogens, release antivirals to kill infecting viruses, and stimulate responses that recruit of additional immune cells to sites of infection. In addition, innate immune cells also promote an adaptive immune response against an invading virus (Murphy & Weaver, 2016). The adaptive immune response is trained on the invading pathogen and consists of T and B cells. T cells encode T cell receptors that bind to fragments of viral proteins presented on the major histocompatibility complexes of infected cells or innate immune cells. Conventional T cells can further be classified as $CD4^+$ or $CD8^+$ T cells with $CD4^+$ T cells generally secreting factors to modify the response of other immune cells and $CD8^+$ T cells recognizing and killing infected cells (Kumar et al., 2018; Murphy & Weaver, 2016).

B cells encode B cells receptors (BCRs) on their surface that will recognize and bind to viral antigens (Hoffman et al., 2016; Murphy & Weaver, 2016). During the development of B cells, unique BCRs are generated through recombination of the V(D)J locus generating the heavy- and light-chains of BCRs. This recombination event results in each naïve B cell having a unique antigen-specificity. Upon binding a viral antigen, naïve B cells differentiate into plasmablasts and secrete immunoglobulins (Ig; also known as an antibody) (Murphy & Weaver, 2016). Alternatively, activated B cells may enter germinal centers and undergo maturation in which additional mutations are introduced into the antigen-recognizing Ig variable regions, enhancing affinity for the targeted antigen. Additionally, germinal center B cells may undergo class-switching where the Ig constant region is swapped resulting in secretion of a different Ig isotype (Cyster & Allen, 2019; Murphy & Weaver, 2016). Antibodies can prevent viral infection

by binding to a viral protein and preventing the virus from entering its target cells or promoting recognition and destruction of the pathogen by innate immune cells (Burton, 2002; Murphy & Weaver, 2016).

Besides leaving germinal centers as plasma cells that secrete antibodies, affinity matured B cells may leave as memory B cells (Akkaya et al., 2020; Murphy & Weaver, 2016). These memory B cells retain their membrane anchored BCRs and, upon re-encountering their target antigen, can proliferate and differentiate into plasma cells that secrete antibodies against the targeted antigen. This memory response allows for a rapid antibody response should reinfection with the same pathogen occur in the future (Cyster & Allen, 2019; Murphy & Weaver, 2016).

1.2 Vaccines and therapeutic antibodies against viral pathogens

From the earliest documented vaccines that involved using cowpox virus to prevent of smallpox by Edward Jenner in 1798 to the recent SARS-CoV-2 spike-encoding mRNA vaccines (Knipe & Howley, 2013; Pollard & Bijker, 2021), vaccines have fundamentally improved outcomes against infectious diseases, significantly reducing both disease severity and mortality rates. Vaccines aim to the train the adaptative immune to recognize viral antigens, thereby inducing a rapid memory recall response upon infection. A number of different vaccines platforms are currently used for the prevention of infectious diseases. These platforms include live attenuated, inactivated, viral vectored, virus like particle, protein subunit, and nucleic acid vaccines (Murphy & Weaver, 2016; Pollard & Bijker, 2021). Live attenuated and inactivated vaccines both induce a robust immune response against the entirety of a virus as whole

virions are supplied in these vaccines. In contrast, viral vectored, virus like particle, protein subunit, and nucleic vaccines present or encode one or a subset of virus's proteins to the immune system. The one or subset of antigens included in these vaccines often follows studies on the immune correlates of protection from infection for the targeted virus to ensure these vaccines induce an immune response that mirrors a protective immune response for that virus (Burton, 2002; Pollard & Bijker, 2021).

For many viruses, the primary immune correlate of protection is a neutralizing antibody response against the glycoproteins that recognize receptors on host cells and mediate fusion between the viral and host membranes (Burton, 2023). These neutralizing antibodies typically protect against viral infection by blocking interactions between the viral glycoprotein and host receptor or by preventing the glycoproteins from completing membrane fusion. As such, these neutralizing antibodies generally recognize the prefusion conformation of viral glycoprotein rather than the post-fusion conformation. Recent vaccine design has centered around identifying stabilizing mutations that lock viral glycoproteins in the prefusion conformation (Hsieh et al., 2020; Pallesen et al., 2017). Vaccination with these prefusion stabilized glycoproteins have proved to induce significantly greater neutralizing antibody titers and provide superior protection from disease as exemplified by the recently approved respiratory syncytial virus prefusion F protein vaccines (McLellan et al., 2013; Simões et al., 2022).

Monoclonal antibodies are emerging therapeutics used for both the prevention and treatment of infectious diseases (Corti et al., 2021). Therapeutic monoclonal antibodies are typically discovered by first isolating antigen-specific memory B cells from infected or vaccinated individuals or vaccinated humanized mice (Corti et al., 2021;

Laffleur et al., 2012). The BCRs of these memory B cells are sequenced and expressed as antibodies. The antibodies are then selected for desirable properties, including neutralization potency and resilience to mutations in the targeted viral antigens, and may be further modified to enhance these properties or extend their half-lives when administered to humans (Kontermann, 2011; Starr, Czudnochowski, et al., 2021). As these antibodies recognize specific epitopes on viral antigens, the effectiveness of these therapeutics is highly susceptible to mutations in viral proteins that accumulate as the virus evolves (Corti et al., 2021; Starr, Greaney, et al., 2021).

1.3 Coronaviruses and their spike proteins

Coronaviruses are enveloped, positive-sense RNA viruses with large glycoproteins decorating their surface and giving them a characteristic “solar corona” appearance when viewed with an electron microscope (Knipe & Howley, 2013; “Virology,” 1968). Coronaviruses are among the largest RNA viruses due to the unique proof-reading ability of their RNA-dependent RNA polymerase that limits the number of mutations that accumulate in the viral genome during replication. Coronaviruses encode numerous proteins that are either structural, getting incorporated into infectious virions, or nonstructural, being expressed once the virus infects a host cell (Knipe & Howley, 2013; V’kovski et al., 2021).

The *Orthocoronavirinae* subfamily is divided into four genera: *Alphacoronavirus, Betacoronavirus*, *Gammacoronavirus*, and *Deltacoronavirus* (Knipe & Howley, 2013). Seven coronaviruses infecting humans have been identified to date, including 229E, NL63, OC43, HKU1, SARS-CoV-1, SARS-CoV-2, and MERS-CoV. Two of these human

coronaviruses, 229E and NL63, belong to the *Alphacoronavirus* genus with the remaining 5 belonging to the *Betacoronavirus* genus. The *Betacoronavirus* genus is further stratified into the *Embecovirus* (OC43 and HKU1), *Sarbecovirus* (SARS-CoV-1 and SARS-CoV-2), *Merbecovirus* (MERS-CoV), *Nobecovirus*, and *Hibecovirus* subgenera. A number of betacoronaviruses have been identified in bat and other mammalian reservoirs. Many of these viruses can infect human cells after accumulating few or no mutations, highlighting the risk of additional potential zoonotic spillovers of coronaviruses (Knipe & Howley, 2013; Starr, Zepeda, et al., 2022).

The primary glycoprotein found on the surface of the coronavirus virion is known as the spike protein (Bosch et al., 2003; Knipe & Howley, 2013; Tortorici & Veesler, 2019). The spike protein is cleaved by cellular proteases forming two subunits, S_1 and S_2. The S_1 subunit contains the N-terminal domain (NTD), also referred to as domain A, and the receptor binding domain (RBD), also known as domain B. The S_1 subunit is responsible for attachment to host cells through interactions with carbohydrates and protein receptors on surface of the host cell. The S_2 subunit is anchored in the viral membrane and is the membrane fusion machinery (Bosch et al., 2003; Tortorici & Veesler, 2019). Furthermore, the S_2 subunit is activated by cellular proteases, which cleave S_2 into S_2'. Following engagement with host receptors, the S_1 subunit is shed from the spike protein allowing the S_2 subunit to insert its fusion peptide into the host membrane (Bosch et al., 2003; Tortorici & Veesler, 2019). The S_2 subunit undergoes a dramatic conformational change pinching together the viral and host membranes (Walls et al., 2017). As the spike protein is responsible for entry into host cells, vaccines and

therapeutic monoclonal antibodies against coronaviruses target or generate an immune response against the spike protein (Barouch, 2022; Huang et al., 2020).

1.4 Severe acute respiratory syndrome coronavirus 2

Severe acute respiratory syndrome coronavirus 2 (SARS-CoV-2) emerged in December 2019 and rapidly spread across the globe (P. Zhou et al., 2020; Zhu et al., 2020). SARS-CoV-2 is the causative agent of Coronavirus Disease 2019 (COVID-19) and is responsible for the COVID-19 pandemic. SARS-CoV-2 causes significant respiratory illness in infected individuals and, to date, has caused over 700 million infections and 7 million deaths (Allan et al., 2022). SARS-CoV-2 entry into target cells is facilitated by interactions between the SARS-CoV-2 spike protein and the host receptor, angiotensin-converting enzyme 2 (ACE2) (Hoffmann, Kleine-Weber, Schroeder, et al., 2020; Walls, Park, et al., 2020; P. Zhou et al., 2020). In addition, the host transmembrane serine protease 2 (TMPRSS2) participates in viral entry by cleaving the S_2 subunit of the spike protein, priming the protein to mediate fusion (Hoffmann, Kleine-Weber, & Pöhlmann, 2020; Hoffmann, Kleine-Weber, Schroeder, et al., 2020). We and others demonstrated the primary immune correlate of protection against SARS-CoV-2 infections is a neutralizing antibody response directed against the SARS-CoV-2 spike protein (Addetia et al., 2020; Fong et al., 2022; Gilbert et al., 2022). Accordingly, SARS-CoV-2 vaccines encode or present the viral spike protein and aim to elicit a robust humoral immune response against the spike protein (Barouch, 2022). Additionally, all licensed therapeutic monoclonal antibodies used for the treatment of COVID-19 target neutralizing epitopes on the spike protein (Corti et al., 2021).

The recent advancements in next generation sequencing technologies along with the prioritization of diagnostic testing for SARS-CoV-2 has assisted in the identification of viral variants as the virus has continued to evolve ("An Integrated National Scale SARS-CoV-2 Genomic Surveillance Network," 2020; Grubaugh et al., 2021; Rambaut et al., 2020). The swift dissemination of genomic information has permitted prompt assessments on the effectiveness of therapeutics and vaccines against these viral variants. Furthermore, global tracking of SARS-CoV-2 variants has allowed for vaccine updates to provide more robust protection against the circulating viral strains (Chalkias et al., 2023).

1.5 Middle East respiratory syndrome coronavirus

Middle East respiratory syndrome coronavirus (MERS-CoV) was first identified in 2012 and human infections continue to occur in endemic regions (Bermingham et al., 2012; Zaki et al., 2012). Human-to-human transmission occurs infrequently with MERS-CoV and, instead, transmission occurs from camels, a reservoir species for MERS-CoV, to humans (Dudas et al., 2018). The mortality rate associated MERS-CoV infection has been estimated at approximately 35% (Arabi et al., 2014; Ebrahim et al., 2021). The human receptor for MERS-CoV is dipeptidyl peptidase-4 (DPP4) (Lu et al., 2013; Raj et al., 2013; N. Wang et al., 2013). In addition to interacting with DPP4, the MERS-CoV attaches to sialosides on the surface of host cells through a binding pocket in the NTD of the spike protein (W. Li et al., 2017; Y.-J. Park et al., 2019). Currently, no vaccines are licensed for MERS-CoV, however, the ones in development aim to develop a

response against the viral spike protein (Folegatti et al., 2020; Koch et al., 2020; Modjarrad et al., 2019; L. Wang et al., 2015).

The work I will present in the subsequent chapters begins with studies on SARS-CoV-2 and concludes with a study on MERS-CoV. The first story describes a unique mutation that prevented some of the earliest SARS-CoV-2 therapeutics from neutralizing the virus. The second and third stories focus on the SARS-CoV-2 Omicron lineage variants and COVID-19 vaccines. The final story examines the antibody response generated against the MERS-CoV spike protein following infection.

Chapter 2. Structural changes in the SARS-CoV-2 spike E406W mutant escaping a clinical monoclonal antibody cocktail

The first story included here was initiated early in the COVID-19 pandemic when monoclonal antibodies targeting the SARS-CoV-2 spike protein were becoming approved for the treatment of COVID-19. We identified a single mutation that influenced the ability of multiple therapeutic monoclonal antibodies to bind the SARS-CoV-2 protein. In the subsequent sections, I detail our efforts to understand how this unusual mutation influences the binding of many different antibodies to the SARS-CoV-2 spike protein.

Adapted from: Addetia, A., Park, Y., Starr, T., Greaney, A., Sprouse, K., Bowen, J., Tiles, S., Van Voorhis, W., Bloom, J., Corti, D., Walls, A., Veesler. Structural changes in the SARS-CoV-2 spike E406W mutant escaping a clinical monoclonal antibody cocktail. *Cell Reports*. 2023. doi: 10.1016/j.celrep.2023.112621.

2.1 Chapter Introduction

The receptor-binding domain (RBD) of the severe acute respiratory syndrome coronavirus 2 (SARS-CoV-2) spike glycoprotein is responsible for interacting with the host receptor ACE2 and initiating viral entry into cells (Hoffmann, Kleine-Weber, Schroeder, et al., 2020; Walls, Park, et al., 2020; P. Zhou et al., 2020). The SARS-CoV-2 RBD is the target of the majority of neutralizing antibodies elicited by SARS-CoV-2 infection and COVID-19 vaccination, of virtually all vaccine-elicited cross-variant neutralizing antibodies and of monoclonal antibodies (mAbs) used prophylactically or therapeutically

(Bowen, Park, et al., 2022; Corti et al., 2021; Greaney, Loes, Gentles, et al., 2021; McCallum, De Marco, et al., 2021; Piccoli et al., 2020; Stamatatos et al., 2021). Binding and neutralization of SARS-CoV-2 by individual mAbs can be escaped by single RBD residue mutations, which led to the development of therapeutic cocktails comprising two mAbs recognizing non-overlapping epitopes (Baum et al., 2020; Hansen et al., 2020; Starr, Czudnochowski, et al., 2021; Starr, Greaney, et al., 2021). These cocktails have a higher barrier for the emergence of neutralization escape mutants than the individual constituting mAbs, as typically at least two distinct amino-acid substitutions are required to evade neutralization by a two-mAb cocktail.

The REGEN-COV cocktail consists of two mAbs, casirivimab (REGN10933) and imdevimab (REGN10987) that bind non-overlapping RBD epitopes in the receptor-binding motif (RBM), and block ACE2 attachment (Baum et al., 2020; Hansen et al., 2020). We previously mapped all possible RBD residue mutations that permit escape from the REGEN-COV mAb cocktail and the COV2-2130 mAb, which led us to identify that the E406W substitution abrogated binding and neutralization of both REGEN-COV mAbs individually and the cocktail (Starr, Greaney, et al., 2021) as well as binding of COV2-2130 (Dong et al., 2021). Unexpectedly, residue E406 is located outside of the epitopes recognized by REGN10933, REGN10987 and COV2-2130, suggesting that this mutation might influence the overall structure of the RBD (presumably through an allosteric effect) while retaining detectable binding to dimeric human ACE2 (Starr, Greaney, et al., 2021).

2.2 Elucidating structural changes in the SARS-CoV-2 E406W spike protein using cryo-EM

To understand the molecular basis of the E406W-mediated escape from the REGEN-COV cocktail and COV2-2130 mAb, we characterized the SARS-CoV-2 spike (S) ectodomain trimer structure harboring the E406W mutation using single-particle cryo-electron microscopy. 3D classification of the dataset revealed the presence of two conformational states: one with three RBDs closed and one with one RBD open accounting for approximately 70% and 30% of particles, respectively. We determined a structure of the closed S state at 2.3 Å resolution applying C3 symmetry **(Figure 2.1, Figure 2.2 and Table 2.1)**. Symmetry expansion, focused classification, and local refinement yielded an RBD reconstruction at 3.4 Å resolution, which was used for model building (enabling resolving the complete RBD) and analysis **(Figure 2.1, Figure 2.2 and Table 2.1)**.

2.3 Structural basis for escape from the REGEN-COV and COV2-2130 antibodies

The E406W substitution places the introduced side-chain indol ring in a position sterically incompatible with the neighboring Y495 phenol side chain, inducing a rotameric rearrangement of the latter residue relative to the ACE2-bound RBD structure (Lan et al., 2020) or apo S ectodomain trimer structures (Walls, Park, et al., 2020; Wrobel et al., 2020). This results in major conformational reorganization of residues 443-450 and 495-503 which experience up to 4.5 Å shift relative to previously determined structures (Walls, Park, et al., 2020; Wrobel et al., 2020) (the overall root-mean-square deviation [RMSD] between ACE2-bound RBD and E406W RBD is 1.37 Å over 194 C-alpha pairs). Although the organization of residues 475-484 are only subtly

different in the E406W RBD relative to apo S structures (Walls, Park, et al., 2020; Wrobel et al., 2020), it deviates more from the REGEN-COV-bound RBD structure (Hansen et al., 2020) **(Figure 2.1a, Figure 2.3)**. REGN10987 recognizes an epitope residing at the interface between antigenic sites Ia and IIa (Piccoli et al., 2020) and forms extensive interactions with residues 440-449 that would sterically clash with the mAb heavy chain in the E406W RBD structure **(Figure 2.1b)**. REGN10933 interacts with residues 417, 453-456 and 475-490 (within antigenic site Ia (Piccoli et al., 2020)) and the distinct conformation of the latter residues in the REGEN-COV-bound RBD and E406W apo S structures possibly precludes mAb binding through steric clash with the mAb light chain **(Figure 2.1c)**. Our data therefore shows that the E406W mutation disrupts the antigenic sites recognized by REGN10933 and REGN10987 allosterically, which are positioned 5 and 20 Å away, respectively (Starr, Greaney, et al., 2021). Similar to REGN10987, the loss of COV2-2130 binding to the E406W RBD (Dong et al., 2021) is explained by the structural reorganization of residues 443-450 which are recognized by this mAb **(Figure 2.4)**.

2.4 Impact of E406W-induced conformational changes on ACE2 binding

These RBD conformational changes also alter the ACE2-interacting surface resulting in the predicted loss of several hydrogen bonds formed between the ACE2 D38 and SARS-CoV-2 Y449 side chains as well as the ACE2 Q42 side chain and the SARS-CoV-2 Y449 side chain and G446 main chain carbonyl **(Figure 2.1d)**. Moreover, repositioning of residues 496-502 would likely also hinder ACE2 binding sterically. Accordingly, we observed that the monomeric human ACE2 ectodomain bound with a

14-fold reduced affinity to immobilized SARS-CoV-2 E406W RBD (K_D=1.34 μM) relative to wildtype (Wuhan-Hu-1) RBD (K_D=93.9 nM) using biolayer interferometry **(Figure 2.5a-c and Table 2.2)**. This reduction of ACE2 binding affinity is expected to dampen viral fitness, as previously observed for another point mutation decreasing ACE2 binding (Y.-J. Park, De Marco, et al., 2022) **(Figure 2.5d)** and for XBB.1 relative to XBB.1.5 (Yue et al., 2023).

2.5 Assessing the impact of the E406W mutation on the neutralization of other monoclonal antibodies and vaccine-elicited sera

Several broadly neutralizing sarbecovirus human mAbs recognizing distinct RBD antigenic sites have been described. Some of them were shown to be (partially) resilient to the ongoing SARS-CoV-2 evolution and to protect small animals against challenge with SARS-CoV-2 variants of concern or other sarbecoviruses (Jette et al., 2021; Martinez et al., 2022; Y.-J. Park, De Marco, et al., 2022; Y.-J. Park, Pinto, et al., 2022; Pinto et al., 2020; Starr, Czudnochowski, et al., 2021; Tortorici et al., 2020, 2021; Westendorf et al., 2022). To evaluate the influence of the aforementioned structural changes on neutralization by these mAbs, we compared the concentration-dependent inhibition of S309, S2E12 and S2X259 against VSV particles pseudotyped with the Wuhan-Hu-1 spike harboring the G614 or the W406/G614 mutations. Each of these three mAbs neutralized with comparable potency the G614 and W406/G614 pseudoviruses **(Table 2.3)**, indicating they retain activity against this mutant **(Figure 2.6a and Figure 2.7)**. As predicted based on structural data (Piccoli et al., 2020; Starr, Czudnochowski, et al., 2021), the S2H14 mAb failed to neutralize the spike W406/G614

pseudovirus due to the reorganization of the receptor-binding motif **(Figure 2.5a and Figure 2.6)**. Moreover, these data are consistent with the fact that binding to the SARS-CoV-2 W406 RBD was unaffected for S2E12 and abrogated for S2H14 (Starr, Czudnochowski, et al., 2021).

Finally, we set out to assess the impact of the E406W mutation on vaccine-elicited plasma neutralizing activity using samples obtained from individuals who had received a primary vaccine series (2 doses) of either Pfizer BNT162b2 or Moderna mRNA-1273 COVID-19 vaccine **(Table 2.3)**. We observed 2.5-fold (BNT162b2, range: 1.2-4.6) and 2.4-fold (mRNA-1273, range: 1.5-3.8) reduction in neutralization potencies against the W406/G614 spike pseudovirus compared to G614 spike-harboring pseudovirus **(Figure 2.6b-c and Figure 2.7)**. These data indicate that the single E406W mutation leads to moderate erosion of vaccine-elicited polyclonal neutralizing antibodies, comparable to the SARS-CoV-2 Epsilon variant (McCallum, Bassi, et al., 2021) or the Delta variant (Y. Liu et al., 2021).

2.6 Chapter Discussion

The ongoing SARS-CoV-2 evolution yielded variants harboring numerous mutations, some of them altering transmissibility, immune evasion, replication kinetics or disease severity relative to the ancestral SARS-CoV-2 strain (Cameroni et al., 2022; Cele et al., 2022; Davies et al., 2021; Deng et al., 2021; Edara et al., 2021; Faria et al., 2021; C. Liu et al., 2021; Y. Liu et al., 2021; McCallum, Bassi, et al., 2021; McCallum, De Marco, et al., 2021; McCallum et al., 2022; Meng et al., 2022; Plante et al., 2021; Tegally et al., 2021; The CITIID-NIHR BioResource COVID-19 Collaboration et al.,

2021; Thomson et al., 2021; Wibmer et al., 2021). We note that the E406W mutation requires multiple nucleotide substitutions from the Wuhan-Hu-1 spike sequence and has a deleterious effect on ACE2 binding. However, several currently circulating variants harbor amino acid mutations generated through multiple nucleotide substitutions (e.g BA.1 S371L, BA.2.3.20 E484R, or XBB.1.5 G339H, V445P, and F486P) as well as mutations that dampen ACE2 binding in the Wuhan-Hu-1 background but are tolerated through epistatic interactions with other mutations (e.g. Q498R found in Omicron lineages) (Dejnirattisai et al., 2022; Starr, Greaney, Hannon, et al., 2022; Viana et al., 2022). This suggests that epistasis might allow for the future emergence of variants harboring the E406W mutation or other mutations remodeling RBD antigenic sites allosterically, especially as existing immunity drives selection of variants with enhanced capacity to evade neutralizing antibodies (Greaney, Starr, et al., 2022). Furthermore, several emerging variants which were initially detected in wastewater are accumulating mutations in the antigenic sites affected by the E406W mutation (Gregory et al., 2022), underscoring its potential importance. The identification of the N501Y substitution, which enhances ACE2 binding, before its emergence in the Alpha variant and fixation in Omicron variants (Starr et al., 2020) highlights the power of deep-mutational scanning for prospective mapping of the effect of mutations to the SARS-CoV-2 RBD and motivates the characterization of unusual mutants, such as E406W. These results are reminiscent of the BA.2 and BA.4/5 S371F mutation which dampens S309 binding via remodeling of the RBD helix comprising residues 364-372, which are outside the epitope of this mAb, likely by altering the N343 glycan conformation (Y.-J. Park, Pinto, et al., 2022). To conclude, our data showcase the structural and functional plasticity of

the SARS-CoV-2 RBD (Starr et al., 2020), suggesting mutations influencing the organization of RBD may accumulate and can be functionally tolerated within emerging SARS-CoV-2 strains.

2.7 Experimental Model, Study Participant Details, and Method Details

Cell culture

Expi293 cells were grown in Expi293 media at 37ºC and 8% CO_2 rotating at 130 RPM. HEK-293T cells and HEK-293T cells stably expressing the human ACE2 receptor (HEK-ACE2) (Crawford et al., 2020) were grown in DMEM supplemented with 10% FBS and 1% PenStrep at 37ºC and 5% CO_2. Vero cells stably expressing the human protease TMPRSS2 (Vero-TMPRSS2) were grown in DMEM supplemented with 10% FBS, 1% PenStrep, and 8 µg/mL puromycin at 37ºC and 5% CO_2.

Study participants

Blood samples were collected from individuals 7-30 days after receiving the second dose of either Pfizer's BNT162b2 or Moderna's mRNA-1273 COVID-19 vaccine. All study participants were enrolled in the UWARN: COVID-19 in WA study at the University of Washington. The study protocol was approved by the University of Washington Human Subjects Division Institutional Review Board (STUDY00010350). Demographic information, including age and sex, for sera donors is provided in Table 2.4.

Constructs

The construct encoding spike ectodomain harboring the E406W mutation was obtained from the Institute for Protein Design. The spike ectodomain was codon optimized, stabilized with the hexapro mutations (Hsieh et al., 2020) and mutation of the furin cleavage site (682RRAR685 to 682GSAS685), and inserted into the pCDNA3.1 vector containing a C-terminal foldon followed by an avi tag and an octa-histidine tag.

The construct encoding the E406W RBD was generated by performing around-the-horn mutagenesis using a pCMVR vector encoding the wildtype SARS-CoV-2 RBD containing an N-terminal mu-phosphatase signal peptide and a C-terminal avi tag and octa-histidine tag. The boundaries for the SARS-CoV-2 RBD in this construct were 328RFPN331 to 528KKST531.

Recombinant protein expression and purification

To produce the SARS-CoV-2 spike ectodomain containing the E406W mutation, 125 mL of Expi293 cells were grown to density of 2.5 x 106 cells per mL and transfected with 125 µg of DNA using PEI MAX diluted in Opti-MEM. The cells were grown for four days after which the supernatant was clarified by centrifugation. The recombinant ectodomain was purified using a nickel HisTrap FF affinity column, washed with 10 column volumes of 20 mM imidazole, 25 mM sodium phosphate pH 8.0, and 300 mM NaCl, and eluted with a 500 mM imidazole gradient. The purified proteins were buffer exchanged and concentrated in 20 mM sodium phosphate pH 8 and 100 mM NaCl using a 100 kDa centrifugal filter. The proteins were flash frozen and stored at -80ºC until use.

The wildtype, B.1.1.7, and E406W RBDs were produced by transfecting 25 mL of Expi293 cells at a density of 2.5 x 106 cells per mL with 25 µg of DNA using the ExpiFectamine 293 Transfection Kit. The cells were grown for four days and the resulting supernatant was collected and clarified by centrifugation. The recombinant RBD was purified using a nickel HisTrap HP affinity column, washed with 10 column volumes of 20 mM imidazole, 25 mM sodium phosphate pH 8.0, and 300 mM NaCl, and eluted using a 500 mM imidazole gradient. The resulting protein was buffer exchanged and concentrated using a 10 kDa centrifugal filter. Next, the purified RBDs were biotinylated using the BirA biotin-protein ligase reaction kit (Avidity). The biotinylated proteins were re-purified and concentrated as described above. The proteins were flash frozen and stored at -80ºC until use.

Cryo-EM sample preparation and data collection

3 µL of purified SARS-CoV-2 spike ectodomain harboring the E406W mutation at a concentration of 1.6 mg/mL was added to a freshly glow discharged 2.0/2.0 UltraFoil grid52 (200 mesh). The grid was then plunge frozen using a Vitrobot MarkIV (ThermoFisher) with a blotting force of 0 and time of 6.5 seconds at 100% humidity and 23ºC. Data were acquired on a FEI Titan Krios transmission electron microscope operated at 300 kV and equipped with a Gatan K3 direct detector and Gatan Quantum GIF energy filter, operated in zero-loss mode with a slit width of 20 eV. Automated data acquisition was carried out using Leginon (Suloway et al., 2005). The dose rate was adjusted to 15 counts/pixel/s and each movie was acquired in 75 frames of 40 ms with pixel size of 0.843 Å and a defocus range comprised between -0.1 and -2.6 µm.

cryo-EM data processing

Movie frame alignment, estimation of the microscope CTF, particle picking, and extraction (with a downsampled pixel size of 1.686 Å and box size of 260 pixels) were completed using WARP (Tegunov & Cramer, 2019). Reference-free 2D classification was performed using cryoSPARC to select for well-defined particle images (Punjani et al., 2017). These selected particles were then used for 3D classification with 50 iterations (angular sampling 7.5° for 25 iterations followed by 1.8° with local search for 25 iterations) using Relion and a previously reported closed model for the SARS-CoV-2 spike ectodomain (PBD: 6VXX) as the initial model without imposing any symmetry. 3D refinements were carried out using non-uniform refinement along with per-particle defocus refinement in cryoSPARC (Punjani et al., 2020) after which particles images were subjected to Bayesian polishing using Relion (Zivanov et al., 2019) and re-extracted with a box size of 512 pixels and a pixel size of 1 Å. Another round of non-uniform refinement followed by per-particle defocus refinement followed by another non-uniform refinement was conducted in cryoSPARC. Next, 86 optics groups were defined based on the beamtilt angle used for data collection and another round of non-uniform refinement with global and per-particle defocus refinement concurrently was conducted in cryoSPARC. To better resolve the RBD, focus 3D classification was carried out using symmetry expanded particles and a mask over residues 440-452 and 495-505 of the RBD using a tau factor of 200 in Relion (Zivanov et al., 2018, 2019). Particles from the classes with the best resolved local density were selected and then subjected to local refinement using cryoSPARC. Reported resolutions are based on the gold-standard

Fourier shell correlation of 0.143 criterion and Fourier shell correlation curves were corrected for the effects of soft masking by high-resolution noise substitution (S. Chen et al., 2013; Rosenthal & Henderson, 2003).

Model building and refinement

USCF Chimera (Pettersen et al., 2004) and Coot (Emsley et al., 2010) were used to fit atomic models of the SARS-CoV-2 RBD and ectodomain (PBD: 6M0J, 7LXY). Models were refined and rebuilt into the map using Coot (Emsley et al., 2010) and Rosetta (Frenz et al., 2019; R. Y.-R. Wang et al., 2016) with the RBD model being built using the map obtained from local refinement of the RBD and the ectodomain model being built using the map obtained for the three-fold symmetric ectodomain.

Biolayer interferometry

Biotinylated wildtype, B.1.1.7, or E406W RBD at a concentration of 5 ng/μL in 10X kinetics buffer was loaded at 30C onto pre-hydrated streptavidin biosensor to a 1 nm total shift. The loaded tips were then dipped into a 1:3 dilution series of monomeric hACE2 beginning at 900 nM, 300 nM, or 7,500 nM for 300 seconds followed by dissociation in 10X kinetics buffer for 300 seconds. The resulting data were baseline subtracted and curves were fitted using Octet Data Analysis HT software v12.0 and plotted in GraphPad Prism 9.

Pseudotyped VSV production

E406W and wildtype pseudotyped VSV particles were produced as previously described (McCallum, Bassi, et al., 2021; McCallum, Walls, et al., 2021). Briefly, 5 x 106 HEK-293T cells were seeded in 10 cm2 poly-D-lysine coated plates and grown overnight until they reached ~70% confluency. The cells were then washed 5 times with Opti-MEM (Life Technologies) and transfected with 24 µg of plasmid encoding either the wildtype or E406W SARS-CoV-2 spike protein using Lipofectamine 2000 (Life Technologies). Four hours at transfection, an equal volume of DMEM supplemented with 20% FBS and 2% PenStrep was added to the cells. Twenty to 24 hours following transfection, the cells were washed 5 times with DMEM and infected with VSV∆G/Fluc. Two hours after infection, the cells were washed 5 times with DMEM and grown in DMEM supplemented with 10% FBS and 1% PenStrep along with an anti-VSV-G antibody (I1-mouse hybridoma supernatant diluted 1:25, from CRL-2700, ATCC). Twenty to 24 hours later, the supernatant was collected, clarified by centrifugation at 2,500xg for 10 minutes, filtered through a 0.45 µm filter, and concentrated 10x using a 30 kDa filter (Amicon). The resulting pseudovirus was frozen at -80ºC until use.

Neutralization assays with vaccine-elicited sera and monoclonal antibodies

For neutralization assays using vaccine-elicited sera, HEK-ACE2 cells were seeded in 96-well poly-D-lysine coated plates at a density of 30,000 cells per well and grown overnight until they reached approximately 80% confluency. E406W and wildtype pseudoviruses were diluted 1:25 in DMEM and incubated with vaccine-elicited sera for 30 minutes at room temperature. Growth media was removed from the HEK-ACE2 cells and the virus-sera mixture was added to the cells. Two hours after infection, an equal

volume of DMEM supplemented with 20% and 2% PenStrep was added to each well and the cells were incubated overnight. After 20-24 hours, ONE-Glo EX (Promega) was added to each well and the cells were incubated for 5 minutes at 37ºC. Luminescence values were measured using a BioTek plate reader.

For neutralization assays using monoclonal antibodies, Vero-TMPRSS2 cells were seeded in 96-well plates at a density of 18,000 cells per overnight until they reached approximately 80% confluency. Neutralizations were conducted as described above with one modification: prior to the addition of the virus-antibody mixture, Vero-TMPRSS2 cells were washed 3 times with DMEM.

Luminescence readings from the neutralization assays were normalized and analyzed using GraphPad Prism 9. The relative light unit (RLU) values recorded from uninfected cells were used to define 0% infectivity and RLU values recorded from cells infected with pseudovirus without sera or antibodies were used to define 100% infectivity. ID50 and IC50 values for sera and monoclonal antibodies, respectively were determined from the normalized data points using a [inhibitor] vs. normalized response – variable slope model.

Quantification and statistical analysis

GraphPad Prism 9 and Octet Data Analysis HT software v12.0 were used to analyze neutralization and binding data, respectively. Details regarding number of replicates and data analysis can be found in the respective figure legends and Method Details.

Data and code availability

Cryo-EM maps and atomic models have been deposited at the Electron Microscopy Data Bank and the Protein Data Bank under the following accession codes: EMD: EMD-26058 and PDB: 7TPK (SARS-CoV-2 E406W RBD) and EMD: EMD-26056 and PDB: 7TPI (SARS-CoV-2 E406W Ectodomain).

2.8 Figures & Tables

Figure 2.1. The E406W mutation remodels the SARS-CoV-2 RBD allosterically.

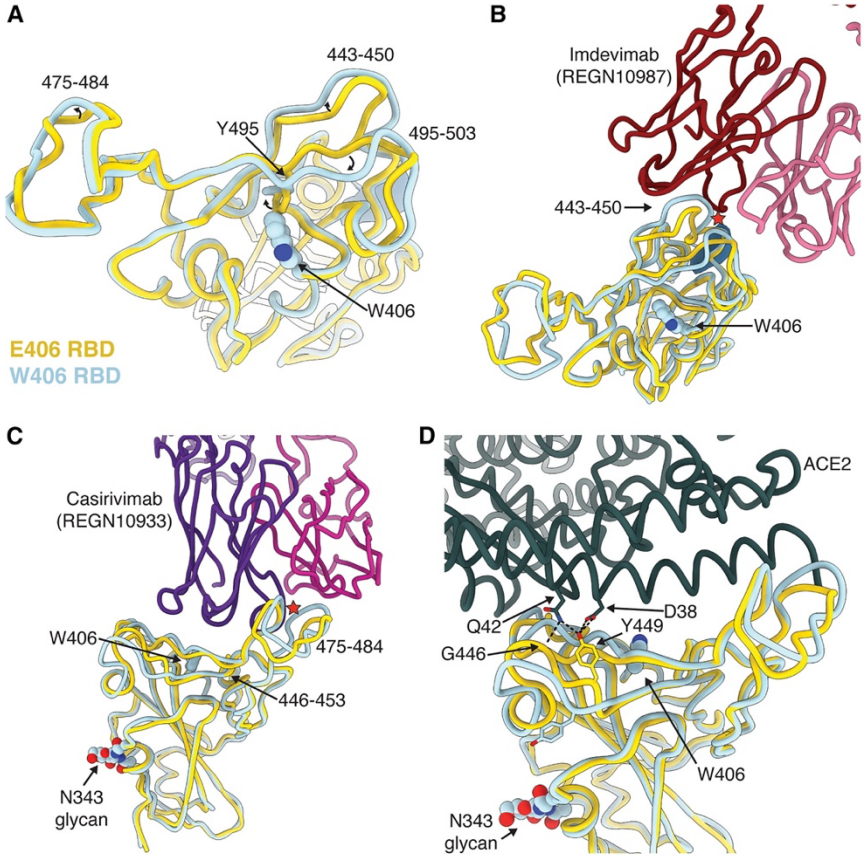

A, Structural superimposition of the Wuhan-Hu-1 RBD (E406, gold, PDB 6M0J, ACE2 not displayed) and the W406 RBD (light blue). **B-C,** Structural superimposition of the REGN10987/REGN10933-bound Wuhan-Hu-1 RBD (E406, gold, PDB 6XDG) and the W406 RBD (light blue). Steric clashes indicated with red stars. **D,** Structural superimposition of the ACE2-bound Wuhan-Hu-1 RBD (E406, gold, PDB 6M0J) and the W406 RBD (light blue). Hydrogen bonds shown as dotted lines.

Figure 2.2. Cryo-EM processing and validation for the SARS-CoV-2 E406W spike dataset.

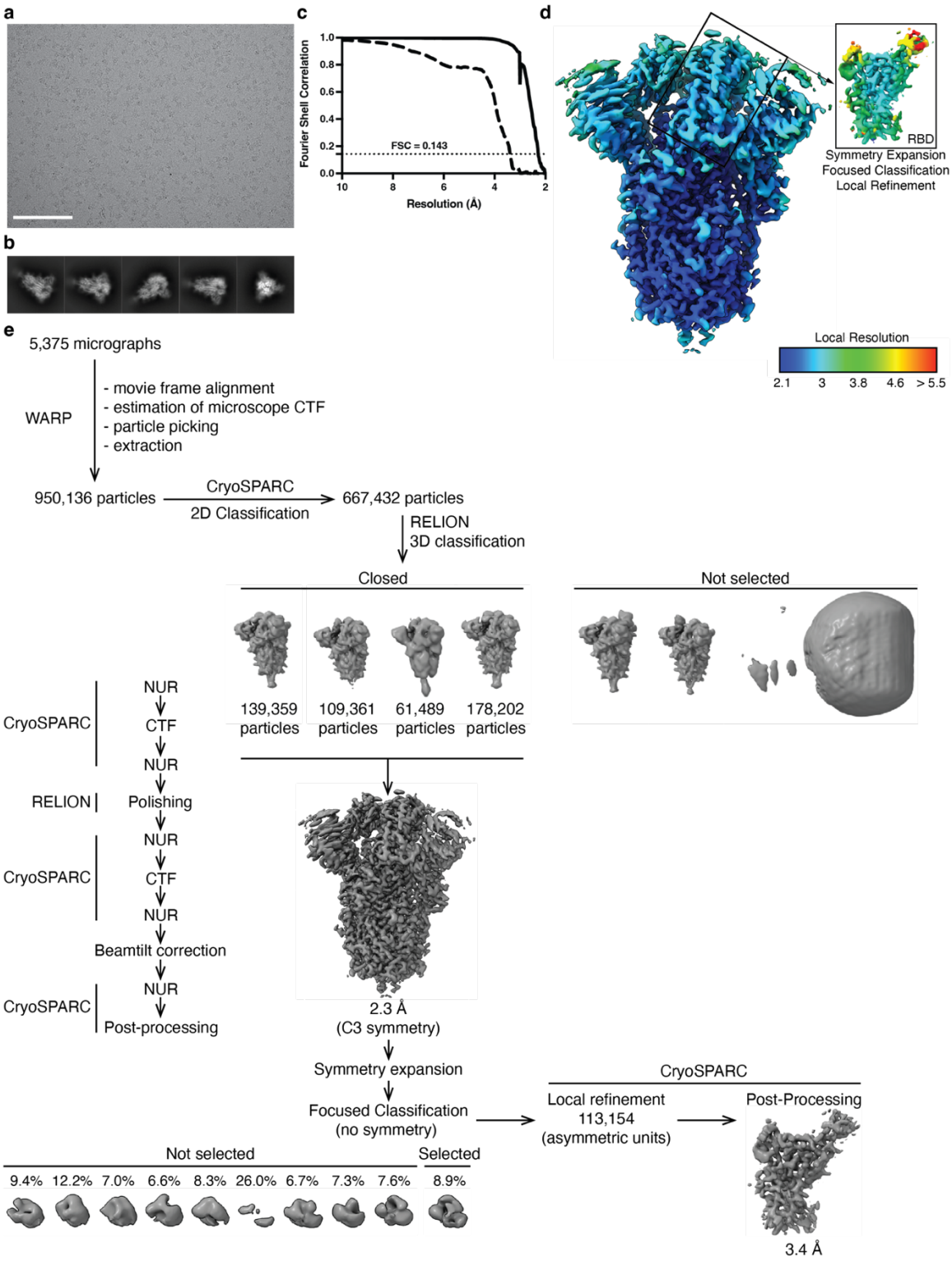

a, Representative electron micrograph and **b,** 2D class averages obtained for the SARS-CoV-2 E406W spike ectodomain. Scale bar: 100 nm. **c,** Gold-standard fourier shell correlation curves for the closed E406W S trimer (solid line) and locally refined E406W RBD (dashed line). **d,** Local resolution calculated using CryoSPARC for the E406W S ectodomain trimer (left, unsharpened map) and the locally refined RBD (right, sharpened map). **e,** cryo-EM processing workflow.

Figure 2.3. Support for the structural rearrangements in the W406 RBD with the locally refined cryo-EM map.

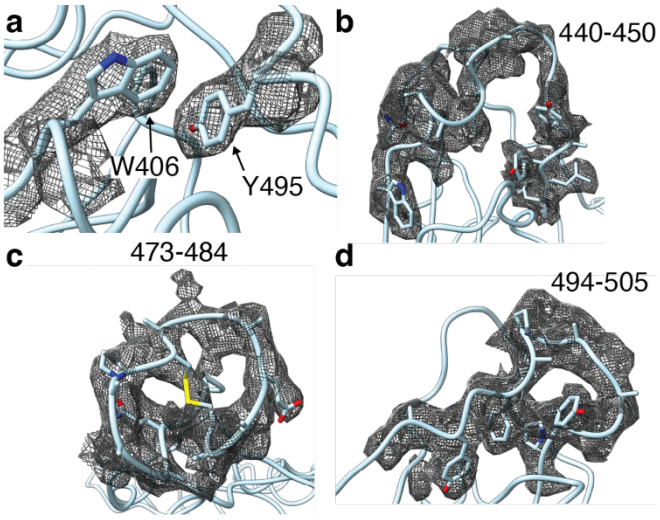

Cryo-EM map, represented as a black mesh, obtained from local refinement of the RBD and the W406 RBD model compared to show the areas in which the W406 RBD diverges most significantly from the E406 RBD, including **a,** the Y495 sidechain, **b,** residues 440-450, **c,** residues 473-484, and **d,** residues 494-505.

Figure 2.4. Repositioning of residues 443-450 in the W406 RBD interferes sterically with cilgavimab binding.

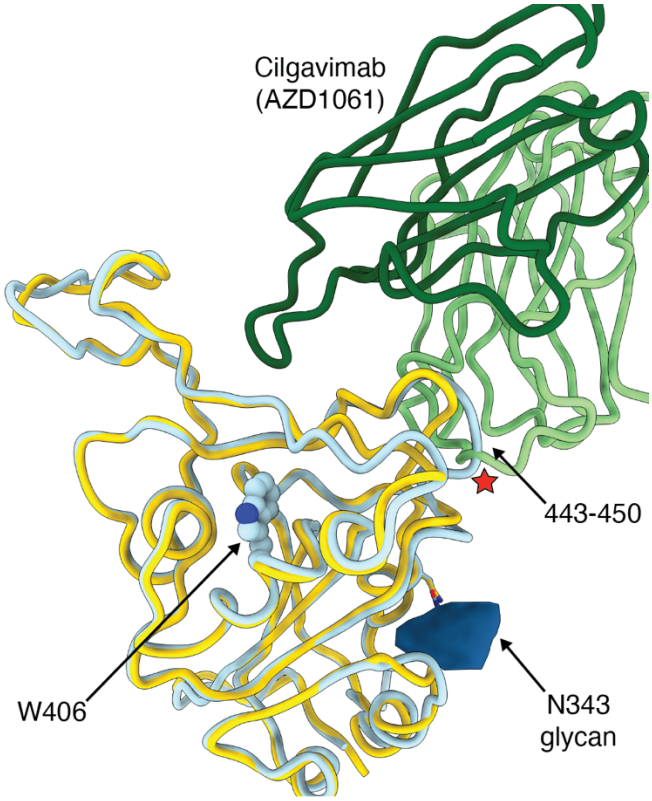

Structural superimposition of the cilgavimab (AZD1061)-bound Wuhan-Hu-1 RBD (E406, gold, PBD 7L7E) and the W406 RBD (light blue). Key reorganized regions are labeled and the steric clash is indicated by a red star.

Figure 2.5. The E406W mutation dampens ACE2 binding severely.

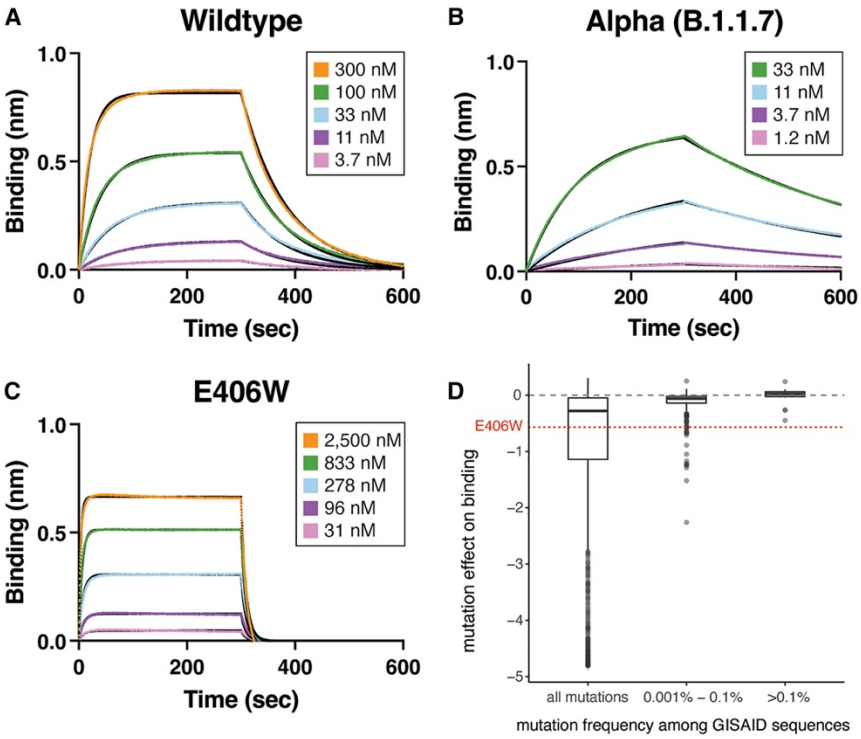

A-C, Biolayer interferometry binding analysis of monomeric human ACE2 to immobilized Wuhan-Hu-1 (A), Alpha (N501Y, B), or E406W (C) RBDs. **D,** Mutation effects on avidity for dimeric human ACE2 as measured by yeast surface display (Starr et al., 2020) for the E406W mutation and RBD mutations found in human-derived SARS-CoV-2 isolates deposited in GISAID as of 27 September 2021 across increasing frequency thresholds.

Figure 2.6. Evaluation of the neutralizing activity of several sarbecovirus broadly neutralizing mAbs and vaccine-elicited polyclonal antibodies.

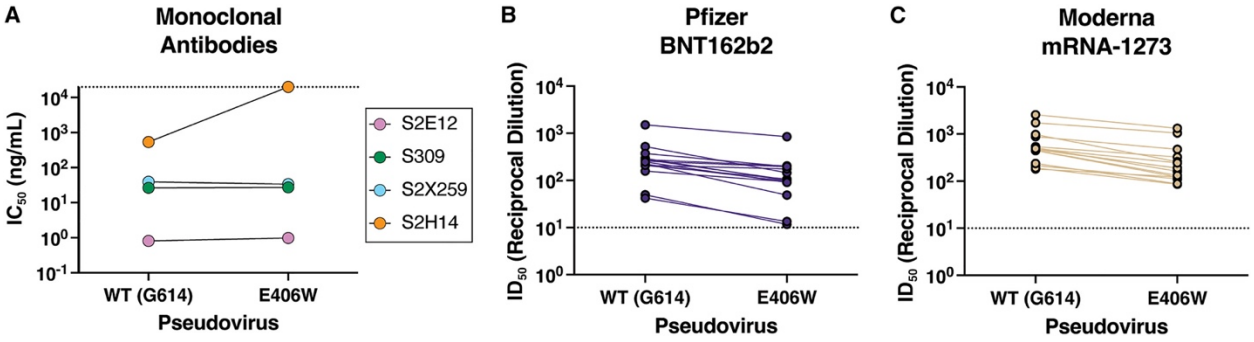

A, Neutralization potency (50% inhibition concentration, IC50) of the monoclonal antibodies S309, S2E12, S2X259, and S2H14 against VSV pseudotyped with either the wildtype (G614) or the E406W mutant spike protein. Non-neutralizing values are shown as 2 x 10^4 ng/mL, the limit of detection of the assay, as indicated by a dotted line. **b-c,** Neutralization potency (50% inhibition dilution, ID50) of sera collected from individuals vaccinated with either Pfizer Comirnaty (B) or Moderna's mRNA-1273 (C) against VSV pseudotyped with SARS-CoV-2 wildtype (G614) or E406W spike. ID50 values measured against the two pseudoviruses for each sample are connected by a line. The dotted line indicates the limit of detection of the assay.

Figure 2.7. Neutralization curves for E406W/G614 or wildtype (G614) pseudotyped VSV using four monoclonal antibodies targeting the SARS-CoV-2 RBD.

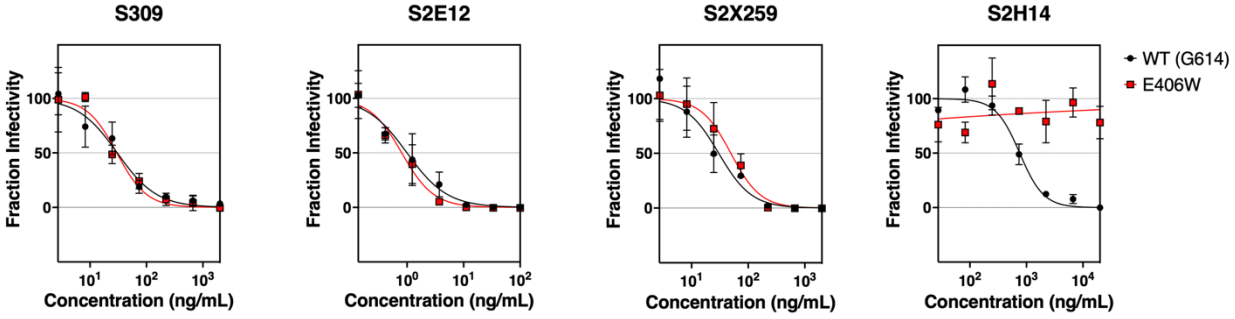

Neutralization assays were performed in triplicate and replicated twice with two batches of pseudovirus.

Figure 2.8. Neutralization curves against E406W/G614 S or wildtype (G614) S pseudotyped VSV for 30 sera samples collected from individuals vaccinated with either Pfizer BNT162b2 or Moderna mRNA1273 COVID-19 vaccines.

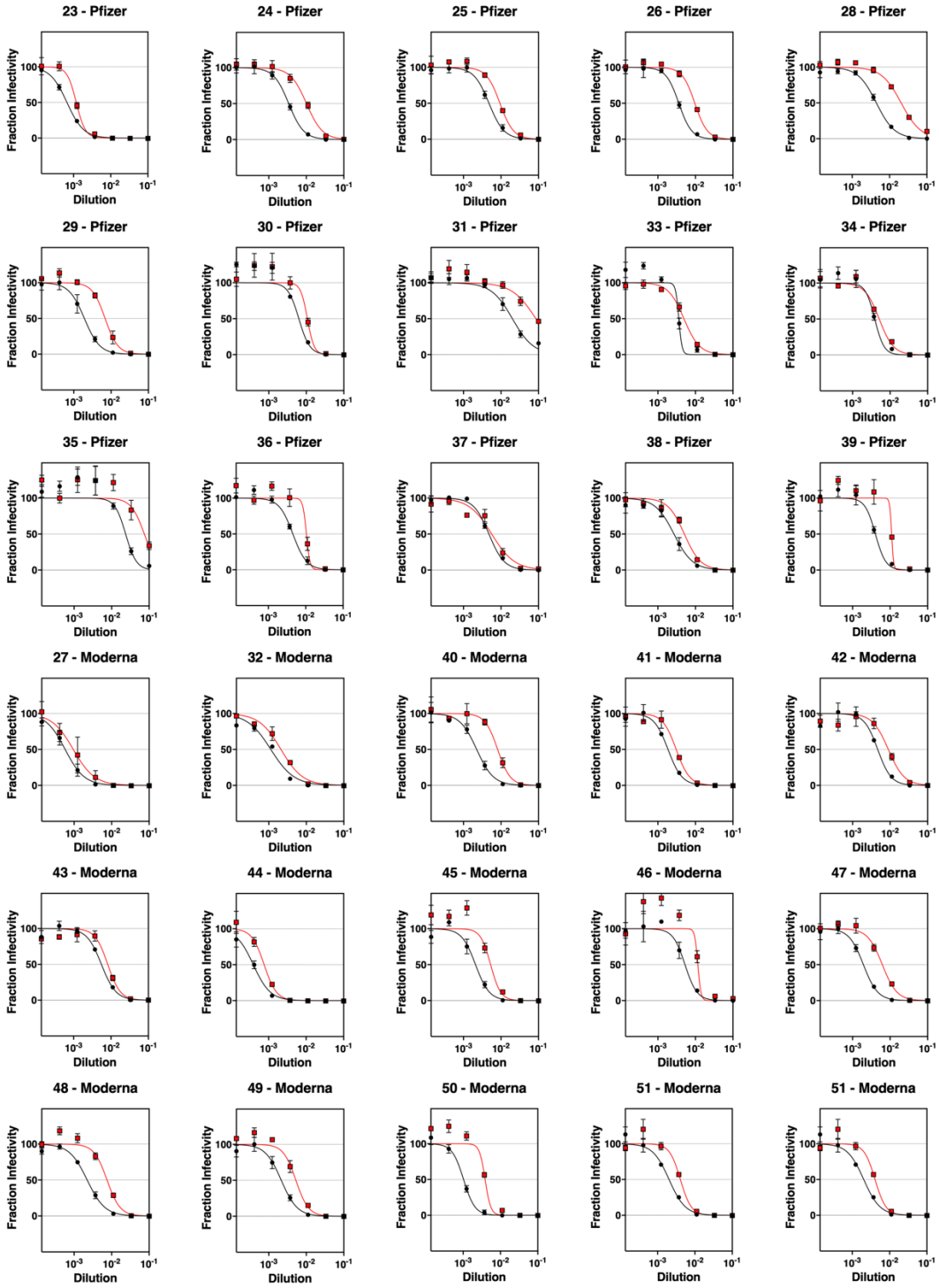

Neutralization assays were performed in triplicate and repeated at least twice with at least two distinct batches of pseudovirus.

Table 2.1. Cryo-EM data collection, refinement and validation statistics.

	SARS-CoV-2 S E406W Ectodomain (EMDB-26056) (PDB 7TPI)	SARS-CoV-2 S E406W RBD (local refinement) (EMDB-26058) (PDB 7TPK)
Data collection and processing		
Magnification	105,000	105,000
Voltage (kV)	300	300
Electron exposure (e–/Å^2)	63	63
Defocus range (μm)	0-2.6	0-2.6
Pixel size (Å)	0.843	0.843
Symmetry imposed	C3	C1
Initial particle images (no.)	950,136	1,281,585
Final particle images (no.)	427,195	113,154
Map resolution (Å) FSC threshold	2.3 0.143	3.4 0.143
Map resolution range (Å)	2.2-8.9	2.8-9.1
Refinement		
Initial model used (PDB code)	7LXY	6M0J
Model resolution (Å) FSC threshold	2.4 0.143	3.4 0.143
Map sharpening *B* factor (Å^2)	-71	-104
Model composition Non-hydrogen atoms Protein residues Ligands	 21,168 2,862 54	 1,446 194 1
B factors (Å^2) Protein Ligand	 38.08 21.98	 26.84 23.50

R.m.s. deviations		
Bond lengths (Å)	0.012	0.012
Bond angles (°)	1.434	1.867
Validation		
MolProbity score	1.01	1.02
Clashscore	2.21	0.37
Poor rotamers (%)	0.49	0
Ramachandran plot		
Favored (%)	97.95	94.27
Allowed (%)	2.05	5.21
Disallowed (%)	0	0.52

Table 2.2. Binding kinetics of the RBD to human ACE2 as measured by biolayer interferometry.

	K_D (nM)	k_{on} ($M^{-1}s^{-1}$)	k_{off} (s^{-1})
WT	93.9 ± 3.3	1.4×10^{5}	1.2×10^{-2}
Alpha	10.9 ± 0.9	2.3×10^{5}	2.5×10^{-3}
E406W	1,335 ± 195	7.6×10^{4}	1.0×10^{-1}

Values are presented as mean ± standard error.

Table 2.3. IC50 values for the four monoclonal antibodies tested against wildtype (G164) and E406W pseudoviruses.

	IC50 against WT pseudovirus (ng/mL)	IC50 against E406W pseudovirus (ng/mL)
S309	26.6 ± 3.7	27.3 ± 2.4
S2E12	0.81 ± 0.19	0.98 ± 0.17
S2X259	39.4 ± 9.2	33.8 ± 15.6
S2H14	535 ± 224	> 20,000

Values are presented as mean ± standard error.

Table 2.4. Demographic information for vaccine-elicited sera donors.

Study ID	Age	Vaccine Type	Days after second vaccination	Sex	Race	Ethnicity
23	60	Pfizer	11	M	White	Not Hispanic or Latino
24	65	Pfizer	10	M	White	Not Hispanic or Latino
25	55	Pfizer	18	M	White	Not Hispanic or Latino
26	42	Pfizer	9	F	White	Not Hispanic or Latino
27	66	Moderna	8	F	White	Not Hispanic or Latino
28	63	Pfizer	10	M	White	Not Hispanic or Latino
29	27	Pfizer	8	F	White	Not Hispanic or Latino
30	38	Pfizer	8	F	Asian	Not Hispanic or Latino
31	37	Pfizer	21	F	Black	Not Hispanic or Latino
32	36	Moderna	7	M	White	Not Hispanic or Latino
33	62	Pfizer	15	M	Pacific Islander	Not Hispanic or Latino
34	54	Pfizer	14	F	White	Not Hispanic or Latino
35	60	Pfizer	14	F	White	Not Hispanic or Latino
36	32	Pfizer	13	F	White	Not Hispanic or Latino
37	52	Pfizer	11	M	White	Not Hispanic or Latino
38	61	Pfizer	9	M	White	Not Hispanic or Latino
39	32	Pfizer	22	F	White	Not Hispanic or Latino
40	40	Moderna	20	M	White	Not Hispanic or Latino
41	64	Moderna	16	M	White	Not Hispanic or Latino
42	34	Moderna	23	F	Asian	Not Hispanic or Latino
43	22	Moderna	20	F	White	Not Hispanic or Latino
44	24	Moderna	18	F	White	Not Hispanic or Latino
45	35	Moderna	20	M	White	Not Hispanic or Latino
46	40	Moderna	24	M	White	Not Hispanic or Latino
47	55	Moderna	20	M	White	Not Hispanic or Latino
48	25	Moderna	22	M	White and Asian	Not Hispanic or Latino
49	26	Moderna	18	F	White	Not Hispanic or Latino
50	36	Moderna	27	F	Asian	Not Hispanic or Latino
51	53	Moderna	20	F	White	Not Hispanic or Latino
52	47	Moderna	21	M	White	Not Hispanic or Latino

Chapter 3. Omicron spike function and neutralizing activity elicited by a comprehensive panel of vaccines

The next two stories are centered on the Omicron lineage variants. The Omicron lineage was the first major antigenically divergent SARS-CoV-2 lineage to emerge. These variants contained far more spike protein mutations than the previously circulating variants. In the following chapter, I describe our investigations into the functional consequences of the Omicron spike protein mutations and into the capacity of vaccine-elicit plasma to neutralize this lineage of variants.

Adapted from: Bowen, J.*, Addetia, A.***,** Dang, H., Stewart, C., Brown, J., Sharkey, W., Sprouse, K., Walls, A., Mazzitelli, I., Logue, J., Franko, N., Czudnochowski, N., Powell, A., Dellota, E., Ahmed, K., Ansari, A., Cameroni, E., Gori, A., Bandera, A., Posavad, C., Dan, J., Zhang, Z., Weiskopf, D., Sette, A., Crotty, S., Iqbal, N., Corti, D., Geffner, J., Snell, G., Grifantini, R., Chu, H., Veesler, D. “Omicron spike function and neutralizing activity elicited by a comprehensive panel of vaccines.” *Science*. 2022. doi: 10.1126/science.abq0203.

3.1 Chapter Introduction

The ongoing COVID-19 pandemic has led to the emergence of severe acute respiratory syndrome coronavirus 2 (SARS-CoV-2) variants with increased transmissibility, viral fitness, and immune evasion (Collier et al., 2022; Hodcroft et al., 2021; McCallum et al., 2022; McCallum, Walls, et al., 2021, 2021; Mlcochova et al.,

2021; R. P. Payne et al., 2021; Tegally et al., 2021, 2021; Viana et al., 2022). The most recently named variant of concern, Omicron, is characterized by the greatest known genetic divergence from the ancestral virus (Wuhan-Hu-1) and consists of several sublineages, including BA.1, BA.2, BA.3, BA.4, and BA.5. BA.1 was first detected in late 2021 and rapidly replaced Delta to become the globally dominant SARS-CoV-2 strain (McCallum, Walls, et al., 2021; Mlcochova et al., 2021; Saito et al., 2022), aided by its high transmissibility and escape from neutralizing antibodies (Allen et al., 2023; Cameroni et al., 2022; Dejnirattisai et al., 2022; Meng et al., 2022; R. P. Payne et al., 2021; Schmidt et al., 2022; Starr, Greaney, Hannon, et al., 2022; Wilhelm et al., 2022). In early March of 2022, BA.2 became the most prevalent SARS-CoV-2 variant globally (Suzuki et al., 2022; Yamasoba et al., 2022) **(Fig. 3.1A)**, and the proportion of BA.2.12.1 in sequenced viruses peaked at >30% worldwide and >60% in the United States by late May of 2022 **(Fig. 3.1B)**. However, BA.4 and BA.5, which share the same spike (S) glycoprotein sequence, are expected to reach global dominance owing to their increasing prevalence and successful replacement of BA.2 in South Africa (Tegally et al., 2021) **(Fig. 3.1C)**.

The receptor-binding domain (RBD) of the SARS-CoV-2 S glycoprotein interacts with the receptor angiotensin-converting enzyme 2 (ACE2) (Hoffmann, Kleine-Weber, Schroeder, et al., 2020; Letko et al., 2020; Walls, Park, et al., 2020; Wrapp et al., 2020; P. Zhou et al., 2020), promoting S conformational changes that lead to membrane fusion and viral entry (Cai et al., 2020; Walls et al., 2017, 2019). S is the main target of neutralizing antibodies, which have been shown to be a correlate of protection against SARS-CoV-2 (Arunachalam et al., 2021; Corbett et al., 2021; Corti et al., 2021; Gilbert

et al., 2022; Greaney, Loes, Gentles, et al., 2021; Khoury et al., 2021; McMahan et al., 2021; Piccoli et al., 2020; Stamatatos et al., 2021), with RBD-targeting antibodies accounting for most neutralizing activity against vaccine-matched virus (Greaney, Loes, Gentles, et al., 2021; Piccoli et al., 2020) and nearly all cross-variant neutralizing activity (Bowen, Park, et al., 2022). SARS-CoV-2 vaccines are based on the S glycoprotein [sometimes the RBD only (Arunachalam et al., 2021; Walls et al., 2021; Walls, Fiala, et al., 2020)] or (inactivated) virus, and they utilize a variety of delivery technologies. Lipid-encapsulated prefusion-stabilized S-encoding mRNA vaccines include Moderna mRNA-1273 and Pfizer-BioNTech BNT162b2. Viral-vectored vaccines encoding for the SARS-CoV-2 S sequence include Janssen Ad26.COV2.S (human adenovirus 26), AstraZeneca AZD1222 (chimpanzee adenovirus), and Gamaleya National Center of Epidemiology and Microbiology Sputnik V (human adenovirus 26 and 5 for prime and boost, respectively). Novavax NVX-CoV2373 is a prefusion-stabilized S protein subunit vaccine formulated with a saponin-based matrix M adjuvant, whereas Sinopharm BBIBP-CorV comprises inactivated virions. The primary vaccine series consisted of two doses for all of these vaccines except for Ad26.COV2.S, which was administered as a single dose.

3.2 Impact of mutations in the Omicron spike proteins on ACE2 binding and cell fusion

We first aimed to understand how the different S mutations in the Omicron variant sublineages affect host receptor engagement and membrane fusion. Whereas the Delta RBD recognized human ACE2 with a comparable affinity to that of the Wuhan-

Hu-1 RBD [1.1-fold enhancement by biolayer interferometry (BLI) (McCallum, Walls, et al., 2021) and 1.5-fold enhancement by surface plasmon resonance (SPR)], the ACE2 binding affinity was greater for the BA.1 RBD (4.4-fold by BLI and 2.6-fold by SPR) (Cameroni et al., 2022; McCallum et al., 2022; The CITIID-NIHR BioResource COVID-19 Collaboration et al., 2021) and for the BA.2 RBD (3.7-fold by BLI and 2.3-fold by SPR) (**Fig. 3.1, D and E; Fig. 3.2 and 3.3; and Tables 3.1 and 3.2)**. The BA.2.12.1 RBD—which differs from the BA.2 RBD only by the L452Q (substitution of leucine for glutamine at position 452) mutation—had an ACE2 binding affinity similar to that of the Wuhan-Hu-1 RBD (1.1-fold and 1.7-fold enhancements determined by BLI and SPR, respectively). The ACE2 binding affinity of the BA.4/BA.5 (BA.4/5) RBD was the greatest among the RBDs evaluated in this work, with 6.1-fold and 4.2-fold increases relative to Wuhan-Hu-1, as determined by BLI and SPR, respectively (**Fig. 3.1, D and E; Fig. 3.2 and 3.3; and Tables 3.1 and 3.2)**.

We next compared the kinetics and magnitude of cell-cell fusion mediated by the Wuhan-Hu-1/G614, Delta, BA.1, BA.2, BA.2.12.2, and BA.4/5 S glycoproteins using a split green fluorescent protein (GFP) system (Kodaka et al., 2015) with VeroE6/TMPRSS2 (VeroE6 cells stably expressing TMPRSS2) target cells (expressing GFP β strands 1 to 10) and BHK-21 effector cells (expressing GFP β strand 11) and transiently transfected with S. We observed slower and markedly reduced overall fusogenicity for all tested Omicron sublineage S glycoproteins compared with Wuhan-Hu-1/G614 S and even more so relative to Delta S (Meng et al., 2022; Suzuki et al., 2022) **(Fig. 3.1, F to H; Fig. 3.4)**, despite the higher apparent BA.4/5 S cell surface expression compared with other S trimers **(Fig. 3.5)**.

3.3 Neutralization potency of vaccine-elicited plasma against Omicron variants

We next assessed the plasma neutralizing activity elicited in humans by each of the seven vaccines or SARS-CoV-2 infection and evaluated the immune evasion associated with the constellation of S mutations present in the BA.1, BA.2, BA.2.12.1, and BA.4/5 Omicron sublineages **(Table 3.3)**. We measured entry of vesicular stomatitis virus (VSV) pseudotyped with the SARS-CoV-2 Wuhan-Hu-1 S harboring the D614G, BA.1, BA.2, BA.2.12.1, or BA.4/5 mutations into VeroE6/TMPRSS2 target cells (Lempp et al., 2021) in the presence of vaccinee or convalescent plasma **(Table 3.4)**. Plasma was obtained from individuals previously infected with a Washington-1–like SARS-CoV-2 strain based on time of infection. These samples were obtained early in the pandemic, so individuals had not been vaccinated. We determined a plasma neutralizing geometric mean titer (GMT) of 39 against Wuhan-Hu-1/G614 VSV S pseudovirus, and only 5 of 24 individuals had detectable, albeit very weak, neutralizing activity against any of the four tested Omicron sublineages **(Fig. 3.6 and Fig. 3.7A)**. Plasma from subjects that received two doses of Moderna mRNA-1273 ~4 weeks apart had Wuhan-Hu-1/G614, BA.1, BA.2, BA.2.12.1, and BA.4/5 S VSV neutralizing GMTs of 633, 33, 44, 30, and 22, respectively, whereas plasma from subjects that received two doses of Pfizer BNT162b2 ~3 weeks apart had neutralizing GMTs of 340, 20, 29, 24, and 19, respectively **(Fig. 3.6 and Fig. 3.7, B and C)**. In total, 19 of 28, 21 of 28, 19 of 28, and 16 of 28 mRNA-vaccinated subjects retained neutralizing activity against BA.1, BA.2, BA.2.12.1, and BA.4/5 S VSV, respectively. The combined Moderna and Pfizer cohorts experienced ≥18-fold, ≥13-fold, ≥17-fold, and ≥23-fold GMT reductions against BA.1,

BA.2, BA.2.12.1, and BA.4/5 S VSV, respectively. A similar trend was observed for plasma from individuals that received two doses of Novavax NVX-CoV2373 (Z. Zhang et al., 2022) in a double-blinded manner; however, these plasma samples were not obtained at peak titers owing to the design of the clinical trial **(Figs. 3.8 and 3.9)**. From this group, we determined a neutralizing GMT of 252 against Wuhan-Hu-1/G614 S VSV with only 2 of 10 individuals having detectable neutralizing activity against BA.1 (GMT: 12, ≥22-fold drop), 7 of 10 against BA.2 (GMT: 15, ≥16-fold drop), 4 of 10 against BA.2.12.1 (GMT: 13, ≥20-fold drop), and 1 of 10 against BA.4/5 (GMT: 11, ≥23-fold drop) **(Fig. 3.6 and Fig. 3.7D)**. Plasma from individuals vaccinated with Janssen Ad26.COV2.S were obtained 9 to 142 days (mean, 79) after their single dose—a time frame expected to capture peak neutralizing titers (Barouch et al., 2021). This resulted in a Wuhan-Hu-1/G614 S VSV GMT of 55, and only 1 of 12 subjects had detectable plasma neutralizing activity against any of the Omicron sublineages **(Fig. 3.6 and Fig. 3.7E)**. Two doses of AZD1222 4 weeks apart induced Wuhan-Hu-1/G614, BA.1, BA.2, BA.2.12.1, and BA.4/5 S VSV neutralizing GMTs of 165, 14, 19, 15, and 14, respectively, with 13 of 16 and 4 of 16 individuals having detectable neutralizing activity against any or all tested subvariants, respectively **(Fig. 3.6 and Fig. 3.7F)**. Sputnik V vaccinee plasma after two doses had Wuhan-Hu-1/G614, BA.1, BA.2, BA.2.12.1, and BA.4/5 S VSV GMTs of 69, 13, 17, 14, and 11, respectively **(Fig. 3.6 and Fig. 3.7G)**. Detectable neutralizing activity against any or all Omicron sublineages was observed for 7 of 13 and 2 of 13 individuals, respectively. Finally, plasma from subjects vaccinated with two doses of Sinopharm BBIBP-CorV had a neutralizing GMT against G614 S VSV of 135, with 3 of 12 samples retaining detectable neutralizing activity against BA.1

(GMT: 14), 7 of 12 against BA.2 (GMT: 17), 5 of 12 against BA.2.12.1 (GMT: 15), and 4 of 12 against BA.4/5 (GMT: 11) **(Fig. 3.6 and Fig. 3.7H)**. Overall, these data underscore the magnitude of evasion of polyclonal plasma neutralizing antibody responses for Omicron sublineages in humans after primary vaccine series or infection [resulting from the accumulation of S mutations (Cameroni et al., 2022)], with a subtle but consistently more marked effect for BA.1 and even more so for BA.4/5 compared with BA.2 and BA.2.12.1.

3.4 An additional booster dose increases the neutralizing activity in vaccine-elicited plasma against Omicron variants

The emergence of the SARS-CoV-2 Delta and subsequently Omicron variants of concern led to an increasing number of reinfections and vaccine breakthrough cases (Bates et al., 2022; Collier et al., 2022; Y.-J. Park, Pinto, et al., 2022; Walls et al., 2022). Public health policies were therefore updated worldwide to recommend administration of an additional vaccine dose (booster) several months after the primary vaccine series, which has been shown to increase the breadth and potency of neutralizing antibodies (Cameroni et al., 2022; Dejnirattisai et al., 2022; Garcia-Beltran et al., 2022; Walls et al., 2022). We thus assessed and compared the benefits provided by homologous or heterologous vaccine boosters on vaccinee plasma neutralizing activity against Wuhan-Hu-1/G614, BA.1, BA.2, BA.2.12.1, and BA.4/5 S VSV pseudotypes. Plasma samples of subjects that received three mRNA vaccine doses had neutralizing GMTs of 2371, 406, 448, 472, and 392 against Wuhan-Hu-1/G614, BA.1, BA.2, BA.2.12.1, and BA.4/5 S VSV, respectively **(Fig. 10 and Fig. 3.11A)**. The five- to sixfold potency losses against

these variants are marked improvements over the >13- to >23-fold reductions observed after two vaccine doses, underscoring an increase in overall neutralizing antibody potency and breadth (Cameroni et al., 2022; Walls et al., 2022). Individuals vaccinated with two doses of NVX-CoV2373 followed by a booster of mRNA-1273 (1 of 5 individuals) or NVX-CoV2373 (4 of 5 individuals) had neutralizing GMTs of 6978 for Wuhan-Hu-1/G614, 505 for BA.1 (14-fold reduction), 948 for BA.2 (sevenfold reduction), 935 for BA.2.12.1 (sevenfold reduction), and 330 for BA.4/5 (21-fold reduction) (Fig. 3 and fig. S8B). Plasma from individuals who received one dose of Ad26.COV2.S followed by either a homologous Ad26.COV2.S (12 of 14 individuals) or a heterologous BNT162b2 booster (2 of 14 individuals) ~4 months later had neutralizing GMTs of 363, 23, 50, 46, and 29 against Wuhan-Hu-1/G614, BA.1, BA.2, BA.2.12.1, and BA.4/5 S VSV, respectively, corresponding to dampening ranging between ≥7- and ≥16-fold with 9 of 14 individuals maintaining neutralizing activity against all sublineages **(Fig. 3.10 and Fig. 3.11C)**. We also investigated individuals that received two doses of AZD1222 4 weeks apart followed by a BNT162b2 (17 of 18 individuals) or mRNA-1273 (1 of 18 individuals) booster ~6 months later. This cohort had respective neutralizing GMTs of 2167, 186, 269, 273, and 135 against Wuhan-Hu-1/G614, BA.1, BA.2, BA.2.12.1, and BA.4/5 S VSV, corresponding to 8- to 16-fold potency reductions **(Fig. 3.10 and Fig. 3.11D)**. Individuals vaccinated with two doses of Sputnik V and boosted with AZD1222 (11 of 12 individuals) or BNT162b2 (1 of 12 individuals) ~9 months later had neutralizing GMTs of 351, 68, 77, 72, and 35 for Wuhan-Hu-1/G614, BA.1, BA.2, BA.2.12.1, and BA.4/5, respectively, amounting to 5- to 10-fold reductions of potency **(Fig. 3.10 and Fig. 3.11E)**. BBIBP-CorV vaccinees boosted with either BNT162b2 (14 of 18

individuals) or mRNA-1273 (4 of 18 individuals) had GMTs of 2047 for G614, 439 for BA.1 (fivefold reduction), 375 for BA.2 (fivefold reduction), 430 for BA.2.12.1 (fivefold reduction), and 252 for BA.4/5 (eightfold reduction) **(Fig. 3.10 and Fig. 3.11F)**. The marked improvement in plasma neutralizing activity for subjects that received a booster dose over those that did not highlights the importance of vaccine boosters for eliciting potent neutralizing antibody responses against Omicron sublineages.

To assess the effect of target cell lines on apparent Omicron immune escape, we compared the aforementioned VeroE6/TMPRSS2 cells (Lempp et al., 2021) with a stable ACE2-overexpressing HEK293T cell line (HEK293T/ACE2) (Crawford et al., 2020) to determine plasma neutralizing activity for a cohort of mRNA-vaccinated individuals. After primary vaccine series, only three subjects had detectable neutralizing activity against any of the tested Omicron sublineage VSV pseudotypes when using HEK293T/ACE2 target cells. By contrast, all but one subject had detectable, albeit very weak, neutralizing activity against Omicron VSV pseudotypes using VeroE6/TMPRSS2 target cells, resulting in >17-fold, >14-fold, >20-fold, and >22-fold reductions against BA.1, BA.2, BA.2.12.1, and BA.4/5, respectively **(Figs. 3.12A and 3.13A)**. After a booster dose, we observed respective 7-fold, 7-fold, 11-fold, and 13-fold reductions of neutralizing activity against BA.1, BA.2, BA.2.12.1, and BA.4/5 VSV pseudotypes using HEK293T/ACE2 target cells, as compared with respective sevenfold, sixfold, fivefold, and eightfold reductions when using VeroE6/TMPRSS2 target cells **(Figs. 3.12B and 3.13B)**. This indicates that the target cell lines used in neutralization assays may affect the observed plasma neutralizing escape of SARS-CoV-2 variants, which may be further compounded on the basis of preferential entry routes (Hoffmann, Kleine-Weber,

& Pöhlmann, 2020; Hoffmann, Kleine-Weber, Schroeder, et al., 2020; Meng et al., 2022).

3.5 Chapter Discussion

We report that the BA.1, BA.2, BA.2.12.1, and BA.4/5 Omicron sublineages, which account for >99% of all infections worldwide over the first half of 2022, have increased ACE2 binding affinity, have decreased fusogenicity, and markedly evade neutralizing antibody responses relative to the Wuhan-Hu-1 and Delta strains (McCallum, Walls, et al., 2021). Collectively, these data suggest that enhanced receptor engagement and immune evasion are key changes that may have promoted the rapid spread of these Omicron sublineages and could contribute to the current rise in prevalence of BA.4 and BA.5.

The development of life-saving vaccines is regarded as one of humanity's greatest medical and scientific achievements, which is exemplified by COVID-19 vaccines (Corbett et al., 2020; Walsh et al., 2020; Wu et al., 2021). Primary COVID-19 vaccine regimens or infection-elicited plasma neutralizing activity was severely dampened by Omicron sublineages BA.1, BA.2, BA.2.12.1, and BA.4/5. However, administration of a booster dose increased neutralizing antibody titers and breadth against all Omicron sublineages to appreciable levels regardless of the vaccine evaluated, concurring with findings for BA.1 (Cameroni et al., 2022; Dejnirattisai et al., 2022; Garcia-Beltran et al., 2022; Meng et al., 2022; Pérez-Then et al., 2022; Planas et al., 2022; Walls et al., 2022). These results are consistent with previous studies demonstrating that a third vaccine dose results in the recall and expansion of

preexisting SARS-CoV-2 S-specific memory B cells, as well as de novo induction, leading to production of neutralizing antibodies with enhanced potency and breadth against variants (Goel et al., 2022; Muecksch et al., 2022). Vaccinees receiving two doses of Ad26.COV2.S (4 months apart) had lesser Omicron immune escape than that in other two-dose vaccine recipients (3 to 4 weeks between doses) but greater than that observed in three-dose vaccinees. These findings suggest that the time interval between immunizations may affect the breadth and potency of vaccine-elicited plasma neutralizing activity and that a third dose may be beneficial for this cohort as well (Meng et al., 2022; Parry et al., 2022; R. P. Payne et al., 2021; Voysey et al., 2021). Moreover, the induction by several currently available vaccines of robust cross-reactive cellular immunity against SARS-CoV-2 Omicron is likely playing a key role in the retained protection observed against severe disease (J. Liu et al., 2022; Tarke et al., 2022).

As SARS-CoV-2 progressively becomes endemic in the human population, vaccination strategies will need to be carefully considered and optimized to provide long-lasting immunity. So far, elicitation of high titers of variant-neutralizing antibodies and protection against severe disease can be accomplished by dosing with the Wuhan-Hu-1 S antigen, as shown in animal models and studies of vaccine efficacy in humans (Accorsi et al., 2022; Andrews et al., 2022; Y.-J. Park, Pinto, et al., 2022; Walls et al., 2022). In fact, an Omicron BA.1 (or other variant) S boost does not offer mice or nonhuman primates significantly more BA.1 protection than a Wuhan-Hu-1 S boost (Arunachalam et al., 2022; Gagne et al., 2022; Hawman et al., 2022; I.-J. Lee et al., 2022; Ying et al., 2022), and Omicron primary infections elicit neutralizing antibody and memory responses of narrow breadth (Richardson et al., 2022; Rössler et al., 2022;

Stiasny et al., 2022). However, continued SARS-CoV-2 evolution will accentuate the antigenic divergence from the ancestral strain, and it is unknown whether vaccines based on Wuhan-Hu-1 S alone will provide satisfactory protection, either as boosters in vaccinated or infected individuals or as an initial vaccine in naïve individuals (mainly children). The recent evaluation of intranasal vaccine administration could also be important to not only prevent severe disease but also curtail viral infection and transmission through induction of mucosal immunity (Hassan et al., 2021; Langel et al., 2022; Mao et al., 2022; Oh et al., 2021). For these reasons, it is important to monitor new variants, assess the effectiveness of currently available vaccines, and continue to test and implement new vaccination strategies that may provide stronger, longer-lasting, or broader protection against SARS-CoV-2 and the entire sarbecovirus subgenus (Cohen et al., 2021; Martinez et al., 2021; Walls et al., 2021).

3.6 Methods

Variant incidence analysis

Average daily prevalence for Alpha (containing B.1.1.7 and all Q sublineages), Delta (containing B.1.617.2 and all AY sublineages), BA.1 (containing all BA.1 sublineages), BA.2 (containing all BA.2 sublineages, including BA.2.12.1), BA.2.12.1, BA.4 (containing all BA.4 sublineages), and BA.5 (containing all BA.5 sublineages) were obtained from GISAID using outbreak.info and RStudio and plotted using GraphPad PRISM software version 9.4.0.

Cell lines

Cell lines used in this study were obtained from ThermoFisher Scientific (HEK293T), Kerafast (BHK-21 clone WI-2), or were kindly gifted by Florian Lempp (VeroE6/TMPRSS2 cells (Lempp et al., 2021)) or Jesse Bloom (HEK293T/ACE2) (Crawford et al., 2020). Cell lines stably expressing components of the split GFP system were generated as described below. None of the cell lines used were authenticated ortested for mycoplasma contamination.

Generation of split GFP stable lines

To generate cell lines stably expressing either GFP1-10 or GFP11, MLV retrovirus was generated as previously described (Walls, Park, et al., 2020) using either the transfer vector pQCXIP-GFP1-10 (Addgene; a gift from Yutaka Hatat) or pQCXIP-BSR-GFP11 (Addgene; a gift from Yutaka Hatat) (Kodaka et al., 2015). BHK-21 or Vero/TMPRSS2 were transduced with MLV-GFP1-10 or MLV-GFP11, respectively, and stable lines were selected for using 2 µg/mL of puromycin or 4 µg/mL of blasticidin. The BHK-21-GFP1-10 line was maintained in DMEM supplemented with 10% FBS, 1% Pen-strep, and 2 µg/mL puromycin. The Vero/TMPRSS2-GFP11 line was maintained in DMEM supplemented with 10% FBS, 1% Pen-strep, 8 µg/mL puromycin, and 4 µg/mL blasticidin.

Sample donors

Convalescent plasma, Ad26.COV2.S, and some BNT162b2 samples were obtained from the HAARVI study approved by the University of Washington Human Subjects Division Institutional Review Board (STUDY00000959). mRNA-1273 and the

rest of BNT162b2 samples were obtained from individuals enrolled in the UWARN: COVID-19 in WA study approved by the University of Washington Human Subjects Division Institutional Review Board (STUDY00010350). AZD1222 samples were obtained from the PolImmune-COVID study conducted by INGM and IRCCS Ca' Granda Ospedale Maggiore Policlinico of Milan, approved by INMI “Lazzaro Spallanzani” Ethics Committee (286_2021). Samples from NVX-CoV2373 immunized individuals were collected in the San Diego region by the La Jolla Institute for Immunology (Z. Zhang et al., 2022). This work was approved by the institutional review board (IRB) of the La Jolla Institute (IRB#: VD-214). Sputnik V samples were obtained from Samples from NVX-CoV2373 immunized individuals were collected in the San Diego region by the La Jolla Institute for Immunology (Z. Zhang et al., 2022). This work was approved by the institutional review board (IRB) of the La Jolla Institute (IRB#: VD-214). Sputnik V samples were obtained from healthcare workers at the hospital de Clínicas "José de San Martín", Buenos Aires, Argentina. BBIBP-CorV samples were obtained from Aga Khan University, Karachi, Pakistan. Demographic data for these individuals are summarized in Table S4. All samples were tested for binding to the SARS-CoV-2 nucleocapsid by ELISA and plasma with area under the curve values ≥4.0 were excluded from the neutralization assay due to likely prior infection (fig. S11-12). Excluded samples (with predicted prior infection) included two individuals that received two Sputnik V doses and two individuals that received two Sputnik V doses followed by a single AZD1222 dose.

Plasmid construction

Full length S constructs used for pseudovirus production: the SARS-CoV-2 G614 S (YP 009724390.1) gene was placed into the HDM vector with a 21 residue C-terminal deletion, as previously described (McCallum, Walls, et al., 2021; Ou et al., 2020; Walls et al., 2021). The plasmids encoding the SARS-CoV-2 Omicron S variants BA.1 and BA.2 were generated by overlap PCR mutagenesis of the wildtype plasmid, pcDNA3.1(+)-spike-D19 (Cameroni et al., 2022; Hsieh et al., 2020). The SARS-CoV-2 BA.2.12.1 and BA.4/5 Omicron subvariant S genes were subcloned by Genscript via mutagenesis of the G614 S construct.

Proteins used for BLI: the SARS-CoV-2 Wuhan-Hu-1 RBD construct was synthesized by GenScript into pcDNA3.1- with an N-terminal mu-phosphatase signal peptide and a C-terminal octa-histidine tag, flexible linker, and avi tag (GHHHHHHHHGGSSGLNDIFEAQKIEWHE). The boundaries of the construct are N-328RFPN331 and 528KKST531-C (Walls, Fiala, et al., 2020). The SARS-CoV-2 Delta (B.1.617.2) RBD (L452R, T478K) construct and the SARS-CoV-2 Omicron BA.1 RBD construct (G339D, S371L, S373P, S375F, K417N, N440K, G446S, S477N, T478K, E484A, Q493R, G496S, Q498R, N501Y, Y505H) are described as above and were cloned into the CMVR plasmid by GenScript. The SARS-CoV-2 Omicron BA.2 RBD (G339D, S371F, S373P, S375F, T376A, D405N, R408S, K417N, N440K, S477N, T478K, E484A, Q493R, Q498R, N501Y, Y505H) construct was synthesized by Genscript into pcDNA3.1(+) with a BM40+A (for Kozak) signal peptide and a C-terminal avi tag, flexible linker, and octa-histidine tag (GGLNDIFEAQKIEWHEGSGHHHHHHHH*). The boundaries of the construct are N-328RFPN331 and 528KKST531-C. Genscript mutagenized the BA.2 RBD construct to

produce the SARS-CoV-2 BA.2.12.1 (BA.2 mutations with L452Q) and BA.4/5 (BA.2 mutations with L452R, F486V, R493Q (Wuhan-Hu-1 reversion)) RBD constructs.

Proteins used for SPR: The SARS-CoV-2 Wuhan-Hu-1 RBD construct contains S residues 328- 531 (GenBank NC_045512.2) with an N-terminal signal peptide and a C-terminal 8xHis-AviTag. RBDs from other SARS-CoV-2 variants were obtained by Gibson Assembly (New England Biolabs) or In-Fusion (Takara) using the digested wildtype plasmid and gBlocks Gene Fragments (IDT) encoding the variant RBD sequences. All plasmids were verified by sequencing. The ACE2 construct encodes for residues 19-615 from Uniprot Q9BYF1 with an N-terminal signal peptide and a C-terminal thrombin cleavage site-TwinStrep-10xHis-GGG-tag.

Recombinant protein production for BLI and ELISA

SARS-CoV-2 S or RBDs were produced in Expi293F Cells (ThermoFisher Scientific) grown in suspension using Expi293 Expression Medium (ThermoFisher Scientific) at 37°C in a humidified 8% CO2 incubator rotating at 130 rpm. Cells grown to a density of 3 million cells per mL were transfected using the ExpiFectamine 293 Transfection Kit (ThermoFisher Scientific) and cultivated for 3-5 days. Proteins were purified from clarified supernatants using a nickel HisTrap HP affinity column (Cytiva) and washed with ten column volumes of 20 mM imidazole, 25 mM sodium phosphate pH 8.0, and 300 mM NaCl before elution on a gradient to 500 mM imidazole, 25 mM sodium phosphate pH 8.0, and 300 mM NaCl. Proteins were buffer exchanged into 20 mM sodium phosphate pH 8 and 100 mM NaCl and concentrated using centrifugal filters (Amicon Ultra) before being flash frozen.

Recombinant protein production for SPR assays

SARS-CoV-2 RBDs were expressed in Expi293F cells (Thermo Fisher Scientific) at 37 °C and 8% CO2. Transfections were performed using the ExpiFectamine 293 Transfection Kit (Thermo Fisher Scientific). Cell culture supernatants were harvested five days after transfection by spinning at 4,000 xg for 20 min. Supernatants were then filtered through a 0.22-μm filter and supplemented with 10x PBS to a final concentration of 2.5x PBS (342.5 mM NaCl, 6.75 mM KCl and 29.75 mM phosphates). SARS-CoV-2 RBDs were purified using HisPur Cobalt resin (Thermo Fisher Scientific) or 5 ml HisTALON Superflow cartridges (Takara) followed by buffer exchange into PBS using Amicon centrifugal filters (MilliporeSigma) or by size exclusion chromatography using a Superdex 200 Increase 10/300 GL column (Cytiva). Recombinant human ACE2 was expressed in Expi293F cells at 37°C and 8% CO2. Transfection was performed using the ExpiFectamine 293 transfection kit (Thermo Fisher Scientific). Cell culture supernatant was collected 7-8 days after transfection and supplemented to a final concentration of 80 mM Tris-HCl pH 8.0, 100 mM NaCl, and then incubated with BioLock (IBA GmbH) solution. ACE2 was purified using a 1 mL StrepTrap HP column (Cytiva) followed by size exclusion chromatography using a Superdex 200 Increase 10/300 GL column (Cytiva) pre-equilibrated in PBS.

Pseudotyped VSV production

SARS-CoV-2 G614 and Omicron BA.1, BA.2, BA.2.12.1, and BA.4/5 pseudotypes were prepared similarly as previously described (McCallum, Walls, et al.,

2021). Briefly, HEK293T cells seeded in poly-D-lysine-coated 100 mm dishes at ~75 % confluency were washed five times with Opti-MEM and transfected using 24 µg of the S glycoprotein plasmid with Lipofectamine 2000 (Life Technologies). After 5 h at 37°C, media supplemented with 20% FBS and 2% PenStrep was added. After 20 hours, cells were washed five times with DMEM and cells were transduced with VSVΔG-luc before a 2 h incubation at 37°C. Infected cells were then washed an additional five times with DMEM prior to adding media supplemented with anti-VSV-G antibody (I1-mouse hybridoma supernatant diluted 1:25, from CRL-2700, ATCC) to reduce parental background. After 18-24 h, the supernatant was harvested and clarified by low-speed centrifugation at 2,500 g for 10 min. The supernatant was then filtered (0.45 µm) and concentrated 10 times using a 30 kDa centrifugal concentrator (Amicon Ultra). The pseudotypes were then aliquoted and frozen at -80 °C.

Pseudotyped VSV neutralization assay

To evaluate neutralization of SARS-CoV-2 G614 and Omicron BA.1, BA.2, BA.2.12.1, and BA.4/5 pseudotypes by plasma of vaccinees or previously infected individuals, VeroE6/TMPRSS2 or HEK293T/hACE2 cells in DMEM supplemented with 10% FBS, 1% PenStrep, and 8 ug/mL puromycin were seeded at 60-70% confluency into white clear-bottom 96 well plates (Corning) and incubated at 37°C. The following day, a half-area 96-well plate (Greiner) was prepared with eight 3-fold serial plasma dilutions. An equal volume of DMEM with pseudovirus and 1:20 anti- VSV-G antibody (I1-mouse hybridoma supernatant from CRL-2700, ATCC) was then added to the half-area plate. Added pseudovirus was 1:15-1:50 depending on the batch to normalize

entry levels, and the same dilution was added regardless of target cell line. The mixture was incubated at room temperature for 20-30 minutes. Media was removed from the cells and 40 µL from each well (containing plasma and pseudovirus) was transferred to the 96-well plate seeded with Vero/TMPRSS2 cells and incubated at 37°C for 2 h. After 2 h, an additional 40 µL of DMEM supplemented with 20% FBS and 2% PenStrep was added to the cells. After 16-20 h, 40 µL of One-Glo-EX substrate (Promega) was added to each well and incubated on a plate shaker in the dark for 5 min. Relative luciferase units were read using a Biotek plate reader. Relative luciferase units were plotted and normalized in Prism (GraphPad): 100% neutralization being cells lacking pseudovirus and 0% neutralizing being cells containing virus but lacking plasma. Prism (GraphPad) nonlinear regression with "[inhibitor] versus normalized response with a variable slope" was used to determine ID50 values from curve fits with 2-3 repeats. 2-4 biological replicates consisting of distinct pseudovirus batches were carried out for each sample.

Cell-cell Fusion Assay

The day prior to the cell fusion assay, Vero-TMPRSS2-GFP11 cells were split into 96-well, glass bottom, black walled plates (CellVis) at a density of 18,000 cells per well. BHK-21-GFP1-10 cells were split into 6-well plates at a density of 1x106 cells per well. The following day, the growth media was removed and replaced with DMEM containing 10% FBS and 1% Pen-strep and the cells were transfected with 4 µg of S protein using Lipofectamine 2000 (Life Technology). Twenty- four hours after transfection, BHK-21-GFP1-10 expressing the S protein were washed three times using FluoroBrite DMEM (Thermo Fisher) and detached using an enzyme-free cell

dissociation buffer (Gibco). The Vero/TMPRSS2-GFP11 were washed three times with FluoroBrite DMEM and 12,000 BHK-21-GFP1-10 cells were plated on top of the Vero/TMPRSS2-GFP11 cells. The cells were incubated at 37°C for 18 h and then imaged with a Cytation 7 Imager (BioTek). Fusogenicity was determined by measuring the area showing GFP fluorescence for each image using Gen5 Image Prime v3.11 software and comparisons between the different S variant proteins were assessed using the Wilcoxon Rank Sum Test in Prism 9.

To measure S expression at the surface of BHK-21-GFP1-10 cells, 1x106 cells were collected by centrifugation at 1,000 x g for 5 mins. The cells were washed once with flow staining buffer (1% BSA, 1 mM EDTA, 0.1% NaN3 in PBS) and labeled with 250 µg/mL of S2L20 (McCallum, De Marco, et al., 2021), for 45 mins, an NTD-directed antibody that binds to all currently characterized SARS-CoV-2 variants. The cells were washed twice with flow staining buffer and labeled with a PE-conjugated anti-Human IgG Fc antibody (Thermo Fisher) for 30 mins. The cells were washed twice with flow staining buffer and once with PBS. The cells were fixed with 2% paraformaldehyde for 15 mins and washed twice with PBS. The labeled cells were analyzed using a BD FACSAria III. Cells were gated on singleton events and a total of 10,000 singleton events were collected for each sample. The fraction of S- positive cells was determined in FlowJo 10.8.1 by gating singleton events for the mock transfected cells on PE intensity.

Biolayer interferometry

All steps of the affinity measurements using biolayer interferometry were carried out at 30oC with a shaking speed of 1,000 r.p.m. Biotinylated Wuhan-Hu-1, Delta, BA.1, BA.2, BA.2.12.1, or BA.4/5 RBDs were diluted to a concentration of 5 ng/μL in 10X kinetics buffer and loaded onto pre- hydrated streptavidin biosensors to a 1 nm total shift. The loaded tips were dipped into a 1:3 dilution series of monomeric human ACE2 starting at 900 nM or 300 nM for 300 seconds followed by dissociation in 10X kinetics buffer for 300 seconds. The resulting data were baseline subtracted and curves were globally fitted using a 1:1 binding model with Octet Data Analysis HT software v12.0 and plotted in GraphPad Prism 9.

Surface plasmon resonance

Measurements were performed using a Biacore T200 instrument. A CM5 chip with covalently immobilized anti-Avi polyclonal antibody (GenScript, Cat #: A00674-40) was used for surface capture of His-Avi tag-containing RBDs. Running buffer was HBS-EP+ pH 7.4 (Cytiva) and measurements were performed at 25℃. Experiments were performed with a 4-fold dilution series of monomeric ACE2 protein: 11.11, 33.33, 100, 300 mM and were run as single-cycle kinetics. Data were double reference-subtracted and fit to a binding model using Biacore Evaluation software. The 1:1 binding model was used to estimate the kinetics parameters. Each RBD-ACE2 pair were measured in at least 4 replicates consisting of a single biological replicate for the BA.1 RBD and two for all other tested RBDs.

Enzyme-linked immunosorbent assay (ELISA)

30 µL of 3 µg/mL prefusion SARS-CoV-2 nucleocapsid protein (The Native Antigen Company) was diluted in PBS and incubated on a 384-well Nunc Maxisorp plate (ThermoFisher 464718) for one hour at 37℃. Plates were slapped dry before addition of 80 µL blocker Casein in PBS (ThermoFisher) and incubation for one hour at 37℃. Plates were slapped dry and a 1:4 serial dilution of plasma in 30 µL TBST was added and incubated for one hour at 37℃. Plates were slapped dry and washed 4x with TBST using a BioTek plate washer followed by addition of Invitrogen anti-Human IgG (ThermoFisher A18817) and one hour incubation at 37℃. Plates were once again slapped dry and washed 4x with TBST before addition of room temperature TMB Microwell Peroxidase (Seracare 5120-0083). The reaction was quenched after 1-2 minutes with 1 N HCl and the absorbance at 450nm (A450) of each well was read using a BioTek plate reader. The x axes were log transformed and Prism (GraphPad) “Area Under Curve” was used to determine binding strength.

3.7 Figures & Tables

Figure 3.1. Omicron sublineage RBDs bind ACE2 with enhanced affinity but exhibit impaired S-mediated fusogenicity relative to the ancestral virus.

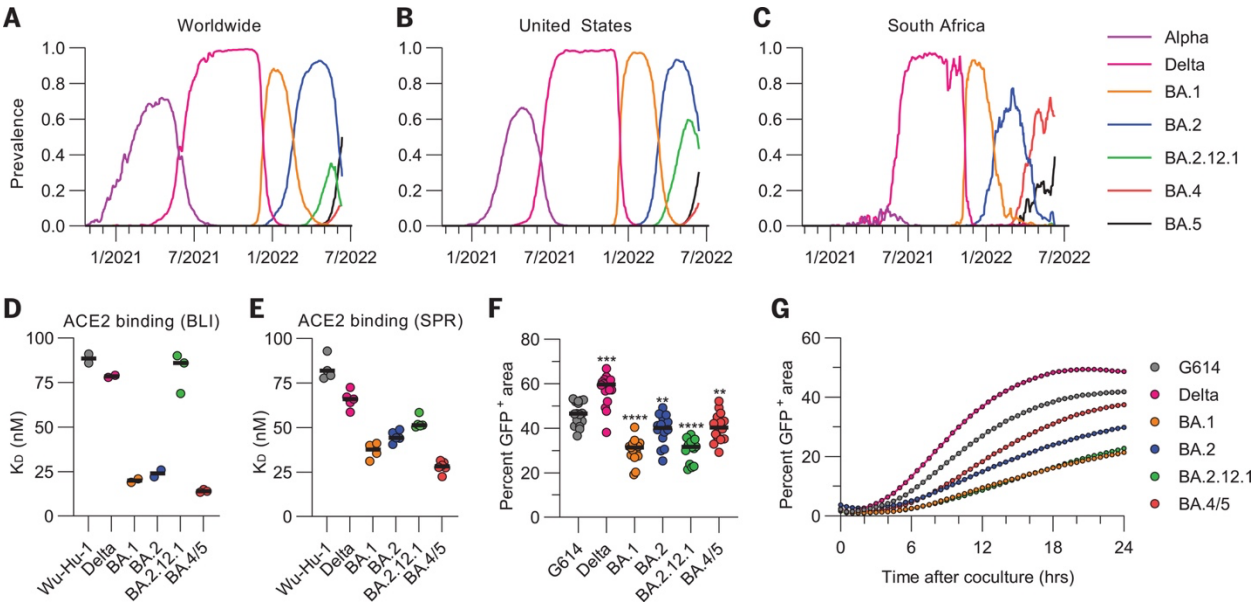

(**A to C**) Prevalence of the different variants of concern measured globally (**A**), in the United States (**B**), or in South Africa (**C**). Alpha comprises B.1.1.7 and all Q sublineages; Delta comprises B.1.617.2 and all AY sublineages; and BA.1, BA.2, BA.4, and BA.5 comprise their respective sublineages (including BA.2.12.1 for BA.2). Prevalence calculations rely on shared GISAID (Global Initiative on Sharing Avian Influenza Data) sequences and may be biased by sampling. (**D and E**) Equilibrium dissociation constants (K_D) of binding of the monomeric ACE2 ectodomain to immobilized biotinylated Wuhan-Hu-1, Delta, BA.1, BA.2, BA2.12.1, and BA.4/5 RBDs assessed by BLI (**D**) or SPR (**E**). Data presented are the results of at least two independent biological replicates for BLI and for SPR (except for the BA.1 RBD SPR data, which come from four technical replicates). (**F**) Quantification of cell-cell fusion after 24 hours mediated by Wuhan-Hu-1/G614, Delta, BA.1, BA.2, BA.2.12.1, and BA.4/5 S glycoproteins expressed as the fraction of the total area with GFP fluorescence assessed using a split GFP system. Data are from 16 fields of view from a single experiment and are representative of results obtained from two independent biological replicates. Comparisons between fusion mediated by the Wuhan-Hu-1/G614 S and other S variants were completed using the Wilcoxon rank sum test. $^{**}P < 0.01$; $^{***}P < 0.001$; $^{****}P < 0.0001$. (**G**) Kinetics of cell-cell fusion mediated by Wuhan-Hu-1/G614, Delta, BA.1, BA.2, BA.2.12.1, and BA.4/5 S glycoproteins expressed as the fraction of the total area with GFP fluorescence assessed using a split GFP system.

Figure 3.2. Biolayer interferometry binding analysis of monomeric human ACE2 to RBDs.

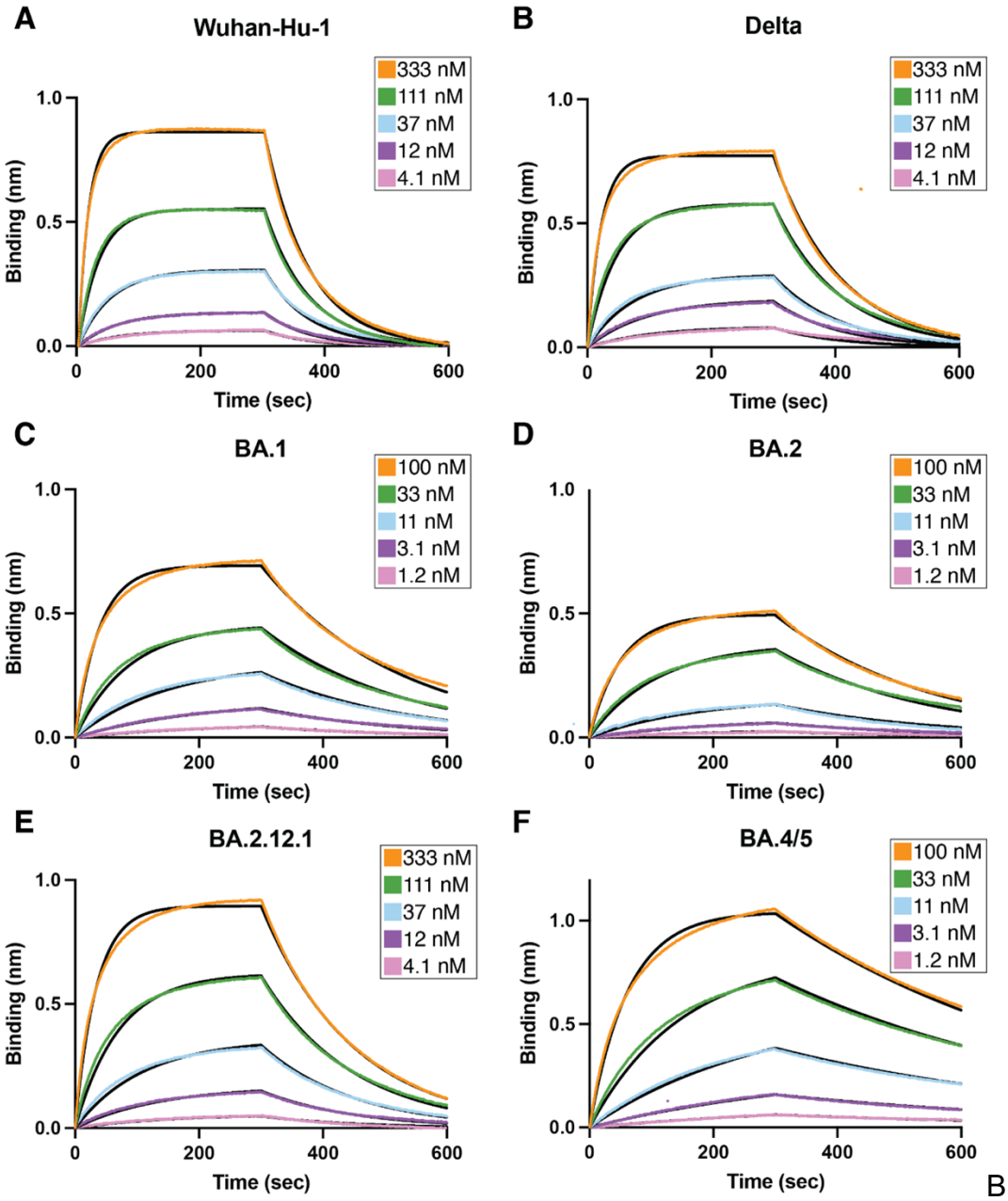

Biolayer interferometry binding analysis of monomeric human ACE2 to biotinylated Wuhan-Hu-1 (A), Delta (B), BA.1 (C), BA.2 (D), BA.2.12.1 (E), or BA.4/5 (F) RBDs immobilized at the surface of SA biosensors. Kinetic rate constants and affinities are presented in **Table 3.1**.

Figure 3.3. Representative surface plasmon resonance binding analysis of monomeric human ACE2 to RBDs

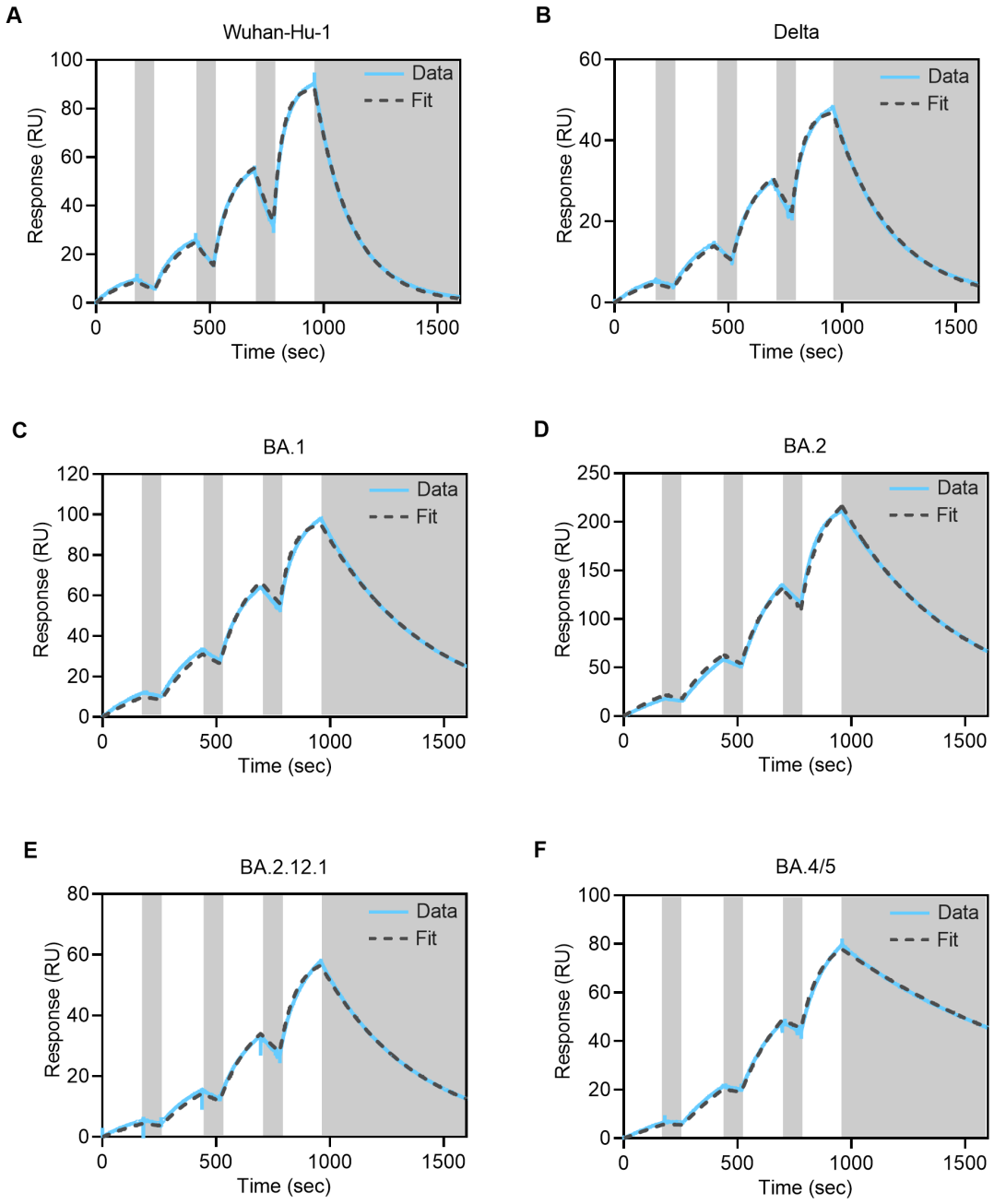

Representative surface plasmon resonance binding analysis of monomeric human ACE2 to Wuhan-Hu-1 (A), Delta (B), BA.1 (C), BA.2 (D), BA.2.12.1 (E), or BA.4/5 (F) RBDs immobilized at the surface of a SPR chip coated with anti-Avi polyclonal antibody. Experiments were performed with a 3-fold dilution series of Fab: 11.11, 33.33, 100, 300nM, and were run as single-cycle kinetics. Gray blocks denote the dissociation phase.

Figure 3.4. Representative cell-cell fusion fluorescence images after 24 h.

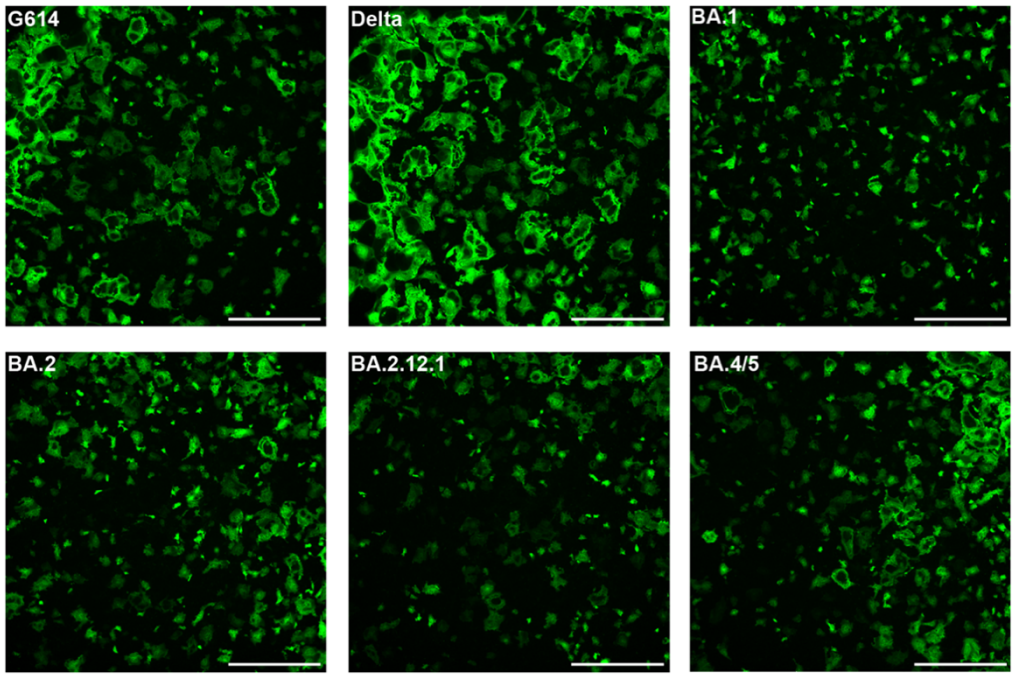

Scale bar: 1 mm.

Figure 3.5. Evaluation of cell surface S expression determined by labeling effector cells with the broadly reactive NTD-directed S2L20 antibody and measuring PE intensity by flow cytometry.

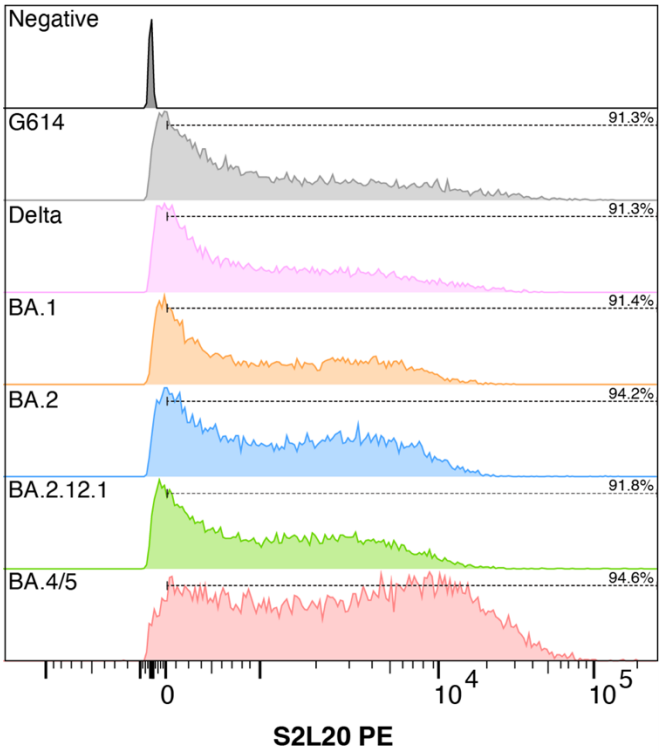

The y-axis of each histogram is presented as a modal scale proportional to the maximum cell count for that plot. The percentage of S-positive cells based on gating for singleton events for the mock transfected (negative) cells, represented by the dashed lines, for each sample is shown above each histogram.

Figure 3.6. SARS-CoV-2 Omicron sublineages evade human plasma neutralizing antibodies elicited by infection or primary vaccine series.

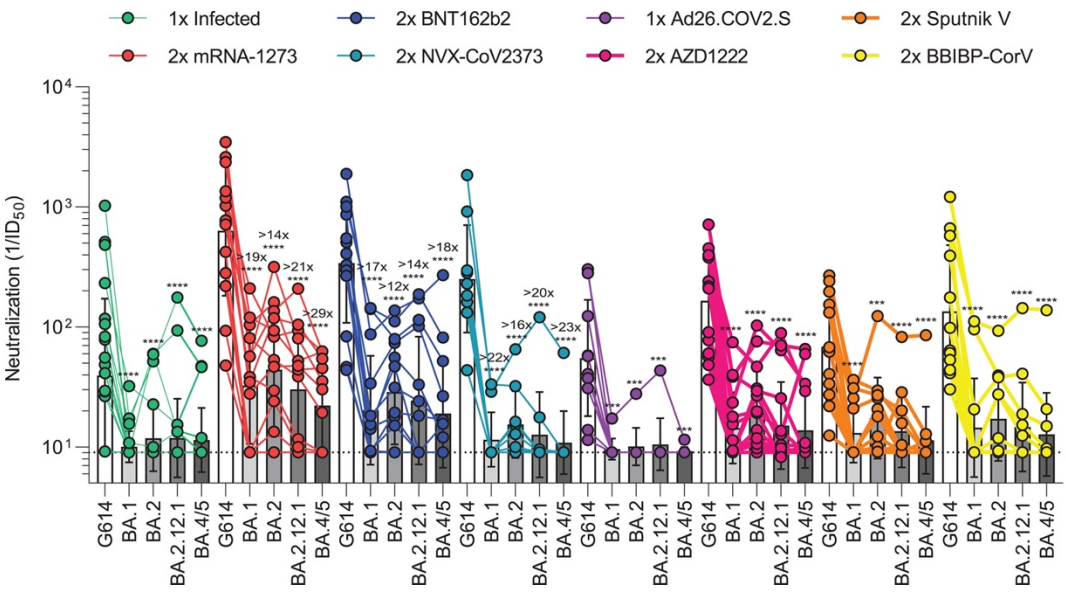

Plasma neutralizing antibody titers elicited by primary COVID-19 vaccination series determined using SARS-CoV-2 S VSV pseudotypes using VeroE6/TMPRSS2 as target cells. One-time (1×) infected samples (*n* = 24) were obtained 26 to 78 days (mean, 41) after symptom onset, two-dose (2×) mRNA-1273 samples (*n* = 14) were obtained 6 to 50 days (mean, 13) after second dose, 2× BNT162b2 samples (*n* = 14) were obtained 6 to 33 days (mean, 14) after second dose, 2× NVX-CoV2373 samples (*n* = 10) were obtained 17 to 168 days (mean, 82) after second dose, one-dose (1×) Ad26.COV2.S samples (*n* = 10) were obtained 9 to 142 days (mean, 79) after first dose, 2× AZD1222 samples (*n* = 16) were obtained ~30 days after second dose, 2× Sputnik V samples (*n* = 12) were obtained 60 to 90 days after second dose, and BBIBP-CorV samples (*n* = 12) were obtained 9 to 104 days (mean, 69) after second dose. Individual points are representative geometric mean titers from two independent experiments consisting of two replicates each. Bars represent geometric means, and error bars represent geometric standard deviations for each group. Statistical significance between groups of paired data was determined by Wilcoxon rank sum test. ***$P < 0.001$; ****$P < 0.0001$. Patient demographics are shown in table S4. Normalized curves and fits are shown in **Fig. 3.7**. G614 indicates Wuhan-Hu-1/G614. ID_{50}, median inhibitory dose.

Figure 3.7. Normalized neutralization curves following infection or primary vaccine series.

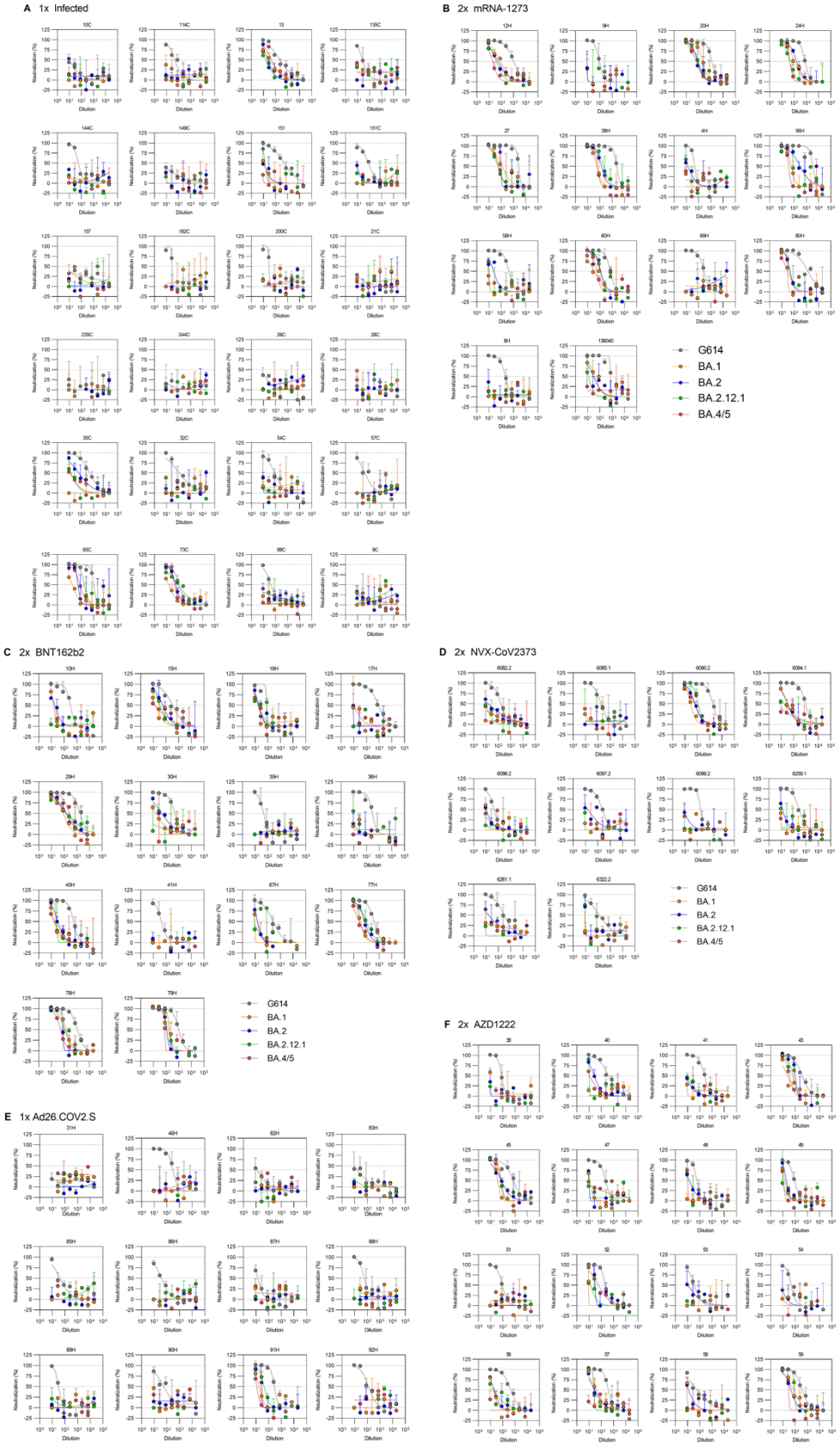

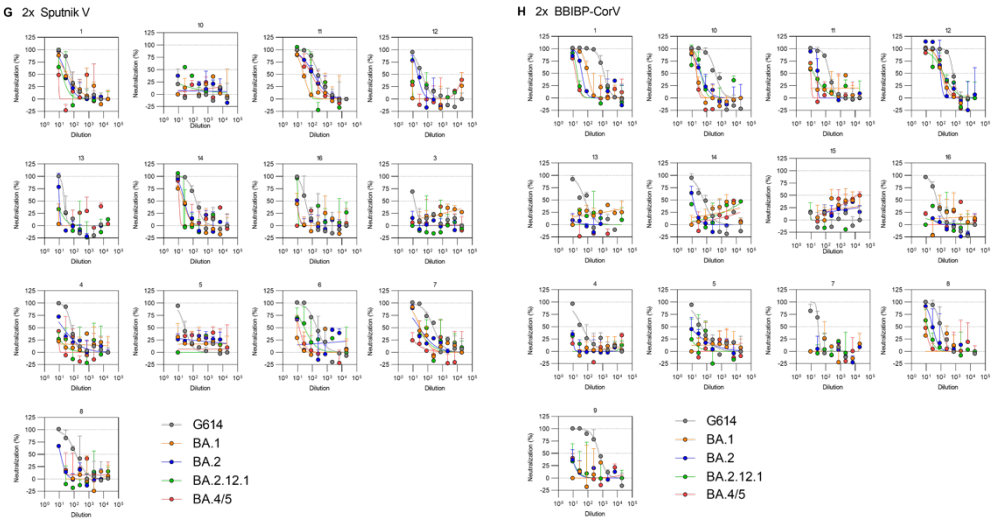

Normalized neutralization curves using VSV pseudovirus harboring SARS-CoV-2 S with the D614G, BA.1, BA.2, BA.2.12.1, or BA.4/5 mutations using VeroE6/TMPRSS2 target cells and plasma from subjects previously infected (A) or administered with a primary vaccine series (B-H).

Figure 3.8 Double blinded immunization scheme for individuals vaccinated with two doses of NVX-CoV2373.

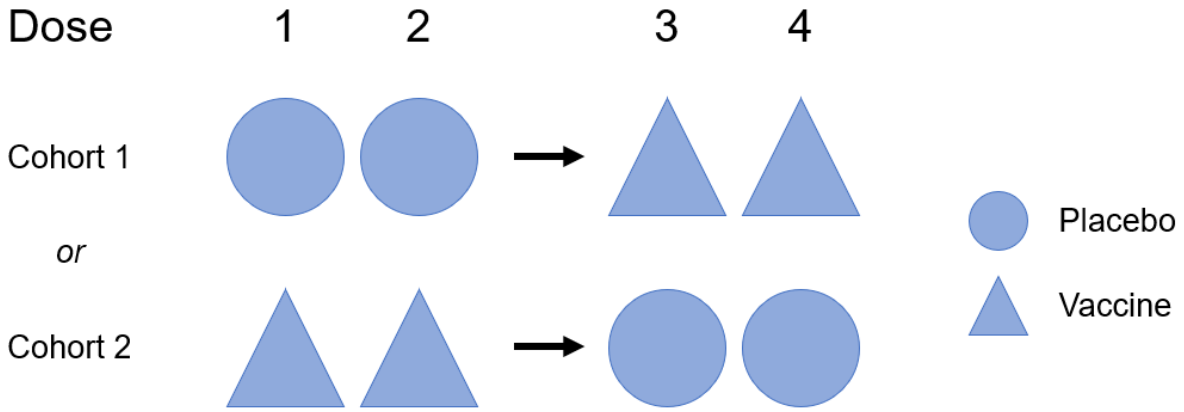

Each subject received two doses of NVX-CoV2373 (either at time points 1 and 2 or at time points 3 and 4) and two doses of placebo (at the other two time points). Each individual thus received a total of two doses of NVX-CoV2373 as part of their primary vaccine series, although the time since vaccination is unknown for some donors (as a result of study double blinding).

Figure 3.9 Analysis of neutralizing activity versus days post symptom onset or last vaccine dose.

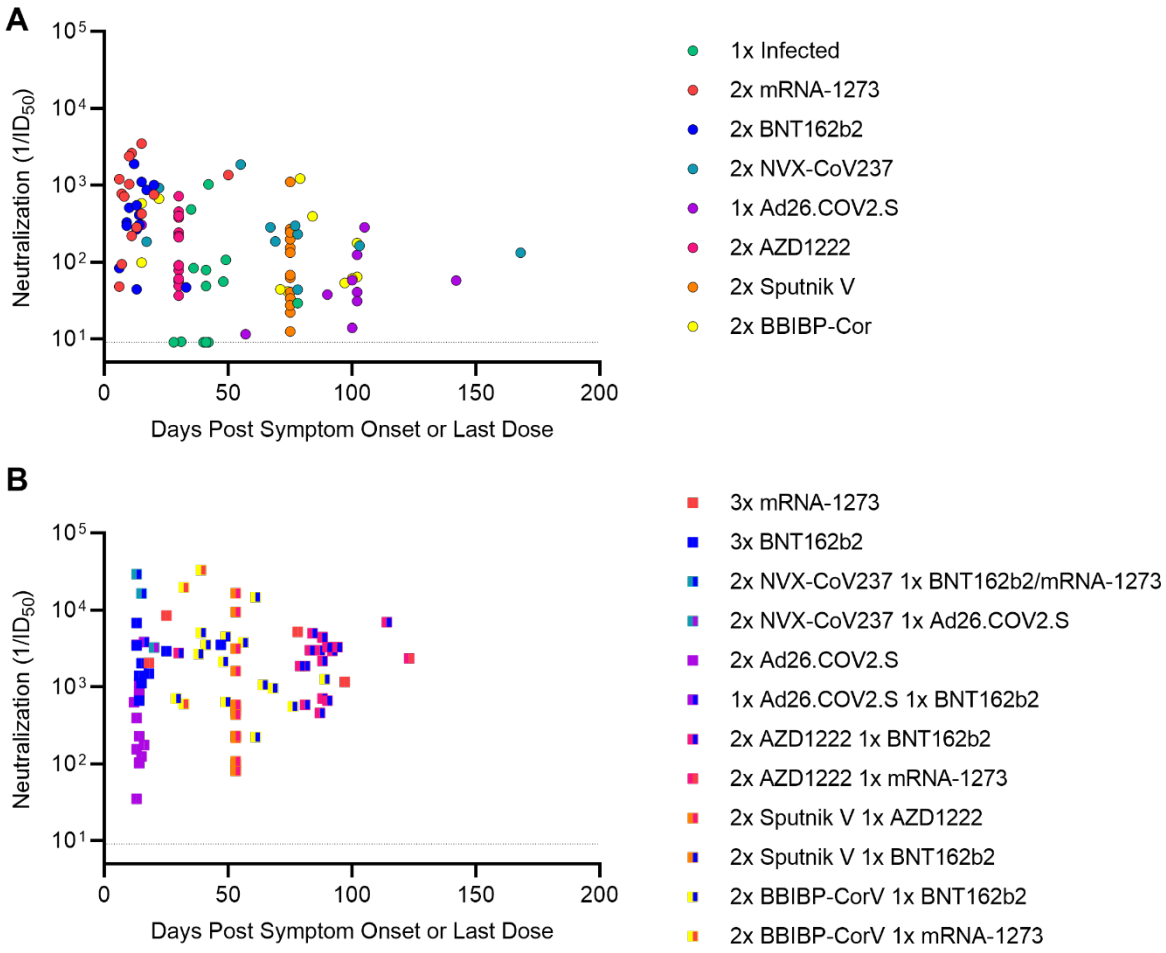

Plasma neutralizing activity against SARS-CoV-2 G614 VSV pseudovirus plotted against the number days since symptoms onset (for 1x infected subjects) or since administration of the last vaccine dose (for all other samples) following primary vaccine series (A) or booster dose (B).

Figure 3.10. Administration of a booster dose rescues neutralization potency against Omicron sublineages for all vaccines.

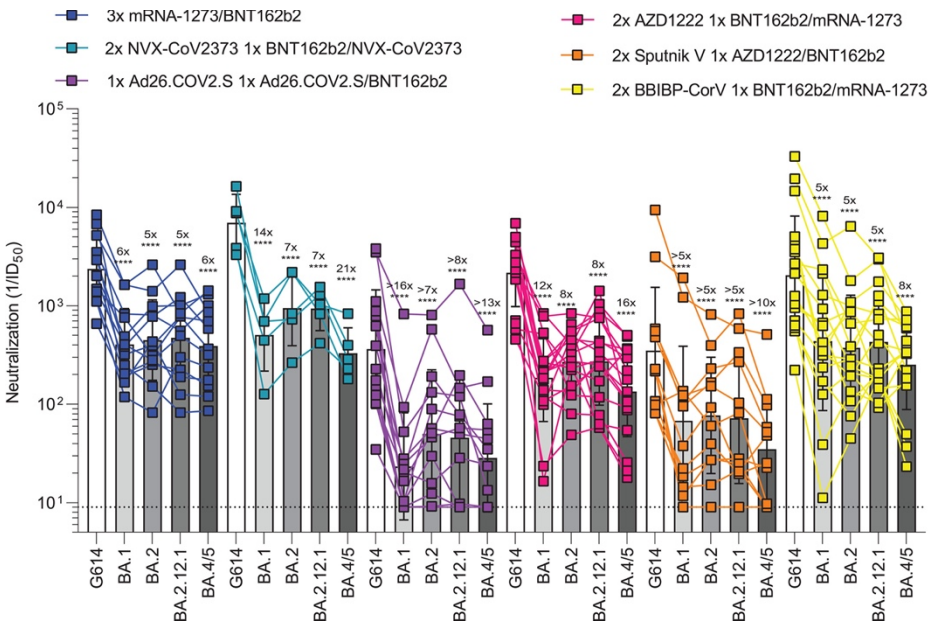

Plasma neutralizing antibody titers elicited by COVID-19 vaccine boosters determined using SARS-CoV-2 S VSV pseudotypes and VeroE6/TMPRSS2 as target cells. Three-dose (3×) mRNA-1273 or BNT162b2 samples (n = 13) were donated 13 to 97 days (mean, 30) after third dose; 2× NVX-CoV2373 plus 1× BNT162b2 or NVX-CoV2373 samples (n = 5) were donated 14 to 20 days (mean, 15) after third dose; 1× Ad26.COV2.S plus 1× Ad26.COV2.S or BNT162b2 samples (n = 14) were donated 12 to 16 days (mean, 14) after second dose; 2× AZD1222 plus 1× BNT162b2 or mRNA-1273 samples (n = 18) were donated 30 to 123 days (mean, 87) after third dose; 2× Sputnik V plus 1× AZD1222 or BNT162b2 samples (n = 14) were donated 45 to 60 days after third dose; and 2× BBIBP-CorV plus 1× BNT162b2 or mRNA-1273 samples (n = 18) were donated 29 to 89 days (mean, 50) after third dose. Individual points are representative geometric mean titers from two to four independent experiments consisting of two replicates each. Bars represent geometric means, and error bars represent geometric standard deviations for each group. Statistical significance between groups of paired data was determined by Wilcoxon rank sum test. **P < 0.01; ***P < 0.001; ****P < 0.0001. Patient demographics are shown in **Table 3.4**. Normalized curves and fits are shown in **Fig. 3.11**.

Figure 3.11. Normalized neutralization curves following booster dose.

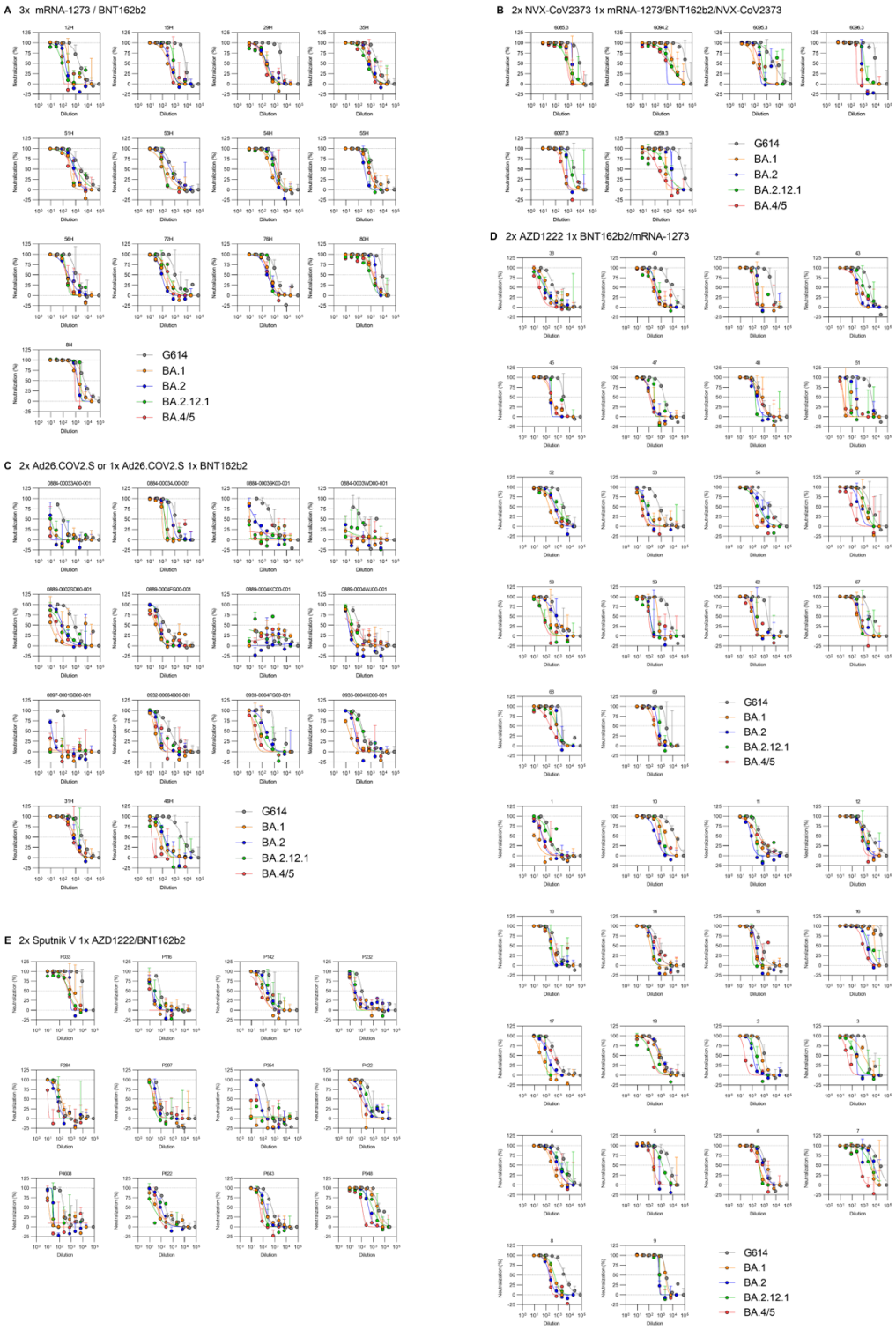

Normalized neutralization curves using VSV pseudovirus containing the SARS-CoV-2 Wuhan-Hu-1/G614, BA.1, BA.2, BA.2.12.1, BA.4/5 S on VeroE6/TMPRSS2 cells using plasma from subjects that received a booster dose.

Figure 3.12. Neutralizing antibody titers determined using VeroE6/TMPRSS or HEK293T-ACE2 as the target cell line.

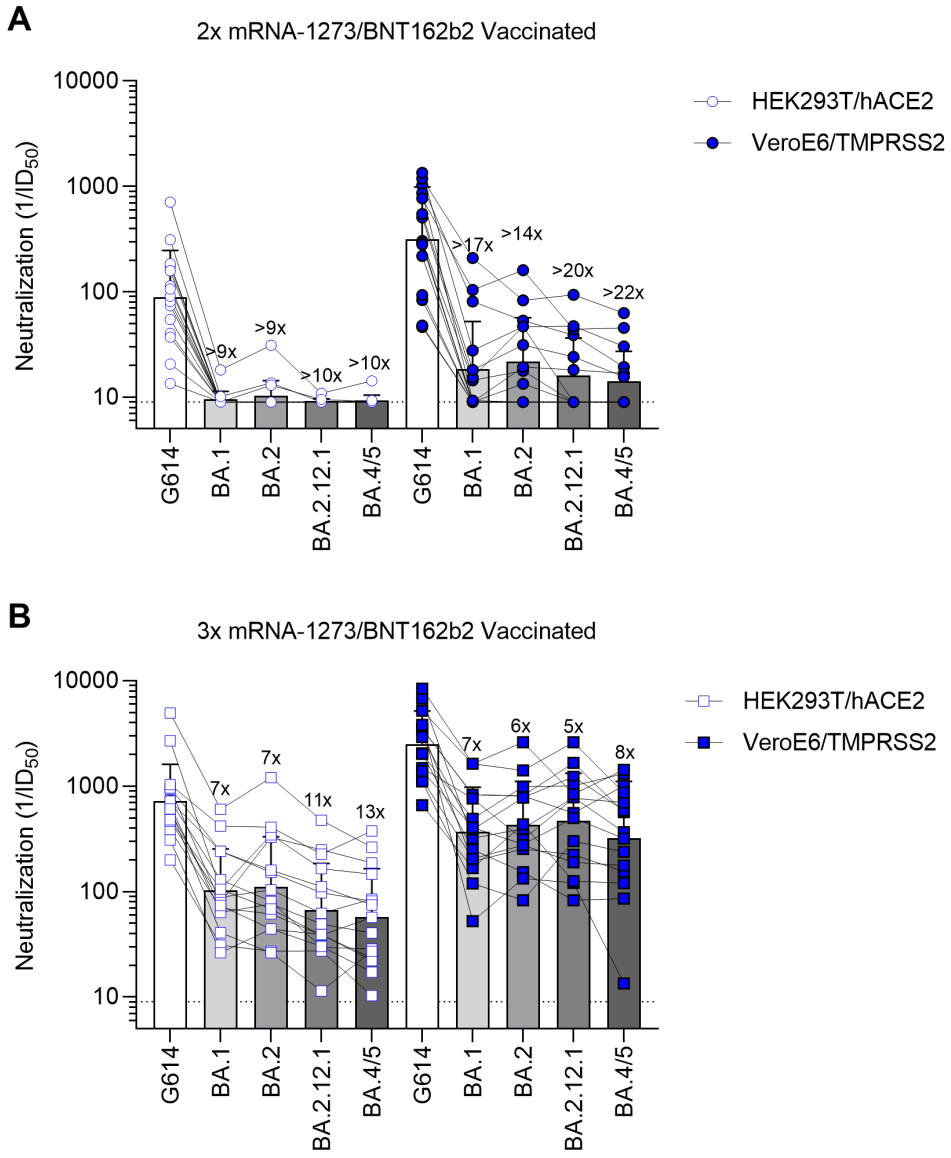

Plasma neutralizing antibody titers elicited by COVID-19 vaccine boosters determined using SARS-CoV-2 S VSV pseudotypes and VeroE6/TMPRSS2 or HEK293T stably expressing human ACE2 (HEK293T/ACE2) as target cells. Individual points are representative geometric mean titers from two independent experiments consisting of two replicates each. Bars represent geometric means and error bars represent geometric standard deviations for each group. Patient demographics are shown in **Table 3.4.** Normalized curves and fits are shown in **Figure 3.13**. G614: Wuhan-Hu-1/G614.

Figure 3.13. Neutralization curves using VeroE6/TMPRSS or HEK293T-ACE2 as the target cell line.

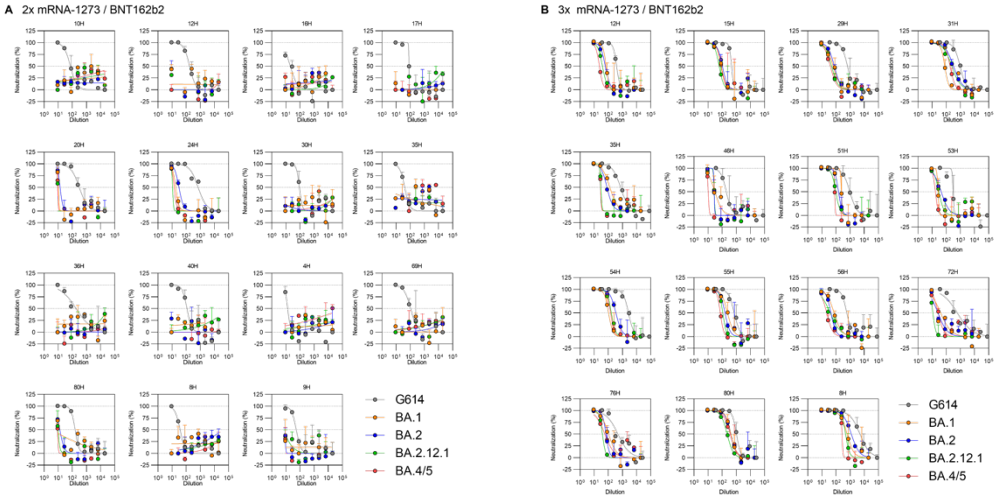

Normalized neutralization curves using VSV pseudotyped with the SARS-CoV-2 S harboring the G614, BA.1, BA.2, BA.2.12.1, or BA.4/5 mutations with HEK293T/ACE2 target cells using plasma from mRNA-vaccinated subjects after their (A) primary series or (B) booster dose.

Figure 3.14. Nucleocapsid antibody binding titers.

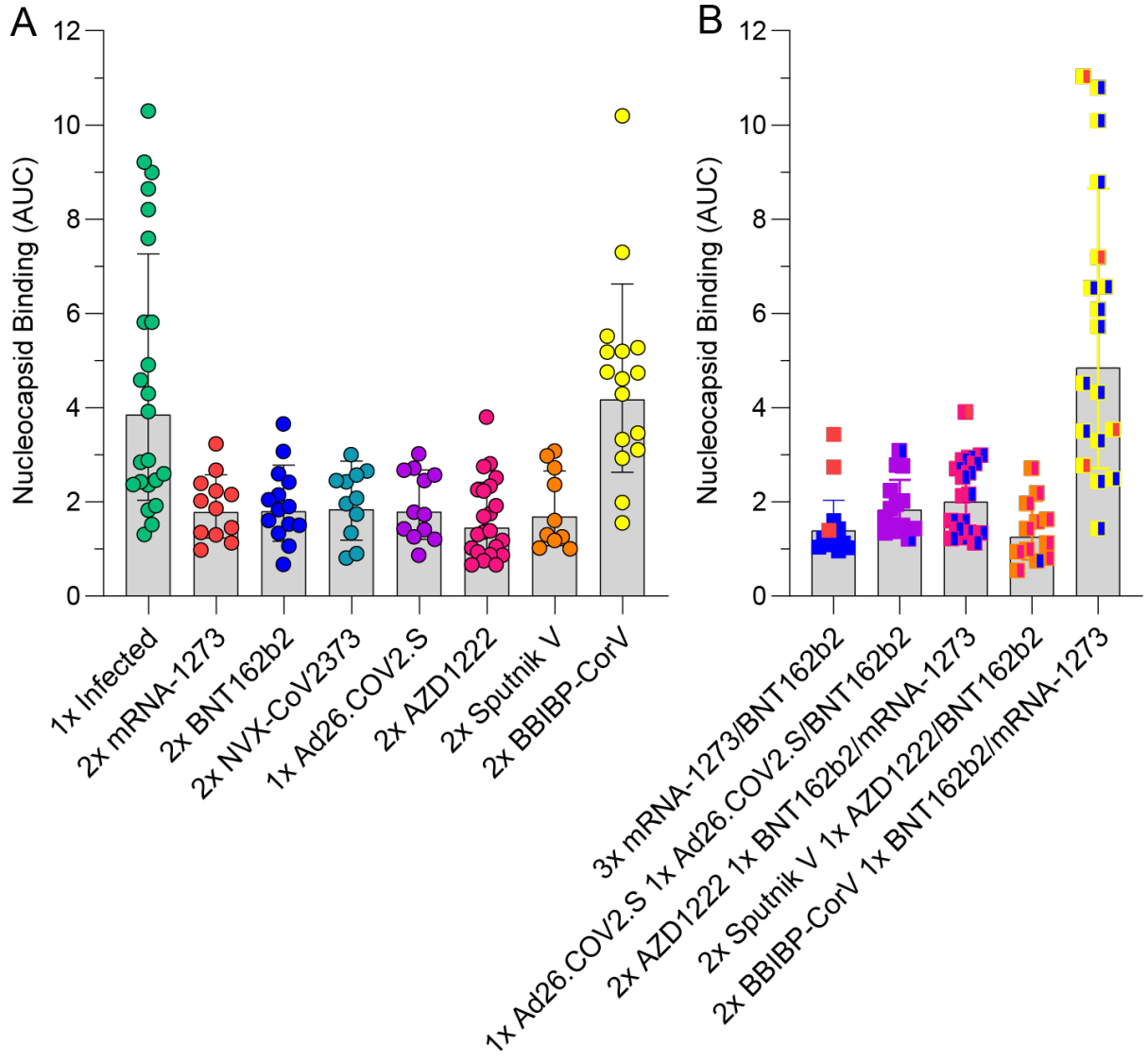

Area under curve of log transformed SARS-CoV-2 nucleocapsid antibody binding titers of plasma samples obtained after primary vaccine series (A) or booster dose (B).

Figure 3.15. ELISA curves against the SARS-CoV-2 nucleocapsid.

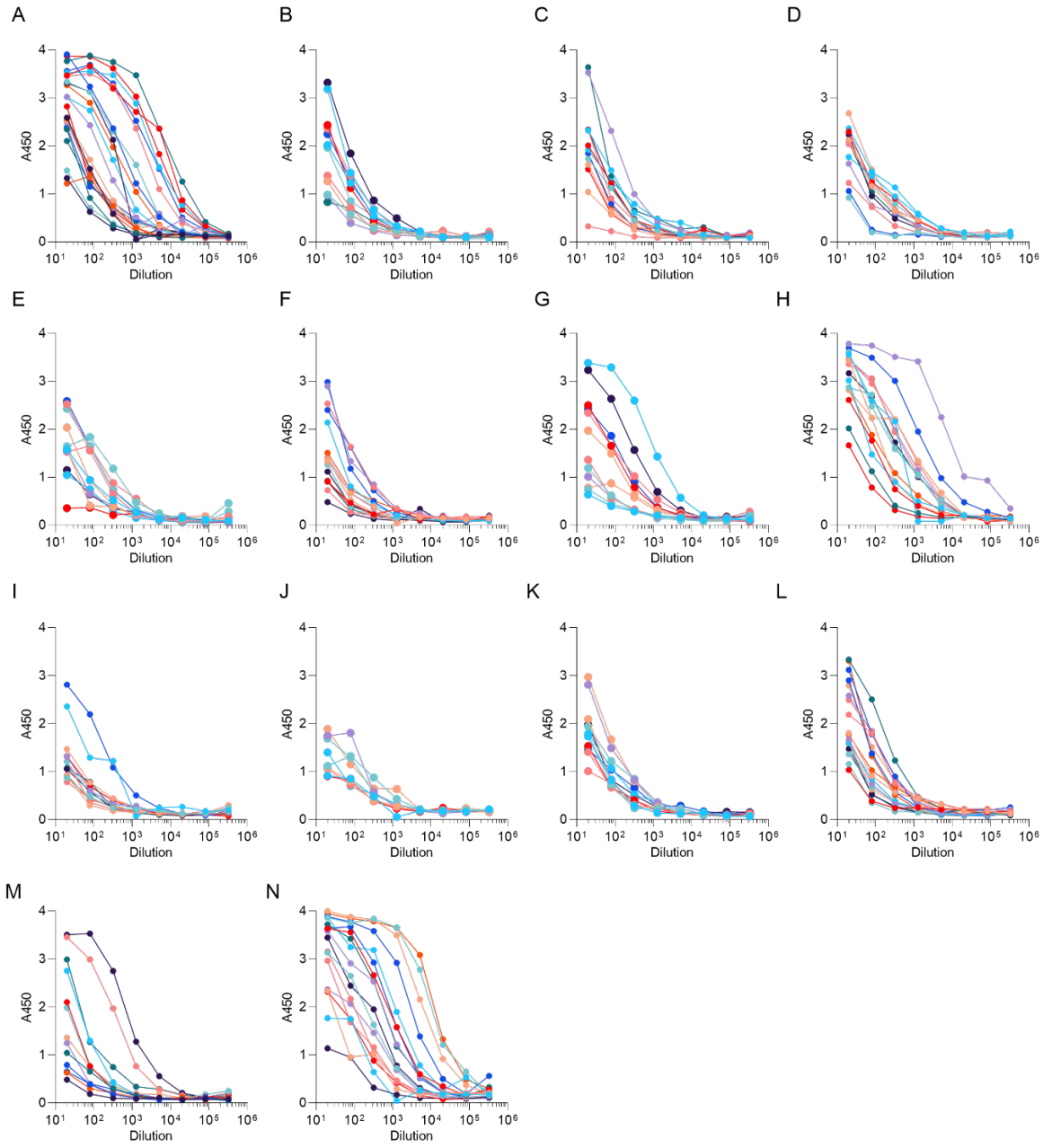

Raw ELISA curves for plasma binding to the SARS-CoV-2 nucleoprotein following infection (A) or administration of two doses of mRNA-1273 (B), two doses of BNT162b2 (C), two doses of NVX-CoV2373 (D), one dose of Ad26.COV2.S (E), two doses of AZD1222 (F), two doses of Sputnik V (G), two doses of BBIBP-CorV (H), three doses of mRNA-1273 or BNT162b2 (I), two doses of NXV-CoV2373 followed by one dose of BNT162b2 or mRNA-1273 (J), two doses of Ad26.COV2.S (K), two doses of AZD1222 followed by one dose of BNT162b2 or mRNA-1273 (L), two doses of Sputnik V followed by one dose of AZD1222 or BNT162b2 (M), or two doses of BBIBP-CorV followed by one dose of BNT162b2 or mRNA-1273 (N).

Table 3.1. Kinetics of human ACE2 binding to immobilized SARS-CoV-2 RBDs determined by biolayer interferometry.

	K_D (nM)	k_{on} ($M^{-1}s^{-1}$)	k_{off} (s^{-1})
Wuhan-Hu-1	88.7 ± 2.4	1.6×10^5	1.4×10^{-2}
Delta	78.2 ± 0.4	1.2×10^5	9.2×10^{-3}
BA.1	19.7 ± 1.1	2.2×10^5	4.4×10^{-3}
BA.2	23.9 ± 2.1	1.6×10^5	3.8×10^{-3}
BA.2.12.1	81.6 ± 6.5	8.7×10^5	6.9×10^{-3}
BA.4/5	14.4 ± 0.3	1.4×10^5	2.0×10^{-3}

Values are presented as mean ± standard error.

Table 3.2. Kinetics of human ACE2 binding to immobilized SARS-CoV-2 RBDs determined by SPR binding assays.

ACE-2 binding					
RBD	**K_D (nM)**	**k_{on} (1/Ms)**	**stdev (k_{on})**	**k_{off} (1/s)**	**stdev (k_{off})**
Wuhan-Hu-1	87.00 ± 10.80	7.11E+04	7.71E+03	6.12E-03	1.41E-04
Delta	65.66 ± 5.01	5.78E+04	1.84E+03	3.79E-03	2.09E-04
BA.1	36.94 ± 4.58	5.30E+04	5.70E+03	1.97E-03	3.61E-04
BA.2	44.96 ± 3.23	4.31E+04	1.06E+03	1.94E-03	1.32E-04
BA.2.12	52.56 ± 3.36	4.39E+04	2.31E+03	2.30E-03	4.07E-05
BA.4/5	28.06 ± 3.15	3.52E+04	1.34E+03	9.85E-04	1.01E-04

K_D, k_{on}, and k_{off} values are reported as the average with the standard deviation from at least 4 replicates.

Table 3.3. SARS-CoV-2 Omicron S mutations as compared to Wuhan-Hu-1.

BA.1	BA.2	BA.2.12.1	BA.4/5
A67V, del69/70, T95I, G142D, del143/145, del211, L212I, ins214EPE, G339D, S371L, S373P, S375F, K417N, N440K, G446S, S477N, T478K, E484A, Q493R, G496S, Q498R, N501Y, Y505H, T547K, D614G, H655Y, N679K, P681H, N764K, D796Y, N856K, Q954H, N969K L981F	T19I, L24S, del25/27, G142D, V213G, G339D, S371F, S373P, S375F, T376A, D405N, R408S, K417N, N440K, S477N, T478K, E484A, Q493R, Q498R, N501Y, Y505H, D614G, H655Y, N679K, P681H, N764K, D796Y, Q954H, N969K	T19I, L24S, del25/27, G142D, V213G, G339D, S371F, S373P, S375F, T376A, D405N, R408S, K417N, N440K, L452Q, S477N, T478K, E484A, Q493R, Q498R, N501Y, Y505H, D614G, H655Y, N679K, P681H, S704L, N764K, D796Y, Q954H, N969K	T19I, L24S, del25/27, del69/70, G142D, V213G, G339D, S371F, S373P, S375F, T376A, D405N, R408S, K417N, N440K, L452R, S477N, T478K, E484A, F486V, Q498R, N501Y, Y505H, D614G, H655Y, N679K, P681H, N764K, D796Y, Q954H, N969K

Table 3.4. Demographics data of enrolled plasma donors.

Vaccine	Sample	Age	Sex	Days since symptoms onset or last vaccine dose	Vaccine	Sample	Age	Sex	Days Since Last Dose
1x Infected	10C	31	F	31	2x BBIBP-CorV	1	47	F	79
	114C	54	F	41		10	27	M	84
	13	54	M	32		11	28	F	102
	135C	43	M	49		12	36	M	22
	144C	30	M	48		13	26	F	102
	149C	25	M	40		14	26	F	100
	151	67	M	-		15	32	F	104
	151C	69	F	41		16	39	M	97
	157	42	F	-		2	36	M	78
	182C	75	M	78		3	41	F	9
	200C	61	M	42		4	25	F	74
	21C	36	F	26		5	26	F	71
	235C	65	M	31		6	34	F	82
	244C	57	F	68		7	29	M	76
	26C	25	F	28		8	34	F	15
	28C	64	F	42		9	33	F	15
	30C	60	F	35	3x mRNA-1273/BNT162b2	8H	79	M	78
	32C	36	M	30		12H	42	F	18
	54C	37	M	36		15H	52	M	13
	57C	56	F	35		29H	64	M	13
	65C	73	M	42		35H	60	M	47
	73C	60	M	49		51H	50	F	25
	98C	33	M	38		53H	38	F	14
	9C	37	F	41		54H	34	F	15
2x mRNA-1273	12H	42	F	10		55H	52	F	18
	136040	40	M	20		56H	46	M	97
	20H	33	F	6		72H	35	F	15
	24H	24	M	7		76H	38	F	14
	27H	59	M	11		80H	35	F	25
	38H	26	F	10	2x NVX-CoV2373 1x mRNA-1273	6085.2	36	M	20

	48H	37	F	12	2x NVX-CoV2373 1x BNT162b2	6094.2	46	F	13
	4H	23	M	6	3x NVX-CoV2373	6095.3	56	F	-
	56H	46	M	15		6096.3	18	M	-
	58H	50	F	15		6097.3	18	M	-
	60H	42	F	8		6259.3	42	F	15
	69H	68	F	13	2x Ad26.COV2.S	0884-00033A00-001	38	M	14
	80H	35	F	50		0884-00034J00-001	72	F	14
	8H	79	M	11		0884-00036K00-001	43	F	12
	9H	75	F	7		0884-0003WD00-001	54	M	13
2x BNT162b2	10H	33	M	14		0889-0002SD00-001	43	M	14
	15H	52	M	9		0889-0004FG00-001	28	F	16
	16H	46	F	6		0889-0004KC00-001	36	F	13
	17H	76	M	17		0889-0004WJ00-001	48	F	14
	25H	60	M	11		0897-0001SB00-001	41	F	15
	29H	64	M	12		0932-00064B00-001	60	F	13
	30H	61	F	10		0933-0004FG00-001	51	M	14
	35H	60	M	33		0933-0004KC00-001	26	F	14
	36H	37	M	9	1x Ad26.COV.2.S 1x BNT162b2	31H	49	F	13
	40H	38	F	13		46H	60	M	16

	41H	36	F	13	2x AZD1222 1x BNT162b2	38	30	F	87
	67H	40	F	13		40	52	F	114
	77H	28	F	14		41	40	F	88
	78H	22	M	15		43	48	M	92
	79H	27	F	20		45	49	F	83
2x NVX-CoV2373	5840.2	F	73	165		47	32	F	81
	6082.2	M	21	103		48	38	F	81
	6085.1	M	36	17 or 92		51	30	F	88
	6090.2	F	36	55		52	47	M	87
	6094.1	F	46	22 or 127		53	38	F	88
	6096.2	M	18	155		54	30	F	88
	6097.2	M	18	78		57	46	F	94
	6099.2	M	20	69 or 156		58	29	F	90
	6259.1	F	42	172		59	48	M	84
	6261.1	M	60	191		62	41	F	79
	6322.2	F	41	168		67	42	F	90
1x Ad26.COV2.S	31H	49	F	9		69	24	M	30
	46H	60	M	15	2x AZD1222 1x mRNA-1273	68	26	M	123
	82H	28	M	57	2x Sputnik V 1x BNT162b2	P643	61	F	45-60
	83H	23	M	24	2x Sputnik V 1x AZD1222	P142	45	F	45-60
	85H	29	M	102		P297	47	F	45-60
	86H	26	F	90		P284	64	M	45-60
	87H	28	F	100		P354	61	M	45-60
	88H	30	F	100		P116	47	F	45-60
	89H	31	M	102		P948	38	F	45-60
	90H	38	M	142		P033	54	M	45-60
	91H	26	F	105		P622	60	M	45-60
	92H	33	F	102		P232	58	M	45-60
2x AZD1222	38	29	F	30		P4608	33	F	45-60
	40	51	F	30		P422	45	F	45-60
	41	39	F	30	2x BBIBP-CorV 1x BNT162b2	1	27	F	61
	43	47	M	30		10	32	M	61
	45	48	F	30		11	35	M	76
	47	31	F	30		12	62	M	41
	48	37	F	30		13	17	M	29
	49	36	F	30		17	34	M	49
	51	29	F	30		18	27	M	68
	52	46	M	30		2	37	M	64
	53	37	F	30		3	33	F	48
	54	29	F	30		4	30	F	49
	56	45	F	30		5	29	M	39

	57	45	F	30		6	30	M	89
	58	28	F	30		8	36	M	56
	59	47	M	30		9	34	M	38
2x Sputnik V	1	-	-	60-90	2x BBIBP-CorV 1x mRNA-1273	7	24	F	32
	10	-	-	60-90		14	30	M	32
	11	-	-	60-90		15	27	F	32
	12	-	-	60-90		16	28	M	39
	13	-	-	60-90					
	14	-	-	60-90					
	15	-	-	60-90					
	16	-	-	60-90					
	2	-	-	60-90					
	3	-	-	60-90					
	4	-	-	60-90					
	5	-	-	60-90					
	6	-	-	60-90					
	7	-	-	60-90					
	8	-	-	60-90					
	9	-	-	60-90					

Chapter 4. Neutralization, effector function and immune imprinting of Omicron variants.

In this chapter, I will describe our efforts to understand the impact of the additional spike protein mutations of the more recently Omicron variants on ACE2 binding and fusogenicity. I will then detail the role of bivalent vaccines and breakthrough infections on shaping the humoral immune response.

Adapted from: Addetia, A.*, Piccoli, L.*, Case, J.*, Park, Y.*, Beltramello, M., Guarino, B., Dang, H., Melo, G., Pinto, D., Sprouse, K., Scheaffer, S., Bassi, J., Silacci-Fregni, C., Muoio, F., Dini, M., Vincenzetti, L., Acosta, R., Johnson, D., Subramanian, S., Salibe, C., Giurdanella, M., Lombardo, G., Leoni, G., Culap, K., McAlister, C., Rajesh, A., Dellota, E., Zhou, J., Farhat, N., Bohan, D., Noack, J., Chen, A., Lempp, F., Quispe, J., Kergoat, L., Larrous, F., Cameroni, E., Whitener, B., Giannini, O., Cippa, P., Ceschi, A., Ferrari, P., Franzetti-Pellanda, A., Biggiogero, M., Garzoni, C., Zappi, S., Bernasconi, L., Kin, M., Rose, L., Schnell, G., Czudnochowski, N., Benigni, F., Franko, N., Logue, J., Yoshiyama, C., Stewart, C., Chu, H., Bourhy, H., Schmid, M., Purcell, L., Snell, G., Lanzavecchia, A., Diamond, M., Corti, D., Veesler, D. “Neutralization, effector functions and immune imprinting of Omicron variants.” *Nature.* 2023. doi: 10.1038/s41586-023-06487-6.

4.1 Chapter Introduction

The emergence of the SARS-CoV-2 Omicron (B.1.1.529) variant at the end of 2021 marked a new phase of the COVID-19 pandemic (Cao, Jian, et al., 2022; Viana et al., 2022), with lineages harbouring tens of amino acid mutations in their spike (S) glycoprotein leading to enhanced receptor engagement, an altered cell internalization route and unprecedented evasion from neutralizing antibodies (Bowen, Addetia, et al., 2022; Cameroni et al., 2022; McCallum et al., 2022; Meng et al., 2022) (nAbs). As a result, repeated waves of infections driven by successive lineages (such as BA.1/BA.1.1, BA.2 and BA.5) occurred globally, including in individuals who had received multiple COVID-19 vaccine doses.

RBD-directed antibodies account for most of the neutralizing activity against vaccine-matched and mismatched viruses, whereas the N-terminal domain is mostly targeted by variant-specific nAbs (Bowen, Park, et al., 2022; McCallum, De Marco, et al., 2021; Piccoli et al., 2020; Robbiani et al., 2020). Owing to convergent evolution, currently circulating Omicron variant lineages independently acquired identical or similar amino acid mutations at key antigenic sites in the RBD and in the N-terminal domain (NTD), relative to their presumed BA.2 and BA.5 ancestors (Cao, Jian, et al., 2022). The BA.2.75.2 lineage increased in frequency in multiple countries (such as India) and has the RBD mutations D339H, R346T, G446S, N460K, F486S and R493Q relative to BA.2 **(Fig. 4.1a)**. CH.1.1 emerged in November 2022 and later accounted for around 12% of infections in Europe and carries the K444T and L452R RBD residue mutations relative to BA.2.75.2. BN.1 descended from BA.2.75 and harbours D339H, R346T, K356T, G446S, N460K, F490S and R493Q RBD mutations relative to BA.2. The BN.1 lineage,

which accounted for more than half of the SARS-CoV-2 genomes sequenced in South Korea in January 2023, features an additional RBD N-linked glycosylation sequon at position N354 due to the K356T mutation (Walls, Park, et al., 2020). XBB is a recombinant from BJ.1 and BM.1.1.1 (BA.2.75 sublineage) and addition of the G252V mutation in S yielded XBB.1, which has D339H, R346T, L368I, V445P, G446S, N460K, F486S, F490S and R493Q RBD substitutions relative to BA.2 **(Fig. 4.1a)**. Furthermore, the XBB.1.5 lineage, which contains a proline at position 486 instead of a serine (F486 in the Wuhan-Hu-1 strain (hereafter referred to as Wu)), had become globally dominant by early March 2023. BQ.1 and BQ.1.1 were dominant in several Western countries and accounted for up to 55% of all sequenced SARS-CoV-2 genomes in the USA in January 2023. BQ.1.1 has R346T, K444T and N460K RBD mutations relative to BA.5 **(Fig. 4.1a)**. In this Article, we set out to understand how the constellation of S mutations in circulating SARS-CoV-2 variants affects viral functional properties and the available clinical countermeasures, including vaccines and therapeutic antibodies. Furthermore, we investigate humoral and memory immune responses in human cohorts representative of real-world exposures to SARS-CoV-2 and COVID-19 vaccines to study immune imprinting and guide future vaccine design and deployment.

4.2 Properties of BQ.1.1, XBB.1.5 and BA.2.75.2 S

We first determined the binding kinetics and affinity of the monomeric human ACE2 ectodomain to immobilized variant RBDs using biolayer interferometry (BLI) **(Figs. 4.1b and 4.2 and Table S1)**. We measured similar affinities for the BQ.1.1 and BA.5 RBDs (equilibrium dissociation constant (K_d) = 12.8 nM and 13.7 nM, respectively),

indicating that the additional BQ.1.1 mutations, which map outside of the ACE2-binding interface, do not influence receptor engagement **(Figs. 4.1b and 4.2 and Table S1)**. The enhanced ACE2 binding affinity of the BA.2.75.2 RBD (K_d = 26.2 nM) relative to BA.2, results from the R493Q reversion, as G446S has a negligible effect and F486S has a deleterious effect on ACE2 engagement (Starr et al., 2020). ACE2 bound to the XBB.1 RBD with an affinity similar to that of the Wu RBD (K_d = 88.4 nM and K_d = 101.1 nM, respectively) whereas it bound more tightly to the XBB.1.5 RBD (K_d = 26.8 nM), owing to substitution of a serine for a proline at S residue 486 enhancing receptor engagement (Starr, Greaney, Stewart, et al., 2022; Yue et al., 2023). We observed a similar ranking of these variant RBDs using surface plasmon resonance (SPR) to determine ACE2 binding affinities **(Figs. 4.1c and 4.2 and Table 4.2)**. Modulation of ACE2 binding affinities resulted largely from off-rate differences, in agreement with observations made with previous variants (Bowen, Addetia, et al., 2022; McCallum et al., 2022; Starr et al., 2020; Starr, Greaney, Stewart, et al., 2022). BQ.1.1, BA.2.75.2, XBB.1.5 and BA.5 have similarly high ACE2 binding affinity, suggesting that their viral fitness is not limited by this step of host cell invasion. The markedly higher ACE2 binding affinity of the XBB.1.5 RBD relative to XBB.1 is likely to explain the rapid rise of XBB.1.5 worldwide, as RBD position 486 is the only difference distinguishing these two genomes.

We next compared the kinetics and magnitude of cell–cell fusion promoted by the Wu-G614, Delta, BA.1, BA.2, BA.5, BQ.1.1, BA.2.75.2, XBB.1 and XBB.1.5 S glycoproteins using a split-GFP system (Bowen, Addetia, et al., 2022). We observed slower and reduced fusogenicity for the BA.5, BA.2 and BA.1 S glycoproteins compared

with Wu-G614 and even more so relative to Delta S (Mlcochova et al., 2021) **(Figs. 4.1d and 4.3)**, in line with previous findings and the lack of syncytia formation observed with authentic viruses (Bowen, Addetia, et al., 2022; Peacock et al., 2022). BQ.1.1, BA.2.75.2, XBB.1 and XBB.1.5 S, however, promoted membrane fusion more efficiently than the earlier Omicron variants **(Figs. 4.1d and 4.3)**, suggesting enhanced fusogenicity, which could augment viral replication kinetics, as described for the Delta variant (Y. Liu et al., 2022; Saito et al., 2022).

BA.1, BA.2 and BA.5 have an altered cell entry pathway relative to previous SARS-CoV-2 variants, and enter preferentially through the endosomal (cathepsin mediated) route as opposed to the plasma membrane (TMPRSS2-mediated) route (Hoffmann, Kleine-Weber, Schroeder, et al., 2020; Meng et al., 2022; Peacock et al., 2022; Willett et al., 2022). To assess the preferred cell entry route of currently circulating variants, we investigated the effect of protease inhibitors on entry of non-replicative vesicular stomatitis virus (VSV) pseudotyped with S glycoproteins into Vero E6-TMPRSS2 cells (which enables both plasma membrane and endosomal entry routes) and HEK293T ACE2 cells (which enable endosomal entry only). The serine protease (TMPRSS2) inhibitors camostat and nafamostat potently blocked entry of Wu-G614 and Delta S VSV in Vero E6-TMPRSS2 cells, but had a limited effect on the Omicron variants **(Fig. 4.1e)**. Reciprocally, the cathepsin B and L inhibitor E64d reduced the entry of BA.1, BA.2 and BA.5 S VSV, whereas there was no significant difference in entry for Delta, BA.2.75.2, BQ.1.1 or XBB.1 S VSV compared with Wu-G614 in Vero E6-TMPRSS2 cells **(Fig. 4.1e)**. Furthermore, entry mediated by BQ.1.1 and XBB.1 S was reduced by E64d to a lower extent than all other variant S proteins

evaluated in HEK293T-ACE2 cells **(Fig. 4.1f)**. This inefficient use of TMPRSS2 concurs with the identical BQ.1.1, BA.2.75.2 and XBB.1 sequences in the C-terminal part of the S_1 subunit and the entire S_2 subunit, which were proposed to mediate the switch in entry route (Meng et al., 2022; Peacock et al., 2022; Willett et al., 2022).

4.3 BQ.1.1, XBB.1 and BN.1 RBD structures

To reveal how amino acid substitutions in the BQ.1.1 and XBB.1 RBDs alter receptor recognition and key antigenic sites, we determined cryo-electron microscopy (cryo-EM) structures for each RBD bound to the human ACE2 ectodomain and to the fragment antigen-binding (Fab) region of the S309 antibody **(Figs. 4.2a,b and 4.5 and Table 4.3)**. The R493Q reversion enhances ACE2 binding relative to BA.212, possibly owing to the removal of the positively charged arginine side chain restoring a network of local interactions similar to that made with the Wu RBD (Lan et al., 2020) **(Figs. 4.2c and 4.6a–c)**. As V445P does not change the conformation of the ACE2-bound XBB.1 RBD in our structure, relative to BQ.1.1, and none of the three residue substitutions relative to BA.2.75.2 involve side-chain-mediated contacts with the host receptor, the V445P mutation might alter the backbone conformational dynamics of the free XBB.1 RBD and possibly dampen ACE2 binding. The BQ.1.1 RBD structure shows that the K444T substitution would abrogate salt bridges with the carboxyl side chains of the LY-CoV1404 (bebtelovimab parent) heavy chain residues D56 and D58 or of the COV2-2130 (cilgavimab parent) heavy chain residue D107 **(Fig. 4.6d,e)**. Moreover, R346T (present in BQ.1.1 and XBB.1) would abrogate a salt bridge with the COV2-2130 heavy chain residue D56 **(Fig. 4.6e)**; G446S (present in XBB.1) is expected to reduce COV2-

2130 binding sterically (McCallum et al., 2022) and V445P (XBB.1) probably reduces binding to LY-CoV1404, owing to a loss of van der Waals interactions (**Fig 4.6d)**. These data explain the markedly reduced binding and neutralization of LY-CoV1404, COV2-2130 and the COV2-2130/COV2-2196 (Evusheld parent) cocktail against the BQ.1.1 and XBB.1 variants (Cao, Jian, et al., 2022; Starr, Greaney, Stewart, et al., 2022; Q. Wang et al., 2023).

The structures demonstrate that S309 binds to both the BQ.1.1 and XBB.1 RBDs and reveal the molecular basis for the accommodation of the H339 residue in the XBB.1 epitope, involving extensive H339 side-chain interactions with S309 heavy chain complementarity-determining region 1 (CDRH1) and CDRH3 **(Fig. 4.4f)**. The S309 binding pose is indistinguishable from that observed when it is bound to the Wu (Pinto et al., 2020) or the BA.1 (McCallum et al., 2022) RBD **(Fig. 4.4f)**. The S371F mutation, which is present in BA.2, BA.5, BQ.1.1, XBB.1, XBB.1.5 and BA.2.75.2, leads to conformational changes of the RBD helix comprising residues 364–372 that are sterically incompatible with the glycan N343 conformation observed in S309-bound S structures (Y.-J. Park, Pinto, et al., 2022). In the S309-BQ.1.1 complex structure, helix 364–372 is weakly resolved and adopts a conformation similar to that observed in the S309-bound BA.1 structure (McCallum et al., 2022) but distinct from apo BA.2 (Stalls et al., 2022) or apo BA.5 S (Cao, Yisimayi, et al., 2022) structures **(Fig. 4.4f)**. Residues 368–373 are disordered in the cryo-EM map of the S309–XBB.1 RBD complex—as is the case for the adjacent residues 380–392—and were therefore not modelled **(Fig. 4.4f)**. These findings underscore the conformational frustration of helix 364–372, which is constrained to adopt an energetically disfavoured conformation for a F371-

harbouring mutant owing to S309 binding, which could explain the reduced neutralizing activity of S309 against these variants (Akerman et al., 2023; Cao, Jian, et al., 2022; Planas et al., 2023; Q. Wang et al., 2023; Yue et al., 2023) **(Figs. 4.7a and Table 4.4)**.

On the basis of the cryo-EM visualization of S309 binding to the BQ.1.1 and XBB.1 RBDs and the fact that sotrovimab remains the only therapeutic antibody with in vitro neutralizing activity against currently circulating variants, we investigated the binding kinetics and affinity of the S309 Fab to the immobilized Wu, Delta, BA.1, BA.2, BA.2.75.2, BQ.1, BQ.1.1, BN.1, XBB.1, XBB.1.5, CH.1.1 and Wu-E340A RBDs using SPR **(Fig. 4.7b and Tables 4.4 and 4.5)**. As expected, the E340A escape mutant in the Wu RBD abolished S309 binding (Pinto et al., 2020; Starr, Czudnochowski, et al., 2021). The binding affinity of S309 against Omicron variant RBDs decreased up to around 160-fold, primarily owing to faster dissociation rates compared with the Wu RBD. For the BN.1 RBD, however, the S309 Fab exhibited a decrease of around 100-fold in the on-rate compared with that of the Wu RBD, resulting in an approximately 370-fold decrease in affinity **(Figs. 4.7b and 4.8 and Table 4.5)**. The K356T mutation is likely to abolish a crucial salt bridge formed with S309 heavy chain variable region (VH) E108 (as resolved in PDB entry 7TN05), as (1) the BN.1 RBD harbouring the T356K reversion bound S309 similarly to the BA.2.75.2 RBD (the BN.1 RBD is distinguished by K356T, S486F and F490S, with only residue 356 being involved in the epitope); and (2) sotrovimab did not neutralize BA.2 S (K356T) VSV pseudovirus **(Figs. 4.8a,b and Table 4.4)**. Moreover, deglycosylation of the BN.1 RBD with peptide:N-glycosidase F (PNGase) did not improve S309 binding compared with untreated BN.1, despite complete removal of the N354 glycan introduced by the K356T mutation, as confirmed

by mass spectrometry **(Figs. 4.8c,d and Table 4.5)**. Finally, we determined a cryo-EM structure of the BN.1 RBD bound to the human ACE2 ectodomain and the S309 Fab (sotrovimab parent) **(Figs. 4.5 and Table 4.3)** which resolves the *N*-acetylglucosamine linked to N354, which is located near—but does not make contact with—the S309 CDRH3 **(Fig. 4.9)**. Collectively, these results indicate that the loss of the K356(RBD)–E108(S309 VH) salt bridge is the main mechanism of dampened binding affinity to and neutralization of BN.1 and that the newly introduced N354 glycan has a minimal effect on S309.

As illustrated by our cryo-EM structures **(Fig. 4.4f)**, S309-induced selection of a structurally frustrated backbone conformation around position F371 and of a subset of amino acid side chain rotamers compatible with Fab binding at position 339 (McCallum et al., 2022), along with the extensive interactions formed between the RBD H339 side chain and S309 CDRH1 and CDRH3, probably participate in modulating the distinct affinities observed by SPR. Moreover, the reduction of S309 neutralization potency against BQ.1.1 relative to BQ.1 is probably due to R346T in BQ.1.1, as this mutation abrogates electrostatic interactions with the S309 light chain variable region (VL) D93. Nevertheless, we found that the sotrovimab IgG cross-reacted with full-length, cell-surface-expressed BQ.1.1, XBB.1 and XBB.1.5 S trimers to a similar or greater degree than those observed for BA.2 S, and to a lesser extent with BN.1 S **(Figs. 4.7c and 4.10a)**. These data show that sotrovimab IgG bound avidly to all currently dominant Omicron SARS-CoV-2 variants, although its neutralization potency varied widely, ranging from a 6.5-fold reduction in potency against XBB.1 to a 94-fold reduction against BQ.1.1 and 778-fold reduction against BN.1 relative to Wu **(Figs. 4.7a and**

4.11a,b), in line with recent reports (Akerman et al., 2023; Cao, Jian, et al., 2022; Planas et al., 2023; Q. Wang et al., 2023; Yue et al., 2023).

4.4 S309 protects against BQ.1.1 and XBB.1.5

We next evaluated the ability of sotrovimab to activate antibody-dependent cellular cytotoxicity (ADCC) using primary natural killer effector cells and antibody-dependent cellular phagocytosis (ADCP) with ExpiCHO-S target cells expressing SARS-CoV-2 S of the different Omicron variants at their surface. Sotrovimab efficiently promoted ADCC and ADCP of cells expressing Wu-D614, BA.2, BQ.1.1, XBB.1, XBB.1.5 and BN.1 S in a concentration- and Fc-dependent manner, but did not do so with the BA.2-E340A S (negative control (Pinto et al., 2020; Starr, Czudnochowski, et al., 2021)) escape mutant or with the S309(G236R/L328R) (hereafter S309-GRLR) Fc mutant, which cannot engage human Fcγ receptors (Bournazos et al., 2020) **(Figs. 4.7d and 4.10c,d and Table 4.4)**. Although we observed a linear relationship between the Fab binding affinity and IgG neutralization potency of S309, we found no correlation with the magnitude of ADCC or ADCP, which was similar for all variants despite up to 100-fold differences in their monovalent binding affinities **(Figs. 4.7e and 4.10b)**.

To determine the in vivo relevance of these findings, we prophylactically administered S309 (human IgG1) at doses of 3, 10 or 30 mg kg^{-1} to K18-hACE2 transgenic mice (which express human ACE2 under the control of the human *KRT18* promoter) 1 day before challenge with BQ.1.1 **(Fig. 4.7f)**. S309 administration completely protected mice from weight loss and reduced lung viral RNA loads and infectious virus titres at all doses compared with animals receiving a control

antibody **(Figs. 4.7f and 4.10e)**, consistent with recent reports on BQ.1.1-challenged hamsters (Driouich et al., 2023) and non-human primates (Hérate et al., 2023). To investigate the role of effector functions in protection, we evaluated the in vivo efficacy of S309-GRLR, which is unable to engage human or mouse Fcγ receptors (Bournazos et al., 2020). Our data reveal that although effector functions are not necessary for S309-mediated protection from weight loss, they participate in reducing lung viral RNA burden at 3 and 10 mg kg^{-1} doses **(Fig. 4.7f)**. Moreover, prophylactic administration of 5 or 15 mg kg^{-1} S309 (hamster IgG2a) to Syrian hamsters challenged with XBB.1.5 reduced weight loss and viral burden **(Fig. 4.7g)**, with a similar effect on body weight loss to that observed against Delta (Y.-J. Park, Pinto, et al., 2022), highlighting a disconnect between in vivo efficacy and in vitro neutralization potency. Collectively, these data demonstrate that S309 protects animals from challenge with two of the most immune-evasive circulating SARS-CoV-2 variants and that the elicited effector functions contribute to this activity at low antibody doses in a prophylactic setting.

4.5 Bivalent vaccines elicit cross-nAbs

Vaccination represents a main line of defense against SARS-CoV-2, and recent mRNA vaccine updates have led to the administration of bivalent formulations. To assess the effects of the constellation of S mutations in the currently dominant variants on vaccine-elicited antibody responses, we quantified plasma neutralizing activity using VSV pseudotyped with Wu-G614, BA.1, BA.5, BQ.1.1, XBB.1, XBB.1.5 or BA.2.75.2 S. We compared plasma from individuals obtained 15–30 days after vaccination or PCR-confirmed breakthrough infection in 8 cohorts: (i) vaccinated 4 times with the Wu

monovalent S mRNA vaccine, with no known infection (Wu_4 vaccinated); (ii) vaccinated 3 times with Wu monovalent S mRNA vaccine and then 1 time with Wu/BA.5 bivalent S mRNA vaccine, with no known infection (Wu/BA.5 bivalent vaccinated); (iii) infected in 2020 and subsequently vaccinated 3 to 4 times with Wu monovalent S mRNA vaccine and then 1 time with Wu/BA.5 bivalent S mRNA vaccine (pre-Omicron infected–Wu/BA.5 bivalent vaccinated); and (iv) vaccinated with Wu monovalent S mRNA vaccine before experiencing a breakthrough infection with Omicron BA.1, BA.2, BA.2.12.1 or BA.5, followed by a vaccination with the Wu/BA.5 bivalent S mRNA vaccine (Omicron BT–Wu/BA.5 bivalent vaccinated). We also studied 4 additional cohorts from Switzerland, where a Wu/BA.1 bivalent S mRNA booster was available: (v) vaccinated 3 times with Wu monovalent S mRNA vaccine, with no known infection (Wu_3 mono); (vi) vaccinated 3 times with Wu monovalent S mRNA vaccine after pre-Omicron infection (pre-Omicron–Wu_3 mono); (vii) vaccinated 3 times with Wu monovalent S mRNA vaccine and then 1 time with Wu/BA.1 bivalent S mRNA vaccine, with no known infection (Wu/BA.1 biv); and (viii) vaccinated 3 times with Wu monovalent S mRNA vaccine and then 1 time with Wu/BA.1 bivalent S mRNA vaccine, with a BA.1 or a BA.2 breakthrough infection (Omicron BT–Wu/BA.1 biv).

Vaccination with Wu/BA.5 or Wu/BA.1 bivalent S mRNA vaccine elicited similar nAb titres against Wu-G614 S pseudovirus to those observed in matched cohorts vaccinated against Wu S but increased nAb titres against BA.1 S and BA.5 S pseudoviruses **(Fig. 4.12a,b, 4.13, and 4.14)**. Moreover, bivalent vaccination elicited detectable neutralizing activity against vaccine-mismatched XBB.1, XBB.1.5, BA.2.75.2 and BQ.1.1 S pseudoviruses, irrespective of prior infection status, whereas little to no

neutralization of these variants was detected after vaccination with monovalent Wu S mRNA vaccine **(Fig. 4.12a,b)**. Moreover, plasma neutralizing activity against currently circulating Omicron variants after four doses of monovalent Wu S vaccine was low for patients on maintenance dialysis and undetectable against any variants for immunosuppressed individuals following kidney transplantation, underscoring the difficulties associated with protecting these at-risk populations **(Fig. 4.15a,b)**. Overall, these data suggest that bivalent Wu/BA.1 and Wu/BA.5 mRNA vaccines elicit more potent and broader antibody responses against vaccine-matched and mismatched Omicron variants than the monovalent Wu S mRNA vaccine.

4.6 Plasma antibodies promote effector functions

On the basis of the findings that Fc-mediated effector functions contribute to S309-mediated protection in a mouse model of BQ.1.1 infection, we assessed binding to RBD and S as well as ADCC mediated by plasma antibodies from cohorts v to viii. The marked reduction of nAb titres against currently dominant Omicron variants was not paralleled by a similar decrease in IgG binding titres to matched RBDs or S trimers **(Fig. 4.12c)**. The lack of plasma antibodies competing for binding of an RBD site Ia (class 1) monoclonal antibody to BQ.1.1 and XBB.1 S **(Fig. 4.15c)** suggests that the reduction of neutralizing activity against these variants is driven by dampened cross-reactivity of receptor-binding motif (RBM)-directed antibodies, a correlate of neutralization potency (Piccoli et al., 2020). This is consistent with the notion that SARS-CoV-2 is evolving primarily to escape nAb responses (Cao, Jian, et al., 2022). Whereas binding titres remained equivalent against all Omicron variants for healthy

individuals and patients undergoing dialysis, the strong immunosuppression of kidney transplant recipients was associated with limited or no detectable binding and neutralizing plasma antibodies **(Fig. 4.15a,b)**. Plasma antibodies retained the ability to promote cell lysis mediated by natural killer cells (ADCC) and activation of Fcγ receptor IIIa (FcγRIIIa) (V158 allele) against BA.5, BQ.1.1 and XBB.1 S variants expressed at the surface of ExpiCHO target cells **(Figs. 4.12d and 4.16)**. Integrating these findings with the in vivo data for S309 presented above suggests that antibodies triggering Fc-mediated effector functions are broadly reactive with Omicron variants and contribute to protection against COVID-19.

4.7 Cross-reactive MBC dominance

We next compared memory B cell (MBC) populations in the Wu_4 vaccinated and the Wu/BA.5 bivalent vaccinated cohorts (which includes one individual (31H) who received the Janssen adenovirus-vectored (Ad26.COV2.S) COVID-19 vaccine rather than the Moderna (mRNA-1273) or Pfizer (BNT162b2) mRNA COVID-19 vaccines as their primary vaccine series), pre-Omicron infected–Wu/BA.5 bivalent vaccinated, and Omicron BT–Wu/BA.5 bivalent vaccinated subjects (cohorts i–iv) by measuring the frequency of Wu RBD-binding, pooled Omicron (BA.1, BA.2 and BA.5) RBD-binding, and both Wu and pooled Omicron (BA.1, BA.2 and BA.5) RBD-binding cross-reactive MBCs by flow cytometry. Individuals who were exposed to Wu S only (Wu_4 vaccinated) exhibited the highest frequency of Wu RBD-binding MBCs (mean frequency: 25.8%) and the lowest frequency of cross-reactive MBCs (mean frequency: 71.1%) of the four cohorts **(Figs. 4.17a,b and 4.18)**. Individuals who were exposed only once to Omicron

S through vaccination had few Omicron RBD-specific MBCs (mean frequency: 4.7%), regardless of whether they had experienced a pre-Omicron SARS-CoV-2 infection (Wu/BA.5 bivalent vaccinated and pre-Omicron infected–Wu/BA.5 bivalent vaccinated cohorts). Most RBD-binding MBCs in these cohorts cross-reacted with the Wu RBD and the pooled Omicron (BA.1, BA.2 and BA.5) RBDs, with uninfected individuals having similar frequencies of cross-reactive MBCs (mean: 77.5%) to individuals who had experienced a pre-Omicron infection (mean frequency: 77.1%) **(Figs. 4.17a,b and 4.18)**. These data are consistent with previous analyses of MBC populations in individuals vaccinated against Wu who had experienced an Omicron breakthrough infection, and suggest that immune imprinting limits the development of new Omicron-specific MBCs, although there is efficient recall of cross-reactive MBCs after a single exposure to Omicron S (Cao, Jian, et al., 2022; Y.-J. Park, Pinto, et al., 2022; Quandt et al., 2022). Although Omicron BT–Wu/BA.5 bivalent vaccinated subjects had two exposures to Omicron S (one through infection and one through vaccination), they had few Omicron-specific MBCs (mean: 5.6%), similar to individuals who received only the bivalent booster. MBCs cross-reactive with the Wu RBD and the Omicron (BA.1, BA.2 and BA.5) RBD pool were further enriched (mean frequency: 81.1%) in this cohort compared with the cohort vaccinated with Wu/BA.5 bivalent vaccine without Omicron BT infection **(Figs. 4.17a,b and 4.18)**.

We then assessed whether MBCs recognizing the Omicron (BA.1, BA.2 and BA.5) RBD pool could bind the BQ.1.1 RBD **(Figs. 4.17c and 4.19a,b)**. Most MBCs that were cross-reactive to Wu and Omicron (BA.1, BA.2 and BA.5) RBDs also recognized the BQ.1.1 RBD (mean frequency: 66.3%), whereas a smaller fraction of MBCs that

bound to the Omicron (BA.1, BA.2 and BA.5) RBD pool but not the Wu RBD also recognized the BQ.1.1 RBD (mean frequency: 16.9%), regardless of infection and vaccination status. These Omicron (BA.1, BA.2 and BA.5) RBD pool-specific MBCs were probably elicited de novo upon exposure to Omicron S (through infection and/or vaccination) and their breadth towards currently dominant Omicron variants may increase over time through affinity maturation, similar to observations made after infection with Wu or the WA-1 variant, or after monovalent Wu vaccination (Cho et al., 2021; Dan et al., 2021; Marzi et al., 2023; Muecksch et al., 2021; Turner et al., 2021; Z. Wang et al., 2021).

We next determined whether the bivalent boosters formulated against BA.5 or BA.1 differentially affected the composition of the RBD-binding MBC population **(Figs. 4.17d-f and 4.19c-e)**. We assessed the cross-reactivity of IgGs secreted by in vitro-stimulated MBCs to the Wu, BA.1, BQ.1.1 and XBB.1 RBDs 2–4 weeks and 3 months following bivalent Wu/BA.1 S vaccination of uninfected individuals and individuals who had experienced an Omicron breakthrough infection (cohorts vii and viii). We did not detect Omicron RBD-specific MBCs after bivalent Wu/BA.1 S vaccination in uninfected or Omicron breakthrough cohorts. Most RBD-binding IgGs, including those that inhibited binding of ACE2 to the Wu RBD, were cross-reactive with the BA.1 RBD, regardless of infection status (mean frequencies at 3 months: 87% in uninfected individuals and 89% in Omicron breakthrough cohorts), whereas a smaller fraction cross-reacted with the BQ.1.1 (66% and 64%, respectively) and XBB.1 (70% and 64%, respectively) RBDs. Consistent with the loss of plasma antibodies cross-reacting with the BQ.1.1 and XBB.1.1 RBMs **(Fig. 4.15c)**, we observed a low frequency

of MBC-derived IgGs that blocked binding of BQ.1.1 and XBB.1.1 RBDs to ACE2, most of which were cross-reactive with the Wu RBD **(Fig. 4.20)**. Analysis of cohorts vii and viii by flow cytometry and of cohorts i–iv by in vitro stimulation of MBCs confirmed that there was limited de novo elicitation of MBCs in these individuals **(Figs. 4.18 and 4.19f-j)**.

Thus, two exposures to Omicron S were not sufficient to overcome the immune imprinting induced by repeated exposures to Wu S, but instead mostly enriched for MBCs cross-reacting with multiple RBD variants. These results concur with the broader plasma nAb responses that we observed upon bivalent mRNA vaccination compared with monovalent Wu mRNA vaccination.

4.8 Chapter Discussion

Here we report that recently emerged SARS-CoV-2 Omicron variants show unprecedented immune evasion, reducing nAb titres up to ~150-fold for XBB.1 and XBB.1.5. BQ.1.1, XBB.1.5 and BA.2.75.2 retain high ACE2 binding affinity, similar to earlier Omicron variants, whereas XBB.1 has a lower affinity, similar to that of the Wu RBD. Although XBB.1 and XBB.1.5 are the most immune-evasive of these Omicron variants, the reduced affinity of XBB.1 for ACE2 relative to other co-circulating strains may have hindered its spread. The enhanced ACE2 binding affinity of the more recently emerged XBB.1.5 variant, which harbours the S486P RBD mutation (relative to XBB.1), may explain the current rapid spread of this variant (Yue et al., 2023). Our findings illustrate the interplay of immune evasion, fusogenicity and ACE2 binding affinity driving SARS-CoV-2 evolution.

ADCC and ADCP are Fc-mediated effector functions that can promote virus clearance and enhance adaptive immune responses in vivo, independently of direct viral neutralization. Indeed, both neutralizing and binding antibody titres were reported as correlates of protection in a phase 3 clinical study (Feng et al., 2021). Sotrovimab retains in vitro effector functions against BA.2 and conferred Fc-dependent protection in the lungs of mice infected with BA.2 (Case et al., 2022), in line with the low rate of hospitalization and death during the BA.2 and BA.5 waves in patients treated with sotrovimab (Cheng et al., 2023; Harman et al., 2023; Martin-Blondel et al., 2022). Here we show that sotrovimab triggered in vitro effector functions against all Omicron variants assessed at levels similar to that observed with Wu. Prophylactic administration of S309 (the sotrovimab parent antibody) protected mice against BQ.1.1 challenge with a contribution of effector functions, and protected hamsters against XBB.1.5 challenge, despite a reduced in vitro neutralizing activity against these variants. Our observation that vaccine-elicited polyclonal plasma antibodies cross-reacted and promoted ADCC upon recognition of the BA.1, BA.5, BQ.1.1 and XBB.1 S glycoproteins concur with observations made with previous Omicron variants (Bartsch et al., 2022; Mackin et al., 2023) and further hint at a protective role for broadly reactive antibodies with effector functions. Our findings suggest that the erosion of nAb titres is associated with an increased frequency of breakthrough infections, and the persistence of cross-reactive antibodies mediating effector functions may contribute to protection against severe COVID-19.

Immune imprinting—also known as ‘original antigenic sin’—describes how the first exposure to a virus shapes the immunological outcome of subsequent exposures to

antigenically related strains. For instance, antibodies secreted by plasmablasts obtained one to two weeks after infection with the antigenically shifted H1N1 influenza virus (formerly known as swine flu) that caused the 2009 flu pandemic were recalled from pre-existing, cross-reactive MBCs (Corti et al., 2011; Wrammert et al., 2011), whereas plasma cells obtained after the subsequent antigenic exposure (through vaccination) were subtype-specific (that is, targeting non-conserved epitopes). Similarly, Omicron breakthrough infections of Wu-vaccinated subjects primarily recall cross-reactive MBCs specific for epitopes shared by multiple SARS-CoV-2 variants rather than priming naive B cells that recognize Omicron RBD-specific epitopes (Cao, Jian, et al., 2022; Y.-J. Park, Pinto, et al., 2022; Quandt et al., 2022). We observed an unexpectedly small number of MBCs specific for Omicron RBDs (and not cross-reacting with the Wu RBD) even after two exposures to Omicron S antigens, including after Wu/BA.5 or Wu/BA.1 bivalent mRNA vaccination. This may be owing to strong immune imprinting resulting from repeated Wu-like S exposures, and possible antigenic dominance of the Wu S antigen in bivalent vaccines (Vu et al., 2023). However, relative to monovalent Wu mRNA vaccination, bivalent Wu/BA.5 mRNA vaccination results in enrichment for MBCs that are cross-reactive with vaccine-matched and mismatched RBD variants.

4.9 Methods

Cells and viruses

Cell lines used in this study were obtained from ATCC (HEK293T and Vero E6), Thermo Fisher Scientific (ExpiCHO-S cells, FreeStyle 293-F cells and Expi293F cells), Takara (Lenti-X 293T cells), a gift from J. Bloom (HEK293T-ACE2) (Crawford et al.,

2020), or generated in-house (Vero E6-TMPRSS2, BHK-21-$GFP_{1–10}$ and Vero E6-TMPRSS2-GFP_{11}) (Bowen, Addetia, et al., 2022; Lempp et al., 2021). None of the cell lines used were authenticated or tested for mycoplasma contamination. SARS-CoV-2 isolates used in this study were obtained through BEI Resources, NIAID, NIH: (hCoV-19/USA-WA1/2020, NR-52281 deposited by the Centers for Disease Control and Prevention; Lineage B.1.1.529, BA.2; Omicron Variant Isolate hCoV-19/USA/CO-CDPHE-2102544747/2021, NR-56520; Lineage XBB.1.5; Omicron Variant Isolate hCoV-19/USA/MD-HP40900/2022, NR-59104, contributed by A. S. Pekosz). Viruses were propagated and titrated on Vero E6-TMPRSS2 cells in house. The genomic sequences of all strains were confirmed by Sanger and/or next generation sequencing.

Human donors

Samples from cohorts v–viii along with those from patients undergoing dialysis (DP) kidney transplant recipients (KTR) and healthcare workers (HCW) were obtained from SARS-CoV-2 convalescent and vaccinated individuals under study protocols approved by the local institutional review boards (Canton Ticino and Canton Aargau Ethics Committees, Switzerland). PBMCs for effector function experiments were collected from healthy human donors under the informed consent and authorization of the Comitato Etico of Canton Ticino (Switzerland). All donors provided written informed consent for the use of blood and blood derivatives (such as peripheral blood mononuclear cells, sera or plasma) for research. Sera and PBMCs from cohorts i–iv were obtained from the HAARVI study approved by the University of Washington

Human Subjects Division Institutional Review Board (STUDY00000959). Demographic data for these individuals is presented in Tables 4.6 and 4.7.

Constructs

The full-length Wu/G614, Delta, BA.1, BA.2, and BA.4/5 S constructs with a 21-amino-acid C-terminal deletion used for pseudovirus assays were previously described elsewhere (Bowen, Addetia, et al., 2022; McCallum, Walls, et al., 2021). The full-length BA.2.75.2 and XBB.1 S constructs containing a 21-amino-acid C-terminal deletion were codon optimized, synthesized, and inserted the HDM vector by Genscript. The full-length BQ.1.1 S construct containing a 21-amino acid C-terminal deletion was generated by mutagenesis of the BA.4/5 S construct and the full-length XBB.1.5 containing a 21-amino-acid C-terminal deletion was generated by mutagenesis of the XBB.1 S construct by Genscript.

S expression plasmids used for the generation of VSV pseudoviruses harbour the following mutations. BA.1: A67V, Δ69-70, T95I, G142D, Δ143–145, Δ211, L212I, ins214EPE, G339D, S371L, S373P, S375F, K417N, N440K, G446S, S477N, T478K, E484A, Q493R, G496S, Q498R, N501Y, Y505H, T547K, D614G, H655Y, N679K, P681H, N764K, D796Y, N856K, Q954H, N969K, L981F; BA.2: T19I, L24-, P25-, P26-, A27S, G142D, V213G, G339D, S371L, S373P, S375F, D405N, R408S, K417N, N440K, S477N, T478K, E484A, Q493R, Q498R, N501Y, Y505H, D614G, H655Y, N679K, P681H, N764K, D796Y, N856K, Q954H, N969K; K417N, N440K, G446S, N460K, S477N, T478K, E484A, Q498R, N501Y, Y505H, D614G, H655Y, N679K, P681H, N764K, D796Y, Q954H, N969K; BA.2.75.2: T19I, L24-, P25-, P26-, A27S, G142D,

K147E, W152R, F157L, I210V, V213G, G257S, G339H, R346T, S371F, S373P, S375F, T376A, D405N, R408S, K417N, N440K, G446S, N460K, S477N, T478K, E484A, F486S, Q498R, N501Y, Y505H, D614G, H655Y, N679K, P681H, N764K, D796Y, Q954H, N969K, D1199N; BQ.1: T19I, L24-, P25-, P26-, A27S, Δ69-70, G142D, V213G, G339D, S371F, S373P, S375F, T376A, D405N, R408S, K417N, N440K, K444T, L452R, N460K, S477N, T478K, E484A, F486V, Q498R, N501Y, Y505H, D614G, H655Y, N679K, P681H, N764K, D796Y, Q954H, N969K; BQ.1.1: T19I, L24-, P25-, P26-, A27S, Δ69-70, G142D, V213G, G339D, R436T, S371F, S373P, S375F, T376A, D405N, R408S, K417N, N440K, K444T, L452R, N460K, S477N, T478K, E484A, F486V, Q498R, N501Y, Y505H, D614G, H655Y, N679K, P681H, N764K, D796Y, Q954H, N969K; BF.7: T19I, L24-, P25-, P26-, A27S, Δ69-70, G142D, V213G, G339D, R436T, S371F, S373P, S375F, T376A, D405N, R408S, K417N, N440K, L452R, S477N, T478K, E484A, F486V, Q498R, N501Y, Y505H, D614G, H655Y, N679K, P681H, N764K, D796Y, Q954H, N969K; XBB.1: T19I, L24-, P25-, P26-, A27S, V83A, G142D, Y144-, H146Q, Q183E, V213E, G252V, G339H, R346T, L368I, S371F, S373P, S375F, T376A, D405N, R408S, K417N, N440K, V445P, G446S, N460K, S477N, T478K, E484A, F486S, F490S, Q498R, N501Y, Y505H, D614G, H655Y, N679K, P681H, N764K, D796Y, Q954H, N969K; XBB.1.5: T19I, L24-, P25-, P26-, A27S, V83A, G142D, Y144-, H146Q, Q183E, V213E, G252V, G339H, R346T, L368I, S371F, S373P, S375F, T376A, D405N, R408S, K417N, N440K, V445P, G446S, N460K, S477N, T478K, E484A, F486P, F490S, Q498R, N501Y, Y505H, D614G, H655Y, N679K, P681H, N764K, D796Y, Q954H, N969K; CH.1.1: T19I, del24–26, A27S, G142D, K147E, W152R, F157L, I210V, V213G, G257S, G339H, R346T, S371F, S373P, S375F, T376A,

D405N, R408S, K417N, N440K, K444T, G446S, L452R, N460K, S477N, T478K, E484A, F486S, Q498R, N501Y, Y505H, D614G, H655Y, N679K, P681H, N764K, D796Y, Q954H, N969K; BN.1: T19I, del24–26, A27S, G142D, K147E, W152R, F157L, I210V, V213G, G257S, G339H, R346T, K356T, S371F, S373P, S375F, T376A, D405N, R408S, K417N, N440K, G446S, N460K, S477N, T478K, E484A, F490S, Q498R, N501Y, Y505H, D614G, H655Y, N679K, P681H, N764K, D796Y, Q954H, N969K.

For BLI and cryo-EM, the SARS-CoV-2 Wu RBD construct containing an N-terminal mu-phosphatase secretion signal and a C-terminal octa-histidine tag followed by flexible linker and Avi tag was previously described elsewhere (Walls, Park, et al., 2020). The BA.4/5 RBD construct containing an N-terminal BM40 secretion tag and a C-terminal octa-histidine tag followed by flexible linker and Avi tag was previously described elsewhere (Bowen, Addetia, et al., 2022). The BA.2.75.2, BQ.1.1, XBB.1, and XBB.1.5 RBD constructs containing an N-terminal BM40 secretion tag and a C-terminal octa-histidine tag followed by flexible linker and Avi tag were codon optimized, synthesized, and inserted into the pcDNA3.1(+) vector by Genscript. The boundaries of the construct are N-328RFPN331 and 528KKST531-C. The monomeric human ACE2 ectodomain (residues 19–615) construct used for BLI contains an N-terminal signal peptide and a 10x His tag and was synthesized and inserted into pTwist-CMV by Twist Bioscience.

For SPR, SARS-CoV-2 RBD plasmids encoding residues 328–531 of the S protein from GenBank NC_045512.2 with an N-terminal signal peptide and a C-terminal 8×His–Avi Tag or thrombin cleavage site–8×His–Avi tag. The ACE2 construct used for SPR and cryo-EM, encodes for residues 19–615 from Uniprot entry Q9BYF1 with a C-

terminal thrombin cleavage site–TwinStrep–10×His–GGG tag, and N-terminal signal peptide.

Generation of VSV pseudoviruses

Replication-defective VSV pseudovirus expressing SARS-CoV-2 Wu and variant S were generated as previously described (Cameroni et al., 2022) with some modifications to evaluate cohorts v–viii, DP, KTP and HCW, and monoclonal antibodies. Lenti-X 293T cells (Takara) were seeded in 15-cm^2 dishes at a density of 10×10^6 cells per dish and the following day were transfected with 25 µg of S expression plasmid with TransIT-Lenti (Mirus, 6600) according to the manufacturer's instructions. One day after transfection, cells were infected with VSV-luc (VSV-G) with a multiplicity of infection (MOI) of 3 for 1 h, rinsed three times with PBS containing Ca^{2+} and Mg^{2+}, then incubated for an additional 24 h in complete medium at 37 °C. The cell supernatant was clarified by centrifugation, aliquoted, and frozen at −80 °C.

Pseudotyped VSV was produced as previously described (Bowen, Addetia, et al., 2022) to evaluate cohorts i–iv. In brief, HEK293T cells were split into poly-D-lysine-coated 15-cm plates and grown overnight until they reached approximately 70–80% confluency. The cells were washed 3 times with Opti-MEM (Gibco) and transfected with either the Wu-G614, Delta, BA.1, BA.2, BA.4/5, BA.2.75.2, BQ.1.1, XBB.1, or XBB.1.5 S constructs using Lipofectamine 2000 (Life Technologies). After 4–6 h, the medium was supplemented with an equal volume of DMEM supplemented with 20% FBS and 2% penicillin-streptomycin. The cells were incubated for 20–24 h, washed 3 times with DMEM, and infected with VSVΔG-luc. Two hours after VSVΔG-luc infection, the cells

were washed an additional five times with DMEM. The cells were grown in DMEM supplemented with anti-VSV-G antibody (I1-mouse hybridoma supernatant diluted 1:25, from CRL-2700, ATCC) for 18–24 h, after which the supernatant was harvested and clarified by low-speed centrifugation at 2,500*g* for 10 min. The supernatant was then filtered (0.45 μm) and some virus stocks were concentrated 10 times using a 30-kDa centrifugal concentrator (Amicon Ultra). The pseudotyped viruses were then aliquoted and frozen at −80 °C.

VSV pseudovirus neutralization

For cohorts v–viii, DP, KTP and HCW, and monoclonal antibodies, Vero E6 cells were grown in DMEM supplemented with 10% FBS and seeded into white-walled 96-well plates (PerkinElmer, 6005688) at a density of 20,000 cells per well. The next day, monoclonal antibodies were serially diluted in pre-warmed complete medium, mixed with pseudoviruses and incubated for 1 h at 37 °C in round bottom polypropylene plates. Medium from cells was aspirated and 50 μl of pseudovirus–monoclonal antibody complexes were added to cells, which were then incubated for 1 h at 37 °C. An additional 100 μl of pre-warmed complete medium was then added on top of complexes and cells were incubated for an additional 16–24 h. Conditions were tested in duplicate or triplicate wells on each plate and 6–8 wells per plate contained untreated infected cells (defining the 0% of neutralization (MAX RLU) value) and uninfected cells (defining the 100% of neutralization (MIN RLU) value). Virus–monoclonal antibody-containing medium was then aspirated from cells and 50 or 100 μl of a 1:2 dilution of SteadyLite Plus (PerkinElmer) or Bio-Glo (Promega) in PBS with Ca^{2+} and Mg^{2+} was added to cells.

Plates were incubated for 15 min at room temperature and then analysed on the Synergy-H1 (BioTek). The average relative light units (RLU) of untreated infected wells (MAX RLUave) were subtracted by the average of MIN RLU (MIN RLUave) and used to normalize percentage of neutralization of individual RLU values of experimental data according to the following formula: (1 − (RLUx – MIN RLUave)/(MAX RLUave – MIN RLUave)) × 100. Data were analysed with Microsoft Excel (v16) and Prism (v.9.1.0). IC_{50} values were calculated from the interpolated value from the log(inhibitor) versus response, using variable slope (four parameters) non-linear regression with an upper constraint of <100. Each neutralization experiment was conducted on at least two independent experiments—that is, biological replicates—in which each biological replicate contains a technical duplicate or triplicate.

For cohorts i–iv, Vero E6-TMPRSS2 were split into white-walled, clear-bottom 96-well plates (Corning) and grown overnight until they reached approximately 70% confluency. Plasma was diluted in DMEM starting at a 1:10 dilution and serially diluted in DMEM at a 1:3 dilution thereafter. Pseudotyped VSV was diluted at a 1:25 to 1:100 ratio in DMEM and an equal volume was added to the diluted plasma. The virus–plasma mixture was incubated for 30 min at room temperature and added to the Vero E6-TMPRSS2 cells. After two hours, an equal volume of DMEM supplemented with 20% FBS and 2% penicillin-streptomycin was added to the cells. After 20–24 h, ONE-Glo EX (Promega) was added to each well and the cells were incubated for 5 min at 37 °C. Luminescence values were measured using a BioTek Synergy Neo2 plate reader. Luminescence readings from the neutralization assays were normalized and analysed using GraphPad Prism 9.1.0. The RLU values recorded from uninfected cells were used

to define 100% neutralization and RLU values recorded from cells infected with pseudovirus without plasma were used to define 0% neutralization. ID_{50} were determined from the normalized data points using a [inhibitor] versus normalized response–variable slope model using at least two technical repeats to generate the curve fits. At least two biological replicates with two distinct batches of pseudovirus were conducted for each sample.

Neutralization of authentic SARS-CoV-2 viruses

Vero E6-TMPRSS2 cells were seeded into black-walled, clear-bottom 96-well plates at 20,000 cells per well and cultured overnight at 37 °C. The next day, 9-point fourfold serial dilutions of monoclonal antibodies were prepared in growth medium (DMEM + 10% FBS). The different SARS-CoV-2 strains were diluted in infection medium (DMEM + 2% BSA) at a final MOI of 0.01 plaque-forming units per cell, added to the monoclonal antibody dilutions and incubated for 30 min at 37 °C. Medium was removed from the cells, monoclonal antibody–virus complexes were added and incubated at 37 °C for 18 h (WA-1 and XBB.1.5) or 24 h (BA.2). Cells were fixed with 4% PFA (Electron Microscopy Sciences, 15714S), permeabilized with Triton X-100 (SIGMA, X100-500ML) and stained with an antibody against the viral nucleocapsid protein (Sino Biologicals, 40143-R001) followed by a staining with the nuclear dye Hoechst 33342 (Fisher Scientific, H1399) and a goat anti-rabbit Alexa Fluor 647 antibody (Invitrogen, A-21245). Plates were imaged on a Cytation5 plate reader. Whole well images were acquired (12 images at 4× magnification per well) and nucleocapsid-positive cells were counted using the manufacturer's software.

Pseudotyped VSV entry assays with protease inhibitors

Vero E6-TMPRSS2 or HEK293T-ACE2 were split into white-walled, clear-bottom 96-well plates (Corning) at a density of 18,000 or 36,000 cells, respectively, and grown overnight. The following day, the growth medium was removed and, for assays conducted with Vero E6-TMPRSS2, the cells washed once with DMEM. The cells were incubated for 2 h with DMEM containing 50 μM of Camostat (Sigma), Nafamostat (Sigma), E64d (Sigma), or 0.5% DMSO. All three protease inhibitors were dissolved in DMSO to a concentration of 10 mM and diluted in DMEM. The protease inhibitors were removed and pseudovirus diluted 1:50 or 1:200 in DMEM was added to the cells. After 2 h, an equal volume of DMEM supplemented with 20% FBS and 2% penicillin-streptomycin was added to the cells. After 20–24 h, ONE-Glo EX (Promega) was added to each well and the cells were incubated for 5 min at 37 °C. Luminescence values were measured using a BioTek Synergy Neo2 plate reader. Luminescence readings from the neutralization assays were normalized and analysed using GraphPad Prism 9.1.0. The RLU values recorded from uninfected cells were used to define 0% infectivity and RLU values recorded from cells incubated with 0.5% DMSO only and infected with pseudovirus were used to define 100% infectivity. Twelve technical replicates were performed for each inhibitor and pseudovirus and at least two biological replicates with two distinct batches of pseudovirus were conducted.

Recombinant protein production for BLI, FACS and cryo-EM

SARS-CoV-2 RBDs and human ACE2 were produced and purified from Expi293F cells as previously described (Bowen, Addetia, et al., 2022). In brief, cells were grown to a density of 3×10^6 cells per ml and transfected using the ExpiFectamine 293 Transfection Kit (Thermo Fisher Scientific). Three to five days post-transfection, proteins were purified from clarified supernatants using HisTrap HP affinity columns (Cytiva) and washed with ten column volumes of 20 mM imidazole, 25 mM sodium phosphate pH 8.0, and 300 mM NaCl before elution on a gradient to 500 mM imidazole, 25 mM sodium phosphate pH 8.0, and 300 mM NaCl. Proteins were buffer exchanged into 20 mM sodium phosphate pH 8 and 100 mM NaCl and concentrated using centrifugal filters (Amicon Ultra) before being flash frozen.

For cryo-EM, recombinant ACE2 was expressed in ExpiCHO-S cells at 37 °C and 8% CO_2 with kifunensine added to 10 μM. Cell culture supernatant was collected eight days post-transfection, supplemented with buffer to a final concentration of 80 mM Tris-HCl pH 8.0, 100 mM NaCl, and then incubated with BioLock (IBA) solution. ACE2 was purified using a 5-ml StrepTrap HP column (Cytiva) followed by isolation of the monomeric ACE2 by size-exclusion chromatography using a Superdex 200 Increase 10/300 GL column (Cytiva) pre-equilibrated in PBS.

Recombinant S309 Fab used for cryo-EM was expressed by ATUM Bio using HEK293-derived suspension cells (lacking the N55Q mutation introduced for improving its manufacturability), purified using CaptureSelect IgG-CH1 resin and buffer exchanged into PBS (ATUM Bio).

Recombinant protein production for SPR binding assays and antigen-specific MBC repertoire analysis by ELISA

Proteins were expressed in Expi293F cells (Thermo Fisher Scientific) at 37 °C and 8% CO_2. Transfections were performed using the ExpiFectamine 293 Transfection Kit (Thermo Fisher Scientific). Cell culture supernatants were collected 4–5 days after transfection and supplemented with 10× PBS to a final concentration of 2.5× PBS (342.5 mM NaCl, 6.75 mM KCl and 29.75 mM phosphates). SARS-CoV-2 RBDs were purified by IMAC using Cobalt or Nickel resin followed by buffer exchange into PBS using Amicon centrifugal filters (Milipore Sigma) or by size-exclusion chromatography using a Superdex 200 Increase 10/300 GL column (Cytiva). For SPR binding measurements, recombinant ACE2 (residues 19–615 from Uniprot entry Q9BYF1 with a C-terminal thrombin cleavage site–TwinStrep–10×His–GGG tag and N-terminal signal peptide) was expressed in Expi293F cells at 37 °C and 8% CO_2. Transfection was performed using the ExpiFectamine 293 Transfection Kit (Thermo Fisher Scientific). Cell culture supernatant was collected 7–8 days after transfection, supplemented to a final concentration of 80 mM Tris-HCl pH 8.0, 100 mM NaCl, and then incubated with BioLock solution (IBA GmbH). ACE2 was purified using a 1-ml StrepTrap HP column (Cytiva) followed by isolation of the monomeric ACE2 by size-exclusion chromatography using a Superdex 200 Increase 10/300 GL column (Cytiva) pre-equilibrated in PBS. Recombinant S309 Fab used for SPR binding studies was produced in either ExpiCHO-S cells and purified using a Capture Select CH1-XL MiniChrom Column (Thermo Fisher), followed by buffer exchange into PBS using a HiPrep 26/10 Desalting Column

(Cytiva) or in HEK293 suspension cells, purified using CaptureSelect IgG-CH1 resin and buffer exchanged into PBS (ATUM Bio).

Biolayer interferometry

BLI was used to assess binding of SARS-CoV-2 RBDs to human ACE2 using an Octet Red96 (Sartorius) and the Octet Data acquisition v11.1. Biotinylated Wu, BA.4/5, BA.2.75.2, BQ.1.1, XBB.1, and XBB.1.5 RBDs were diluted to a concentration of 5 ng μl−1 in 10X Octet kinetics buffer (Sartorius) and loaded onto pre-hydrated Streptavidin biosensors to a 1 nm total shift. The loaded tips were dipped into a 1:3 dilution series of monomeric human ACE2 starting at 900 nM or 300 nM for 300 s followed by dissociation in 10× kinetic buffer for 300 s. All steps of the affinity measurements using BLI were carried out at 30 °C with a shaking speed of 1,000 rpm. The resulting data were baseline subtracted and affinity measurements were calculated using a 1:1 global fit binding model with Octet Data Analysis HT software v12.0. Binding curves were plotted using GraphPad Prism 9.1.0.

In vivo studies

Mouse studies were carried out in accordance with the recommendations in the Guide for the Care and Use of Laboratory Animals of the National Institutes of Health. The protocols were approved by the Institutional Animal Care and Use Committee at the Washington University School of Medicine (assurance number A3381–01). Virus inoculations were performed under anaesthesia that was induced and maintained with ketamine hydrochloride and xylazine, and all efforts were made to minimize animal

suffering. Heterozygous K18-hACE2 C57BL/6 J mice (strain: 2B6.Cg-Tg(K18-ACE2)2Prlmn/J) were obtained from The Jackson Laboratory. All animals were housed in groups of 3 to 5 and fed standard chow diets. The photoperiod was 12 h on/12 h off dark/light cycle. The ambient animal room temperature was 21 °C, controlled within ±1 °C and the room humidity was 50%, controlled within ±5%. Eight- to ten-week-old female K18-hACE2 mice were administered indicated doses of S309 or isotype control (anti-WNV hE16 (Oliphant et al., 2005)) antibody by intraperitoneal injection one day before intranasal inoculation with 10^4 FFU of BQ.1.1. Weight was recorded daily, and animals were euthanized on day 6 after virus inoculation.

All hamster experiments were performed according to the French legislation and in compliance with the European Community Council Directives (2010/63/UE, French Law 2013–118, 6 February 2013) and according to the regulations of Pasteur Institute Animal Care Committees. The Animal Experimentation Ethics Committee (CETEA 89) of the Institut Pasteur approved this study (200023) before experiments were initiated. Hamsters were housed by groups of 4 animals and manipulated in class III biosafety cabinets in the Pasteur Institute animal facilities accredited by the French Ministry of Agriculture for performing experiments on live rodents. All animals were handled in strict accordance with good animal practice. Male golden Syrian hamsters (*Mesocricetus auratus;* RjHan:AURA) of 5–6 weeks of age (average weight 60–80 grams) were purchased from Janvier Laboratories and handled under specific pathogen-free conditions. The animals were housed and manipulated in isolators in a Biosafety level-3 facility, with ad libitum access to water and food. Before manipulation, animals underwent an acclimation period of one week. Twenty-four hours before infection, the

hamsters received an intraperitoneal injection of different concentrations of the monoclonal antibodies S309 (0.6, 1.7, 5 and 15 mg kg^{-1}, hamster IgG2a), or the control isotype MPE8 (15 mg kg^{-1}, hamster IgG2a). Animal infection was performed as previously described (de Melo et al., 2021). In brief, the animals were anaesthetized with an intraperitoneal injection of 200 mg kg^{-1} ketamine (Imalgène 1000, Merial) and 10 mg kg^{-1} xylazine (Rompun, Bayer), and 100 µl of physiological solution containing 6×10^4 plaque-forming units of SARS-CoV-2/Omicron_XBB.1.5 (GISAID ID: EPI_ISL_16353849, kindly provided by O. Schwartz and colleagues) was then administered intranasally to each animal (50 µl per nostril). Mock-infected animals received the physiological solution only. Infected and mock-infected hamsters were housed in separated isolators and were followed-up daily, for four days, when the body weight and the clinical score were noted. At day 4 post-inoculation, the animals were euthanized with an excess of anaesthetics (ketamine and xylazine) and exsanguination. Blood samples were collected by cardiac puncture; after coagulation, the tubes were centrifuged at 2,000*g* during 10 min at 4 °C, the serum was collected and frozen at −80 °C until further analyses. The lungs were collected, weighted and frozen at −80 °C until further analyses.

Measurement of viral RNA levels

Mouse tissues were weighed and homogenized with zirconia beads in a MagNA Lyser instrument (Roche Life Science) in 1 ml of DMEM medium supplemented with 2% heat-inactivated FBS. Tissue homogenates were clarified by centrifugation at approximately 10,000*g* for 5 min and stored at −80 °C. RNA was extracted using the

MagMax mirVana Total RNA isolation kit (Thermo Fisher Scientific) on the Kingfisher Flex extraction robot (Thermo Fisher Scientific). RNA was reverse transcribed and amplified using the TaqMan RNA-to-CT 1-Step Kit (Thermo Fisher Scientific). Reverse transcription was carried out at 48 °C for 15 min followed by 2 min at 95 °C. Amplification was accomplished over 50 cycles as follows: 95 °C for 15 s and 60 °C for 1 min. Copies of total (genomic and subgenomic) SARS-CoV-2 *N* gene RNA in samples were determined using a previously published assay (Case et al., 2020). In brief, a TaqMan assay was designed to target a highly conserved region of the *N* gene (forward primer: ATGCTGCAATCGTGCTACAA; reverse primer: GACTGCCGCCTCTGCTC; probe: /56-FAM/TCAAGGAAC/ZEN/AACATTGCCAA/3IABkFQ/). This region was included in an RNA standard to allow for copy number determination down to 10 copies per reaction. The reaction mixture contained final concentrations of primers and probe of 500 and 100 nM, respectively.

For hamster studies, frozen lung fragments were weighted and homogenized with 1 ml of ice-cold DMEM (31966021, Gibco) supplemented with 1% penicillin/streptomycin (15140148, Thermo Fisher) in Lysing Matrix M 2 ml tubes (116923050-CF, MP Biomedicals) using the FastPrep-24 system (MP Biomedicals), and the following scheme: homogenization at 4.0 m s^{-1} for 20 s, incubation at 4 °C for 2 min, and new homogenization at 4.0 m s^{-1} for 20 s. The tubes were centrifuged at 10,000*g* for 1 min at 4 °C. Afterwards, 125 µl of the tissue homogenate supernatant were mixed with 375 µl of Trizol LS (10296028, Invitrogen) and the total RNA was extracted using the Direct-zol RNA MiniPrep Kit (R2052, Zymo Research). The presence of SARS-CoV-2 RNA in these samples was evaluated by one-step

quantitative PCR with reverse transcription in a final volume of 12.5 µl per reaction in 384-wells PCR plates using a thermocycler (QuantStudio 6 Flex, Applied Biosystems). In brief, 2.5 µl of RNA were added to 10 µl of a master mix containing 6.25 µl of 2× reaction mix, 0.2 µl of $MgSO_4$ (50 mM), 0.5 µl of Superscript III RT/Platinum Taq Mix (2 UI μl^{-1}) and 3.05 µl of nuclease-free water containing the nCoV_IP2 primers (nCoV_IP2-12669Fw: 5′-ATGAGCTTAGTCCTGTTG-3′; nCoV_IP2-12759Rv: 5′-CTCCCTTTGTTGTGTTGT-3′) at a final concentration of 400 nM, and the nCoV_IP2 probe (5′-FAM-AGATGTCTTGTGCTGCCGGTA-3′-TAMRA) at a final concentration of 200 nM. The amplification conditions were as follows: 55 °C for 20 min, 95 °C for 3 min, 50 cycles of 95 °C for 15 s and 58 °C for 30 s, and a last step of 40 °C for 30 s. Viral load quantification (expressed as RNA copy number per mg of tissue) was assessed by linear regression using a standard curve of six known quantities of RNA transcripts containing the *RdRp* sequence (ranging from 10^7 to 10^2 copies).

Viral plaque assay

Vero E6-TMPRSS2-ACE2 cells were seeded at a density of 1×10^5 cells per well in 24-well tissue culture plates. The following day, medium was removed and replaced with 200 µl of material to be titrated diluted serially in DMEM supplemented with 2% FBS. One hour later, 1 ml of methylcellulose overlay was added. Plates were incubated for 72 h, and then fixed with 4% paraformaldehyde (final concentration) in PBS for 20 min. Plates were stained with 0.05% (w/v) crystal violet in 20% methanol and washed twice with distilled, deionized water.

End-point virus titration in hamsters

Lung tissues were homogenized as described above for measurement of viral RNA. To quantify infectious SARS-CoV-2 particles, lung homogenates titrations were performed on confluent Vero E6 cells in 96- well plates. Viral titres were expressed as 50% tissue culture infectious dose ($TCID_{50}$) per mg tissue (Lindenbach, 2009).

Transient expression of recombinant SARS-CoV-2 S and flow cytometry

ExpiCHO-S cells were seeded at 6×10^6 cells per ml in a volume of 5 ml in a 50-ml bioreactor. The following day, cells were transfected with SARS-CoV-2 S glycoprotein-encoding pcDNA3.1(+) plasmids (BetaCoV/Wuhan-Hu-1/2019, accession number MN908947, Wu-D614; Omicron BA.2, BQ.1.1, XBB.1, XBB.1.5, BN.1 or BA.2-E340A generated by overlap PCR mutagenesis of the Wu-D614 plasmid) harbouring the Δ19 C-terminal truncation. S-encoding plasmids were diluted in cold OptiPRO SFM (Life Technologies, 12309-050), mixed with ExpiFectamine CHO Reagent (Life Technologies, A29130) and added to cells. Transfected cells were then incubated at 37 °C with 8% CO_2 with an orbital shaking speed of 250 rpm (orbital diameter of 25 mm) for 24 to 48 h. Transiently transfected ExpiCHO-S cells were harvested and washed twice in wash buffer (PBS 2% FBS, 2mM EDTA). Cells were counted and distributed into round bottom 96-well plates (Corning, 3799) and incubated with serial dilutions of mAb starting at 10 μg ml^{-1}. Alexa Fluor 647-labelled Goat anti-human IgG secondary antibody (Jackson ImmunoResearch, 109-606-098) was prepared at 2 μg ml^{-1} and added onto cells after two washing steps. Cells were then washed twice and resuspended in wash buffer for data acquisition at Ze5 cytometer (Bio-Rad).

Measurement of effector functions triggered by monoclonal antibodies

ADCC assays were performed using ExpiCHO-S cells transiently transfected with SARS-CoV-2 S glycoproteins (Wu-D614, BA.2, BQ.1.1, XBB.1, XBB.1.5, BN.1 or BA.2-E340A) as target cells. Natural killer cells were isolated from fresh blood of healthy donors using the MACSxpress WB NK cell isolation kit, human (Miltenyi Biotec, 130-127-695). Target cells were incubated with titrated concentrations of monoclonal antibody for 10 min and then with primary human natural killer cells at an effector to target ratio ranging from 6:1 to 9:1. ADCC was measured using the LDH release assay (Cytotoxicity Detection Kit (LDH) (Roche, 11644793001)) after 4 h incubation at 37 °C.

ADCP assays were performed using ExpiCHO-S cells transiently transfected with SARS-CoV-2 S glycoproteins and labelled with PKH67 (Sigma-Aldrich) as target cells. PMBCs from healthy donors were labelled with CellTrace Violet (Invitrogen) and used as source of phagocytic effector cells. Target cells (10,000 per well) were incubated with titrated concentrations of monoclonal antibody for 10 min and then mixed with PBMCs (200,000 per well). The next day, cells were stained with APC-labelled anti-CD14 antibody (BD Pharmingen), BV605-labelled anti-CD16 antibody (Biolegend), BV711-labelled anti-CD19 antibody (Biolegend), PerCP/Cy5.5-labelled anti-CD3 antibody (Biolegend), APC/Cy7-labelled anti-CD56 antibody (Biolegend) for the identification of $CD14^+$ monocytes. After 20 min, cells were washed and fixed with 4% paraformaldehyde before acquisition on a ZE5 Cell Analyzer (Bio-Rad). Data were analysed using FlowJo software (v10.8.1). The percentage ADCP was calculated as the percentage of monocytes ($CD3^-CD19^-CD14^+$ cells) positive for PKH67.

Measurement of effector functions triggered by plasma antibodies

Antibody-dependent activation of human FcγRIIIa by plasma antibodies was quantified using a bioluminescent reporter assay. ExpiCHO-S cells transiently expressing full-length SARS-CoV-2 S from Wu-D614, BA.5, BQ.1.1 or XBB.1 (target cells) were incubated with serial dilutions of plasma from immune donors. After a 20-min incubation, Jurkat reporter cells stably expressing FcγRIIIa V158 and a NFAT-driven luciferase reporter gene (effector cells) were added at an effector to target ratio of 6:1. Signalling was quantified by the luciferase signal produced via activation of the NFAT pathway. Luminescence was measured after 22 h of incubation at 37 °C with 5% CO_2 with a luminometer using the Bio-Glo-TM Luciferase Assay Reagent according to the manufacturer's instructions (Promega).

Natural killer cell-mediated ADCC induced by plasma antibodies was measured as described for ADCC except that ExpiCHO-S cells transiently expressing full-length SARS-CoV-2 S from Wu-D614, BA.1, BA.5, BA.2.75.2, BQ.1.1 or XBB.1 (target cells) were incubated with plasma from immune donors at a single dilution (1:200).

Antigen-specific MBC repertoire analysis of secreted IgGs

Replicate cultures of total unfractionated PBMCs obtained from SARS-CoV-2 infected and/or vaccinated individuals were seeded in 96 U-bottom plates (Corning) in RPMI1640 supplemented with 10% fetal calf serum (Hyclone), sodium pyruvate, MEM non-essential amino acids, stable glutamine, 2-mercaptoethanol, penicillin-streptomycin, kanamycin and transferrin. MBC stimulation and differentiation was induced by adding

2.5 µg ml^{-1} R848 (3 M) and 1,000 U ml^{-1} human recombinant IL-2 at 37 °C and 5% CO_2, as previously described (Pinna et al., 2009). After 10 days, the cell culture supernatants were collected for ELISA analysis.

Enzyme-linked immunosorbent assay

Ninety-six half-area well plates (Corning, 3690) were coated overnight at 4 °C with 25 µl of sarbecovirus RBDs prepared at 5 µg ml^{-1} in PBS pH 7.2. Plates were then blocked with PBS 1% BSA (Sigma-Aldrich, A3059) and subsequently incubated with serial dilutions of monoclonal antibodies for 1 h at room temperature. After 4 washing steps with PBS 0.05% Tween-20 (PBS-T) (Sigma-Aldrich, 93773), goat anti-human IgG-AP secondary antibody (Southern Biotech, 2040-04, diluted 1/500) was added and incubated for 1 h at room temperature. Plates were then washed four times with PBS-T and 4-nitrophenyl phosphate (pNPP, Sigma-Aldrich, 71768) substrate was added. After 30 min incubation, absorbance at 405 nm was measured using a plate reader (BioTek) and data were plotted using Prism GraphPad 9.1.0. To test plasma and MBC-derived antibodies, Spectraplate-384 with high protein binding treatment (custom made from PerkinElmer) were coated overnight at 4 °C with 3 µg ml^{-1} of different SARS-CoV-2 RBDs (produced in house) and S trimers (Acrobiosystems AG, SPN-C52H3, SPN-C522a, SPN-C522e, SPN-C522r, SPN-C522s, SPN-C522t and SPN-C524i) in PBS pH 7.2 or PBS alone as control. Plates were subsequently blocked with Blocker Casein (1%) in PBS (Thermo Fisher Scientific, 37528) supplemented with 0.05% Tween-20 (Sigma-Aldrich, 93773-1KG). The coated plates were incubated with diluted B cell supernatant for 1 h at room temperature. Plates were washed with PBS containing

0.05% Tween-20 (PBS-T), and binding was revealed using secondary goat anti-human IgG-AP (Southern Biotech, 2040-04). After washing, pNPP substrate (Sigma-Aldrich, 71768-25G) was added and plates were read at 405 nm after 1 h or 30 min.

Blockade of RBD binding to human ACE2

MBC culture supernatants were diluted in PBS and mixed with SARS-CoV-2 Wu RBD mouse Fc-tagged antigen (Sino Biological, 40592-V05H) or with biotinylated BQ.1.1 or XBB.1 RBDs (Acrobiosystems) at a final concentration of 20 ng ml^{-1} and incubated for 30 min at 37 °C. The mix was added for 30 min to ELISA 384-well plates (NUNC, P6366-1CS) pre-coated overnight at 4 °C with 4 µg ml^{-1} human ACE2 (produced in house) in PBS. Plates were washed with PBS containing 0.05% Tween-20 (PBS-T), and RBD binding was revealed using secondary goat anti-mouse IgG-AP (Southern Biotech, 1032-04) or Streptavidin-AP (Jackson ImmunoResearch). After washing, pNPP substrate (Sigma-Aldrich, 71768-25G) was added and plates were read at 405 nm after 1 h.

Blockade of binding to S

Human anti-S monoclonal antibodies (S2V29 for RBD site Ia, SA55 for RBD site IIa, S309 for RBD site IV (Pinto et al., 2020), S3H3 for domain C/SD1 (Hong et al., 2022) and S2P6 for the stem helix (Pinto et al., 2021)) were biotinylated using the EZ-Link NHS-PEO solid phase biotinylation kit (Pierce). Labelled monoclonal antibodies were tested for binding to Wu-G614, BQ.1.1 and XBB.1 S by ELISA and the optimal concentration of each monoclonal antibody to achieve 80% maximal binding was

determined. Plasma samples were serially diluted and added to ELISA 96-well plates (Corning) pre-coated overnight at 4 °C with 1 μg ml^{-1} of S (Acrobiosystems) in PBS. After 30 min, biotinylated anti-S monoclonal antibodies were added at the concentration achieving 80% maximal binding and the mixture was incubated at room temperature for 30 min. Plates were washed and antibody binding was revealed using alkaline phosphatase-conjugated streptavidin (Jackson ImmunoResearch). After washing, pNPP substrate (Sigma-Aldrich) was added and plates were read at 405 nm. The percentage of inhibition was calculated as follow: (1 − (absorbance of sample − absorbance of negative control)/(absorbance of positive control − absorbance of negative control)) × 100.

PNGase F reaction to remove N-linked glycans on BN.1 RBD

Twenty micrograms of purified BN.1 RBD was combined with 2 μl PNGase F (500 units per μl, New England BioLabs, P0704S) and 5 μl of 10× GlycoBuffer 3and H2O (if necessary) to bring the total reaction volume to 50 μl. The reaction was incubated at room temperature overnight and used for SPR and mass intact mass spectrometry.

Intact mass spectrometry analysis and liquid chromatography–mass spectrometry analysis

Four micrograms of PNGase F-treated BN.1 RBD was used for each injection on the liquid chromatography–mass spectrometry (LC–MS) system to acquire intact mass spectrometry signal after separation of protease and protein by liquid chromatography

(Agilent PLRP-S reversed phase column). Thermo MS (Q Exactive Plus Orbitrap) was used to acquire intact protein mass under denaturing conditions. BioPharma Finder 3.2 software was used to deconvolute the raw *m*/*z* data to protein average mass.

Peptide mapping with LC–MS was used to profile the site-specific glycosylation sites on BN.1 RBD. Glycopeptides containing only one specific glycan were achieved by selectively digesting with chymotrypsin protease. Twenty micrograms of each digest product (peptide with a single glycan) was analysed by LC–MS (Agilent AdvanceBio peptide mapping column and Thermo Q Exactive Plus Orbitrap MS). Peptide mapping data were analysed on Biopharma Finder 3.2 data analysis software.

SPR assays to measure binding of ACE2 and S309 Fab to RBDs

Measurements were performed using a Biacore T200 instrument or a Biacore 8k instrument using the Biacore Evaluation software (v.3.2.1). CM5 chips with covalently immobilized anti-Avi polyclonal antibody diluted to a final concentration of 25 μg ml^{-1} (GenScript, A00674-40) were used for surface capture of His–Avi tag containing RBDs. Running buffer was HBS-EP+ pH 7.4 (Cytiva) and measurements were performed at 25 °C. Experiments were performed with a fourfold dilution series of monomeric S309 Fab or ACE2 at 300, 75, 18.8 and 4.7 nM and were run as single-cycle kinetics. Data were double reference-subtracted and fit to a binding model using Biacore Insight software (v4.0.8.20368). The 1:1 binding model was used to determine the kinetic parameters. 2–14 replicates were performed for each ligand (RBDs) and analyte (ACE2 or S309 Fab) pair. For BN.1 RBD–S309 Fab binding, due to a low binding signal because of a slow association rate constant, a constant Rmax calculated

from a control analyte was applied to calculate the kinetic parameters. K_d values are reported as the average of all replicates with the corresponding standard deviation (Table 4.2 for ACE2 binding data and Table 4.5 for S309 Fab binding data)

Cell–cell fusion assay

Cell–cell fusion assays using a split-GFP system was conducted as previously described(Bowen, Addetia, et al., 2022). In brief, Vero E6-TMPRSS2-GFP_{11} cells were split into 96-well, glass bottom, black-walled plates (CellVis) at a density of 36,000 cells per well. BHK-21-$GFP_{1–10}$ cells were split into 6-well plates at a density of 1×10^6 cells per well. The following day, the growth medium was removed and replaced with DMEM containing 10% FBS and 1% penicillin-streptomycin and the cells were transfected with 4 μg of S protein using Lipofectamine 2000. Twenty-four hours after transfection, BHK-21-$GFP_{1–10}$ cells expressing the S protein were washed three times using FluoroBrite DMEM (Thermo Fisher) and detached using an enzyme-free cell dissociation buffer (Gibco). The Vero E6-TMPRSS2-GFP_{11} were washed 3 times with FluoroBrite DMEM and 9,000 BHK-21-$GFP_{1–10}$ cells were plated on top of the Vero E6-TMPRSS2-GFP_{11} cells. The cells were incubated at 37 °C and 5% CO_2 in a Cytation 7 plate Imager (BioTek) and both bright-field and GFP images were collected every 30 min for 18 h. Fusogenicity was assessed by measuring the area showing GFP fluorescence for each image using Gen5 Image Prime v3.11 software.

To measure surface expression of the variant SARS-CoV-2 S protein, 1×10^6 transiently transfected BHK-21-$GFP_{1–10}$ cells were collected by centrifugation at 1,000*g* for 5 min. The cells were washed once with PBS and fixed with 2%

paraformaldehyde. The cells were washed twice with flow staining buffer (1% BSA, 1 mM EDTA, 0.1% NaN_3 in PBS) and labelled with 25 μg ml^{-1} S2L20, an NTD-directed antibody that recognizes all currently and previously circulating SARS-CoV-2 variants, for 45 min. The cells were washed three times with flow staining buffer and labelled with a PE-conjugated anti-human IgG Fc antibody (Thermo Fisher) for 30 min. The cells were washed an additional three times and resuspended in flow staining buffer. The labelled cells were analysed using a BD FACSymphony A3. Cells were gated on singleton events and a total of 10,000 singleton events were collected for each sample. The fraction of S-positive cells was determined in FlowJo 10.8.1 by gating singleton events for the mock transfected cells on PE intensity.

Flow cytometry analysis of SARS-CoV-2 RBD-reactive MBCs

RBD–streptavidin tetramers conjugated to fluorophores were generated by incubating biotinylated Wu, BA.1, BA.2, BA.4/5 or BQ.1.1 with streptavidin at a 4:1 molar ratio for 30 min at 4 °C. Excess free biotin was then added to the reaction to bind any unconjugated sites in the streptavidin tetramers. The RBD-streptavidin tetramers were washed once with PBS and concentrated with a 30-kDa centrifugal concentrator (Amicon). An additional streptavidin tetramer conjugated to biotin only was generated and included in the staining.

Approximately 5 to 15 million PMBCs were collected 5–72 days post-vaccination for individuals who received either the Wu monovalent mRNA booster or Wu/BA.5 bivalent mRNA booster. The cells were collected by centrifugation at 1,000*g* for 5 mins at 4 °C and washed twice with PBS. The cells were then stained with Zombie Aqua dye

(Biolegend; diluted 1:100 in PBS) for 30 min at room temperature after which the cells were washed twice with FACS staining buffer (0.1% BSA, 0.1% NaN_3 in PBS). The cells were then stained with antibodies for CD20-PECy7 (BD), CD3-Alexa eFluor780 (Thermo Fisher), CD8-Alexa eFluor780 (Thermo Fisher), CD14-Alexa eFluor780 (Thermo Fisher), CD16-Alexa eFluor780 (Thermo Fisher), IgM-Alexa Fluor 647 (BioLegend), IgD-Alexa Fluor 647 (BioLegend), and CD38-Brilliant Violet 785 (BioLegend), all diluted 1:200 in Brilliant Stain Buffer (BD), along with the RBD-streptavidin tetramers for 30 min at 4 °C. The cells were washed three times, resuspended in FACS staining buffer, and passed through a 35-μm filter. The cells were examined using a BD FACSAria III and FACSDiva for acquisition and FlowJo 10.8.1 for analysis. Single live $CD20^+CD3^-CD8^-CD14^-CD16^-IgM^{lo}IgD^{lo}CD38^{lo}RBD^+$ cells were sorted based on reactivity to the Omicron and Wu RBDs into RNAlater and stored at −80 °C.

Cryo-EM sample preparation, data collection and data processing

Cryo-EM grids of BQ.1.1 RBD–ACE2–S309, XBB.1 RBD–ACE2–S309 or BN.1 RBD–ACE2–S309 complex were prepared fresh after purification by size-exclusion chromatography. For BQ.1.1 RBD–ACE2–S309 complex, 3 μl of 0.25 mg ml^{-1} BQ.1.1 RBD–ACE2–S309 were loaded onto freshly glow-discharged R 2/2 UltrAuFoil grids (Russo & Passmore, 2014), prior to plunge freezing using a vitrobot Mark IV (Thermo Fisher Scientific) with a blot force of 0 and 6 s blot time at 100% humidity and 22 °C. Data were acquired using an FEI Titan Krios transmission electron microscope operated at 300 kV and equipped with a Gatan K3 direct detector and Gatan Quantum GIF

energy filter, operated in zero-loss mode with a slit width of 20 eV. For BQ.1.1 RBD–ACE2-S309 data set, automated data collection was carried out using Leginon v3.4 (Suloway et al., 2005) at a nominal magnification of 105,000× with a pixel size of 0.843 Å and stage tilt angle of 0° and 30°. 6,487 micrographs were collected with a defocus range comprised between −0.5 and −2.5 µm. For XBB.1 RBD–ACE2–S309 complex, samples were prepared using a Vitrobot Mark IV (Thermo Fisher Scientific) with R 2/2 UltrAuFoil grids and a Chameleon (SPT Labtech) with self-wicking nanowire Cu R1.2/0.8 holey carbon grids. For XBB.1 RBD–ACE2-S309 data set, 6,355 micrographs from UltrAuFoil grids were collected with a defocus range comprised between −0.2 and −3 µm and stage tilt angle of 0° and 30° and 2,889 micrographs from chameleon grids were collected with a defocus range comprised between −0.2 and −3 µm without tilting the stage. For BN.1 RBD–ACE2–S309 complex, samples were prepared using a Vitrobot Mark IV (Thermo Fisher Scientific) with R 2/2 UltrAuFoil grids, manual blotting/plunging with C-flat holey thick carbon grids and Chameleon (SPT Labtech) with self-wicking nanowire Cu R1.2/0.8 holey carbon grids. For BN.1 RBD–ACE2–S309 data set, 3,822 micrographs from UltrAuFoil grids, 2,000, micrographs from chameleon grids and 1,915 micrographs from C-flat holey thick carbon grids were collected with a defocus range comprised between −0.2 and −3.5 µm and stage tilt angle of 0° and 30°. The dose rate was adjusted to 15 counts per pixel per s, and each movie was acquired in super-resolution mode fractionated in 75 frames of 40 ms. Movie frame alignment, estimation of the microscope contrast transfer function parameters, particle picking, and extraction were carried out using Warp (Tegunov & Cramer, 2019) (v1.0.9).

Two rounds of reference-free 2D classification were performed using cryoSPARC (Punjani et al., 2017) (v4.2.2) to select well-defined particle images. These selected particles were subjected to two rounds of 3D classification with 50 iterations each (angular sampling 7.5° for 25 iterations and 1.8° with local search for 25 iterations) using Relion (Scheres, 2012; Zivanov et al., 2018) (v3.1) with an initial model generated with ab-initio reconstruction in cryoSPARC. 3D refinements were carried out using non-uniform refinement (Punjani et al., 2020) along with per-particle defocus refinement in CryoSPARC. Selected particle images were subjected to the Bayesian polishing procedure (Zivanov et al., 2019) implemented in Relion before performing another round of non-uniform refinement in cryoSPARC followed by per-particle defocus refinement and again non-uniform refinement. To further improve the density of the BQ.1.1 RBD and XBB.1 RBD, the particles were subjected to focus 3D classification without refining angles and shifts using a soft mask encompassing the ACE2, RBD and S309 variable domains using a tau value of 60 in Relion. To further improve the density of the BN.1 RBD, the particles were subjected to cryoSPARC heterogeneous refinement. Particles belonging to classes with the best resolved local density were selected and subjected to non-uniform refinement using cryoSPARC. Local resolution estimation, filtering, and sharpening were carried out using CryoSPARC. Reported resolutions are based on the gold-standard Fourier shell correlation (FSC) with 0.143 criterion and Fourier shell correlation curves were corrected for the effects of soft masking by high-resolution noise substitution (S. Chen et al., 2013; Rosenthal & Henderson, 2003).

Model building and refinement

UCSF Chimera (Pettersen et al., 2004) (v1.17.1) and Coot (Emsley et al., 2010) (v0.9.6) were used to fit atomic models into the cryo-EM maps. RBD, ACE2 and S309 Fab models were refined and relaxed using Rosetta using sharpened and unsharpened maps (Frenz et al., 2019; R. Y.-R. Wang et al., 2016).

Statistical analysis

All statistical tests were performed as described in the indicated figure legends using Prism v9.1.0. The number of independent experiments performed are indicated in the relevant figure legends. Comparisons of means between multiple groups of unpaired data were made with Kruskal–Wallis rank test and corrected with Dunn's test. Statistical significance is set as $P < 0.05$, and P values are indicated with: NS, not significant; *$P < 0.05$; **$P < 0.01$; ***$P < 0.001$, ****$P < 0.0001$. ED_{50}, 80% of the maximum binding response (BD_{80}), ID_{50} and IC_{50} titres were calculated from the interpolated value from the log(agonist) and the log(inhibitor), versus response using variable slope (four parameters) non-linear regression. Data were plotted and analysed with GraphPad Prism software (version 9.1.0).

4.10 Figures and Tables

Figure 4.1 Functional properties of the BQ.1.1, XBB.1, XBB.1.5 and BA.2.75.2 variant S glycoproteins

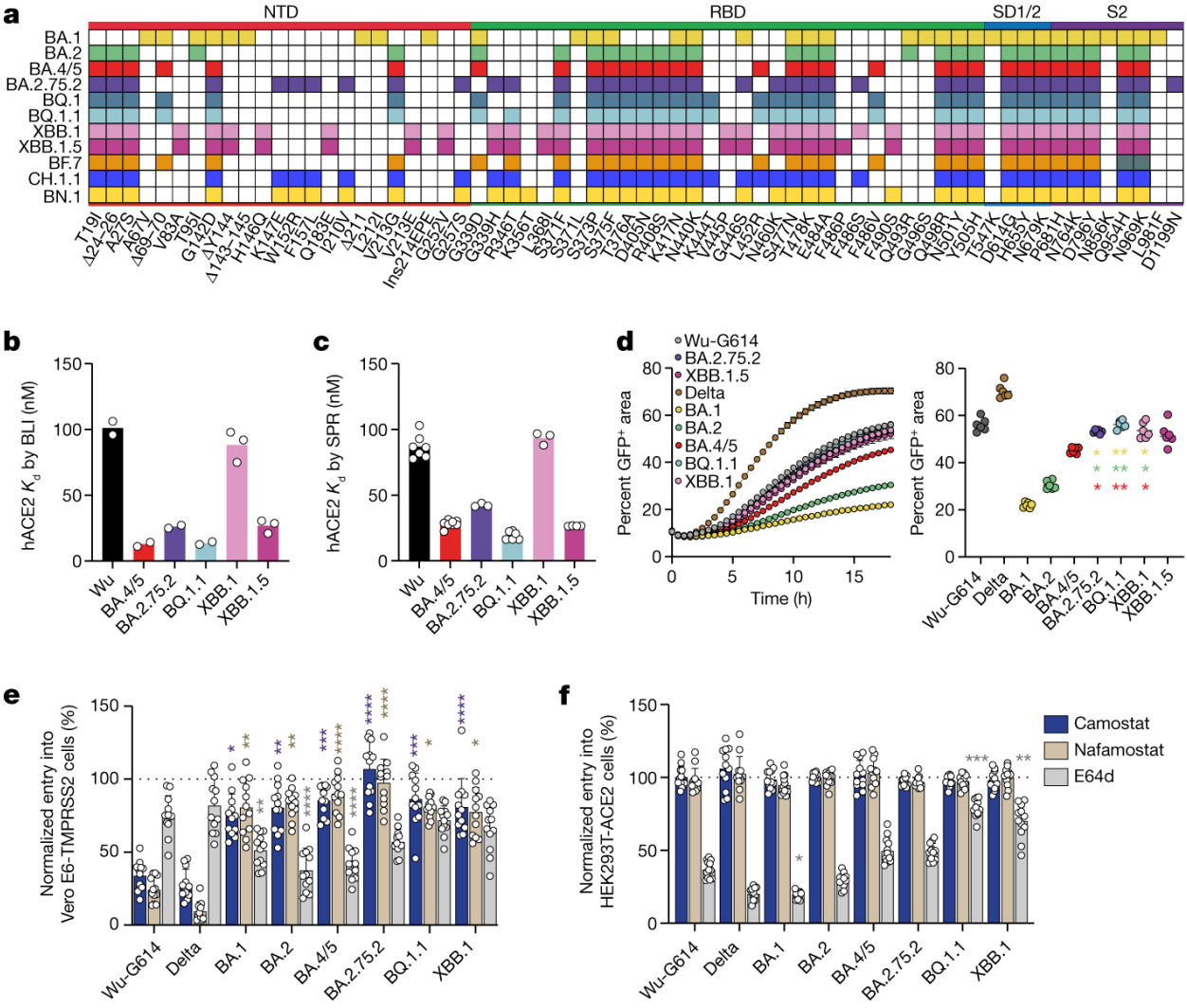

a, Schematic view of S mutations in SARS-CoV-2 variants evaluated in this study. Ins, insertion; SD1/2, subdomains 1 and 2**. b,c,** Equilibrium dissociation constants (K_d) measured by BLI (**b**; $n = 2$ or 3 independent experiments) and SPR (**c**) for binding of the monomeric human ACE2 (hACE2) ectodomain to the indicated immobilized variant RBDs. **d,** Left, cell–cell fusion (indicated as the percentage of GFP$^+$ area) between cells expressing the indicated variant S glycoproteins and Vero E6-TMPRSS2 cells measured over an 18-h time-course experiment using a split-GFP system. Right, cell–cell fusion at 18 h (mean ± s.e.m.). Data are from six fields of view from a single experiment and representative of results from two biological replicates. Comparisons of fusogenicity mediated by BA.1, BA.2, or BA.4/5 S to BA.2.75.2, BQ.1.1, XBB.1 and

XBB.1.5 S were completed using the one-sided Dunnett's test; colours of asterisks indicate the reference group for the comparison (BA.1, gold; BA.2, green; BA.4/5, red). **e,f,** Relative entry of VSV pseudotyped with the indicated S variant in Vero E6-TMPRSS2 (**e**) or HEK293T-ACE2 (**f**) cells treated with 50 μM camostat, nafamostat or E64d. Normalized entry was calculated on the basis of entry values obtained for Vero E6-TMPRSS2 or HEK293T-ACE2 cells treated with DMSO only for each pseudovirus. Data are mean ± s.d. Twelve technical replicates were performed for each pseudovirus and inhibitor and one experiment representative of two independent biological replicates is shown. Comparison of relative entry values were made between Wu-G614 S VSV pseudovirus and each of the examined SARS-CoV-2 variant S VSV pseudoviruses using the one-sided Dunnett's test. *$P < 0.05$; **$P < 0.01$; ***$P < 0.001$; ****$P < 0.0001$.

Figure 4.2 Evaluation of human ACE2 binding to SARS-CoV-2 variant RBDs

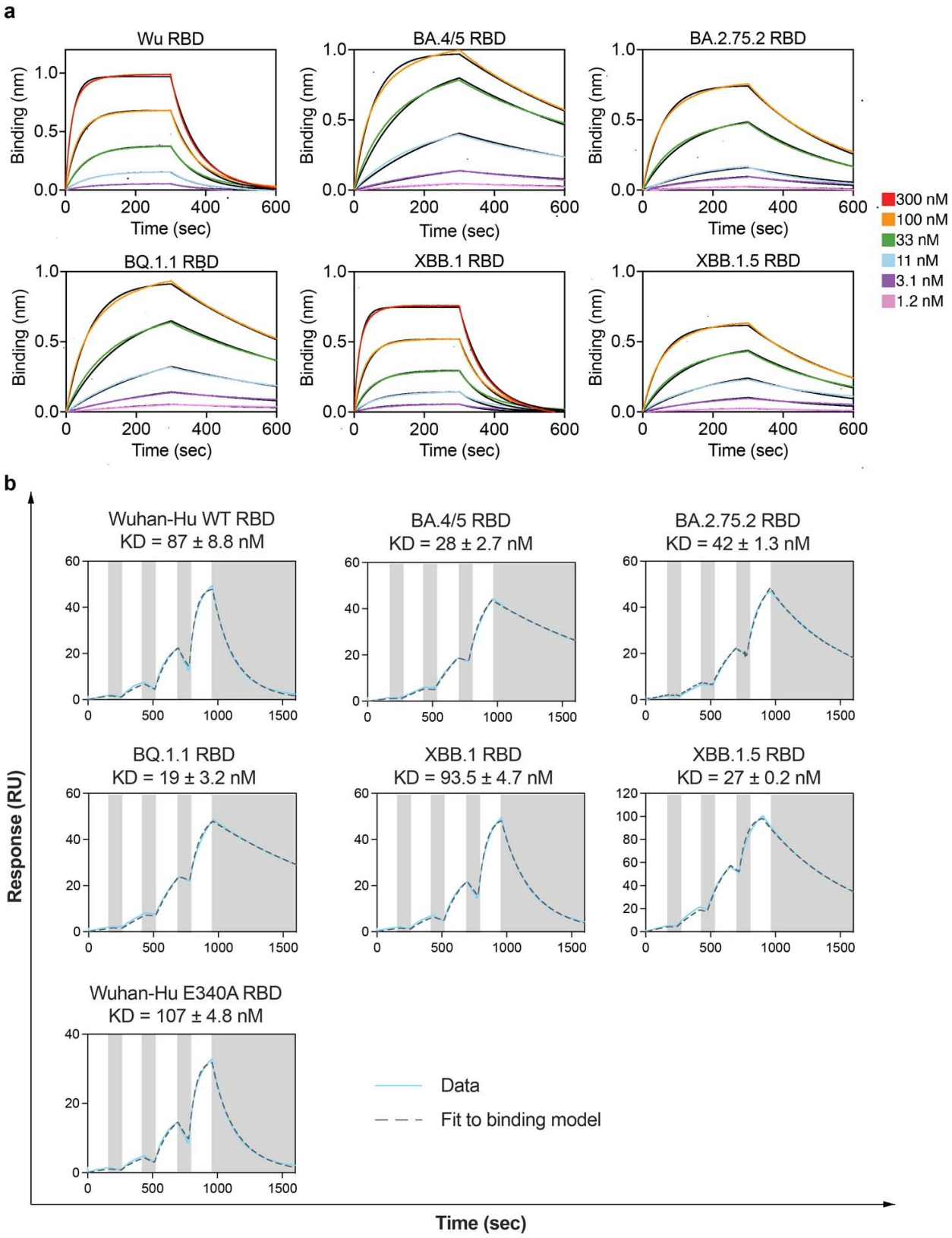

a, Biolayer interferometry binding curves obtained for monomeric human ACE2 binding to biotinylated Wu, BA.4/5, BA.2.75.2, BQ.1.1, XBB.1 or XBB.1.5 RBDs immobilized at the surface of streptavidin biosensors. Kinetic rate constants and affinities are shown in Table 4.1. Fits are shown as solid black lines. **b,** Sensorgrams of monomeric human ACE2 binding to the Wu, BA.2.75.2, BA.4/5, BQ.1.1, XBB.1, XBB.1.5 and Wu E340A RBDs immobilized at the surface of an SPR chip coated with anti-Avi polyclonal Ab. Experiments were performed with serial dilutions of Fabs and run as single-cycle kinetics. Gray blocks denote the dissociation phase. Fits are shown as dashed grey lines. Kinetic rate constants and affinities are shown in Supplementary Table 4.2.

Figure 4.3 Membrane fusion assay

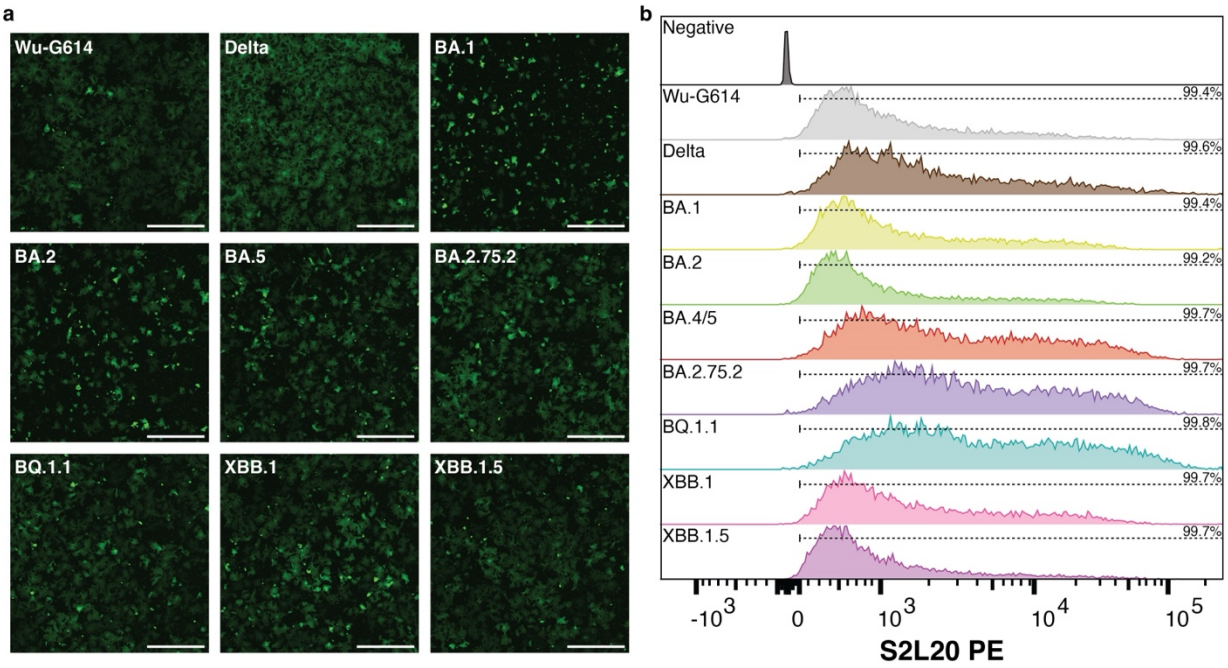

a, Representative cell-cell fusion images showing reconstitution of GFP fluorescence after 18 h. Scale bar: 1 mm. Six images were collected at each 30 minute interval for each variant S analyzed and two independent biological replicates were conducted. **b,** Quantification of SARS-CoV-2 S surface expression by flow cytometry using the NTD-directed Ab S2L20[8,54] for BHK-21 GFP_{1-10} cells transfected with Wu-G614, Delta, BA.1, BA.2, BA.4/5, BA.2.75.2, BQ.1.1, XBB.1, or XBB.1.5 S proteins. The y-axis is presented as a modal scale scaled to maximum singleton events for that plot. The percentage of S-positive cells is indicated in the top right corner based on the PE intensity relative to mock transfected (negative) cells and represented by the dashed line above each plot.

Figure 4.4 Structural analysis of BQ.1.1 and XBB.1 RBDs

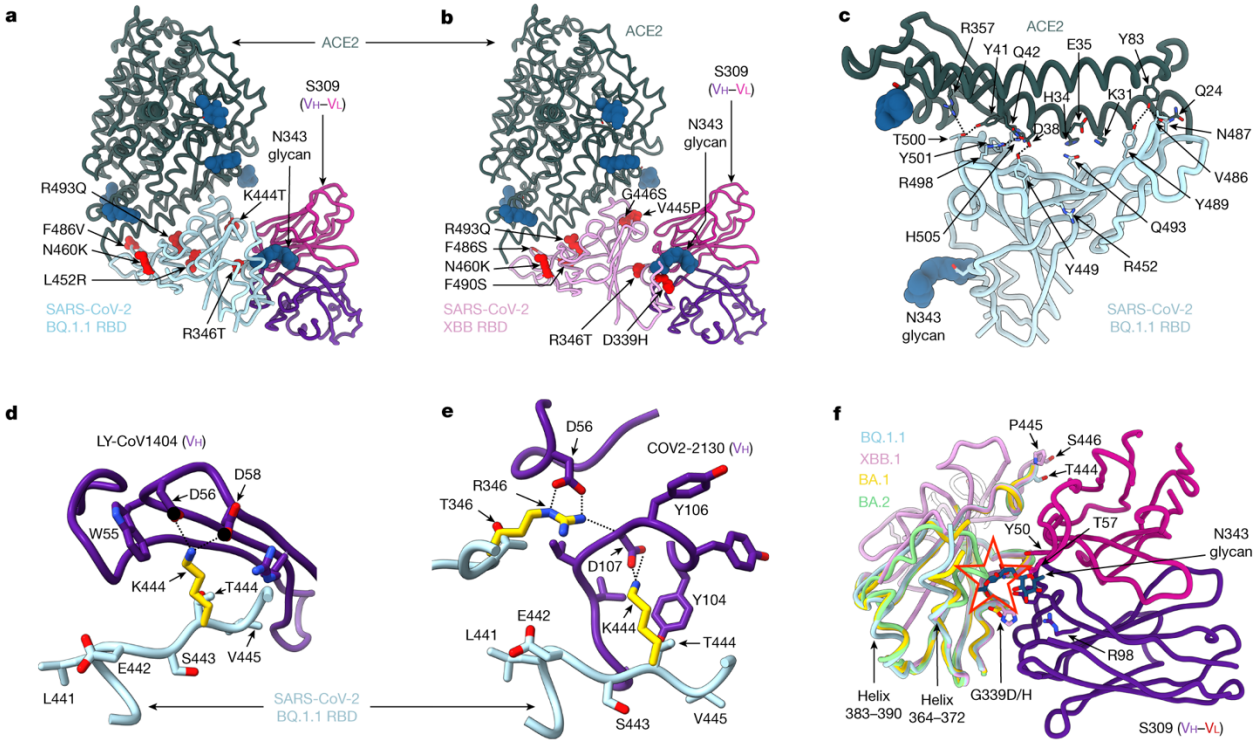

a,**b**, Cryo-EM structures of the BQ.1.1 RBD (**a**; cyan) or the XBB.1 RBD (**b**; pink) bound to the human ACE2 ectodomain (green) and the S309 Fab fragment (VH in purple and VL in magenta). Amino acid residues mutated relative to Omicron BA.2 are shown as red spheres. **c**, Zoomed-in view of the BQ.1.1 RBD interactions formed with human ACE2 with select amino acid residue side chains shown as sticks. N-linked glycans are shown as dark blue spheres in **a**–**c**. **d**,**e**, RBD-based superimposition of the LY-CoV1404-bound Wu RBD structure (**d**; purple, Protein Data Bank (PDB) ID: 7MMO) or of the COV2-2130-bound Wu RBD structure (**e**; purple, PDB ID: 7L7E) onto the BQ.1.1 RBD cryo-EM structure, highlighting the expected disruptions of electrostatic interactions with the monoclonal antibodies resulting from the K444T and the R346T RBD mutations. **f**, RBD-based superimpositions of the S309-bound BA.1 S (gold, PDB ID: 7TLY), apo BA.2 S (green, PDB ID: 7UB0), S309- and ACE2-bound BQ.1.1 (cyan) and XBB.1 (pink) RBD cryo-EM structures. The N343 glycan along with select side chains are rendered as sticks. The expected N343 glycan clashes with BA.2 residues N370 and F371 (sticks) are indicated with a red star. Residues 368–373 are disordered in the XBB.1 RBD cryo-EM map, as is the case for the adjacent residues 380–392 and were not modelled. Select electrostatic interactions are highlighted with dotted lines in **c**–**e**.

Figure 4.5 CryoEM data processing of the BQ.1.1, XBB.1 and BN.1 RBDs bound to ACE2 and S309

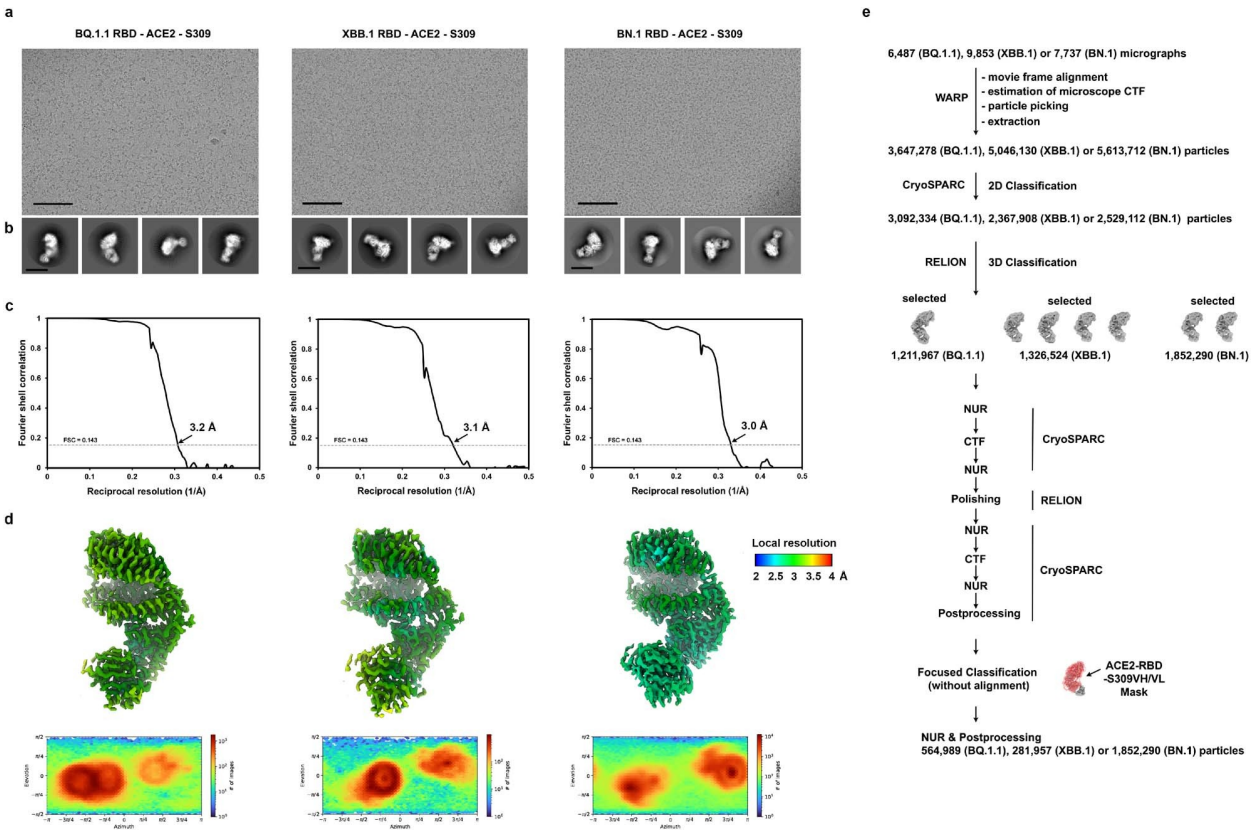

a-**b**, Electron micrographs representative of 6,487, 6,355, or 3,822 micrographs, respectively, (a) and 2D class averages (b) of the BQ.1.1 RBD (left), the XBB.1 RBD (middle) or BN.1 RBD (right) bound to the human ACE2 ectodomain and the S309 Fab fragment embedded in vitreous ice. The scale bar represents 100 nm (a) or 100 Å (b). **c**-**d**, Gold-standard Fourier shell correlation curves (c) and local resolution maps along with angular distribution heat maps calculated using cryoSPARC (d) for the 3D reconstructions of the BQ.1.1 RBD (left), the XBB.1 RBD (middle) or BN.1 RBD (right) bound to the human ACE2 ectodomain and the S309 Fab fragment. The 0.143 cutoff is indicated by a horizontal dashed line. **e**, Data processing flowchart. CTF: contrast transfer function; NUR: non-uniform refinement.

Figure 4.6 Structural comparisons of the Wu, BA.1, BQ.1.1 and XBB.1 RBD interactions with human ACE2 or therapeutic antibodies

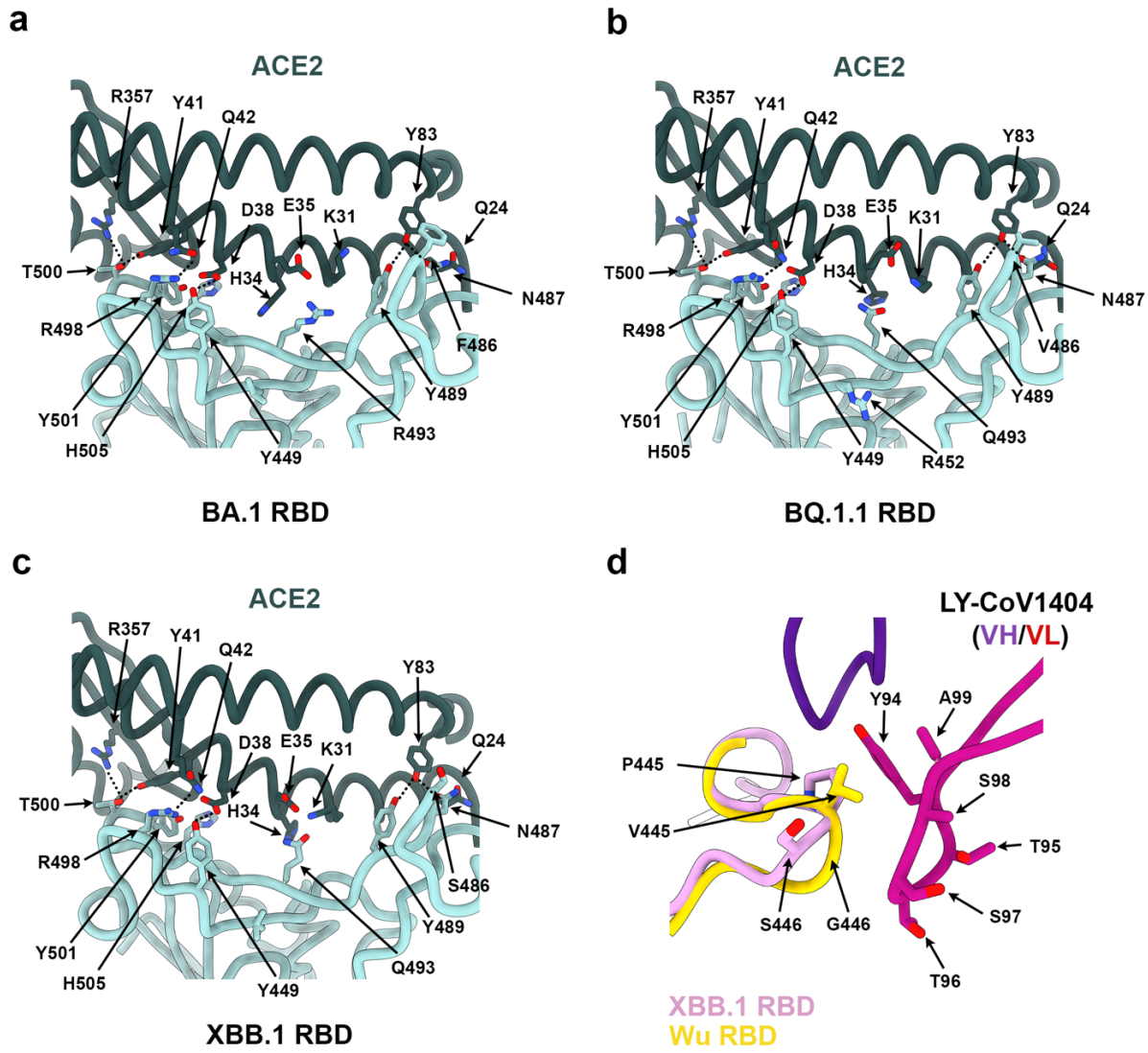

a-c, Zoomed-in views of the BA.1 RBD (PDB 7TN0, cyan), BQ.1.1 RBD (cyan) or XBB.1 RBD (cyan) interactions with the human ACE2 ectodomain (green). Select side chains are shown and electrostatic interactions are highlighted with dotted lines**. d,** Superimposition of the LYCoV1404-bound Wu RBD (gold, PDB 7MMO) crystal structure to the ACE2- and S309-bound XBB.1 RBD (pink) cryoEM structure (S309 and ACE2 are not shown for clarity).

Figure 4.7 S309-mediated neutralization, effector functions and in vivo protection

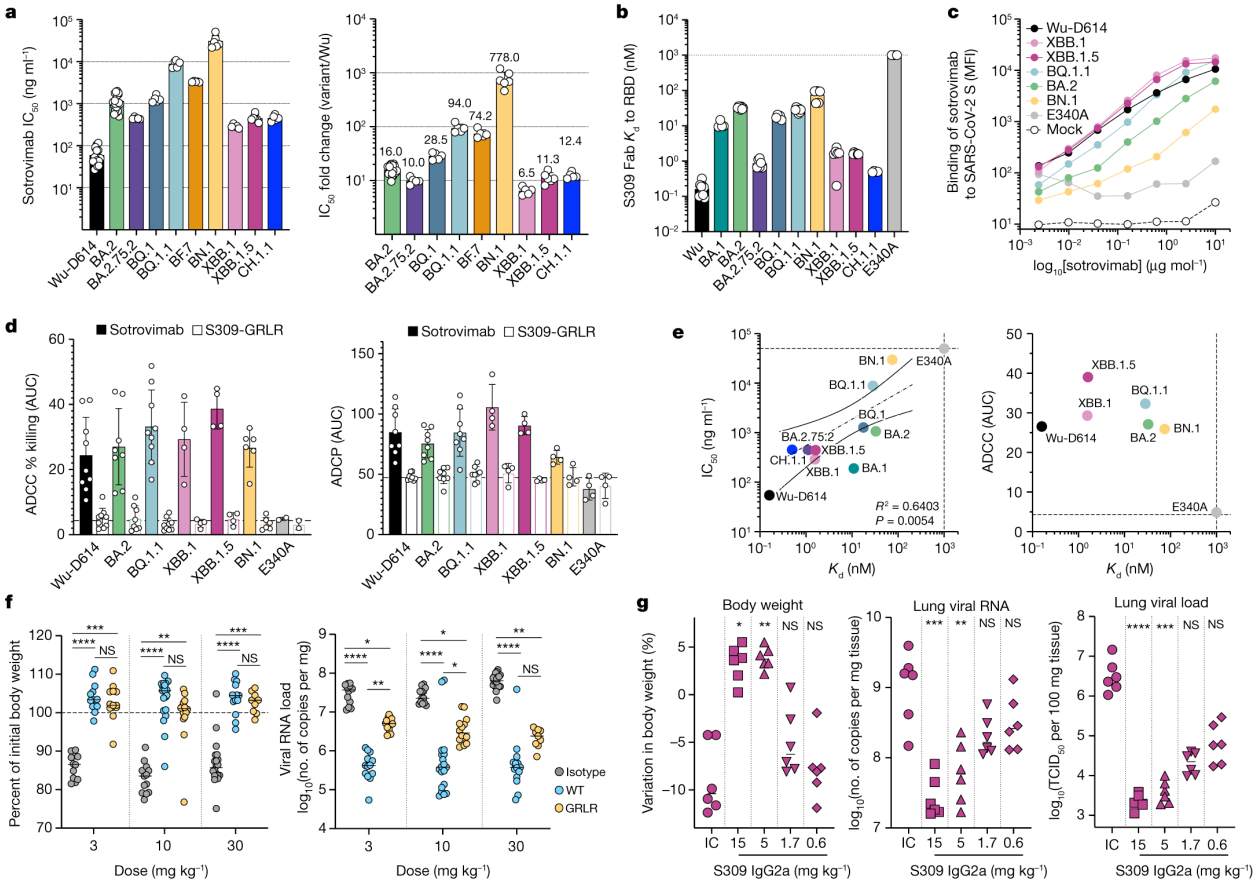

a, Sotrovimab-mediated neutralization of SARS-CoV-2 variant S VSV pseudoviruses presented as absolute potency (half-maximal inhibitory concentration (IC_{50})) (left) or relative to neutralization of Wu-D614 S VSV (right). Each symbol represents individual biological replicates ($n = 5–20$). **b**, SPR analysis of S309 Fab binding to SARS-CoV-2 RBD variants. Each symbol represents K_d values from independent experiments ($n = 3–10$). **c**, Binding of sotrovimab immunoglobulin G (IgG) to cell-surface expressed SARS-CoV-2 S variants. **d**, Left, natural killer cell-mediated ADCC in the presence of sotrovimab or S309-GRLR. Data are presented as mean area under the curve (AUC) ± s.d. of percentage killing ($n = 4–10$ donors). Right, ADCP of target cells via $CD14^+$ peripheral blood mononuclear cells in the presence of sotrovimab or S309-GRLR. Data are presented as mean AUC ± s.d. ($n = 4–8$ donors). **e**, Correlation of sotrovimab Fab binding affinity (from **b**) with neutralizing activity (from **a**) or ADCC (from **d**). Dotted lines indicate the limit of detection for neutralization and binding affinity or the mean S309-GRLR AUCs for different variants. R^2 and P values are derived from two-tailed Pearson correlation. **f**, Body weight loss (left) and lung viral RNA load (right) on day 6 after infection of K18-hACE2 mice receiving S309, S309-GRLR or 30 mg kg^{-1} of an isotype-matched control antibody (anti-WVN51) one day before challenge. Solid lines represent the median; dotted lines represent the lower limit of

quantification; $n = 9–20$ mice per group. Kruskal–Wallis ANOVA with Dunn's post-test. **g**, Body weight (left), viral genomic RNA (middle) and replicating viral titres (right) measured in lungs on day 4 after infection of Syrian hamsters receiving S309 hamster IgG2a or 15 mg kg^{-1} of an isotype control (IC) monoclonal antibody (MPE8 IgG2a) one day before challenge. $n = 6$ hamsters per group. Kruskal–Wallis ANOVA with Dunn's post-test between isotype control and S309. NS, not significant.

Figure 4.8 Cross-reactivity of S309 with SARS-CoV-2 variant RBDs

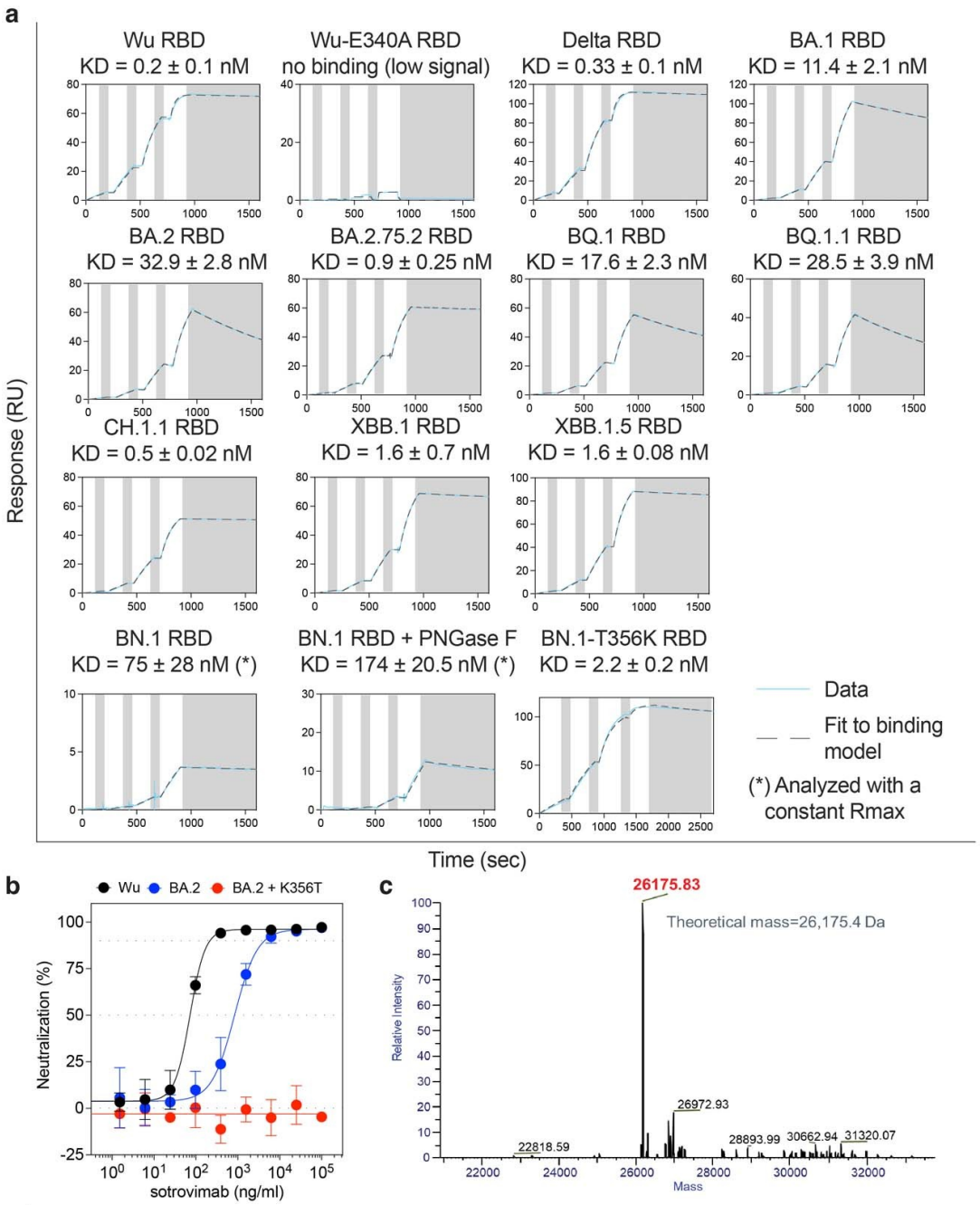

glycan	%
A2G0F/B	10.0
A2G1F/B	9.5
A2G2F/B	5.9
A2S1G0F/B	21.9
A2S1G1F/B	29.0
A2S2F/B	22.0
M5	0.4
nG	2.4

glycan	%
A1G0F	0.6
A2G0F/B	9.5
A2G1F/B	7.1
A2G2F/B	5.8
A2S1G0F/B	16.6
A2S1G1F/B	39.7
A2S2/B	39.3
A2S2F/B	15.0

glycan	%
A2S1G0F	38.7
A2S1G1FB	48.4
A2S2FB	17.0

a, Representative sensograms of S309 Fab binding to the SARS-CoV-2 Wu, Wu E340A, Delta, BA.1, BA.2, BA.2.75.2, BA.5, BQ.1, BQ.1.1, CH.1.1, XBB.1, XBB.1.5, BN.1 (deglycosylated or not with PNGase F) and BN.1-T356K RBDs immobilized at the surface of a SPR chip coated with anti-Avi polyclonal Ab. Experiments were performed with serial dilutions of Fabs and were run as single-cycle kinetics. Gray blocks denote the dissociation phase. Fits are shown as dashed grey lines. Kinetic rate constants and affinities are shown in Table 4.5. **b**, Sotrovimab-mediated neutralization of Wu-D614, BA.2 and BA.2-K356T S VSV pseudoviruses using VeroE6 as target cells. Dose-response curves of one representative experiment out of 2. **c**, Intact mass-spectrometry analysis of PNGase F-treated BN.1 RBD showing complete removal of N-linked glycans. **d**, Individual glycan profiling of the three glycosylation sites of the BN.1 RBD (N331, N343, N354) by LC-MS peptide map analysis. nG: no glycan detected.

Figure 4.9 BN.1 cryoEM structure

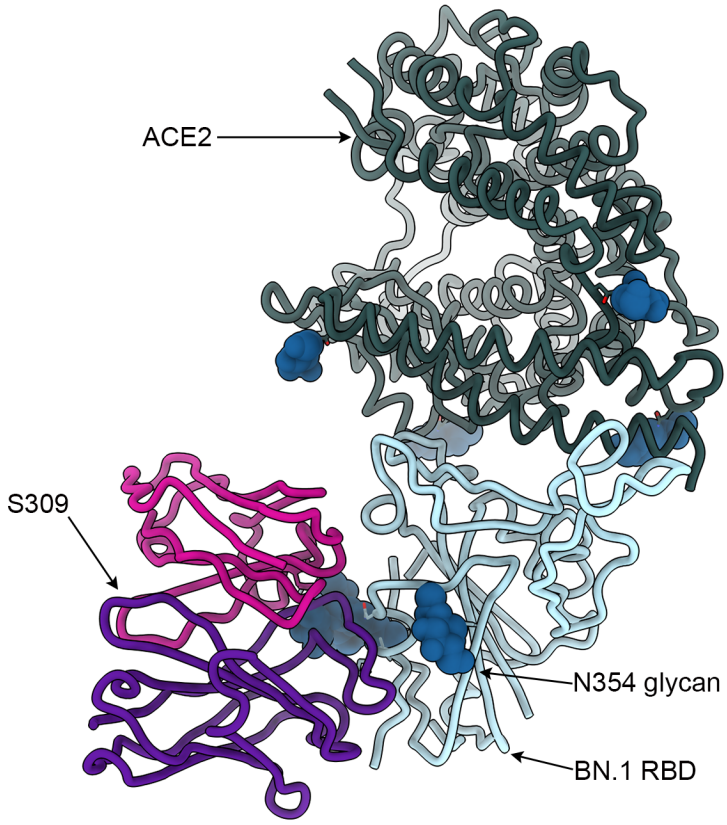

BN.1 cryoEM structure showing the position of the N354 glycan relative to S309.

Figure 4.10 Sotrovimab promotes Fc-mediated effector functions and protects against viral challenge with the SARS-CoV-2 BQ1.1 and XBB.1.5 variants

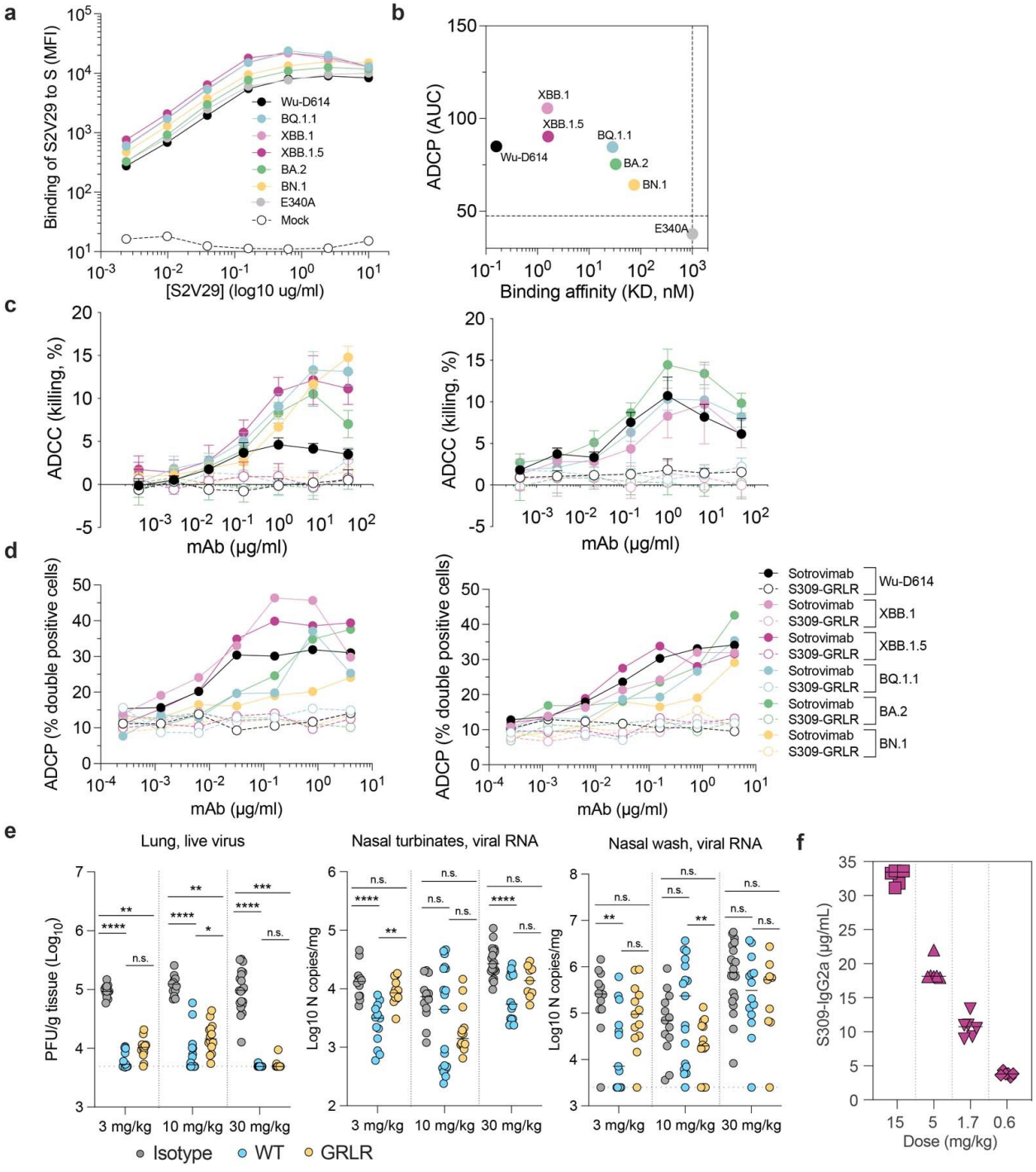

a, Binding of the S2V29 monoclonal Ab to SARS-CoV-2 S variants expressed at the surface of ExpiCHO-S cells as measured by flow cytometry. S2V29 retains potent and

equal binding against Wu-D614, BQ.1.1, XBB.1, XBB.1.5, BA.2, BN.1 and BA.2-E340A VSV pseudoviruses and was therefore used for quantifying cell-surface S expression. **b**, Correlation of sotrovimab Fab binding affinity with ADCP. The ADCP AUC values from Fig. 4.7d are plotted on the y-axis and the binding affinity to each RBD variant obtained in Fig. 4.7b is plotted on the x-axis. Dotted lines indicate the limit of detection for binding affinity and the mean of S309-GRLR AUCs from the different variants. **c**, ExpiCHO cells transiently transfected with S variants were incubated with the indicated concentrations of sotrovimab or S309-GRLR (G236R/L328R loss-of-function mutations introduced in the Fc domain of the human IgG1 heavy chain) and mixed with NK cells isolated from healthy donors in a range from 6:1 to 9:1 (NK:target cells). Target cell lysis was determined by a lactate dehydrogenase release assay. Data are presented as mean values +/– standard deviations (SD) from duplicates obtained using NK cells from two representative donors, both being homozygous for genotype V/V158 FcγRIIIa. **d**, ExpiCHO cells transiently transfected with S variants were fluorescently labelled with PKH67, incubated with the indicated concentrations of sotrovimab or S309-GRLR mAb and mixed with PBMCs labelled with CellTrace Violet from two healthy donors heterozygous for genotype R/H131 FcγRIIa at a ratio of 20:1 (PBMC:target cells). Association of $CD14^+$ monocytes with S-expressing target cells (ADCP) was determined by flow cytometry. **e**, Eight-week-old female K18-hACE2 mice received 3, 10 or 30 mg/kg of S309 (parent of sotrovimab) or S309-GRLR or 30 mg/kg of an isotype-matched control monoclonal Ab (anti-West Nile virus hE1651) by intraperitoneal injection one day before intranasal inoculation with 10^4 FFU of SARS-CoV-2 BQ.1.1. n = 9–20 animals per group. Tissues were collected at six days after infection. Lung live virus titer (left panel) and nasal turbinate (center panel) or nasal wash (right panel) viral RNA determined by RT-qPCR on day 6 are plotted (short, solid lines indicate the median; dotted lines indicate the LLOQ; n = 9–20 mice per group; Kruskal-Wallis ANOVA with Dunn's post-test; ns, not significant; $^*P < 0.05$, $^{**}P < 0.01$, $^{***}P < 0.001$, **** $P < 0.0001$). **f**, Serum concentration of S309 hamster IgG2a measured by ELISA at day 4 post-infection. n = 6 hamsters per group.The horizontal bar represents the median.

Figure 4.11 Sotrovimab neutralization of SARS-CoV-2 Omicron variants

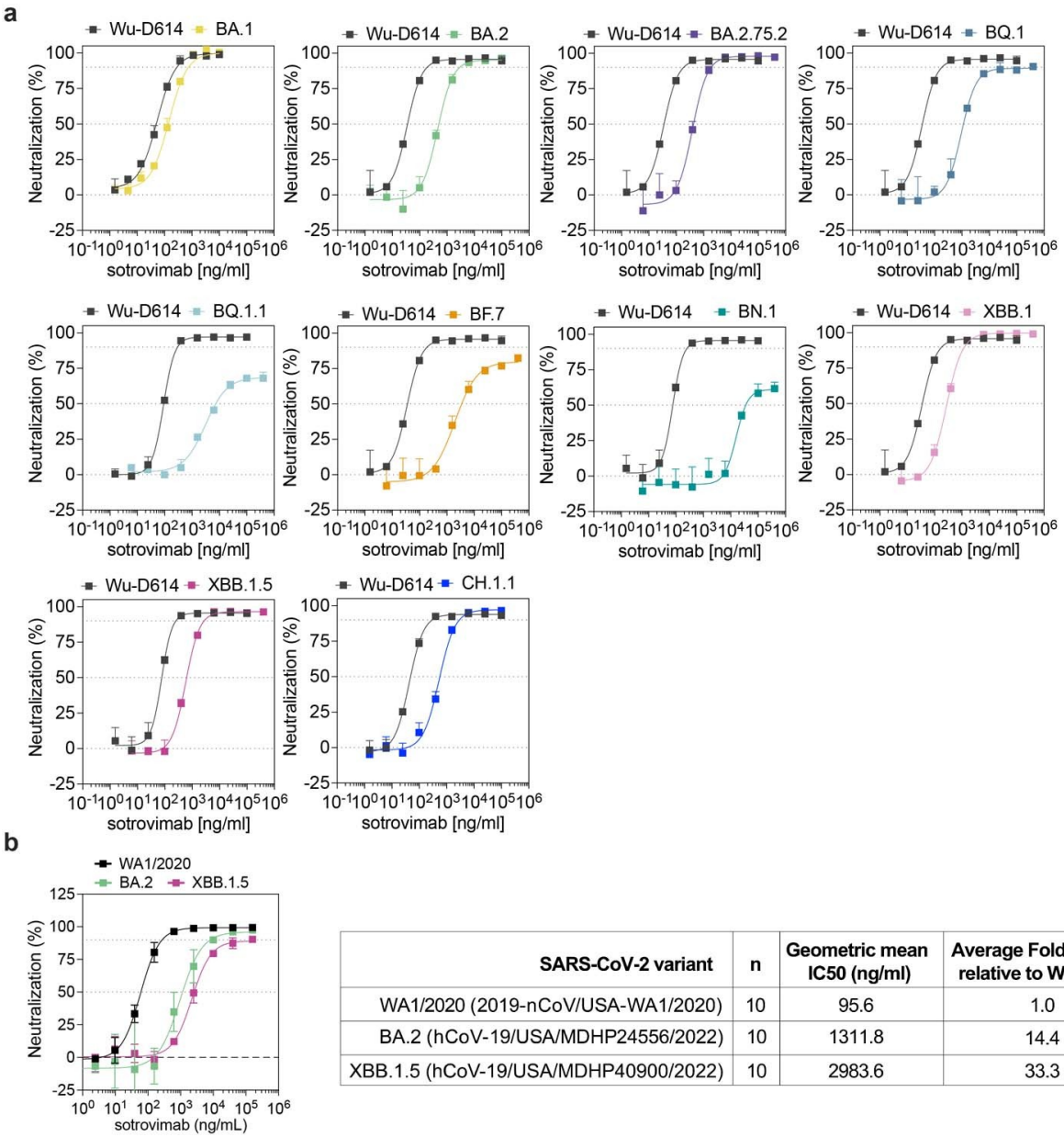

SARS-CoV-2 variant	n	Geometric mean IC50 (ng/ml)	Average Fold-change relative to Wild-type
WA1/2020 (2019-nCoV/USA-WA1/2020)	10	95.6	1.0
BA.2 (hCoV-19/USA/MDHP24556/2022)	10	1311.8	14.4
XBB.1.5 (hCoV-19/USA/MDHP40900/2022)	10	2983.6	33.3

a, Sotrovimab-mediated neutralization of Wu-D614, BA.2, BA.2.75.2, BQ.1, BQ.1.1, BF.7, XBB.1, BN.1, XBB.1.5. and CH.1.1 S VSV pseudoviruses using VeroE6 as target cells. Dose-response curves displaying the means of triplicates ± SD of one representative experiment out of at least 5 experiments are shown. **b**, Sotrovimab-mediated neutralization of WA1/2020 (2019-nCoV/USA-WA1/2020), Omicron BA.2 (hCoV-19/USA/MDHP24556/2022) and Omicron XBB.1.5 (hCoV-19/USA/MDHP40900/2022) authentic viruses using VeroE6-TMPRSS2 as target cells. Neutralization data (left panel) represent the means of triplicates ± standard deviation from one representative of n = 10 biologically independent experiments. Shown is also the geometric mean IC_{50} and average fold-change relative to wild-type of the 10 performed experiments (right panel).

Figure 4.12 Neutralization, binding and Fc-dependent effector functions of vaccine- and infection-elicited antibodies against emerging Omicron variants

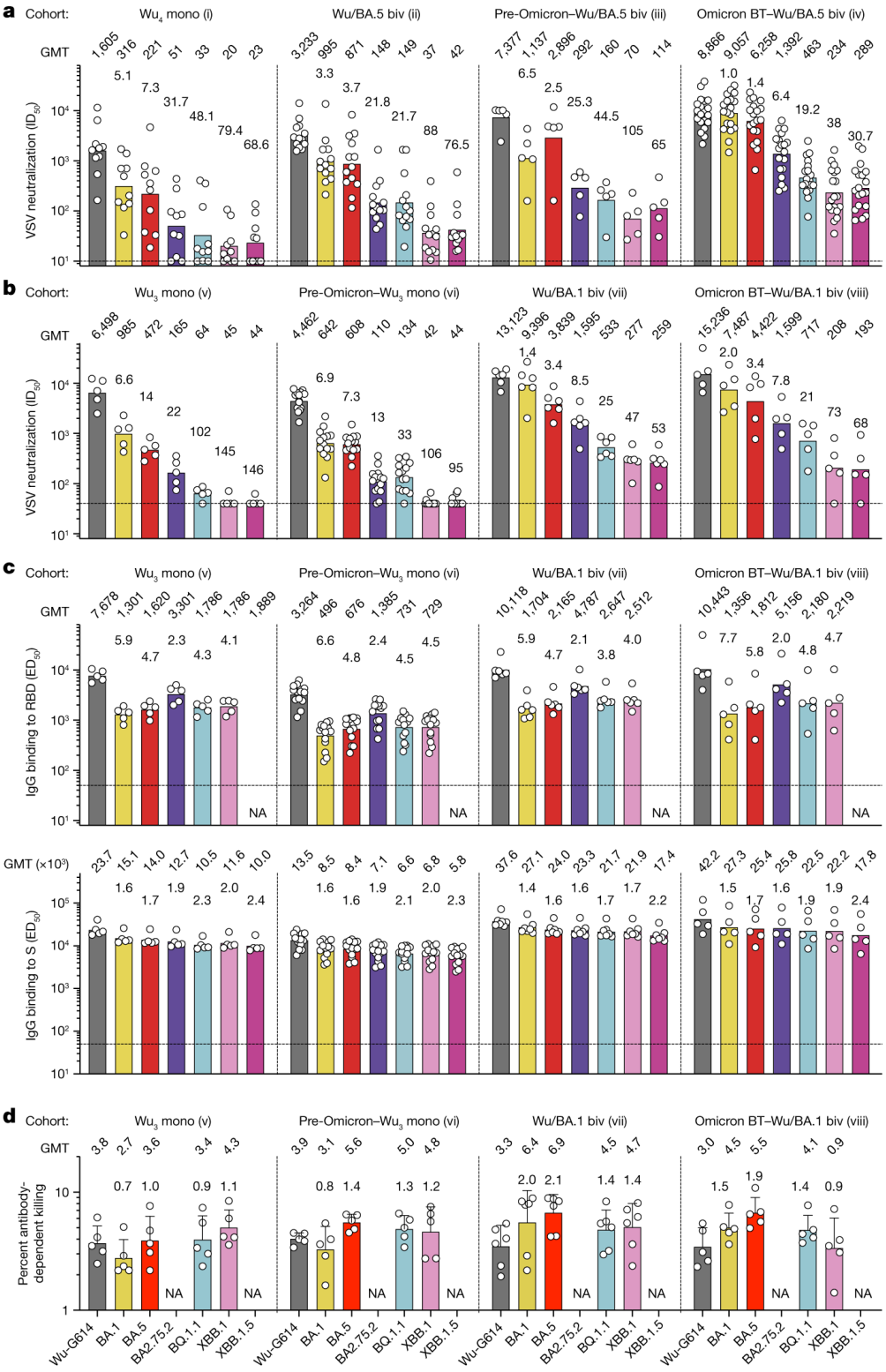

a,**b**, Neutralization of VSV pseudotyped with the indicated SARS-CoV-2 variant S by plasma samples from cohorts i–iv (**a**) and cohorts v–viii (**b**). Plasma neutralizing titres are expressed as half-maximal inhibitory dilution (ID_{50}) values from $n = 2$ biological (**a**) and technical (**b**) replicates. Bars and values above graphs represent geometric mean titre (GMT). The fold loss of neutralization against each Omicron variant compared with Wu-G614 is shown above each bar. Horizontal dashed lines indicate the limit of detection (In **a**, $ID_{50} = 10$; in **b**, $ID_{50} = 40$). Cohorts: (i) vaccinated 4 times with the Wu monovalent S mRNA vaccine, with no known infection (Wu_4 mono); (ii) vaccinated 3 times with Wu monovalent S mRNA vaccine and then 1 time with Wu/BA.5 bivalent S mRNA vaccine, with no known infection (Wu/BA.5 biv); (iii) infected in 2020 and subsequently vaccinated 3 to 4 times with Wu monovalent S mRNA vaccine and then 1 time with Wu/BA.5 bivalent S mRNA vaccine (pre-Omicron–Wu/BA.5 biv); (iv) vaccinated with Wu monovalent S mRNA vaccine before experiencing a breakthrough infection with Omicron BA.1, BA.2, BA.2.12.1 or BA.5, followed by a vaccination with the Wu/BA.5 bivalent S mRNA vaccine (Omicron BT–Wu/BA.5 biv); (v) vaccinated 3 times with Wu monovalent S mRNA vaccine, with no known infection (Wu_3 mono); (vi) vaccinated 3 times with Wu monovalent S mRNA vaccine after pre-Omicron infection (pre-Omicron–Wu_3 mono); (vii) vaccinated 3 times with Wu monovalent S mRNA vaccine and then 1 time with Wu/BA.1 bivalent S mRNA vaccine, with no known infection (Wu/BA.1 biv); and (viii) vaccinated 3 times with Wu monovalent S mRNA vaccine and then 1 time with Wu/BA.1 bivalent S mRNA vaccine, with a BA.1 or a BA.2 breakthrough infection (Omicron BT–Wu/BA.1 biv). **c**, Binding of plasma IgGs to SARS-CoV-2 RBDs and S trimers from indicated variants as measured by ELISA. Bars and values above the graphs represent GMT from $n = 2$ technical replicates. The fold change of binding titre to the Omicron variant compared with Wu is shown above each bar. Horizontal dashed lines indicate the cut-off in the assay based on binding to uncoated plates (median effective dose (ED_{50}) = 50). **d**, ADCC as measured by natural killer cell-mediated cell lysis of ExpiCHO-S cells transiently transfected with Wu-D614, BA.5, BQ.1.1 or XBB.1 S and incubated with plasma samples. The percentage of cell lysis is shown for each donor plasma sample diluted 1/200 from cohorts v–viii ($n = 5$ donors for cohort v, $n = 5$ for cohort vi, $n = 6$ for cohort vii and $n = 5$ for cohort viii). Bars and values above the graphs represent GMT. Error bars show s.d. The fold change of activation with Omicron variants compared with Wu-G614 is shown above each bar. NA, not assayed. Demographics are summarized in Table 4.6. Statistically significant differences of mean neutralization and binding titres within and between cohorts are shown in Supplementary Table 4.8. Samples from cohorts i–iv were obtained in Seattle, USA; samples from cohorts v–viii were obtained from Ticino, Switzerland.

Figure 4.13 Dose-response plasma neutralization curves for cohorts i-iv.

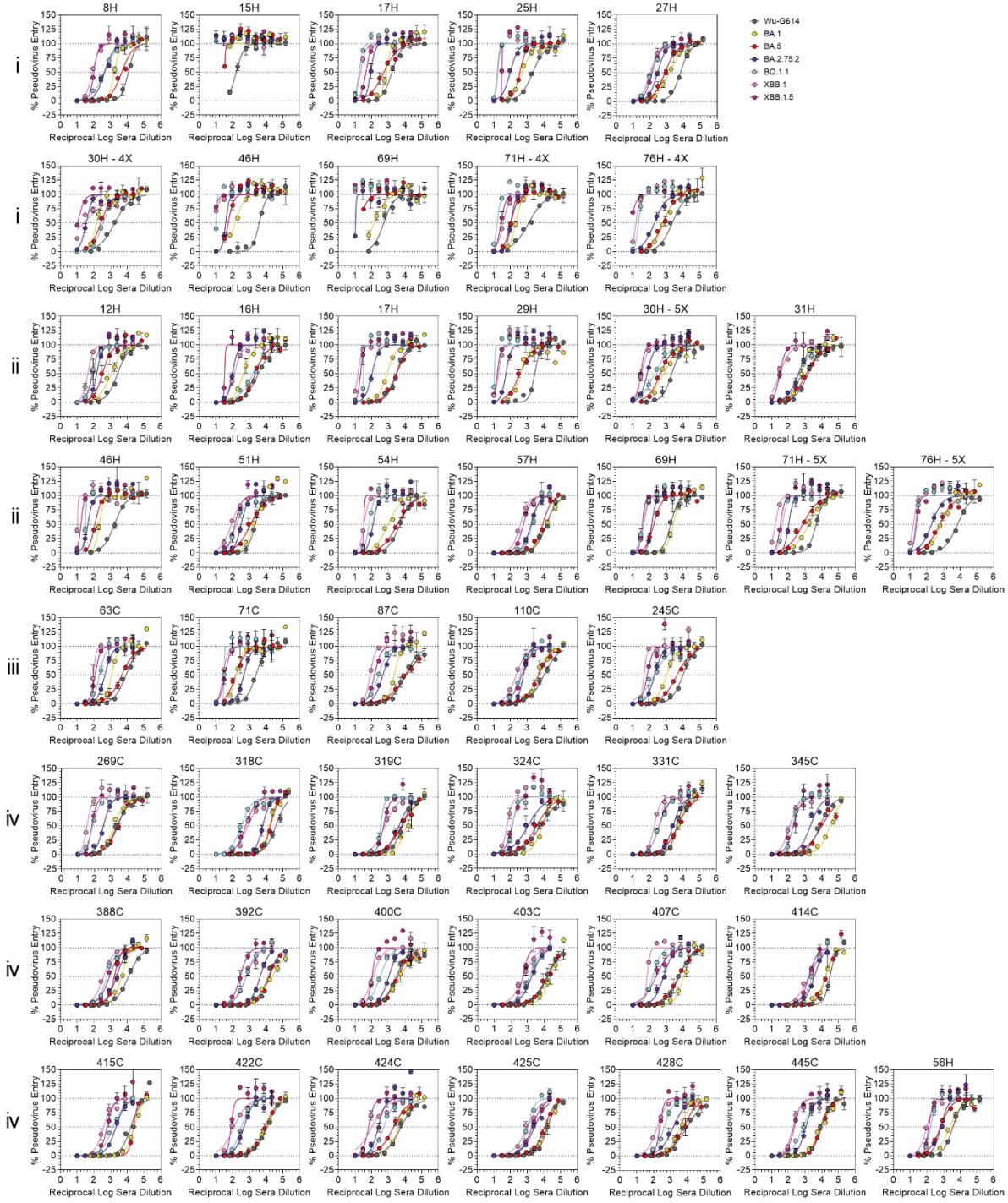

Means of duplicates ± standard deviation of one representative experiment of at least two biological replicates are presented.

Figure 4.14. Dose-response plasma neutralization curves for cohorts v-viii

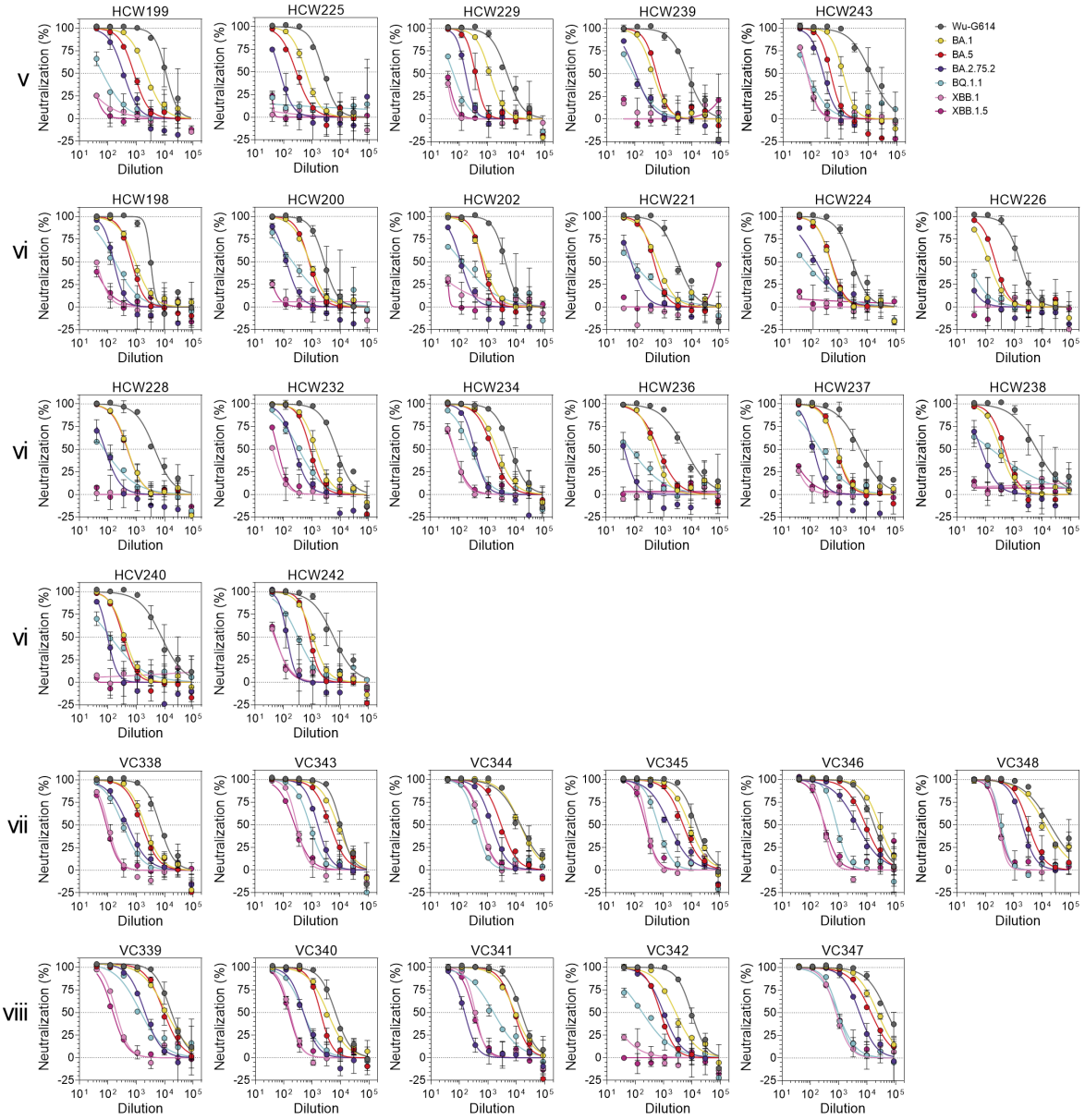

Means ± standard deviation of two technical replicates from of one representative experiment are shown.

Figure 4.15 Neutralization, binding and fine specificity of vaccine- and infection-elicited plasma Abs against emerging Omicron variants in dialysis patients, kidney transplant recipients and healthy individuals

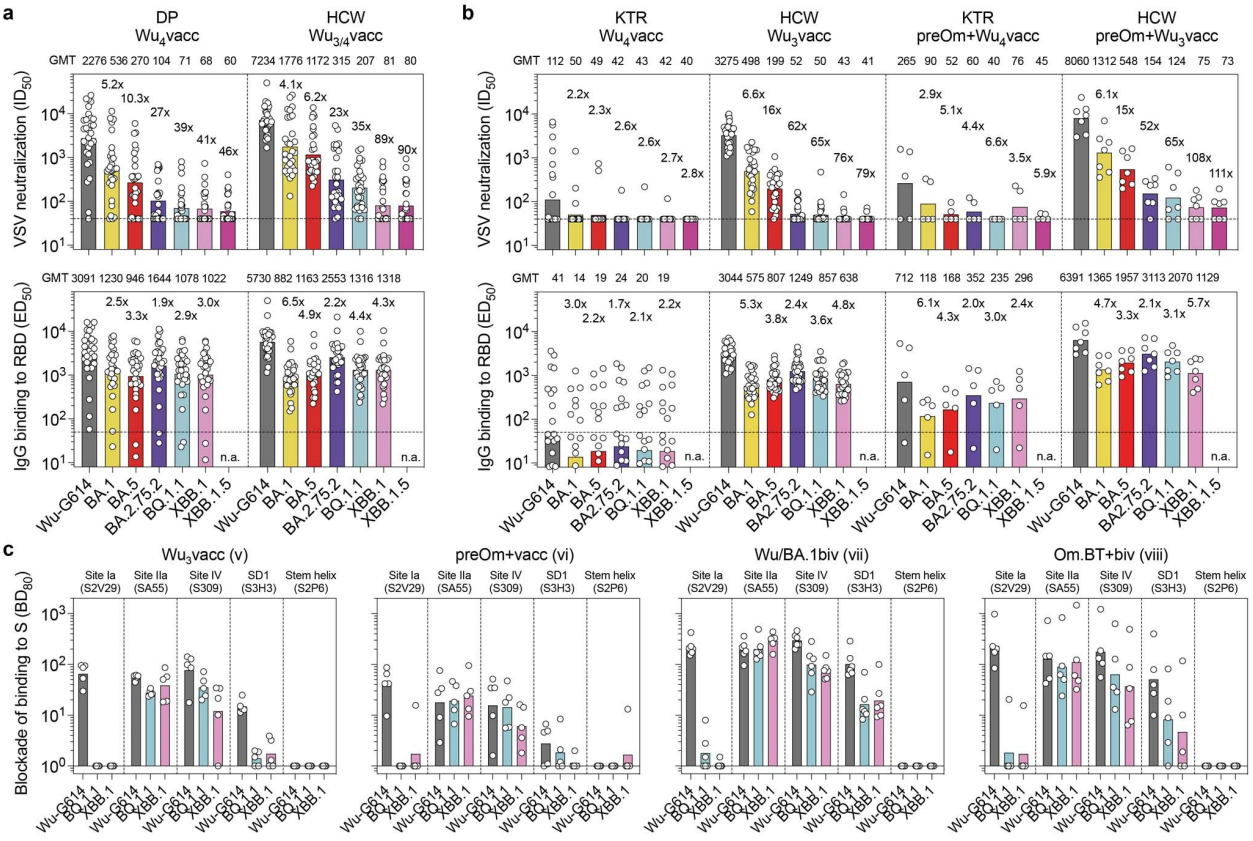

a,**b**, Neutralization of SARS-CoV-2 pseudotyped VSV carrying Wu-G614, BA.1, BA.5, BA.2.75.2, BQ.1.1, XBB.1 and XBB.1.5 (upper panels) by plasma Abs and binding to matched RBDs by plasma IgGs from dialysis patients (DP) (a) or kidney transplant recipients (KTR) (b) after receiving 4 (Wu_4vacc) doses. Samples are compared to those from healthcare workers (HCW) collected 2–4 weeks (a) or 2–4 months (b) after receiving 3 or 4 doses of monovalent Wu vaccine. Shown are ID_{50} values from n = 2 technical replicates. Bars and values on top represent geometric mean ID_{50} titers (GMT). Fold-loss of neutralization against Omicron variants as compared to Wu-G614 is shown above each corresponding bar. Horizontal dashed lines indicate the limit of detection in the neutralization assay (ID_{50} = 40) and the cut-off in the ELISA assay based on binding to uncoated plates (ED_{50} = 50). Cohort demographics are summarized in Table 4.6. Statistically significant differences of mean neutralization and binding titers within and between cohorts are shown in Table 4.9. **c**, Competition ELISA (blockade of binding) between individual S site-specific monoclonal Abs and plasma from vaccinated individuals (cohorts v-viii). S2V29 binds to the RBM. Each plot shows the magnitude of inhibition of binding to immobilized Wu-G614, BQ.1.1 and XBB.1 S in the presence of each monoclonal Ab, expressed as reciprocal plasma dilution blocking 80% of the maximum binding response (BD_{80}). Points represent the BD_{80} measured for each

individual plasma donor as determined from n = 1 experiment and bars represent geometric mean BD_{80} titers.

Figure 4.16 Activation of FcγRIIIa by individual plasma samples.

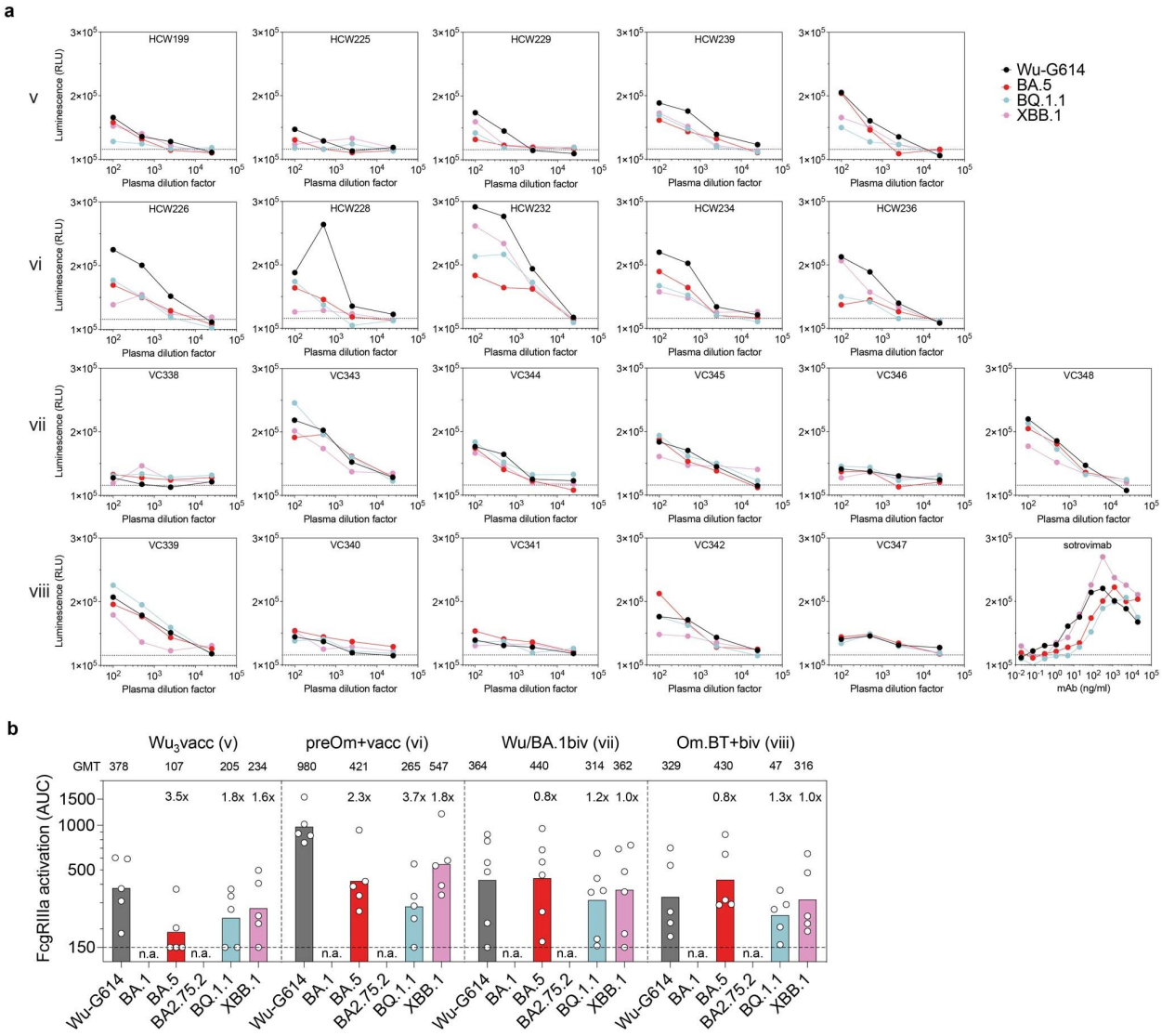

a Activation of high-affinity (V158) FcγRIIIa measured using Jurkat reporter cells and SARS-CoV-2 Wu-G614, BA.5, BQ.1.1 and XBB.1 S-expressing ExpiCHO as target cells. Luminescence (RLU) values from one experiment are shown with plasma samples from cohorts v-viii (n = 5 donors for cohort v, n = 5 for cohort vi, n = 6 for cohort vii and n = 5 for cohort viii) and compared to sotrovimab. Horizontal dotted line indicates the lowest limit of detectable activation (RLU = 115,737). **b**, AUC values from one experiment. Bars and values on top represent geometric mean AUC titers (GMT). Fold-change of activation with Omicron variants as compared to Wu-G614 is shown above each corresponding bar. Horizontal dashed line indicates the lowest limit of detectable activation (AUC = 150). n.a., not assayed.

Figure 4.17 Cross-reactivity of vaccine- and infection-elicited SARS-CoV-2 RBD-binding MBCs

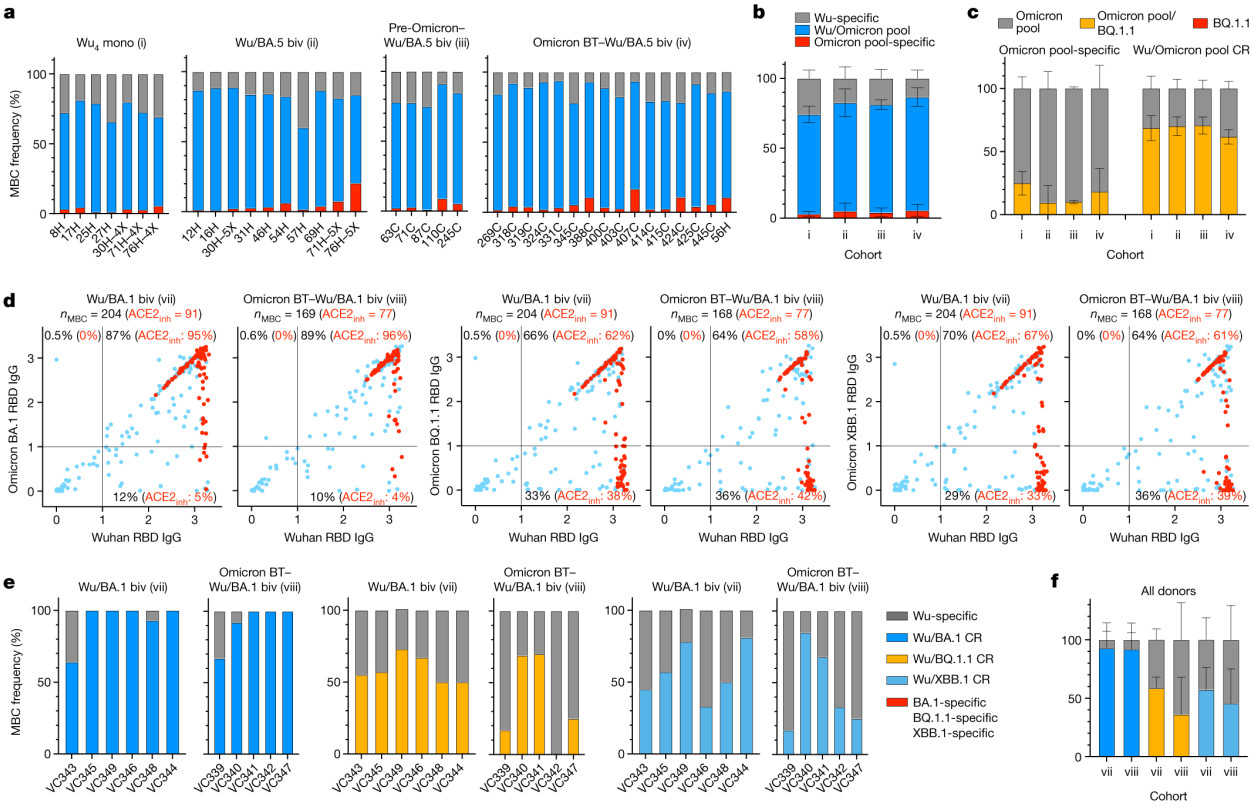

a,**b**, Frequency of Wu RBD-binding (grey), Omicron (BA.1, BA.2 and BA.5) RBD pool-binding (red) and cross-reactive (blue) MBCs from donors of cohorts i–iv, as measured by flow cytometry. Data are individual frequencies for each donor (**a**) and mean frequency ± s.d. for each cohort (n = 4–16 donors) (**b**). **c**, Analysis of cross-reactivity with the BQ.1.1 RBD of Omicron (BA.1, BA.2 and BA.5) RBD pool-binding (red bars in **b**) and Wu/Omicron (BA.1, BA.2 and BA.5) RBD pool-cross-reactive (CR) (blue bars in **b**) MBCs. Data are mean frequency ± s.d. for each cohort (n = 4–16 donors). **d**, Cumulative cross-reactivity with the Wu RBD and the Omicron BA.1, BQ.1.1 or XBB.1 RBDs of IgGs secreted from in vitro-stimulated MBCs, as measured by ELISA. Data are mean absorbance values with the blank subtracted from n = 2 replicates of MBC cultures analysed from donors in cohorts vii and viii approximately 3 months after receiving their last vaccine dose. RBD-directed IgGs inhibiting binding of ACE2 to the Wu RBD are depicted in red. The total number (n_{MBC}) and the number of ACE2-inhibiting ($ACE2_{inh}$) RBD-directed IgG-positive cultures are indicated on top of each graph. Percentages of total (black) and ACE2-inhibiting (red) Wu-binding, Omicron-binding and Wu/Omicron-cross-reactive IgG-positive cultures are indicated within each quadrant. **e**,**f**, Individual frequencies (**e**) and mean (± s.d.) frequencies for each cohort (n = 5–6 donors) (**f**) of Wu RBD-specific, Omicron-specific and RBD cross-reactive (BA.1, BQ.1.1 and XBB.1) IgG-positive cultures from donors of cohorts vii and viii.

Figure 4.18 MBC analysis by flow cytometry

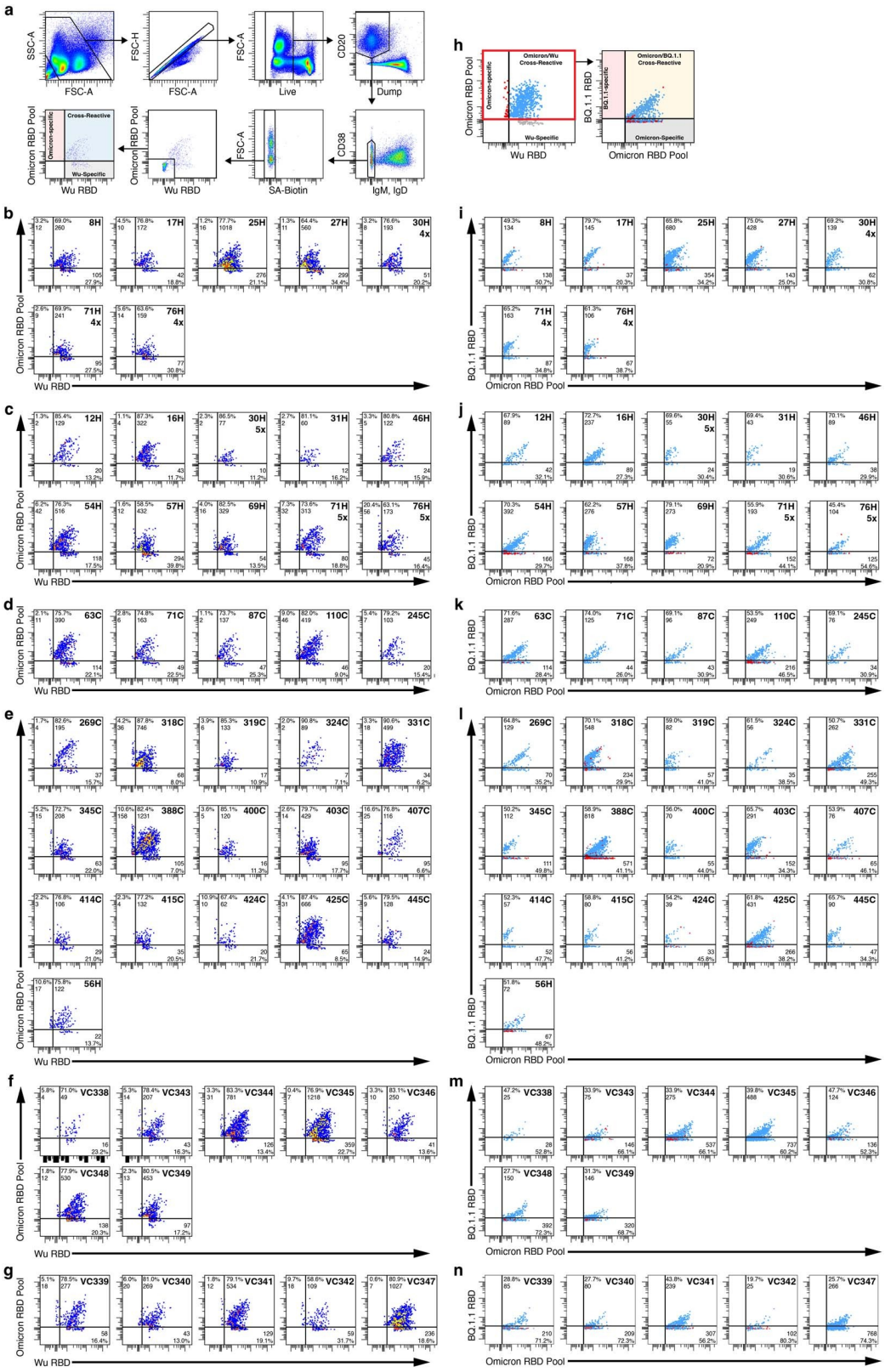

a, Gating strategy to identify Omicron (BA.1/BA.2/BA.5) RBD pool- and Wu RBD-recognizing MBCs. Dump includes markers for CD3, CD8, CD14, and CD16. Gating for RBD-positive memory B cells was based on staining of PBMCs from healthy donors collected in 2019 prior to the COVID-19 pandemic. Individual plots showing Omicron (BA.1/BA.2/BA.5) RBD pool- and Wu RBD-positive MBCs for Wu_4 vaccinated (b), Wu/BA.5 bivalent vaccinated (c), pre-Omicron infected-Wu/BA.5 bivalent vaccinated (d), Omicron BT-Wu/BA.5 bivalent vaccinated (e), Wu/BA.1 bivalent vaccinated (f), and Omicron BT-Wu/BA.1 bivalent vaccinated individuals (g). **h**, Gating strategy to determine whether Omicron (BA.1, BA.2, and BA.4/5) RBD pool-positive MBCs recognize the BQ.1.1 RBD. Individual plots showing Omicron (BA.1, BA.2, and BA.4/5) RBD pool and BQ.1.1 RBD-recognizing memory B cells for Wu4 vaccinated (i), Wu/BA.5 bivalent vaccinated (j), pre-Omicron infected-Wu/BA.5 bivalent vaccinated (k), Omicron BT-Wu/BA.5 bivalent vaccinated (l), Wu/BA.1 bivalent vaccinated (m), and Omicron BT-Wu/BA.1 bivalent vaccinated individuals (n). Proportion and counts of memory B cells recognizing one or more RBD(s) is presented for each individual.

Figure 4.19 Antigen-specific MBC repertoire analysis of secreted IgG.

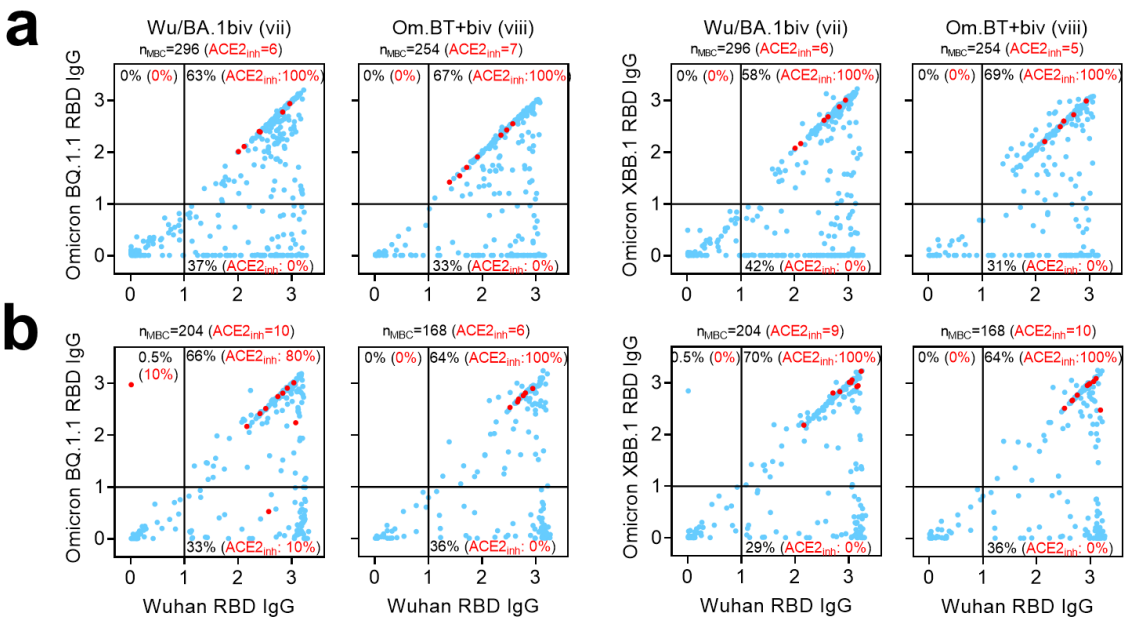

MBC-derived RBD-directed IgGs inhibiting binding of ACE2 to BQ.1.1 or to XBB.1 RBDs are depicted in red from cohorts vii and viii at 14 days (**a**) and 3 months (**b**) after last vaccination. Total and ACE2-inhibiting (ACE2inh) RBD-directed IgG positive cultures are indicated above each graph and reactivity frequencies within each quadrant.

Figure 4.20 Subanalysis of cross-reactivity of vaccine- and infection-elicited MBCs.

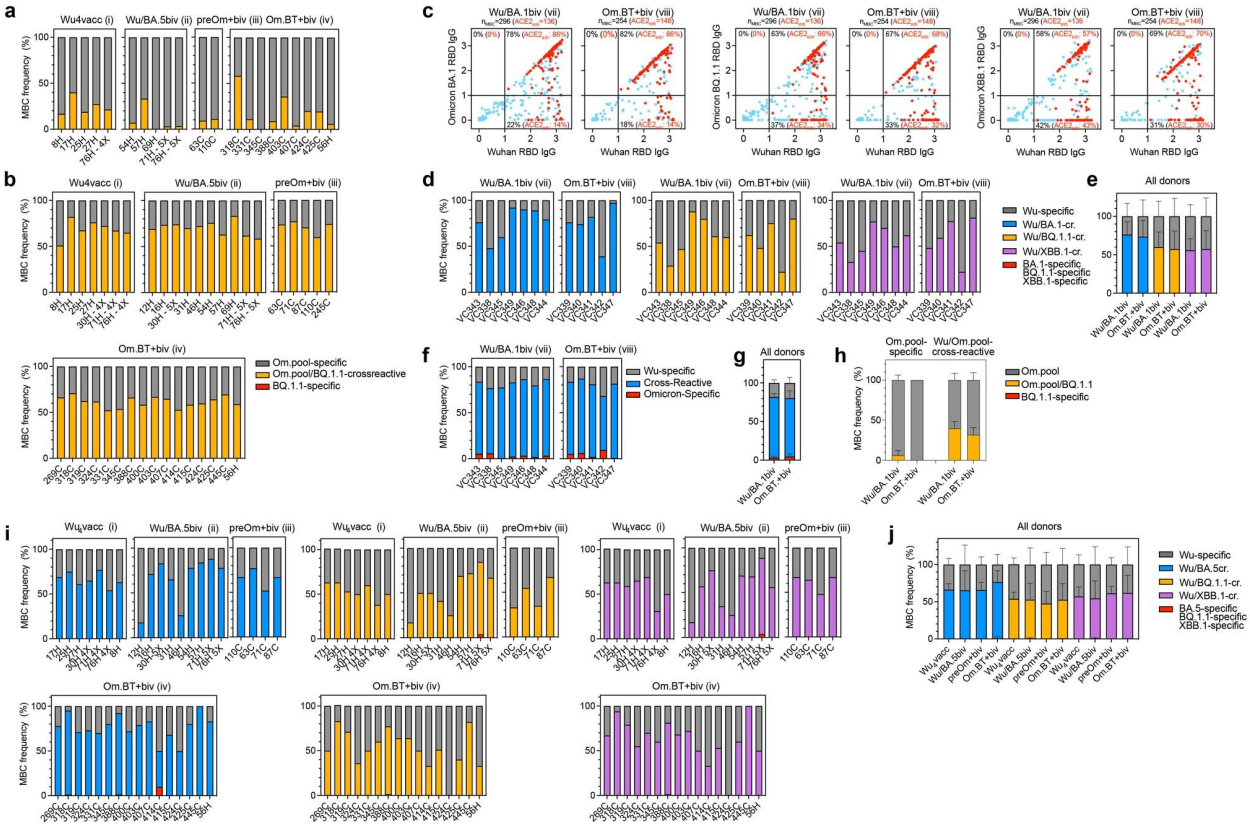

a,**b**, Analysis of cross-reactivity with the BQ.1.1 RBD of Omicron (BA.1/BA.2/BA.5) RBD pool-specific (a) and Wu/Omicron (BA.1/BA.2/BA.5) RBD pool-cross-reactive (b) MBCs. Om.pool: MBCs reactive with the Omicron (BA.1/BA.2/BA.5) RBD pool in cohorts i–iv. **c**, Cumulative cross-reactivity with the Wu RBD and the Omicron BA.1, BQ.1.1 or XBB.1 RBDs of IgGs secreted from in vitro stimulated MBCs as measured by ELISA. Data represent average OD values with blank subtracted from n = 2 replicates of MBC cultures analyzed from donors of cohorts vii and viii at about 14 days after receiving the last vaccine dose. RBD-directed IgGs inhibiting binding of ACE2 to the Wu RBD are depicted in red. Number of total and ACE2-inhibiting ($ACE2_{inh}$) RBD-directed IgG positive cultures are indicated on top of each graph. Percentages of Wu-specific, Omicron-specific and Wu/Omicron-cross-reactive IgG positive cultures are indicated within each quadrant. **d**,**e**, Individual frequencies (d) and mean frequencies ± SD for each cohort (n = 5-6) (e) of Wu RBD-specific (grey), Omicron-specific (red) and RBD cross-reactive (blue for BA.1, yellow for BQ.1.1 and purple for XBB.1) IgG positive cultures from donors of cohorts vii and viii at about 14 days after receiving the last vaccine dose. **f**,**g**, Frequency of Wu RBD-specific (grey), Omicron (BA.1/BA.2/BA.5) RBD pool-specific (red) and cross-reactive (blue) MBCs from donors of cohorts vii-viii at about 14 days after receiving the last vaccine dose, as measured by flow cytometry. Individual frequencies are shown in panels f and and mean frequencies ± SD for each

cohort (n = 4–16) are shown in g. **h**, Analysis of cross-reactivity with the BQ.1.1 RBD of Omicron (BA.1/BA.2/BA.5) RBD pool-specific (red bars of panel g) and Wu/Omicron (BA.1/BA.2/BA.5) RBD pool-cross-reactive (blue bars of panel g) MBCs. Om.pool, MBCs recognizing the Omicron (BA.1/BA.2/BA.5) RBD pool. **M**ean frequencies ± SD are presented for each cohort (n = 5-6). **i**,**j**, Frequency of IgGs specific for the Wu RBD (grey), cross-reactive with the Wu/BA.5 RBDs (blue), the Wu/BQ.1.1 RBDs (orange), the Wu/XBB.1 RBDs (purple) or specific for either the BA.5, BQ.1.1 or XBB.1 RBD (red) as measured by ELISA after in vitro stimulation of MBCs from cohorts i–iv. Individual frequencies and mean ± SD (n = 4–16) are shown in panels i and j, respectively.

Table 4.1 Kinetics of monomeric human ACE2 binding to immobilized SARS-CoV-2 variant RBDs as measured by biolayer interferometry

	K_D (nM)	k_{on} ($M^{-1}s^{-1}$)	k_{off}(s^{-1})
Wu	101.1 ± 7.3	1.30×10^5	1.31×10^{-2}
BA.4/5	12.8 ± 2.2	1.45×10^5	1.82×10^{-3}
BA.2.75.2	26.2 ± 1.7	1.35×10^5	3.52×10^{-3}
BQ.1.1	13.7 ± 1.4	1.39×10^5	1.89×10^{-3}
XBB.1	88.4 ± 11.9	1.47×10^5	1.29×10^{-2}
XBB.1.5	26.8 ± 5.0	1.20×10^5	3.14×10^{-3}

Values are presented as mean ± standard deviations obtained from 2-3 batches of each RBD and ACE2.

Table 4.2 Kinetics of monomeric human ACE2 binding to immobilized SARS-CoV-2 variant RBDs as measured by surface plasmon resonance

RBD	Average k_{on} (1/Ms)	stdev(ka)	Average k_{off} (1/s)	stdev(kd)	Average K_D(nM)	stdev(K_D)	# of replicates
Wu	7.18E+04	6.39E+03	6.19E-03	1.62E-04	86.91	8.82	7
Wu-E340A	5.66E+04	8.96E+03	6.01E-03	8.01E-04	106.71	4.78	6
BQ.1.1	4.22E+04	7.97E+03	7.91E-04	2.08E-05	19.26	3.21	6
BA.2.75.2	3.53E+04	7.28E+02	1.50E-03	5.43E-05	42.38	1.32	3
BA.4/5	3.31E+04	3.97E+03	9.32E-04	1.30E-04	28.22	2.74	8
XBB	4.48E+04	8.15E+03	4.19E-03	8.52E-04	93.48	4.72	3
XBB.1.5	5.58E+04	1.20E+03	1.48E-03	2.45E-05	26.58	0.16	4

Table 4.3 Cryo-EM data collection, refinement and validation statistics

	SARS-CoV-2 BQ.1.1 RBD-ACE2-S309 PDB 8FXC EMD 29531	SARS-CoV-2 XBB.1 RBD-ACE2-S309 PDB 8FXB EMD 29530	SARS-CoV-2 BN.1 RBD-ACE2-S309 PDB 8S9G EMD 40240
Data collection and processing			
Magnification	105,000	105,000	105,000
Voltage (kV)	300	300	300
Electron exposure (e–/Å^2)	60	60	60
Defocus range (μm)	-0.5 - -2.5	-0.2 - -3.0	-0.2 - -3.5
Pixel size (Å)	0.843	0.843	0.843
Symmetry imposed	C1	C1	C1
Initial particle images (no.)	3,647,278	5,046,130	5,613,712
Final particle images (no.)	564,989	281,957	1,852,290
Map resolution (Å)	3.2	3.1	3.0
FSC threshold	0.143	0.143	0.143
Refinement			
Model resolution (Å)	3.5	3.6	3.4
FSC threshold	0.5	0.5	0.5
Map sharpening *B* factor (Å^2)	-150	-120	-121
Model composition			
Non-hydrogen atoms	7639	7347	7004
Protein residues	1002	976	986
Ligands	8	7	10
B factors (Å^2)			
Protein	21.36	25.87	17.23
Ligand	26.64	27.33	17.43
R.m.s. deviations			
Bond lengths (Å)	0.010	0.010	0.009
Bond angles (°)	1.242	1.221	1.105
Validation			
MolProbity score	1.70	1.62	1.47
Clashscore	4.61	6.34	5.11
Poor rotamers (%)	1.76	0.96	1.43
Ramachandran plot			
Favored (%)	95.95	96.05	97.63
Allowed (%)	3.34	3.64	2.16
Disallowed (%)	0.71	0.31	0.21

Table 4.4 Statistically significant differences of mean neutralization titers

Fig. 3a	**Mean rank diff.**	**Significant?**	**Adjusted P Value**
Wu-D614 vs. BA.2	-40.4	***	<0.001
Wu-D614 vs. BQ.1	-44.9	***	<0.001
Wu-D614 vs. BQ.1.1	-61.5	***	<0.001
Wu-D614 vs. BF.7	-56.5	***	<0.001
Wu-D614 vs. BN.1	-67	***	<0.001
Fig. 3b	**Mean rank diff.**	**Significant?**	**Adjusted P Value**
Wuhan vs. BA.2	-48.4	Yes	<0.001
Wuhan vs. BQ.1	-35.1	Yes	0.01
Wuhan vs. BQ.1.1	-43.1	Yes	<0.001
Wuhan vs. BN.1	-56.3	Yes	<0.001
Wuhan vs. E340A	-60.3	Yes	<0.001
Fig. 3d	**Mean rank diff.**	**Significant?**	**Adjusted P Value**
sotrovimab vs. S309-GRLR	35.2	*	0.04
sotrovimab vs. S309-GRLR	42.2	**	0.003
sotrovimab vs. S309-GRLR	40.7	*	0.02
Fig. 3d	**Mean rank diff.**	**Significant?**	**Adjusted P Value**
sotrovimab vs. S309-GRLR	40.3	**	0.007
sotrovimab vs. S309-GRLR	37	*	0.02
sotrovimab vs. S309-GRLR	34.6	*	0.04
sotrovimab vs. S309-GRLR	48.3	**	0.009
sotrovimab vs. S309-GRLR	41.5	*	0.05
sotrovimab vs. sotrovimab	53.8	**	0.002
sotrovimab vs. S309-GRLR	48.8	**	0.008

Table 4.5 Kinetics of S309 Fab binding to immobilized SARS-CoV-2 variant RBDs as measured by surface plasmon resonance

RBD	average k_{on} (1/Ms)	stdev(k_{on})	average k_{off} (1/s)	stdev (k_{off})	average K_D (nM)	stdev(K_D)	number of replicates
Wu	8.86E+04	8.76E+03	1.38E-05	1.05E-05	0.20	0.12	12
Wu-E340A	NB	N/A	NB	N/A	NB	N/A	6
Delta (His avi)	8.42E+04	1.02E+04	2.56E-05	4.89E-06	0.33	0.08	4
BA.1	2.21E+04	2.27E+03	2.48E-04	2.54E-05	11.35	2.08	6
BA.2	2.16E+04	2.01E+03	7.05E-04	5.25E-05	32.88	2.79	8
BA.2.75.2	2.55E+04	3.14E+03	2.80E-05	5.52E-06	0.86	0.25	6
BQ.1	2.51E+04	1.39E+03	4.40E-04	3.60E-05	17.63	2.31	5
BQ.1.1	2.27E+04	1.67E+03	6.43E-04	7.37E-05	28.47	3.89	8
XBB	2.57E+04	2.24E+03	4.12E-05	2.00E-05	1.56	0.74	6
XBB.1.5	2.76E+04	2.41E+03	4.45E-05	3.01E-06	1.61	0.08	8
CH.1.1	3.33E+04	6.40E+02	1.67E-05	4.56E-07	0.50	0.02	4
BN.1	8.92E+02	1.14E+02	6.85E-05	3.08E-05	74.70	28.01	5
BN.1 + PNGase F	1.50E+03	1.97E+02	2.59E-04	3.58E-06	174.4	20.5	2
BN.1-T356K	2.09E+04	8.70E+00	4.50E-05	4.27E-06	2.16	0.2	2

NB: no binding; N/A: not applicable

Table 4.6 Donors' demographics

Donor ID	Gender	Age	Vaccine doses	COVID diagnosis	SARS-CoV-2 variant	Δ sample-vaccine (days)	Cohort
8H	M	79	4	no	/	72	Wu_4vacc
15H	M	52	4	no	/	5	Wu_4vacc
17H	M	76	4	no	/	21	Wu_4vacc
25H	M	60	4	no	/	16	Wu_4vacc
27H	M	59	4	no	/	42	Wu_4vacc
30H - 4X	F	61	4	no	/	17	Wu_4vacc
46H	M	60	4	no	/	15	Wu_4vacc
69H	F	68	4	no	/	97	Wu_4vacc
71H - 4x	F	58	4	no	/	48	Wu_4vacc
76H - 4x	F	38	4	no	/	13	Wu_4vacc
12H	F	42	4	no	/	34	Wu/BA.5biv
16H	F	46	4	no	/	33	Wu/BA.5biv
17H	M	76	5	no	/	18	Wu/BA.5biv
29H	M	64	5	no	/	37	Wu/BA.5biv
30H - 5x	F	61	5	no	/	30	Wu/BA.5biv
31H*	F	/	3	no	/	54	Wu/BA.5biv
46H	M	60	5	no	/	16	Wu/BA.5biv
51H	F	50	4	no	/	33	Wu/BA.5biv
54H	F	34	4	no	/	27	Wu/BA.5biv
57H	M	36	5	no	/	46	Wu/BA.5biv
69H	F	68	5	no	/	42	Wu/BA.5biv
71H - 5x	F	58	5	no	/	20	Wu/BA.5biv
76H - 5x	F	38	5	no	/	60	Wu/BA.5biv
110C	M	51	5	yes	WA-1	38	preOm+biv
245C	F	28	4	yes	WA-1	25	preOm+biv
63C	F	36	4	yes	WA-1	33	preOm+biv
71C	F	69	5	yes	WA-1	28	preOm+biv
87C	M	76	5	yes	WA-1	30	preOm+biv
269C	M	41	4	yes	Gamma/P.1 & Om. BA.1	30	Om.BT+biv
318C	F	/	4	yes	Omicron	42	Om.BT+biv
319C	M	/	4	yes	Omicron	28	Om.BT+biv
324C	F	24	4	yes	Omicron	32	Om.BT+biv
331C	M	25	5	yes	Omicron	33	Om.BT+biv
345C	M	/	4	yes	Omicron	28	Om.BT+biv
388C	M	34	4	yes	Omicron BA.5	45	Om.BT+biv
392C	M	/	6	yes	Omicron BA.5	40	Om.BT+biv
400C	F	21	4	yes	Omicron BA.2	22	Om.BT+biv
403C	F	21	4	yes	Omicron BA.2.12.1	33	Om.BT+biv
407C	F	33	4	yes	Omicron BA.2	34	Om.BT+biv
414C	M	/	4	yes	Omicron BA.4	51	Om.BT+biv
415C	F	/	4	yes	Omicron BA.2	30	Om.BT+biv
422C	F	20	4	yes	Omicron BA.2	27	Om.BT+biv
424C	F	21	4	yes	Omicron BA.2.12.1	29	Om.BT+biv
425C	M	45	4	yes	Omicron BA.2.12.1	31	Om.BT+biv
428C	F	22	4	yes	Omicron BA.5	13	Om.BT+biv
445C	F	/	4	yes	Omicron BA.5	36	Om.BT+biv
56H	M	46	4	yes	Omicron[&]	28	Om.BT+biv
HCW199	M	67	3	no	/	18	Wu_3vacc
HCW225	F	50	3	no	/	25	Wu_3vacc
HCW229	F	45	3	no	/	20	Wu_3vacc
HCW239	F	33	3	no	/	26	Wu_3vacc
HCW243	F	29	3	no	/	27	Wu_3vacc
HCW198	M	52	3	yes	pre Omicron	18	preOm+vacc
HCW200	F	41	3	yes	pre Omicron	13	preOm+vacc
HCW202	M	46	3	yes	pre Omicron	13	preOm+vacc
HCW221	F	39	3	yes	pre Omicron	20	preOm+vacc
HCW224	F	49	3	yes	pre Omicron	18	preOm+vacc
HCW226	F	48	3	yes	pre Omicron	25	preOm+vacc
HCW228	M	35	3	yes	pre Omicron	20	preOm+vacc

HCW232	F	32	3	yes	pre Omicron	25	preOm+vacc
HCW234	M	27	3	yes	pre Omicron	19	preOm+vacc
HCW236	F	34	3	yes	pre Omicron	27	preOm+vacc
HCW237	F	45	3	yes	pre Omicron	20	preOm+vacc
HCW238	M	27	3	yes	pre Omicron	26	preOm+vacc

[§]TP, timepoint. *Donor 31H received the Janssen COVID-19 vaccination as the primary vaccine series.
[&]determined by longitudinal N ELISA.

Table 4.7 Kidney transplant recipients' and healthcare workers' demographics

Donor ID	Gender	Age	No. of immuno-suppressive drugs*	Vaccine doses	COVID diagnosis	SARS-CoV-2 variant	Δ sample-vaccine (days)	Cohort
KTR-004	M	68	2	4	no	/	83	KTR Wu_4vacc
KTR-007	M	77	3	4	no	/	140	KTR Wu_4vacc
KTR-009	M	72	2	4	no	/	46	KTR Wu_4vacc
KTR-010	F	70	3	4	no	/	51	KTR Wu_4vacc
KTR-011	M	56	2	4	no	/	80	KTR Wu_4vacc
KTR-013	F	46	1	4	no	/	92	KTR Wu_4vacc
KTR-026	M	37	2	4	no	/	63	KTR Wu_4vacc
KTR-027	F	66	3	4	no	/	35	KTR Wu_4vacc
KTR-030	M	58	2	4	no	/	71	KTR Wu_4vacc
KTR-039	M	66	2	4	no	/	77	KTR Wu_4vacc
KTR-042	M	78	3	4	no	/	40	KTR Wu_4vacc
KTR-047	M	52	2	4	no	/	76	KTR Wu_4vacc
KTR-050	M	34	2	4	no	/	84	KTR Wu_4vacc
KTR-054	M	70	2	4	no	/	18	KTR Wu_4vacc
KTR-056	M	74	2	4	no	/	70	KTR Wu_4vacc
KTR-059	M	63	2	4	no	/	78	KTR Wu_4vacc
KTR-060	M	50	2	4	no	/	71	KTR Wu_4vacc
KTR-061	M	71	2	4	no	/	54	KTR Wu_4vacc
KTR-071	F	59	3	4	no	/	35	KTR Wu_4vacc
KTR-083	M	71	3	4	no	/	82	KTR Wu_4vacc
KTR-085	F	59	2	4	no	/	71	KTR Wu_4vacc
KTR-094	M	66	2	4	no	/	41	KTR Wu_4vacc
KTR-095	M	63	3	4	no	/	74	KTR Wu_4vacc
KTR-096	M	62	2	4	no	/	43	KTR Wu_4vacc
KTR-101	M	61	2	4	no	/	72	KTR Wu_4vacc
KTR-102	M	72	3	4	no	/	133	KTR Wu_4vacc
KTR-017	F	81	2	4	yes	pre Omicron	58	KTR preOm+Wu_4vacc
KTR-021	M	45	2	4	yes	pre Omicron	84	KTR preOm+Wu_4vacc
KTR-031	F	77	2	4	yes	pre Omicron	59	KTR preOm+Wu_4vacc
KTR-084	F	24	3	4	yes	pre Omicron	65	KTR preOm+Wu_4vacc
KTR-099	M	52	2	4	yes	pre Omicron	93	KTR preOm+Wu_4vacc
HCW-001	M	52	/	3	no	/	90	HCW Wu_3vacc
HCW-002	F	44	/	3	no	/	78	HCW Wu_3vacc
HCW-003	F	41	/	3	no	/	76	HCW Wu_3vacc
HCW-004	M	48	/	3	no	/	90	HCW Wu_3vacc
HCW-005	F	57	/	3	no	/	83	HCW Wu_3vacc
HCW-008	F	48	/	3	no	/	86	HCW Wu_3vacc
HCW-009	F	54	/	3	no	/	81	HCW Wu_3vacc
HCW-011	M	69	/	3	no	/	93	HCW Wu_3vacc
HCW-012	F	60	/	3	no	/	94	HCW Wu_3vacc
HCW-013	F	43	/	3	no	/	55	HCW Wu_3vacc
HCW-016	F	62	/	3	no	/	6	HCW Wu_3vacc
HCW-017	F	33	/	3	no	/	50	HCW Wu_3vacc
HCW-018	M	33	/	3	no	/	110	HCW Wu_3vacc
HCW-019	F	62	/	3	no	/	29	HCW Wu_3vacc
HCW-020	F	64	/	3	no	/	90	HCW Wu_3vacc
HCW-021	M	44	/	3	no	/	28	HCW Wu_3vacc
HCW-022	F	44	/	3	no	/	28	HCW Wu_3vacc
HCW-023	F	46	/	3	no	/	22	HCW Wu_3vacc
HCW-024	M	63	/	3	no	/	35	HCW Wu_3vacc
HCW-025	F	54	/	3	no	/	94	HCW Wu_3vacc
HCW-026	F	63	/	3	no	/	28	HCW Wu_3vacc
HCW-027	F	49	/	3	no	/	38	HCW Wu_3vacc
HCW-028	F	56	/	3	no	/	29	HCW Wu_3vacc
HCW-031	F	58	/	3	no	/	35	HCW Wu_3vacc
HCW-033	F	59	/	3	no	/	31	HCW Wu_3vacc
HCW-037	F	59	/	3	no	/	45	HCW Wu_3vacc
HCW-038	F	22	/	3	no	/	61	HCW Wu_3vacc
HCW-039	F	60	/	3	no	/	23	HCW Wu_3vacc
HCW-010	F	39	/	3	yes	pre Omicron	69	HCW preOm+Wu_3vacc
HCW-014	F	29	/	3	yes	pre Omicron	89	HCW preOm+Wu_3vacc
HCW-015	F	36	/	3	yes	pre Omicron	86	HCW preOm+Wu_3vacc
HCW-029	F	49	/	3	yes	pre Omicron	77	HCW preOm+Wu_3vacc
HCW-030	F	56	/	3	yes	pre Omicron	35	HCW preOm+Wu_3vacc
HCW-034	F	38	/	3	yes	pre Omicron	28	HCW preOm+Wu_3vacc
HCW-036	F	49	/	3	yes	pre Omicron	34	HCW preOm+Wu_3vacc

*any of the following: cyclosporin, tacrolimus, MMF/MPA, azathioprine, everolimus/sirolimus, belatacept or glucocorticoids

Table 4.8 Statistically significant differences of mean neutralization and binding titers within and between cohorts

Fig. 4a	Mean rank diff.	Significant?	Adjusted P Value	Cohort
Wu-G614 vs. BQ.1.1	169	*	0.03	Wu4vacc (i)
Wu-G614 vs. XBB.1	192	**	0.003	Wu4vacc (i)
Wu-G614 vs. XBB.1.5	187	**	0.004	Wu4vacc (i)
BA.1 vs. BA.1	-145	*	0.04	Wu4vacc (i)/Om.BT+biv (iv)
BA.5 vs. BA.5	-148	*	0.03	Wu4vacc (i)/Om.BT+biv (iv)
BA.2.75.2 vs. BA.2.75.2	-151	*	0.02	Wu4vacc (i)/Om.BT+biv (iv)
Wu-G614 vs. BA.2.75.2	148	*	0.03	Wu/BA.5biv (ii)
Wu-G614 vs. BQ.1.1	147	*	0.03	Wu/BA.5biv (ii)
Wu-G614 vs. XBB.1	202	***	<0.001	Wu/BA.5biv (ii)
Wu-G614 vs. XBB.1.5	198	***	<0.001	Wu/BA.5biv (ii)
BA.1 vs. XBB.1	148	*	0.03	Wu/BA.5biv (ii)
BA.1 vs. XBB.1.5	144	*	0.04	Wu/BA.5biv (ii)
Wu-G614 vs. BQ.1.1	129	*	0.01	Om.BT+biv (iv)
Wu-G614 vs. XBB.1	162	***	<0.001	Om.BT+biv (iv)
Wu-G614 vs. XBB.1.5	152	***	<0.001	Om.BT+biv (iv)
BA.1 vs. BQ.1.1	129	*	0.01	Om.BT+biv (iv)
BA.1 vs. XBB.1	162	***	<0.001	Om.BT+biv (iv)
BA.1 vs. XBB.1.5	152	***	<0.001	Om.BT+biv (iv)
BA.5 vs. XBB.1	149	***	<0.001	Om.BT+biv (iv)
BA.5 vs. XBB.1.5	139	**	0.002	Om.BT+biv (iv)
Fig.4b	**Mean rank diff.**	**Significant?**	**Adjusted P Value**	**Cohort**
Wu-G614 vs. XBB.1	159	*	0.01	Wu3vacc (v)
Wu-G614 vs. XBB.1.5	161	*	0.01	Wu3vacc (v)
Wu-G614 vs. BA.2.75.2	114	***	<0.001	preOm+vacc (vi)
Wu-G614 vs. BQ.1.1	108	***	<0.001	preOm+vacc (vi)
Wu-G614 vs. XBB.1	151	***	<0.001	preOm+vacc (vi)
Wu-G614 vs. XBB.1.5	151	***	<0.001	preOm+vacc (vi)
BA.1 vs. XBB.1	99.6	**	0.005	preOm+vacc (vi)
BA.1 vs. XBB.1.5	98.9	**	0.006	preOm+vacc (vi)
BA.5 vs. XBB.1	97	**	0.009	preOm+vacc (vi)
BA.5 vs. XBB.1.5	96.3	*	0.01	preOm+vacc (vi)
Fig. 4c RBD	**Mean rank diff.**	**Significant?**	**Adjusted P Value**	**Cohort**
Wu-G614 vs. BA.1	108	***	<0.001	preOm+vacc (vi)
Wu-G614 vs. BA.5	94.9	***	<0.001	preOm+vacc (vi)
Wu-G614 vs. BQ.1.1	90.9	**	0.001	preOm+vacc (vi)
Wu-G614 vs. XBB.1	90.8	**	0.001	preOm+vacc (vi)
Fig. 4c S	**Mean rank diff.**	**Significant?**	**Adjusted P Value**	**Cohort**
BA.1 vs. BA.1	-112	*	0.04	preOm+vacc (vi)/Wu/BA.5biv (ii)
BA.2.75.2 vs. BA.2.75.2	-116	*	0.02	preOm+vacc (vi)/Wu/BA.5biv (ii)
BQ.1.1 vs. BQ.1.1	-117	*	0.02	preOm+vacc (vi)/Wu/BA.5biv (ii)
XBB.1 vs. XBB.1	-113	*	0.04	preOm+vacc (vi)/Wu/BA.5biv (ii)
Fig. 4d	**Mean rank diff.**	**Significant?**	**Adjusted P Value**	**Cohort**
		no		

*** (p-value < 0.001); ** (p < 0.002), * (p < 0.033) Kruskal-Wallis rank test and corrected with Dunn's test

Table 4.9 Statistically significant differences of mean neutralization and binding titers within and between cohorts

ED Fig. 7a (neutralization)	Mean rank diff.	Significant?	Adjusted P Value	Cohort
Wu-G614 vs. BA.5	127	**	0.004	DP Wu4vacc
Wu-G614 vs. BA.2.75.2	194	***	<0.001	DP Wu4vacc
Wu-G614 vs. BQ.1.1	224	***	<0.001	DP Wu4vacc
Wu-G614 vs. XBB.1	229	***	<0.001	DP Wu4vacc
Wu-G614 vs. XBB.1.5	238	***	<0.001	DP Wu4vacc
BA.1 vs. BA.2.75.2	113	*	0.03	DP Wu4vacc
BA.1 vs. BQ.1.1	144	***	<0.001	DP Wu4vacc
BA.1 vs. XBB.1	148	***	<0.001	DP Wu4vacc
BA.1 vs. XBB.1.5	157	***	<0.001	DP Wu4vacc
BA.5 vs. XBB.1.5	111	*	0.03	DP Wu4vacc
Wu-G614 vs. BA.2.75.2	156	***	<0.001	HCW Wu3/4vacc
Wu-G614 vs. BQ.1.1	179	***	<0.001	HCW Wu3/4vacc
Wu-G614 vs. XBB.1	261	***	<0.001	HCW Wu3/4vacc
Wu-G614 vs. XBB.1.5	262	***	<0.001	HCW Wu3/4vacc
BA.1 vs. BQ.1.1	121	**	0.009	HCW Wu3/4vacc
BA.1 vs. XBB.1	203	***	<0.001	HCW Wu3/4vacc
BA.1 vs. XBB.1.5	204	***	<0.001	HCW Wu3/4vacc
BA.5 vs. XBB.1	185	***	<0.001	HCW Wu3/4vacc
BA.5 vs. XBB.1.5	186	***	<0.001	HCW Wu3/4vacc
ED Fig. 7a (binding)	**Mean rank diff.**	**Significant?**	**Adjusted P Value**	**Cohort**
Wu-G614 vs. BA.5	111	**	0.004	DP Wu4vacc
Wu-G614 vs. BQ.1.1	98.9	*	0.02	DP Wu4vacc
Wu-G614 vs. XBB.1	103	*	0.01	DP Wu4vacc
Wu-G614 vs. BA.1	191	***	<0.001	HCW Wu3/4vacc
Wu-G614 vs. BA.5	162	***	<0.001	HCW Wu3/4vacc
Wu-G614 vs. BQ.1.1	147	***	<0.001	HCW Wu3/4vacc
Wu-G614 vs. XBB.1	146	***	<0.001	HCW Wu3/4vacc
BA.1 vs. BA.2.75.2	-116	**	0.002	HCW Wu3/4vacc
ED Fig. 7b (neutralization)	**Mean rank diff.**	**Significant?**	**Adjusted P Value**	**Cohort**
Wu-G614 vs. Wu-G614	-208	***	<0.001	KTR Wu4vacc / HCW Wu3vacc
Wu-G614 vs. Wu-G614	-224	**	0.003	KTR Wu4vacc / HCW preOm+Wu3vacc
BA.1 vs. BA.1	-217	***	<0.001	KTR Wu4vacc / HCW Wu3vacc
BA.1 vs. BA.1	-247	***	<0.001	KTR Wu4vacc / HCW preOm+Wu3vacc
BA.5 vs. BA.5	-178	***	<0.001	KTR Wu4vacc / HCW Wu3vacc
BA.5 vs. BA.5	-220	**	0.004	KTR Wu4vacc / HCW preOm+Wu3vacc

Wu-G614 vs. BA.2.75.2	238	***	<0.001	HCW Wu3vacc

*** (p-value < 0.001); ** (p < 0.002), * (p < 0.033) Kruskal-Wallis rank test and corrected with Dunn's test

Chapter 5. Dissecting immunodominant sites on the MERS-CoV spike protein in convalescent plasma

The final chapter of this dissertation examines the antibody response generated against the spike protein following infection with MERS-CoV. In this chapter, I describe how we determined which domains and epitopes of the spike protein are targeted by plasma binding and neutralizing antibodies.

5.1 Chapter Introduction

Coronaviruses (CoV) have a propensity to cross zoonotic barriers and cause significant morbidity and mortality in humans as exemplified by the recent emergence of severe acute respiratory syndrome coronavirus (SARS-CoV-1), Middle East respiratory syndrome coronavirus (MERS-CoV), and severe acute respiratory syndrome coronavirus-2 (SARS-CoV-2) (Bermingham et al., 2012; Drosten et al., 2003; Peiris et al., 2003; Zaki et al., 2012; P. Zhou et al., 2020; Zhu et al., 2020). MERS-CoV first emerged in 2012 and human infections have continued to be documented in endemic regions (Ebrahim et al., 2021). MERS-CoV causes severe respiratory illness in infected individuals with a reported case fatality rate of approximately 35% (Arabi et al., 2014; Ebrahim et al., 2021). Sustained human-to-human MERS-CoV transmission infrequently occurs with the majority of new cases occurring between infected camels and humans (Alshukairi et al., 2018; Dudas et al., 2018).

MERS-CoV entry into target cells is facilitated by the viral spike (S) protein (Millet & Whittaker, 2014; Raj et al., 2013), which consists of two subunits, S_1 and S_2 (Tortorici & Veesler, 2019). The S_1 subunit contains the receptor binding domain (RBD) and the

N-terminal domain (NTD), that permit attachment to the target cell through interactions with dipeptidyl peptidase 4 (DPP4) and sialosides, respectively (W. Li et al., 2017; Lu et al., 2013; Y.-J. Park et al., 2019; Raj et al., 2013; N. Wang et al., 2013). The S_2 subunit is the machinery promoting fusion of the viral and host membranes to initiate infection (Tortorici & Veesler, 2019; Walls et al., 2017). To mediate fusion, the MERS-CoV S protein first undergoes proteolytic cleavage by either furin during viral morphogenesis or cathepsins after virions are endocytosed generating the S_1 and S_2 subunits. The S_2 subunit is again cleaved by TMPRSS2 at surface of the cell membrane or cathepsins in endosomes to form S_2', which then undergoes dramatic conformational changes to fuse the two membranes together (Earnest et al., 2017; Millet & Whittaker, 2014; J.-E. Park et al., 2016; Walls et al., 2017). Similar to SARS-CoV-2, neutralizing antibodies against the S protein have been suggested to be the primary correlate of protection against MERS-CoV infection (L. Wang et al., 2015; Widjaja et al., 2019; Zhao et al., 2017). As such, MERS-CoV vaccines currently under development encode the MERS-CoV spike protein and aim to develop a neutralizing antibody response that blocks viral entry (Folegatti et al., 2020; Koch et al., 2020; Modjarrad et al., 2019; L. Wang et al., 2015).

MERS-CoV vaccine and therapeutic design will benefit from a detailed understanding of the contribution of different domains and epitopes on the spike protein to neutralization. Several neutralizing antibodies targeting the MERS-CoV S protein have been isolated and characterized to date (Corti et al., 2015; Jiang et al., 2014; Y. Li et al., 2015; Pallesen et al., 2017; Pinto et al., 2021; Sauer et al., 2021; Silva et al., 2023; Sun et al., 2022; Tang et al., 2014; Tse et al., 2023; Walls et al., 2019; N. Wang et al., 2019; S. Zhang et al., 2018; H. Zhou et al., 2019). These antibodies target the

RBD, NTD, and S_2 subunit, suggesting each of these domains can contribute to neutralization. However, the identification of neutralizing antibodies does not indicate whether the targeted epitopes are immunodominant and contribute significantly to the overall neutralizing activity of convalescent plasma.

The contribution of domains and epitopes to the neutralization potency of convalescent plasma can be deciphered by leveraging structural epitope mapping approaches, as exemplified by studies conducted on the antibody response in convalescent sera against the SARS-CoV-2 S (Bowen, Park, et al., 2022; Greaney, Eguia, et al., 2022; Greaney, Loes, Crawford, et al., 2021; Greaney, Starr, et al., 2022; Piccoli et al., 2020). These studies revealed the SARS-CoV-2 RBD is immunodominant (Piccoli et al., 2020; Premkumar et al., 2020). Furthermore, these studies indicated antibodies targeting the SARS-CoV-2 RBD account for the majority of sera neutralizing activity and are responsible for nearly all sera cross-neutralization against viral variants (Bowen, Park, et al., 2022; Greaney, Eguia, et al., 2022; Greaney, Loes, Crawford, et al., 2021; Greaney, Starr, et al., 2022). A similar analysis of convalescent sera collected from MERS-CoV infected individuals may provide insights into the best spike domains and epitopes to target in MERS-CoV vaccines and therapeutics.

Here, we analyzed binding and neutralizing antibody titers in plasma samples collected from individuals who were hospitalized with MERS-CoV infections prior to the SARS-CoV-2 pandemic. We further examined the contribution of the different subunits and domains of the MERS-CoV spike protein to plasma neutralizing activity. Finally, we dissected the immunodominant epitopes on the MERS-CoV S protein. Our findings

reveal the immunodominant sites on the MERS-CoV S protein that contribute to the neutralization potency of convalescent plasma.

5.2 MERS-CoV infection induces S-directed plasma binding and neutralizing antibodies

To understand humoral immune responses against MERS-CoV, we collected plasma samples from 30 individuals hospitalized with MERS between 2017 and 2019 (i.e. prior to the COVID-19 pandemic). A total of 98 plasma samples were collected with individuals contributing between 1 and 12 samples collected 3 to 191 days post-symptom onset or hospitalization **(Table 5.1)**.

We first measured plasma binding antibody titers against the prefusion MERS-CoV S 2P ectodomain trimer EMC/2012 strain; GenBank accession no. NC_019843.3) by ELISA. We detected S-directed IgG binding titers in 97 out of 98 plasma samples with half-maximal effective dilution (ED_{50}) titers ranging from <10 to 55,978 (GMT: 875; **Figure 5.1A and 5.2**). We next evaluated the neutralizing antibody titers of these plasma samples using VSV pseudotyped with the MERS-CoV EMC/2012 S protein. Detectable neutralizing antibody titers were observed for 95 out of 98 samples with half-maximal inhibitory dilution (ID_{50}) values ranging from <10 to 2,120 (GMT: 192; **Figure 5.1B and 5.3**). We then examined the relationship between S-directed binding and neutralizing antibody titers. Plasma binding antibody titers were positively correlated with neutralizing antibody titers (Spearman r = 0.79) when all 98 samples were included in the analysis as well as when only the sample with the highest IgG binding titer from each individual was included (Spearman r = 0.81; **Figure 5.4**).

5.3 Durability of S-directed IgG binding and neutralizing antibodies in MERS convalescent plasma

To understand the kinetics of elicitation and waning of antibody responses in MERS-CoV convalescent plasma, we examined S IgG binding and neutralizing antibody titers across 90 plasma samples from 22 individuals who contributed two or more samples. Time points were recorded as the number of days post symptom onset or hospitalization. All 22 individuals exhibited detectable S IgG binding **(Figure 5.1D)** and neutralizing antibody titers **(Figure 5.1E)** by 12 days post symptom onset or hospitalization. Furthermore, we observed detectable S IgG binding and neutralizing antibody titers as early as 3 days post symptom onset or hospitalization. For the 21 individuals with at least two samples collected within 60 days after symptom onset or hospitalization, we observed peak S IgG binding titers occurring between 7 to 38 days post symptom onset or hospitalization and neutralization antibody titers peaking between 6 to 45 days after symptom onset or hospitalization. We next examined S IgG binding and neutralizing antibody titers in the 6 individuals with at least one sample collected 46 or greater days post symptom onset or hospitalization. All of these individuals had detectable S IgG binding titers at least 49 and up to 191 days post symptom onset or hospitalization. One individual had neutralizing antibody titers below the limit of detection of our assay at 109 days post symptom onset or hospitalization, while another had detectable neutralizing antibody titers at 191 days after symptom onset or hospitalization. These data are consistent with previous reports on the antibody response following MERS-CoV infection in which titers peak soon after symptom onset

and can persist for several years following infection (Alshukairi et al., 2021; Cheon et al., 2022; Choe et al., 2017; W. B. Park et al., 2015; D. C. Payne et al., 2016).

5.4 MERS-CoV infection elicits broadly neutralizing antibodies against variants

Next, we examined the neutralization potency of the plasma samples against VSV pseudotyped with the S glycoprotein of four additional MERS-CoV strains: United Kingdom/H123990006/2012 (GenBank accession no. NC_038294.1), Hu/Riyadh-KSA-3181/2015 (GenBank accession no. KT806049.1), Korea/Seoul/168-1-2015 (GenBank accession no. KT374056.1), and Camel/Kenya/M23C14/2019 (GenBank accession no. OK094446.1). Relative to MERS-CoV EMC/2012, these S variants contain between 2 and 8 amino acid substitutions **(Table 5.2)**. One of these variants, Camel/Kenya/M23C14/2019, was identified from a MERS-CoV outbreak in Kenya (Ngere et al., 2022), while the other three variants and the EMC/2012 strain were identified from humans. Both the United Kingdom/H123990006/2012 and Korea/Seoul/168-1-2015 strains harbor S mutations previously shown to reduce the neutralizing activity of monoclonal antibodies or convalescent sera (Jang et al., 2022; Kleine-Weber et al., 2019; Tai et al., 2017). The D510G S mutation of the Korea/Seoul/168-1-2015 strain has further been shown to reduce DPP4 binding affinity and impair viral entry in human cells (Kim et al., 2016; Wong et al., 2021). The sample with the highest spike IgG binding titers for each individual was tested for neutralization breadth.

Relative to the EMC/2012 strain (GMT: 338), neutralization titers were reduced 1.35-fold against the United Kingdom/H123990006/2012 S VSV (GMT: 250; **Figure**

5.1E and 5.5), 1.13-fold against the Hu/Riyadh-KSA-3181/2015 S VSV (GMT: 298) and slightly increased against Korea/Seoul/168-1-2015 S VSV (GMT: 389). Strikingly, plasma neutralizing activity was enhanced 2.3-fold against Camel/Kenya/M23C14/2019 S VSV (GMT: 750). These data indicate recent human MERS-CoV infections are likely driven by zoonotic spillover of strains circulating in camel reservoirs, consistent with prior phylodynamic analysis that suggested MERS-CoV transmission occurs primarily from repeated spillover from camels to humans (Dudas et al., 2018). Furthermore, these data demonstrate that the few mutations observed in MERS-CoV strains to date do not completely dampen the neutralizing activity of convalescent plasma.

To assess neutralization breadth against a phylogenetically distant merbecovirus, we measured plasma neutralizing activity against the recently described HKU4-related isolate from pangolins (MjHKU4). MjHKU4 S shares 65.4% amino acid sequence identity with MERS-CoV S, including conservation of 8 out of 16 residues in the receptor-binding motif, likely explaining retention of human DPP4 utilization (J. Chen et al., 2023). Only 2 out of 30 plasma samples had detectable but weak neutralization of MjHKU4 S VSV, suggesting that although a single MERS-CoV infection elicits neutralizing antibodies against variants, it is insufficient to induce pan-merbecovirus neutralizing antibodies **(Figure 5.1E and 5.5)**.

5.5 S_1-directed antibodies account for most plasma neutralizing activity

Given that S_1-directed plasma antibodies, particularly those targeting the RBD, account for virtually all neutralizing activity against SARS-CoV-2 upon infection or vaccination (Bowen, Park, et al., 2022; Piccoli et al., 2020), we sought to determine if

MERS-CoV infection-elicited antibodies share a similar specificity. To answer this question, we first assessed IgG binding titers against the MERS-CoV S EMC/2012 S_1 subunit by ELISA and found that they ranged from < 10 to 20,101 (GMT: 936; **Figure 5.6A and 5.7**) for the 29 plasma samples evaluated. Examination of the relationship between plasma binding and neutralizing antibody titers revealed that S_1-directed IgG binding titers were positively correlated with neutralizing activity (Spearman r = 0.68; **Figure 5.6B**), as was the case for S IgG binding titers.

To further understand the contribution of S_1-directed antibodies to plasma neutralizing activity, we depleted the plasma samples of S_1-directed antibodies by incubation with magnetic beads coupled to the MERS-CoV S_1 subunit. The sample with the highest S IgG binding titer from each individual was included in the analysis with samples from individual 2 and individual 31 excluded due to low plasma spike IgG binding and neutralizing titers and from individual 22 excluded due to insufficient sample volumes. Following incubation with the S_1-coated beads, IgG binding titers were undetectable for 13 out of 27 samples (ED_{50} < 10; **Figure 5.6C and 5.8A**) and reduced 74.5 to 98.7% for the remaining 14 samples.

We first compared the residual spike IgG binding titers of the mock- and anti-S_1 antibody depleted plasma samples. The spike IgG binding titers were significantly reduced after depleting S_1-directed antibodies (p = 0.0002; Mock-depleted GMT: 1002 versus S_1-depleted GMT: 150; **Figure 5.6D and 5.8B**). We observed an 89.5% reduction in S IgG binding titers upon depletion of S_1-directed antibodies with 3 of the 27 samples having binding titers below the limit of detection (ED_{50} < 10). These data suggest that S_1-directed antibodies account for the majority of S IgG binding antibodies

in convalescent plasma. Furthermore, depletion of S_1-directed antibodies resulted in a near complete loss of neutralizing activity with a single sample retaining detectable neutralizing activity (ID_{50} > 10; **Figure 5.6E and 5.8C**), which was, however, reduced by 95.2%. These data suggest that S_1-directed antibodies account for nearly all of the neutralizing activity in convalescent plasma post MERS-CoV infection.

5.6 Antibodies targeting the MERS-CoV RBD account for the majority of the neutralizing activity of convalescent plasma

As the S_1 subunit comprises at least two domains targeted by neutralizing antibodies, namely the RBD and the NTD (Tortorici & Veesler, 2019), we set out to understand the contribution of antibodies directed against each of these domains to plasma neutralizing activity. We first measured the RBD and NTD IgG binding titers in these samples including the plasma sample with the highest S IgG binding titer from each individual in the analysis. RBD IgG binding titers ranged from < 10 to 14,253 (GMT: 1,023; **Figure 5.9A and 5.10A**) and NTD IgG binding titers ranged from < 10 to 821 (GMT: 45; **Figure 5.9C and 5.10B**). We observed that both RBD and NTD IgG binding titers were positively correlated with neutralizing antibodies titers (Spearman r = 0.79 and 0.70, respectively; **Figure 5.9B and 5.9D**), concurring with the fact that the S_1 subunit is the main target of neutralizing antibodies.

To further resolve the contribution of RBD-directed and NTD-directed antibodies to spike binding and neutralizing activity, we depleted the plasma samples of domain-specific antibodies using RBD- or NTD-coated magnetic beads. The sample with the highest S IgG binding titer from each individual was included in the analysis with

samples from individual 2 and individual 31 excluded due to low plasma spike IgG binding and neutralizing titers. Twenty-six out of 28 plasma samples had RBD-directed IgG binding titers below the limit of detection (ED_{50} < 10; **Figure 5.9E and 5.11**) following incubation with the RBD-coated beads whereas the remaining 2 samples experienced 96.6% and 99.0% reductions. Following depletion with the NTD-coated magnetic beads, none of the plasma samples had detectable NTD IgG binding titers **(Figure 5.9F and 5.11)**.

We then examined the spike IgG binding titers in the mock-, anti-RBD-, and anti-NTD-antibody depleted samples. We observed a significant reduction in spike IgG binding titers for both plasma samples depleted of RBD-directed antibodies (p = < 0.0001; GMT: 460; **Figure 5.9G and 5.11**) and of NTD-directed antibodies (p = < 0.0001; GMT: 512) compared to the mock-depleted plasma (GMT: 1,014). Depletion of RBD-directed antibodies resulted in a 54.6% reduction in spike IgG binding titers across the 28 samples while depletion of NTD-directed antibodies resulted in a 49.5% reduction in spike IgG binding titers with one sample having a residual spike IgG binding below the limit of detection.

Next, we examined the residual neutralization potency of the depleted samples. Neutralizing antibody titers were significantly reduced in plasma samples depleted of RBD-directed antibodies (p = <0.0001; **Figure 5.9H and 5.11**) or of NTD-directed antibodies (p = 0.0151) compared to the mock-depleted samples (GMT: 282). For the samples depleted of RBD-directed antibodies, we observed an 85.8% (GMT: 40) reduction in neutralization potency with 6 of the 28 samples having neutralizing antibody titer below the limit of detection (ID_{50} < 10). In contrast, we observed a 29.4% (GMT:

199) reduction in neutralization potency of the samples depleted of the NTD-directed antibodies. Only 1 of the NTD antibody-depleted samples exhibited a neutralizing antibody titer below the limit of detection. Together, these data suggest that both RBD-directed and NTD-direct antibodies contribute to spike binding and neutralizing antibody titers, however, RBD-direct antibodies account for the majority of the neutralizing activity of convalescent plasma.

5.7 MERS-CoV infection induces neutralizing antibodies targeting S_1 but rarely S_2 epitopes

Several MERS-CoV S epitopes targeted by neutralizing antibodies have been identified through structural and functional studies (Corti et al., 2015; Jiang et al., 2014; Y. Li et al., 2015; Pallesen et al., 2017; Pinto et al., 2021; Sauer et al., 2021; Silva et al., 2023; Sun et al., 2022; Tang et al., 2014; Tse et al., 2023; Walls et al., 2019; N. Wang et al., 2019; S. Zhang et al., 2018; H. Zhou et al., 2019). To determine the epitopes targeted by antibodies in convalescent patient plasma, we selected a panel of monoclonal antibodies that target unique epitopes on MERS-CoV S spanning the RBD, NTD, and S_2 subunit. We then performed competition ELISAs using these monoclonal antibodies as probes to quantify the magnitude of plasma antibodies targeting each site. The sample with highest IgG S biding titer for individual was included in the analysis.

We examined the magnitude of competition to bind to MERS-CoV S of convalescent plasma with the RBD-directed antibodies LCA60, S41, and 4C2, along with the receptor, human DPP4, by ELISA **(Figure 5.12A)**. LCA60 binds the saddle of the receptor binding motif, overlapping partially with the DPP4 binding site (Corti et al.,

2015; Walls et al., 2019). The S41 epitope overlaps entirely with the DPP4 binding site, but is narrower than the RBM (S. Zhang et al., 2022). 4C2 binds the face of the RBD that remains exposed in the closed S trimer, partially overlapping with the RBM (Y. Li et al., 2015). Of the 28 convalescent plasma samples tested, 37% (n = 11; **Figure 5.12B**) had detectable competition (half-maximum blocking titers, BD50 > 10) with DPP4 binding whereas 33% (n = 10), 20% (n = 6) and 53% (n = 16) competed with LCA60, S41 and 4C2, respectively. These data suggest that antibody responses elicited by MERS-CoV infection more prevalently target RBD antigenic sites that are fully exposed in the closed S trimer relative to epitopes that are fully or partially occluded.

We further examined the capacity of convalescent plasma to block binding of the NTD-directed neutralizing antibody G2 to the spike protein. G2 binds the viral membrane distal side of the NTD, which is the only NTD neutralizing epitope identified to date **(Figure 5.12A)** (N. Wang et al., 2019). Only 23% (n = 7) of the convalescent plasma samples had detectable blocking titers against G2 **(Figure 5.12B)**. The low frequency of G2-blocking antibodies in convalescent plasma is consistent with the depletion data, which suggest that NTD-directed antibodies make a smaller overall contribution to plasma neutralizing activity, relative to RBD-directed antibodies.

We next measured competition in convalescent plasma against a panel of S_2-directed antibodies including RAY53, 76E1, G4, and B6 **(Figure 5.12C)**. RAY53 is a weakly neutralizing antibody that binds to the hinge region of the S_2 subunit in the prefusion conformation (Silva et al., 2023). 76E1 targets the fusion peptide and broadly reacts with both alphacoronaviruses and betacoronaviruses (Sun et al., 2022). G4 binds specifically to a variable loop in the MERS-CoVS_2 connector domain (Pallesen et al.,

2017). B6 targets the S stem helix and cross-react with all human-infecting betacoronaviruses (albeit weakly with HKU1) (Sauer et al., 2021). 27% (n = 8) of samples competed with RAY53 binding (BD_{50} > 10; **Figure 5.12D**) and four of these samples had RAY53 blocking titers (BD_{50}: 404 to 2,588) greater than those observed for the RBD- and NTD-directed antibodies. We speculate that RAY53 binding may be hindered by some RBD-directed antibodies, particularly those that lock the spike protein in the closed conformation, as observed for some SARS-CoV-2 mAbs (Tortorici et al., 2020). For the remaining three S_2-directed monoclonal antibodies, 7% (n= 2) of plasma samples had detectable competition with 76E1 and none of the 28 samples tested could compete with G4 or B6. These findings coupled with the S_1-antibody depletion data suggest that MERS-CoV infection does not induce a robust neutralizing antibody response towards the MERS-CoV S_2 subunit.

5.8 Chapter Discussion

Here, we examined the antibody response in convalescent plasma samples obtained from individuals hospitalized with MERS-CoV infections between 2017-2019. We observed S binding titers and neutralizing antibody titers peaking between 1 to 6 weeks post symptom onset or hospitalization. We determined plasma antibodies neutralize MERS-CoV variants with similar potencies, but display minimal neutralizing activity against the related merbecovirus MjHKU4. We further showed the S_1 subunit is immunodominant with S_1-direct antibodies accounting for the majority of the neutralization potency of convalescent plasma. Additionally, we determined both the RBD and NTD contribute to the S IgG binding activity of convalescent plasma, but RBD-

directed antibodies were responsible for most of the neutralizing activity. Finally, we used a panel of structurally characterized neutralizing antibodies to show plasma antibodies target neutralizing epitopes on the S_1 subunit, but not those on the S_2 subunit.

Prior studies on the plasma antibody response generated against the SARS-CoV-2 S following either SARS-CoV-2 infection or vaccination with S-encoding mRNA vaccines demonstrated the RBD is immunodominant accounting for the majority of plasma neutralizing activity (Bowen, Park, et al., 2022; Greaney, Eguia, et al., 2022; Greaney, Loes, Crawford, et al., 2021; Greaney, Starr, et al., 2022; Piccoli et al., 2020). These studies further indicated that NTD-directed antibodies contribute to plasma neutralizing activity against infection- or vaccine-matched variants, albeit to a lesser extent than RBD-directed antibodies (Bowen, Park, et al., 2022; McCallum, De Marco, et al., 2021). Our results on the contribution of MERS-CoV S domains to the neutralizing activity of convalescent plasma are consistent with the observations noted for SARS-CoV-2 convalescent and vaccine-elicited plasma. As RBD-directed antibodies are responsible for the majority of plasma neutralizing activity for both SARS-CoV-2 and MERS-CoV, we speculate RBD-directed antibodies will account for most of the plasma neutralization activity for all betacoronaviruses. As such, betacoronavirus RBD-based vaccines will likely confer high neutralizing antibody titers and robust protection across this genus (Walls et al., 2021; Walls, Fiala, et al., 2020).

Our plasma epitope mapping analysis indicated the ridge of the RBM exposed in the closed S trimer is frequently targeted by plasma antibodies, while RBD epitopes partially or fully occluded in the closed S conformation are less frequently targeted.

These data for MERS-CoV convalescent plasma are consistent with epitope mapping data for SARS-CoV-2 convalescent plasma, which suggested the analogous site on the SARS-CoV-2 RBD (site Ib) is frequently targeted by plasma antibodies and occluded sites (sites IIa, IIb, and IIc) are less commonly targeted (Piccoli et al., 2020). However, as far fewer neutralizing RBD-directed antibodies for MERS-CoV (Corti et al., 2015; Jiang et al., 2014; Y. Li et al., 2015; Walls et al., 2019; S. Zhang et al., 2018) have been characterized than SARS-CoV-2 (Barnes et al., 2020; Piccoli et al., 2020; Starr, Czudnochowski, et al., 2021), it is likely there are additional neutralizing epitopes on the MERS-CoV RBD that contribute to the neutralizing activity of convalescent plasma. Additional studies focused on discovering and characterizing antibodies targeting the MERS-CoV RBD will further resolve immunodominant epitopes as well as elucidate those epitopes that are resilient to viral evolution and contribute to the cross-neutralization of related merbecoviruses (Tse et al., 2023).

We observed minimal contribution of the S_2 subunit to the neutralization potency of convalescent plasma and determined S_2 neutralizing epitopes are rarely targeted by plasma antibodies. We speculate the lack of plasma antibodies targeting S_2 neutralizing epitopes may be due to these epitopes being inaccessible until the S_1 subunit binds DPP4 or is shed, as is the case for 76E1 and RAY53 (Silva et al., 2023; Sun et al., 2022), or being located close to the viral membrane and likely less accessible to recognition by B cells, as is the case for G4 and B6 (Pallesen et al., 2017; Sauer et al., 2021). While the development of S_2 subunit antigens has been a recent goal for SARS-CoV-2 vaccine design due to the resiliency of S_2-directed antibodies to the rapid evolution of SARS-CoV-2 (Halfmann et al., 2022; Hsieh et al., 2021; J. Lee et al., 2023;

Ng et al., 2022; Nuqui et al., 2023; Pang et al., 2022; P. Zhou et al., 2023), similar vaccine antigens may not be necessary for MERS-CoV. Our demonstration of the retention of plasma neutralizing activity against human and camel MERS-CoV strains along with the relatively few S_1 mutations in MERS-CoV strains sequenced to date (Dudas et al., 2018; Wong et al., 2021) suggest vaccination with prefusion S or RBD-based vaccines may be sufficient for resiliency against MERS-CoV evolution.

In conclusion, our data demonstrate MERS-CoV RBD-directed antibodies account for the majority of neutralizing activity of convalescent plasma, consistent with similar studies on SARS-CoV-2 convalescent plasma, and suggest vaccines in development for MERS-CoV and other betacoronaviruses should focus on eliciting a robust RBD-directed neutralizing antibody response.

5.9 Methods

Cell culture

Expi293 cells were grown in Expi293 media at 37°C and 8% CO_2 rotating at 130 RPM. HEK-293T cells were grown in DMEM supplemented with 10% FBS and 1% PenStrep at 37°C at 5% CO_2. Vero E6 cells stably expressing the human protease TMPRSS2 (Vero-TMPRSS2) were grown in DMEM supplemented with 10% FBS, 1% PenStrep and 8 µg/mL puromycin at 37°C and 5% CO_2 (Lempp et al., 2021).

Plasma donors

Plasma samples were collected from individuals hospitalized with MERS-CoV infections by 2017-2019 at King Faisal Specialist Hospital Research Center in Riyadh, Saudi Arabia.

Constructs

The construct encoding the prefusion stabilized MERS-CoV spike (S2P) ectodomain was previously described (Y.-J. Park et al., 2019; Walls et al., 2019). Constructs encoding the B6 heavy and light chains were previously described (Sauer et al., 2021), those encoding the G2 and G4 heavy and light chains were gifted by Jason McLellan (Pallesen et al., 2017; N. Wang et al., 2019), those encoding the RAY53 heavy and light chains were gifted by Jennifer Maynard (Silva et al., 2023), and the construct encoding the full-length MERS-CoV EMC/2012 spike protein was gifted by Gary Whittaker (Millet & Whittaker, 2014).

The full-length MERS-CoV United Kingdom/H123990006/2012, MERS-CoV Hu/Riyadh-KSA-3181/2015, MERS-CoV Camel/Kenya/M23C14/2019, MERS-CoV Korea/Seoul/168-1-2015 and MjHKU4r-CoV-1 ∆16 spike proteins were codon optimized, synthesized, and inserted into pcDNA3.1(+) by Genscript. The heavy chain Fab sequences for LCA60, S41, 4C2, and 76E1 fused to an N-terminal μ-phosphatase or mouse Ig heavy signal peptide sequence and C-terminal human FC tag were codon optimized, synthesized, and inserted into pcDNA3.1(+) by Genscript. The light chain Fab sequence for these antibodies with an N-terminal μ-phosphatase or mouse Ig heavy signal peptide sequence were codon optimized, synthesized, and inserted into pcDNA3.1(+) by Genscript. The MERS-CoV NTD (1-357) with a C-terminal octa-his tag,

MERS-CoV RBD (382-588) with an N-terminal μ-phosphatase signal peptide and C-terminal thrombin cleavage site followed by an octa-his tag, and MERS-CoV S1 (1-747) with a C-terminal octa-his tag were codon optimized, synthesized, and inserted into pcDNA3.1(+), pCMVR, and pcDNA3.4, respectively, by Genscript. The human DPP4 ectodomain (39-766) with a N-terminal CD5 leader sequence and C-terminal human FC tag was synthesized and inserted into pcDNA3.1(-).

Recombinant protein expression and purification

The MERS-CoV RBD, MERS-CoV NTD, and MERS-CoV S_1 were expressed and purified as previously described (Addetia, Park, et al., 2023; Addetia, Piccoli, et al., 2023; Bowen, Addetia, et al., 2022; Y.-J. Park et al., 2019; Walls et al., 2019). In brief, Expi293 cells were grown to a density of 3 x 10^6 cells/mL and transfected using the Expifectamine293 transfection kit following the manufacturer's recommendations. Four to five days following transfection, the supernatants were collected, clarified by centrifugation, and flowed over HisTrap FF or HP affinity columns. The columns were then washed with ten column volumes of 20 mM imidazole, 25 mM sodium phosphate pH 8.0, and 300 mM NaCl after which the proteins were eluted using a gradient up to 500 mM imidazole. The proteins were then buffer exchanged into 20 mM sodium phosphate pH 8.0 and 100 mM NaCl and concentrated using centrifugal filters, flash frozen, and stored at -80°C until use.

The MERS-CoV S2P was expressed and purified similar to above. Following elution from the affinity column, the protein was further purified by size-exclusion chromatography using a Superose 6 Increase 10/300 GL column. The protein was

concentrated, flash frozen, and stored at -80°C. For the biotinylated MERS-CoV S2P, MERS-CoV S2P was expressed and purified as described above. After elution from the affinity column, the protein was buffer exchanged into 25 mM Tris-HCl pH 8.0 and 150 mM NaCl. The purified spike protein was biotinylated using the BirA biotin-protein ligase reaction kit (Avidity) following the manufacturer's recommendation. The biotinylated protein was re-purified using an HisTrap HP column followed by size-exclusion chromatography using a Superose 6 Increase 10/300 GL column. The protein was concentrated, flash frozen, and stored at -80°C.

Recombinant monoclonal antibodies were produced by transfecting Expi293 cells at a density of 3 x 10^6 cells/mL with equal masses of the heavy and light chain constructs using Expifectamine293. Four to five days following transfection, the supernatants were harvested and clarified by centrifugation. The recombinant antibodies were captured using HiTrap Protein A HP affinity columns after which the columns were washed with ten column volumes of 20 mM sodium phosphate pH 8.0 and the proteins were eluted 0.1 M citric acid pH 3.0, which was neutralized with 1 M Tris-HCl pH 9.0. The antibodies were buffer exchanged into 20 mM sodium phosphate pH 8.0 and 100 mM NaCl and concentrated using centrifugal filters and stored at 4°C until use. The human DPP4 ectodomain was expressed and purified as described above, flash frozen, and stored at -80°C until use.

Enzyme-linked immunosorbent assay (ELISA)

The MERS-CoV S2P, RBD, NTD, or S_1 recombinant proteins were diluted to 0.003 mg/mL and added to 384-well Maxisorp plates overnight at room temperature.

The following day, plates were slapped dry and blocked with Blocker Casein for 1 hour at 37°C. The plates were slapped dry and plasma samples diluted in Tris-buffered saline with 0.1% Tween 20 (TBST) at a starting dilution of 1:10 to 1:270 and serially diluted 1:3 thereafter were added to the plates. The plates were incubated for 1 hour at 37°C, slapped dry, and washed four times with TBST. A goat anti-human IgG (H+L) HRP conjugated antibody (diluted 1:5,000 in TBST; Seracare) was added to each well. The plates were again incubated for 1 hour at 37°C, slapped dry, and washed four times with TBST. SureBlue Reserve TMB 1-Component Microwell Peroxidase Substrate was added to each well and allowed to develop for 90 seconds after which an equal volume of 1 N HCl was added to quench the reaction. The absorbance at 450 nm was immediately measured using a BioTek Synergy Neo2 plate reader. The resulting data were analyzed in GraphPad Prism 10 using a four parameter logistic curve to determine the ED_{50} for each sample. At least two biological replicates using two distinct batches of recombinant protein were performed for each sample and antigen.

Pseudotyped VSV production

VSV pseudotyped with the MERS-CoV or MjHKU4r-CoV-1 spike proteins were produced as previously described (Addetia, Park, et al., 2023; Addetia, Piccoli, et al., 2023; Bowen, Addetia, et al., 2022; Xiong et al., 2022). In brief, HEK293T cells were seeded onto poly-D-lysine coated 10 cm^2 plates at a density of 5 x 10^6 cells and grown overnight until they reached approximately 80-90% confluency. The following day, the growth media was exchanged to DMEM containing 10% FBS and the cells were transfected with the spike constructs using Lipofectamine 2000. After 20 to 24 hours,

the cells were washed three times with DMEM and infected with VSVΔG/luc. Two hours after infection, the cells were washed five times with DMEM and left overnight in DMEM supplemented with an anti-VSV-G antibody (I1-mouse hybridoma supernatant diluted 1:25, from CRL-2700, ATCC). Twenty to 24 hours later, the supernatant was harvested, clarified by centrifugation at 4,200 RPM for 10 minutes, filtered using a 0.45 μm filter, and concentrated with a 100 kDa filter (Amicon). The resulting pseudovirus was frozen at -80°C until use.

Pseudovirus neutralization assays

Neutralization assays were performed as previously described (Addetia, Park, et al., 2023; Addetia, Piccoli, et al., 2023; Bowen, Addetia, et al., 2022; Xiong et al., 2022). In brief, Vero-TMPRSS2 cells were split in white-walled, clear bottom plates at a density of 18,000 cells per well. The cells were grown overnight until they reached 90-95% confluency. Plasma samples were diluted in DMEM starting at a 1:10 dilution and serially diluted 1:3 thereafter and mixed with an equal volume of pseudotyped VSV diluted 1:50 to 1:100 in DMEM. The virus-plasma mixtures were incubated for 30 minutes at room temperature after which the growth media was removed from the Vero-TMPRSS2 cells and replaced with the virus-plasma mixture. The cells were incubated for 2 hours at 37°C after which an equal volume of DMEM supplemented with 20% FBS and the 2% PenStrep was added to each well. Twenty to 24 hours later, ONE-Glo EX was added directly to each well, the plates were then incubated for 5 minutes at 37°C, and the luminescence values were recorded using a BioTek Synergy Neo2 plate reader. The data were normalized in GraphPad Prism 10 using the relative light unit (RLU)

values measured for uninfected cells to define 0% infectivity and RLU values recorded for cells infected with pseudovirus without plasma to define 100% infectivity. ID_{50} values for sera samples were determined from the normalized data using a [inhibitor] vs. normalized response – variable slope model using two technical replicates to generate the curve fits. At least two biological replicates using distinct batches pseudoviruses were performed for each sample.

Depletion Assays

Dynabeads His-Tag Isolation and Pulldown beads (ThermoFisher) were washed once with Tris-buffered saline (TBS) containing 0.01% Tween 20. His-tagged MERS-CoV RBD, NTD, or S_1 was added to the magnetic beads at a 1.5-fold mass excess relative to the reported binding capacity of the beads. The beads and proteins were incubated for 30 minutes at room temperature with constant rotation. Unbound protein was then removed by washing the beads three times with TBS with 0.01% Tween 20. The antigen coated beads were resuspended in TBS with 0.01% Tween 20 and stored at 4°C until use.

Plasma samples were mixed with the RBD, NTD or S_1 coated beads in TBS with 0.01% Tween 20 at a 1:4 volume ratio and incubated at 37°C for 1 hour. Following this incubation, the supernatant was transferred to a new tube that contained an additional 4 volumes of beads. The mixture was incubated for an additional hour at 37°C after which the supernatant was transferred to a new tube. A mock depletion was performed concurrently following the same protocol as above except the plasma was incubated with uncoated beads. ELISAs against the depleting antigen and MERS-CoV spike and

neutralization assays against VSV pseudotyped with the MERS-CoV EMC/2012 spike were performed as described above using the depleted plasma as input. The starting 1:10 dilution factor incorporates the dilutions performed to deplete the plasma of the domain-specific antibodies. At least two biological replicates using distinct batches of proteins and pseudoviruses were performed for each sample.

Competition ELISA

To determine the EC_{50} of the antibodies used in the competition ELISAs, the antibodies were diluted to 0.003 mg/mL, plated on 384-well Maxisorp plates, and incubated overnight at room temperature. The following day, the plates were slapped dry and blocked with Blocker Casein at 37°C for 1 hour. The plates were again slapped dry and biotinylated MERS-CoV S2P diluted to 0.3 mg/mL and serially diluted 1:3 in TBST thereafter was added to each well. The plates were incubated for 37°C for 1 hour, slapped dry, and washed four times with TBST. Ultra streptavidin-HRP diluted 1:2,000 in TBST was added to each well after which the plates were again incubated at 37°C for 1 hour, slapped dry, and washed four times with TBST. SureBlue Reserve TMB 1-Component Microwell Peroxidase Substrate was added to each well and allowed to develop for 120 seconds after which an equal volume of 1 N HCl was added to quench the reaction. The absorbance at 450 nm was immediately measured using a BioTek Synergy Neo2 plate reader. The resulting data were analyzed in GraphPad Prism 10 using a four parameter logistic curve to determine the EC_{50} for each antibody.

For the competition ELISAs, 384-well Maxisorp plates were coated with the monoclonal antibodies and blocked as described above. Plasma samples were diluted

in non-binding 384-well plates beginning with a 1:5 dilution in TBST followed by a 1:3 serial dilution thereafter. Biotinylated MERS-CoV S2P was diluted to a concentration twice the determined EC_{50} in TBST and added to each well of the non-binding plates. The plasma-spike mixtures were incubated for 1 hour at 37°C after which the plasma-spike mixtures were transferred to monoclonal antibody coated plates. The plates were incubated for 1 hour at 37°C, slapped dry, and washed four times with TBST. Ultra streptavidin-HRP diluted 1:2,000 in TBST was added to the plates and the plates were incubated for 1 hour at 37°C, slapped dry, and washed four times with TBST. SureBlue Reserve TMB 1-Component Microwell Peroxidase Substrate was added to each well and allowed to develop for 120 seconds after which an equal volume of 1 N HCl was added to quench the reaction. The absorbance at 450 nm was immediately measured using a BioTek Synergy Neo2 plate reader. The resulting data was normalized using the absorbance values from wells without spike added to define 0% binding and the absorbance values from wells with spike but no plasma added to define 100% binding. BD_{50} values were determined using the [inhibitor] vs. normalized response – variable slope model using two technical replicates to generate the curve fits. Two biological replicates using distinct batches of spike protein and monoclonal antibodies were performed for each sample.

5.10 Figure and Tables

Figure 5.1. MERS-CoV infection induces robust S binding and neutralizing antibody responses.

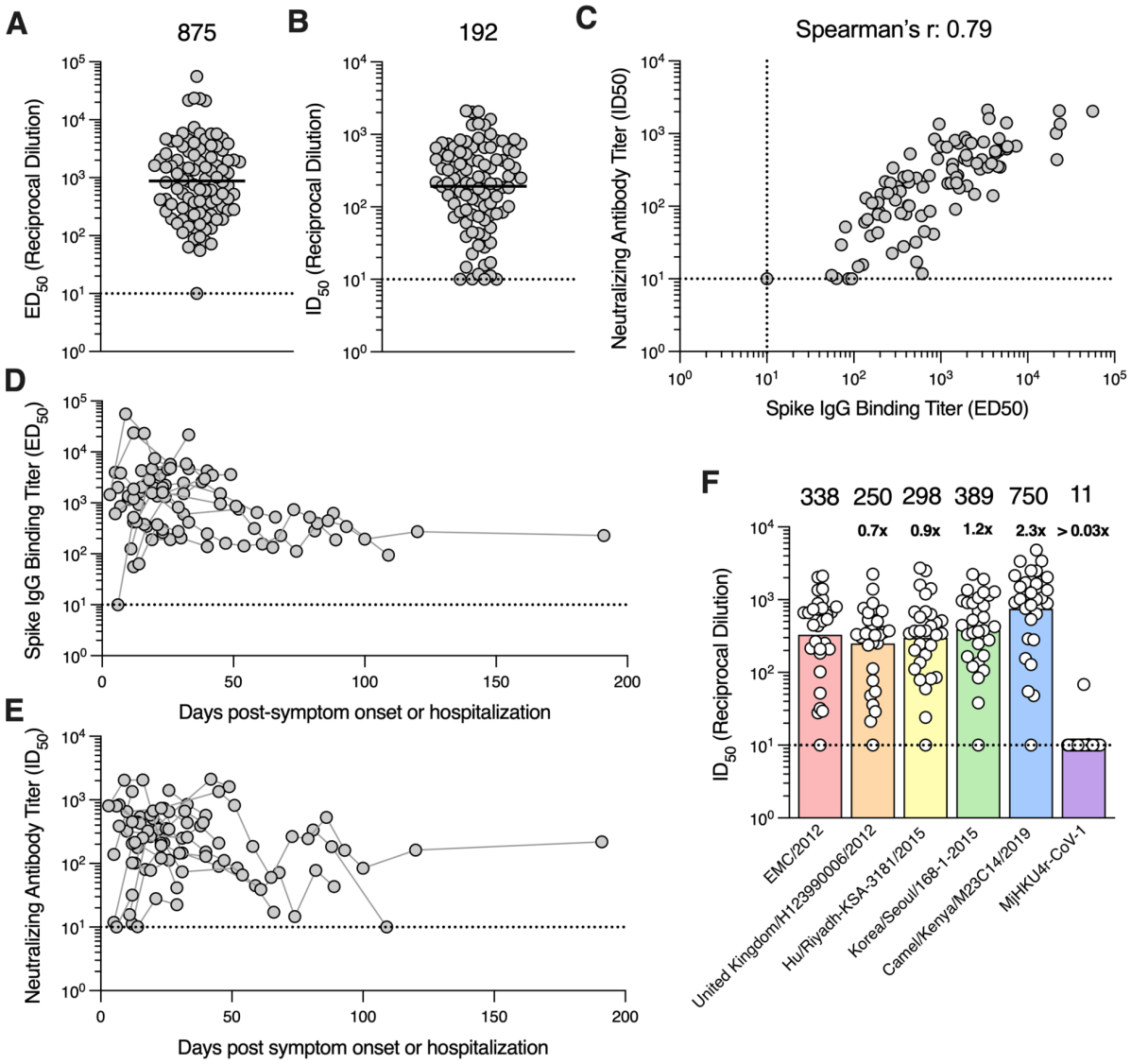

A) IgG binding titers (half-maximal effective dilution [ED_{50}]) against the prefusion MERS-CoV EMC/2012 S ectodomain trimer and **B)** neutralizing antibody titers (half-maximal inhibitory dilution [ID_{50}]) against VSV pseudotyped with the MERS-CoV EMC/2012 S measured for 98 convalescent plasma samples collected from 30 individuals hospitalized with MERS-CoV infection between 2017-2019 in Saudi Arabia. The geometric mean titer (GMT) is represented by the black bar and displayed above the plot and the limit of detection (ED_{50} or ID_{50}: 10) is represented by the dashed line. Data reflect results obtained from one biological replicate and are representative of data obtained from at least two biological replicates conducted with unique batches of spike protein or pseudovirus. **C)** Correlation analysis between neutralizing antibody and spike

IgG binding titers in the 98 convalescent plasma samples analyzed in this study. Kinetics of the **D)** S IgG binding titers and **E)** neutralizing antibody titers for 90 convalescent plasma samples collected from 22 individuals who contributed two or more samples. Samples collected from the same individual are connected with gray lines. **F)** Neutralization potency (ID_{50}) of convalescent plasma samples against VSV pseudotyped with the spike protein of the indicated MERS-CoV variant or the related merbecovirus MjHKU4r-CoV-1. GMTs are represented by the bars and displayed above the plot. The fold-change in GMT compared to MERS-CoV EMC/2012 pseudovirus is indicated below the GMT for each pseudovirus. Data reflect results obtained from one biological replicate and are representative of data obtained from at least two biological replicates conducted with unique batches of pseudoviruses.

Figure 5.2. Spike IgG binding titers.

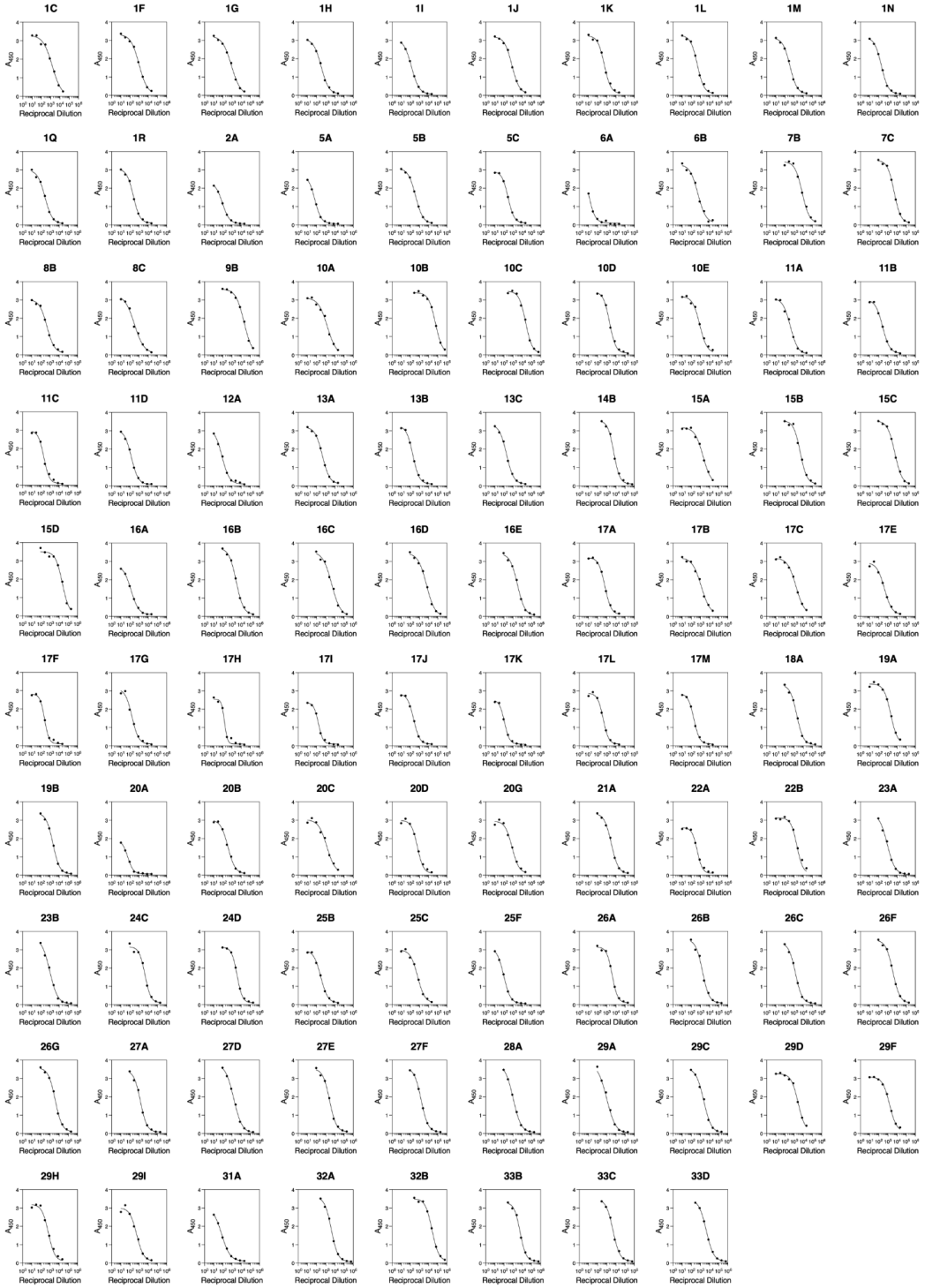

Spike IgG binding curves for each of the 98 convalescent plasma samples analyzed in this study. Data are presented for one representative biological replicate. At least two biological replicates with two unique batches of spike protein were conducted for each sample.

Figure 5.3. Neutralization curves for MERS-CoV EMC/2012.

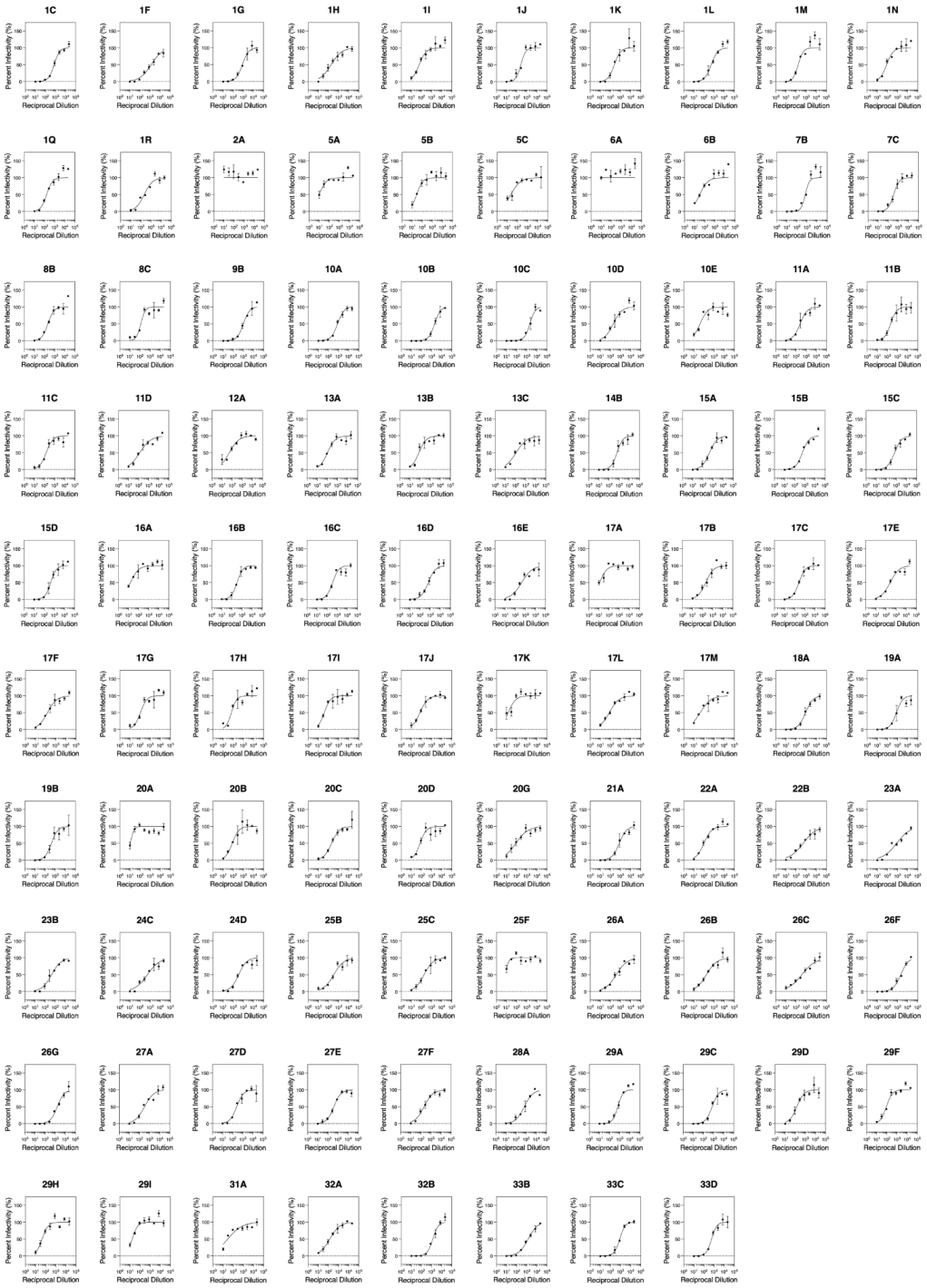

Neutralization curves against VSV pseudotyped with the MERS-CoV EMC/2012 spike protein for each of the 98 convalescent plasma samples analyzed in this study. Data are presented as the mean ± standard error of two technical replicates from one representative biological replicate. At least two biological replicates with two technical replicates were completed for each sample using two distinct batches of pseudovirus.

Figure 5.4 Correlation analysis between spike IgG binding titers versus neutralizing antibody titers.

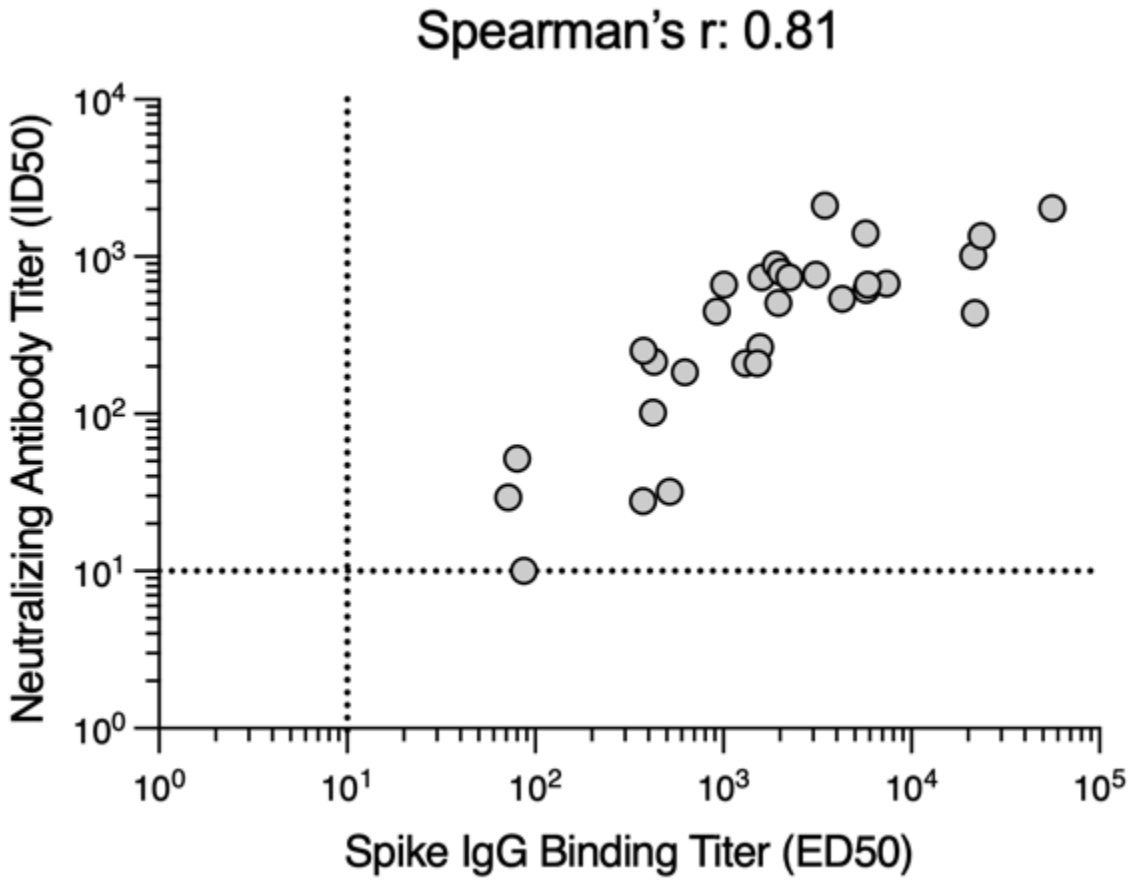

One sample per individual was included in the analysis. The limit of detection (ED_{50} or ID_{50}: < 10) is indicated by the dashed line.

Figure 5.5 Neutralization curves for MERS-CoV variants and MjHKU4r-CoV-1.

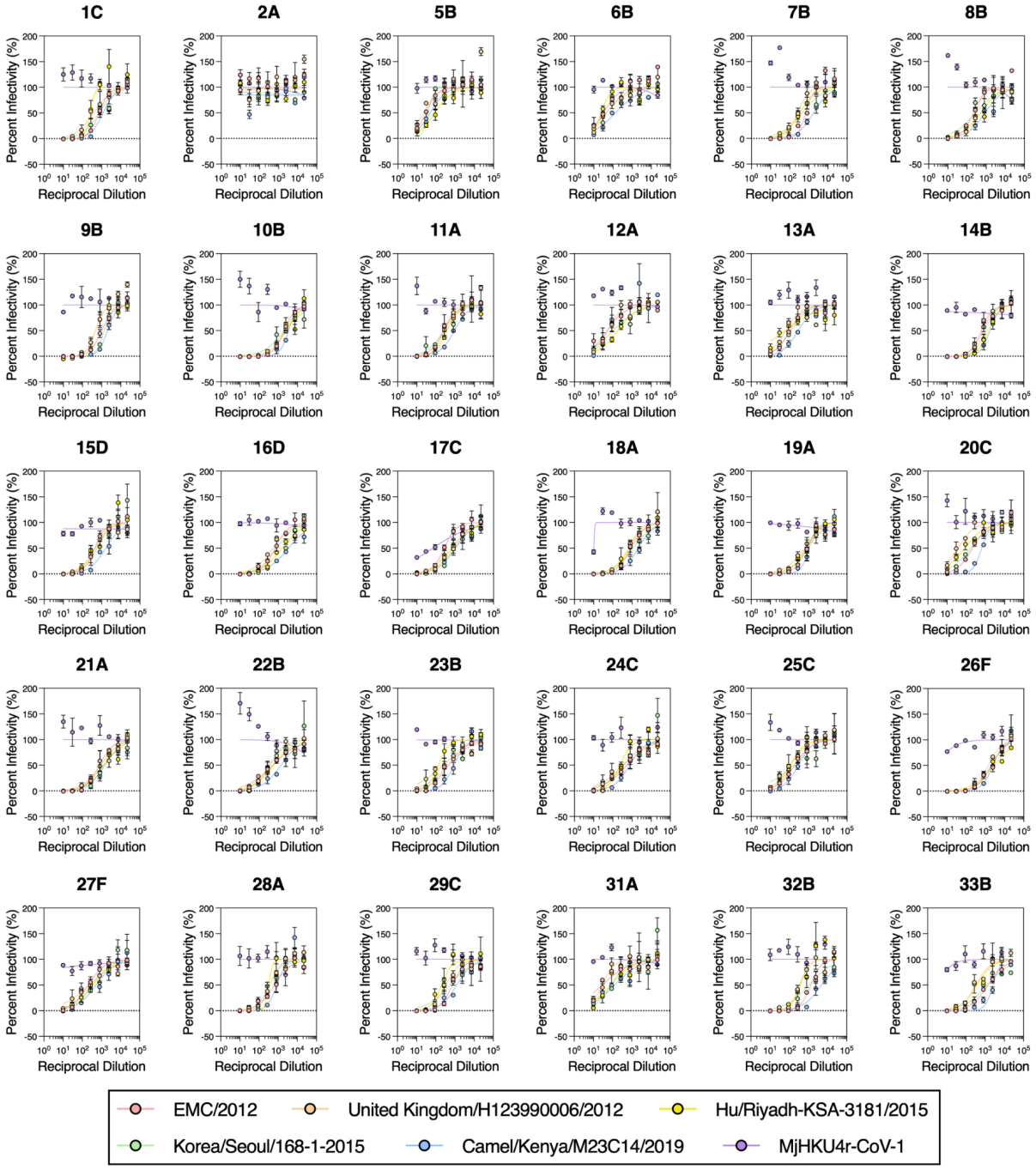

Neutralization curves for each of the 30 convalescent plasma samples included in the analysis using VSV pseudotyped with the indicated MERS-CoV variant or MjHKU4-CoV-1 spike protein. Data are presented as mean ± standard error from one representative biological replicate. At least two biological replicates, each with two technical replicates, were conducted for each sample and each variant tested using unique batches of pseudovirus.

Figure 5.6. Antibodies directed against the S_1 subunit of the MERS-CoV spike protein are responsible for nearly all neutralizing activity of convalescent plasma.

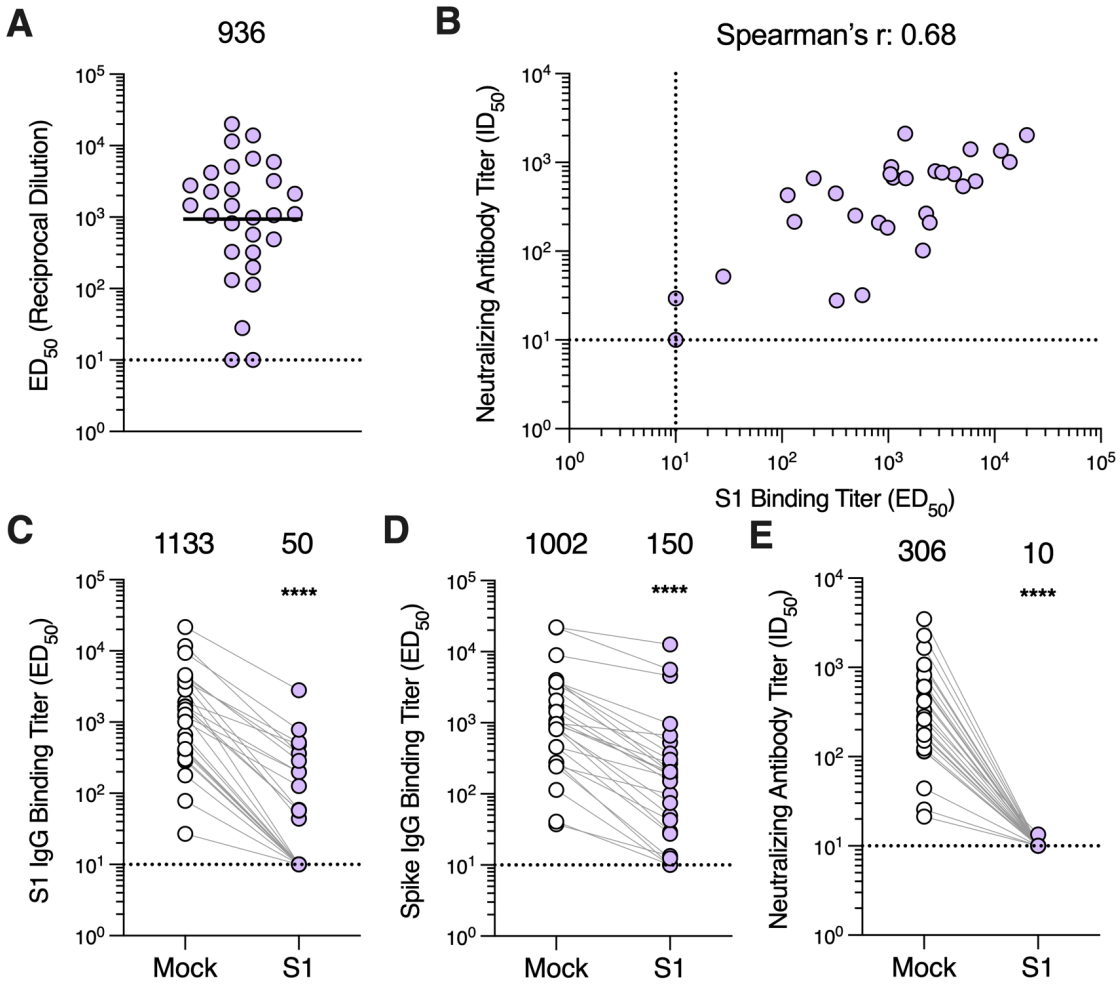

A) IgG binding titers (ED_{50}) against the MERS-CoV EMC/2012 S_1 subunit measured for convalescent plasma samples. One sample per individual was included in the analysis. The GMT is represented by the black bar and displayed above the plot. The limit of detection (ED_{50}: 10) of the assay is represented by the dashed line. Data reflect results obtained from one biological replicate and are representative of data obtained from at least two biological replicates conducted with unique batches S_1 protein. **B)** Correlation analysis between S_1 IgG binding titers and neutralizing antibody titers. **C)** S_1 and **D)** spike IgG binding titers and **E)** neutralizing antibody titers in mock-depleted and S_1-depleted plasma samples. One sample per individual was included in the analysis with 27 samples being included in total. Mock- and S_1-depleted samples from the same individual are connected with a gray line. GMTs are displayed above the plot and the limit of detection (ED_{50} or ID_{50}: 10) is represented by the dashed line. Data reflect results obtained from one biological replicate and are representative of data obtained from at least two biological replicates conducted with unique batches of S_1 and spike proteins and pseudovirus. Comparisons between mock- and S1-depleted groups were made using the Wilcoxon matched-pairs signed rank test. ****$p < 0.0001$.

Figure 5.7. S_1 IgG binding curves.

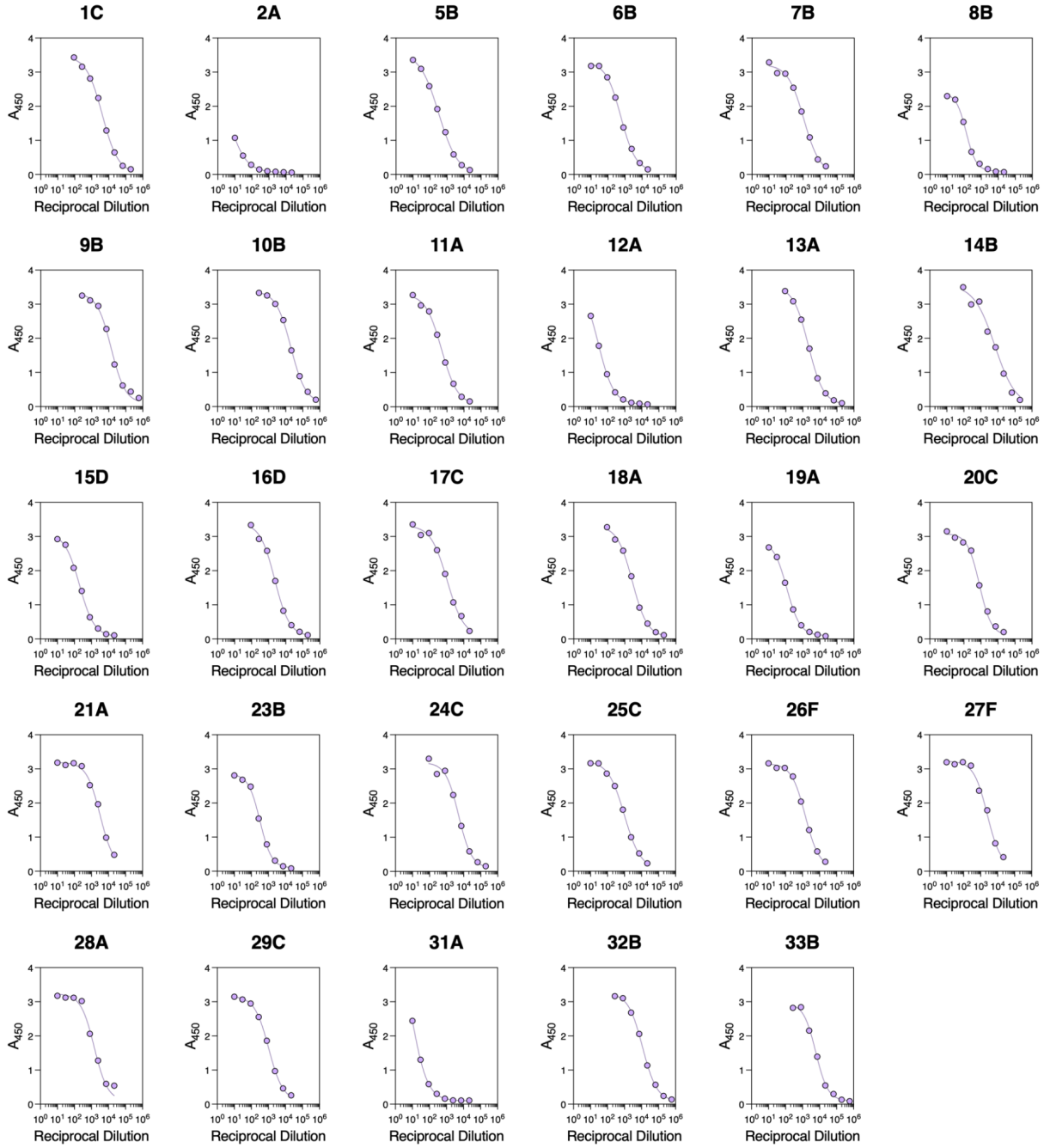

S_1 IgG binding curves for the 29 convalescent plasma samples included in the analysis. Data obtained from one representative biological replicate are presented. Two biological replicates using distinct batches of S_1 protein were completed for each sample.

Figure 5.8 IgG binding and neutralization curves following depletion with MERS-CoV S_1.

A) S_1 and **B)** spike IgG binding curves in mock- and S_1-depleted plasma for each of the 27 samples included in the analysis. **C)** Neutralization curves for the mock- and S_1-depleted plasma samples analyzed in this study. Neutralization data are presented as mean ± standard error for the two technical replicates conducted. Data presented are from one representative biological replicate. Two independent biological replicates were performed using distinct batches of S_1 protein for the antibody depletions as well as unique batches of S_1 and spike proteins and pseudovirus for the ELISAs and neutralization assays, respectively.

Figure 5.9 RBD-directed antibodies account for the majority of neutralizing activity in convalescent plasma.

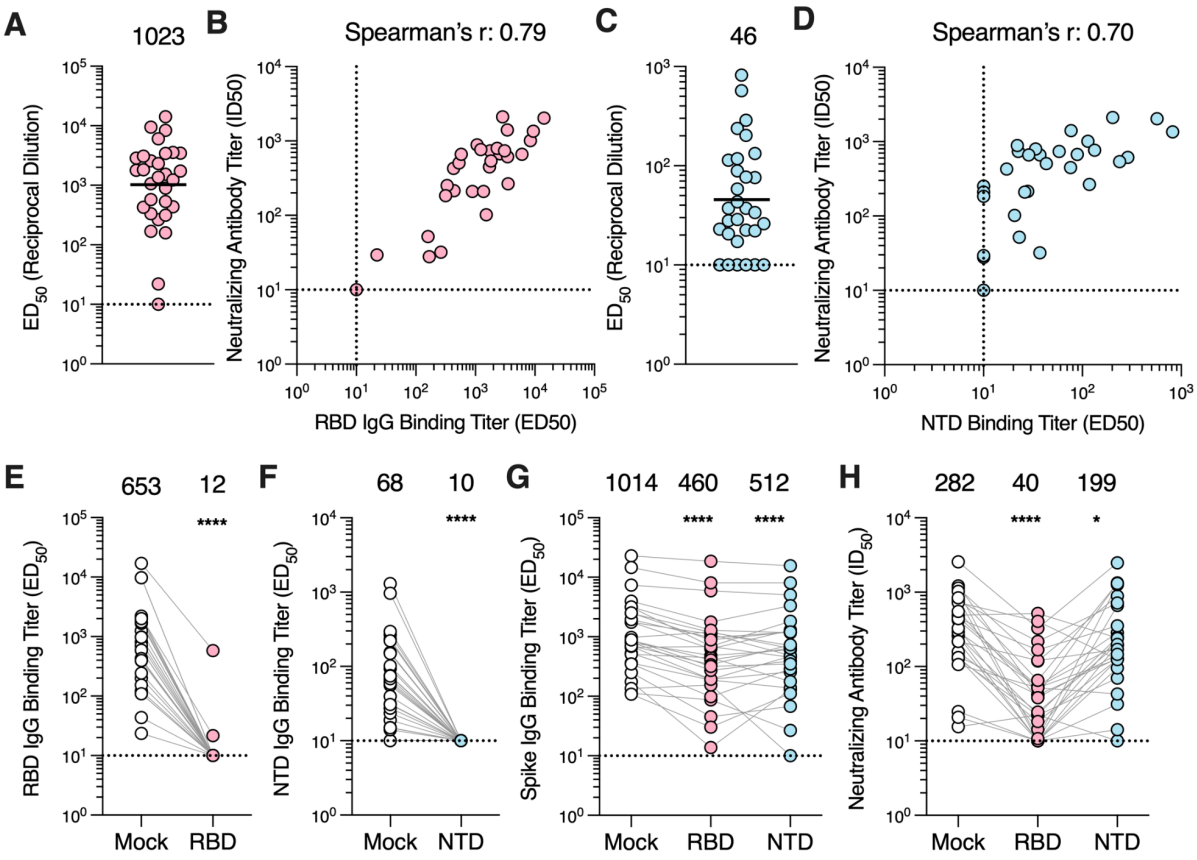

A) IgG binding titers (ED_{50}) against the MERS-CoV EMC/2012 RBD measured for the convalescent plasma samples. One sample was included per individual in the analysis. The GMT is displayed above the plot and indicated by the black bar. The limit of detection (ED_{50}: 10) is represented by the dashed line. The data for one biological replicate are presented and the data are reflective of at least two biological replicates conducted with two distinct batches of RBD protein. **B)** Correlation analysis between RBD IgG binding titers and neutralization potency of the convalescent plasma samples. **C)** IgG binding titers (ED_{50}) against the MERS-CoV EMC/2012 NTD determined for the convalescent plasma samples. One sample per individual was included in the analysis. The GMT is represented by the black bar and presented above the plot. The limit of detection (ED_{50}: 10) of the assay is indicated by the dashed line. Data reflect results obtained from one biological replicate and are representative of data obtained from at least two biological replicates conducted with unique batches of NTD protein. **D)** Correlation analysis between NTD IgG binding titers and neutralizing antibody titers in the convalescent plasma samples. **E)** RBD IgG binding titers for mock- and RBD-depleted plasma samples. **F)** NTD IgG binding titers for mock- and NTD-depleted plasma samples. **G)** Spike IgG binding titers and **H)** neutralizing antibody titers for mock-, RBD-, and NTD-depleted plasma. One sample per individual was included in the analysis. Data presented are from one biological replicate and reflective of two biological replicates completed with unique batches of RBD, NTD, and spike proteins as

well as distinct batches of pseudovirus. GMTs are displayed above the plots and the limit of detection (ED_{50} or ID_{50}: 10) is indicated by the dashed line. Comparisons between RBD or NTD IgG binding titers of the mock- and RBD or NTD-depleted groups, respectively, were made using the Wilcoxon matched-pairs signed. Comparison between the spike IgG bindings titers and neutralizing antibody titers of mock-, RBD- and NTD-depleted groups were made using Dunn's multiple comparison test. *$p<0.05$; ****$p < 0.0001$.

Figure 5.10 RBD and NTD IgG binding curves.

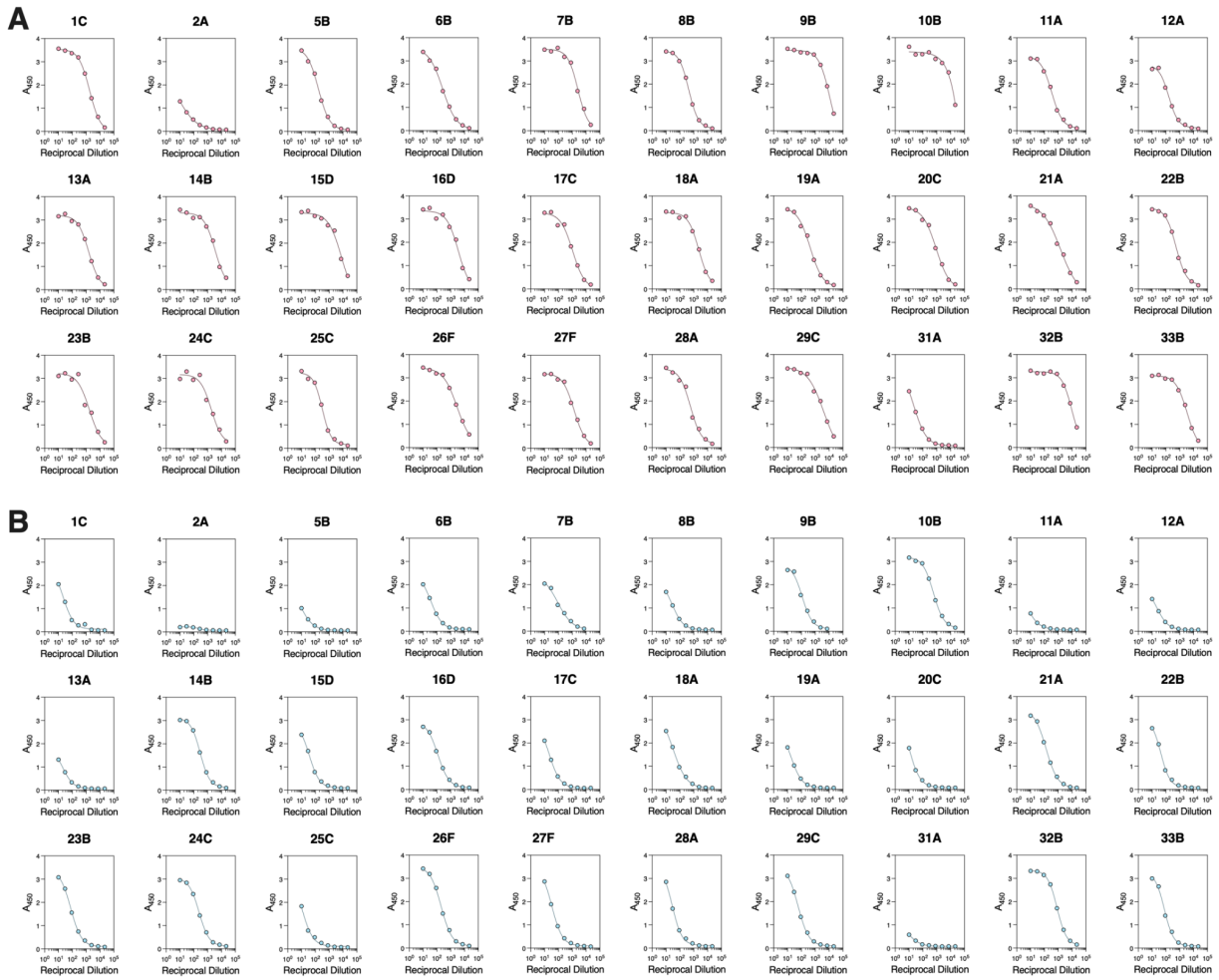

A) RBD and **B)** NTD IgG binding curves for the 30 convalescent plasma samples included in this analysis. Data are presented from one representative biological replicate. At least two biological replicates were conducted using distinct batches of RBD or NTD proteins.

Figure 5.11 IgG binding and neutralization curves following depletion with MERS-CoV RBD and NTD.

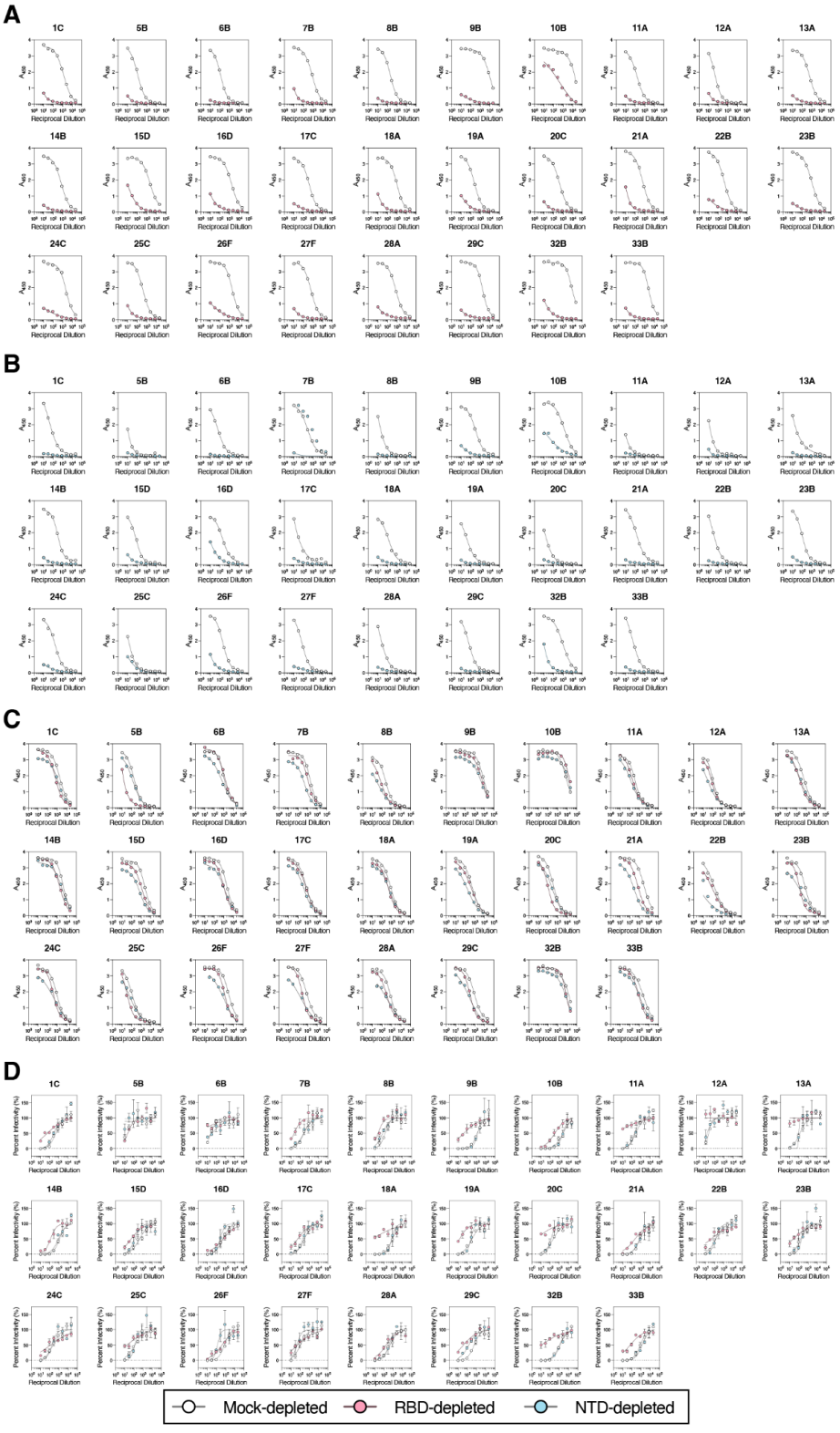

A) RBD IgG binding curves for mock- and RBD-depleted plasma for each of the 28 samples included in the analysis. **B)** NTD IgG binding curves for mock- and NTD-depleted samples. **C)** Spike IgG binding curves and **D)** Neutralization curves for the mock-, RBD-, and NTD-depleted plasma samples analyzed in this study. Neutralization data are presented as mean ± standard error for the two technical replicates conducted. Data presented are from one representative biological replicate. Two independent biological replicates were performed using distinct batches of RBD and NTD proteins for the antibody depletions as well as unique batches of RBD, NTD, and spike proteins and pseudovirus for the ELISAs and neutralization assays, respectively.

Figure 5.12 Convalescent plasma antibodies target S_1 neutralizing epitopes, but rarely S_2 epitopes.

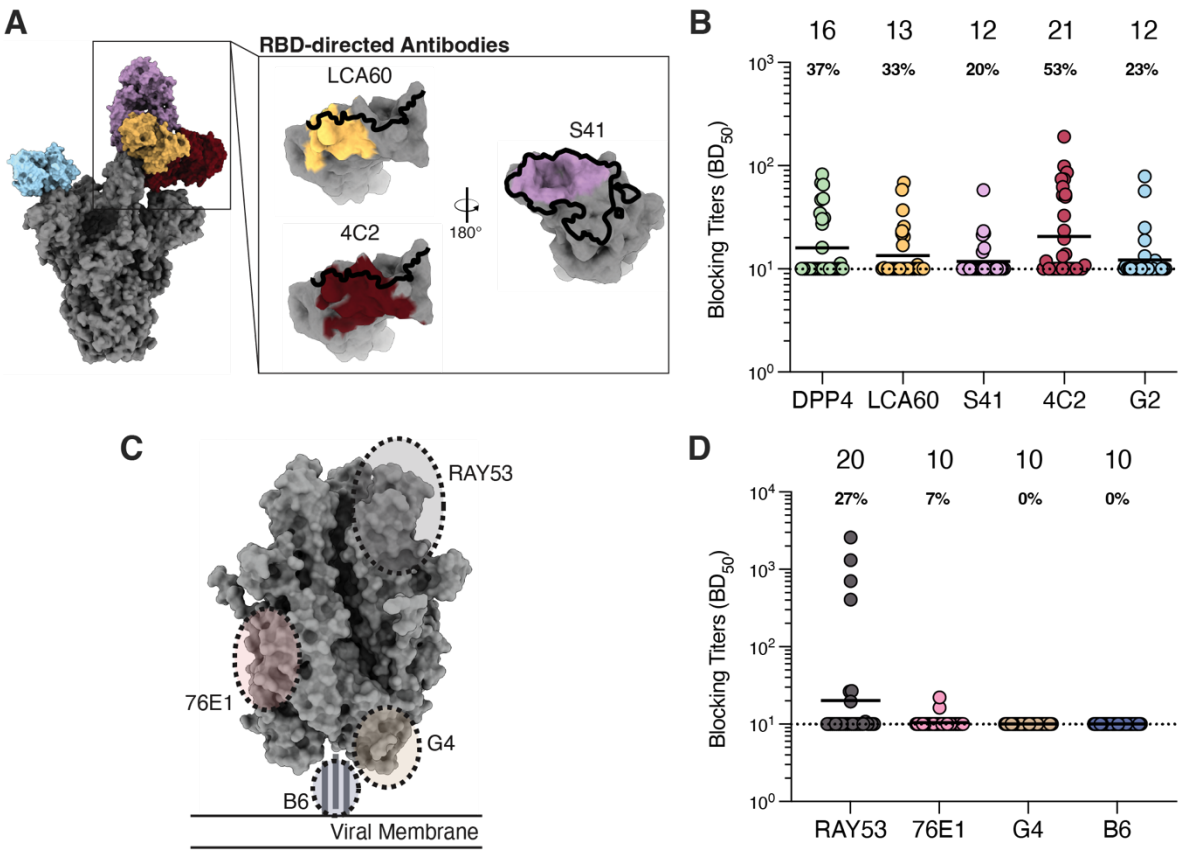

A) Epitopes targeted by S_1-directed antibodies included for the competition ELISAs. The RBM is outlined in black. **B)** Blocking titers (half-maximal blocking dilution [BD_{50}]) measured for convalescent plasma samples against the indicated S_1-directed antibodies. One sample per individual was included in the analysis. GMTs are displayed above the plot and represented by the black bar. The percentage of individuals having blocking titers above the limit of detection (BD_{50} > 10; indicated by the dashed line) is displayed below the GMT for each antibody tested. Data reflect results obtained from one biological replicate and are representative of data obtained from at least two biological replicates conducted with unique batches antibodies and biotinylated spike protein. **C)** Epitopes targeted by S_2-directed antibodies included in the competition ELISAs. **D)** Blocking titers (BD_{50}) in convalescent plasma samples against the specified S_2-directed antibodies. One sample per individual was analyzed. GMTs are displayed above the plot (indicated by black bar) and the portion of individuals exhibiting detectable blocking titers is displayed below the GMT for each antibody. Data presented are from one biological replicate and representative of data collected from at least two biological replicates conducted with distinct batches of antibodies and biotinylated spike protein.

Figure 5.13. Competition ELISA curves.

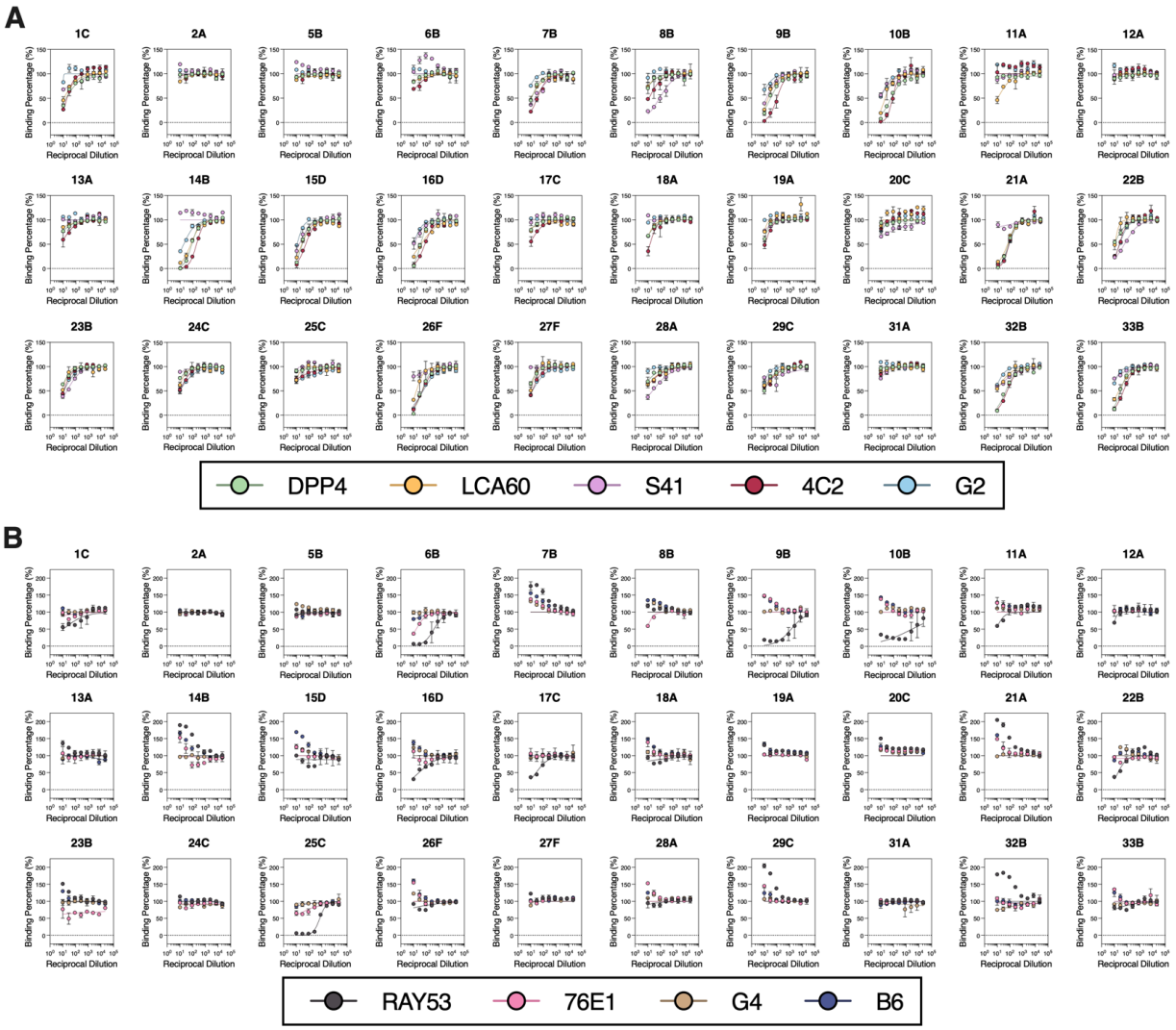

Competition ELISA curves for the 30 plasma samples analyzed against the indicated **A)** S_1- and B) S_2-directed monoclonal antibodies. Data are presented as mean ± standard error for two technical replicates from one representative biological replicate. Two independent biological replicates using unique batches of biotinylated spike protein as well as monoclonal antibodies were performed for each sample.

Table 5.1. Collection timepoints for the convalescent plasma samples analyzed in this study.

Individual	Sample ID	Days post symptom onset or hospitalization
1	1C	23
	1F	45
	1G	51
	1H	58
	1I	65
	1J	73
	1K	79
	1L	86
	1M	93
	1N	100
	Q	120
	1R	191
2	2A	12
5	5A	14
	5B	21
	5C	29
6	6A	6
	6B	12
7	7B	20
	7C	26
8	8B	13
	8C	23
9	9B	18
10	10A	3

	10B	9
	10C	16
	10D	23
	10E	29
11	11A	16
	11B	23
	11C	30
	11D	40
12	12A	NA
13	13A	12
	13B	19
	13C	26
14	14B	15
15	15A	12
	15B	19
	15C	26
	15D	33
16	16A	11
	16B	18
	16C	25
	16D	32
	16E	39
17	17A	5
	17B	12
	17C	19
	17E	33
	17F	40

	17G	47
	17H	54
	17I	61
	17J	68
	17K	74
	17L	82
	17M	89
18	18A	10
19	19A	6
	19B	15
20	20A	12
	20B	17
	20C	24
	20D	31
	20G	52
21	21A	7
22	22A	13
	22B	20
23	23A	7
	23B	14
24	24C	15
	24D	22
25	25B	81
	25C	88
	25F	109
26	26A	7
	26B	14
	26C	21

	26F	42
	26G	49
27	27A	10
	27D	31
	27E	38
	27F	45
28	28A	10
29	29A	10
	29C	24
	29D	31
	29F	45
	29H	59
	29I	66
31	31A	20
32	32A	5
	32B	12
33	33B	26
	33C	33
	33D	40

Table 5.2. Spike protein mutations in MERS-CoV variants used in this study relative to MERS-CoV EMC/2012 (NC_019843.3).

MERS-CoV Variant	Genbank Accession Number	Spike Protein Mutations
United Kingdom/H123990006/2012	NC_038294.1	L506F, Q1020H
Hu/Riyadh-KSA-3181/2015	KT806049.1	L507R, Q1020R
Korea/Seoul/168-1-2015	KT374056.1	H91Y, D510G, Q1020R
Camel/Kenya/M23C14/2019	OK094446.1	V26A, D158Y, H194Y, S390F, L450F, V597A, R626P, A1158S

Chapter 6. Concluding Remarks

From the studies I have presented here, we have learned that the SARS-CoV-2 spike protein, and especially the receptor binding domain of the spike protein, shows incredible plasticity. The receptor binding can both incorporate mutations that alter the structure of the receptor binding motif (Chapter 2) and accumulate numerous mutations at the ACE2 binding interface (Chapter 3 and 4). Despite acquiring these mutations, the spike retains its capacity to bind ACE2 with high affinity and mediate membrane fusion. From these findings, we can expect SARS-CoV-2 to accumulate more mutations in its spike protein that balance immune evasion, ACE2 affinity, and fusogenicity.

As viruses evolve, updated vaccine formulations can help induce a humoral immune response that better targets the circulating viral strains. The COVID-19 vaccines were updated twice to reflect the ongoing emergence of new SARS-CoV-2 variants – first a bivalent vaccine encoding either the Wuhan-Hu-1 and Omicron BA.1 or Wuhan-Hu-1 and Omicron BA.5 spike proteins was introduced and then a monovalent vaccine just encoding the Omicron XBB.1.5 spike protein (Chalkias et al., 2023; Scheaffer et al., 2023). We showed these vaccines do increase neutralizing antibody titers against the Omicron variants as well as increase titers of spike binding antibody titers that can mediate effector functions (Chapter 4). However, both the bivalent vaccine and, as we recently demonstrated (Tortorici et al., 2023), the monovalent XBB.1.5 booster do not generate a humoral response specific to the variant spike protein encoded by these vaccines. Instead, immune imprinting induced by the primary Wuhan-Hu-1 vaccine series limits the development a *de novo* humoral immune response. As progressively more immune evasive variants emerge, I suspect the

central questions surrounding COVID-19 vaccine updates will be: Can we overcome immune imprinting? And do we need to?

Another central question that should be considered is whether we can design a SARS-CoV-2 vaccine antigen that primes the humoral immune response for a continuingly evolving virus better than current vaccine strategies. With rising vaccine hesitancy and low rates of uptake of the XBB.1.5 booster (Larson et al., 2022), shifting to a strategy that induces an immune response that favors breadth of neutralization against historical, current, and future variants rather than potency towards the currently circulating variant may prove beneficial.

The COVID-19 pandemic accelerated science, particularly the immunology, virology, and vaccinology fields. We can apply the lessons we learned from this pandemic to both currently circulating viruses and those viruses that may emerge or re-emerge in the future. Understanding which domains and epitopes on viral glycoproteins contribute to neutralizing activity (Chapter 5) as well as identifying those epitopes that are immutable and targeted by broadly neutralizing antibodies will guide the future vaccine and therapeutic design. Furthermore, we can expect more vaccines to incorporate prefusion stabilizing mutations given the success of the SARS-CoV-2 spike 2P vaccines and the recently licensed RSV prefusion F vaccines (McLellan et al., 2013; Pallesen et al., 2017). Lastly, we can anticipate both monoclonal antibodies and other antivirals will be increasingly used for prophylaxis and therapy.

My scientific career these past few years has been intertwined with the COVID-19 pandemic. In the months prior to starting graduate school, I was testing and implementing SARS-CoV-2 sequencing methods, investigating the function of the

SARS-CoV-2 accessory proteins, and examining immune correlates of protection. The studies I have led and participated in while in graduate school have followed both SARS-CoV-2 vaccines and therapeutics as they were successively approved for use and the viral variants that emerged. It has been a surreal experience seeing my work and findings shape public policy and inform SARS-CoV-2 vaccine design. As I continue with my career, I hope to continue doing science that makes positive impacts.

References

Accorsi, E. K., Britton, A., Fleming-Dutra, K. E., Smith, Z. R., Shang, N., Derado, G., Miller, J., Schrag, S. J., & Verani, J. R. (2022). Association Between 3 Doses of mRNA COVID-19 Vaccine and Symptomatic Infection Caused by the SARS-CoV-2 Omicron and Delta Variants. *JAMA*, *327*(7), 639–651. https://doi.org/10.1001/jama.2022.0470

Addetia, A., Crawford, K. H. D., Dingens, A., Zhu, H., Roychoudhury, P., Huang, M.-L., Jerome, K. R., Bloom, J. D., & Greninger, A. L. (2020). Neutralizing Antibodies Correlate with Protection from SARS-CoV-2 in Humans during a Fishery Vessel Outbreak with a High Attack Rate. *Journal of Clinical Microbiology*, *58*(11), e02107-20, /jcm/58/11/JCM.02107-20.atom. https://doi.org/10.1128/JCM.02107-20

Addetia, A., Park, Y.-J., Starr, T., Greaney, A. J., Sprouse, K. R., Bowen, J. E., Tiles, S. W., Van Voorhis, W. C., Bloom, J. D., Corti, D., Walls, A. C., & Veesler, D. (2023). Structural changes in the SARS-CoV-2 spike E406W mutant escaping a clinical monoclonal antibody cocktail. *Cell Reports*, *42*(6), 112621. https://doi.org/10.1016/j.celrep.2023.112621

Addetia, A., Piccoli, L., Case, J. B., Park, Y.-J., Beltramello, M., Guarino, B., Dang, H., De Melo, G. D., Pinto, D., Sprouse, K., Scheaffer, S. M., Bassi, J., Silacci-Fregni, C., Muoio, F., Dini, M., Vincenzetti, L., Acosta, R., Johnson, D., Subramanian, S., … Veesler, D. (2023). Neutralization, effector function and immune imprinting of Omicron variants. *Nature*, *621*(7979), 592–601. https://doi.org/10.1038/s41586-023-06487-6

Akerman, A., Milogiannakis, V., Jean, T., Esneau, C., Silva, M. R., Ison, T., Fichter, C., Lopez, J. A., Chandra, D., Naing, Z., Caguicla, J., Li, D., Walker, G., Amatayakul-Chantler, S., Roth, N., Manni, S., Hauser, T., Barnes, T., Condylios, A., … Turville, S. G. (2023). Emergence and antibody evasion of BQ, BA.2.75 and SARS-CoV-2 recombinant sub-lineages in the face of maturing antibody breadth at the population level. *eBioMedicine*, *90*, 104545. https://doi.org/10.1016/j.ebiom.2023.104545

Akkaya, M., Kwak, K., & Pierce, S. K. (2020). B cell memory: Building two walls of protection against pathogens. *Nature Reviews Immunology*, *20*(4), 229–238. https://doi.org/10.1038/s41577-019-0244-2

Allan, M., Lièvre, M., Laurenson-Schafer, H., de Barros, S., Jinnai, Y., Andrews, S., Stricker, T., Formigo, J. P., Schultz, C., Perrocheau, A., & Fitzner, J. (2022). The World Health Organization COVID-19 surveillance database. *International Journal for Equity in Health*, *21*(Suppl 3), 167. https://doi.org/10.1186/s12939-022-01767-5

Allen, H., Tessier, E., Turner, C., Anderson, C., Blomquist, P., Simons, D., Løchen, A., Jarvis, C. I., Groves, N., Capelastegui, F., Flannagan, J., Zaidi, A., Chen, C., Rawlinson, C., Hughes, G. J., Chudasama, D., Nash, S., Thelwall, S., Lopez-Bernal, J., … Lamagni, T. (2023). Comparative transmission of SARS-CoV-2 Omicron (B.1.1.529) and Delta (B.1.617.2) variants and the impact of vaccination: National cohort study, England. *Epidemiology and Infection*, *151*, e58. https://doi.org/10.1017/S0950268823000420

Alshukairi, A. N., Zhao, J., Al-Mozaini, M. A., Wang, Y., Dada, A., Baharoon, S. A., Alfaraj, S., Ahmed, W. A., Enani, M. A., Elzein, F. E., Eltayeb, N., Layqah, L., El-Saed, A., Bahaudden, H. A., Haseeb, A., El-Kafrawy, S. A., Hassan, A. M., Siddiq, N. A., Alsharif, I., … Memish, Z. A. (2021). Longevity of Middle East Respiratory Syndrome Coronavirus Antibody Responses in Humans, Saudi Arabia. *Emerging Infectious Diseases*, *27*(5). https://doi.org/10.3201/eid2705.204056

Alshukairi, A. N., Zheng, J., Zhao, J., Nehdi, A., Baharoon, S. A., Layqah, L., Bokhari, A., Al Johani, S. M., Samman, N., Boudjelal, M., Ten Eyck, P., Al-Mozaini, M. A., Zhao, J., Perlman, S., & Alagaili, A. N. (2018). High Prevalence of MERS-CoV Infection in Camel Workers in Saudi Arabia. *mBio*, *9*(5), e01985-18. https://doi.org/10.1128/mBio.01985-18

An integrated national scale SARS-CoV-2 genomic surveillance network. (2020). *The Lancet Microbe*, *1*(3), e99–e100. https://doi.org/10.1016/S2666-5247(20)30054-9

Andrews, N., Stowe, J., Kirsebom, F., Toffa, S., Rickeard, T., Gallagher, E., Gower, C., Kall, M., Groves, N., O'Connell, A.-M., Simons, D., Blomquist, P. B., Zaidi, A., Nash, S., Iwani Binti Abdul Aziz, N., Thelwall, S., Dabrera, G., Myers, R., Amirthalingam, G., … Lopez Bernal, J. (2022). Covid-19 Vaccine Effectiveness against the Omicron (B.1.1.529) Variant. *The New England Journal of Medicine*, *386*(16), 1532–1546. https://doi.org/10.1056/NEJMoa2119451

Arabi, Y. M., Arifi, A. A., Balkhy, H. H., Najm, H., Aldawood, A. S., Ghabashi, A., Hawa, H., Alothman, A., Khaldi, A., & Al Raiy, B. (2014). Clinical Course and Outcomes of Critically Ill Patients With Middle East Respiratory Syndrome Coronavirus Infection. *Annals of Internal Medicine*, *160*(6), 389–397. https://doi.org/10.7326/M13-2486

Arunachalam, P. S., Feng, Y., Ashraf, U., Hu, M., Walls, A. C., Edara, V. V., Zarnitsyna, V. I., Aye, P. P., Golden, N., Miranda, M. C., Green, K. W. M., Threeton, B. M., Maness, N. J., Beddingfield, B. J., Bohm, R. P., Scheuermann, S. E., Goff, K., Dufour, J., Russell-Lodrigue, K., … Pulendran, B. (2022). Durable protection against the SARS-CoV-2 Omicron variant is induced by an adjuvanted subunit vaccine. *Science Translational Medicine*, *14*(658), eabq4130. https://doi.org/10.1126/scitranslmed.abq4130

Arunachalam, P. S., Walls, A. C., Golden, N., Atyeo, C., Fischinger, S., Li, C., Aye, P., Navarro, M. J., Lai, L., Edara, V. V., Röltgen, K., Rogers, K., Shirreff, L., Ferrell, D. E., Wrenn, S., Pettie, D., Kraft, J. C., Miranda, M. C., Kepl, E., … Pulendran, B. (2021). Adjuvanting a subunit COVID-19 vaccine to induce protective immunity. *Nature*, *594*(7862), 253–258. https://doi.org/10.1038/s41586-021-03530-2

Barnes, C. O., Jette, C. A., Abernathy, M. E., Dam, K.-M. A., Esswein, S. R., Gristick, H. B., Malyutin, A. G., Sharaf, N. G., Huey-Tubman, K. E., Lee, Y. E., Robbiani, D. F., Nussenzweig, M. C., West, A. P., & Bjorkman, P. J. (2020). SARS-CoV-2 neutralizing antibody structures inform therapeutic strategies. *Nature*, *588*(7839), 682–687. https://doi.org/10.1038/s41586-020-2852-1

Barouch, D. H. (2022). Covid-19 Vaccines—Immunity, Variants, Boosters. *New England Journal of Medicine*, *387*(11), 1011–1020. https://doi.org/10.1056/NEJMra2206573

Barouch, D. H., Stephenson, K. E., Sadoff, J., Yu, J., Chang, A., Gebre, M., McMahan, K., Liu, J., Chandrashekar, A., Patel, S., Le Gars, M., de Groot, A. M., Heerwegh, D., Struyf, F., Douoguih, M., van Hoof, J., & Schuitemaker, H. (2021). Durable Humoral and Cellular Immune Responses 8 Months after Ad26.COV2.S Vaccination. *The New England Journal of Medicine*, *385*(10), 951–953. https://doi.org/10.1056/NEJMc2108829

Bartsch, Y. C., Tong, X., Kang, J., Avendaño, M. J., Serrano, E. F., García-Salum, T., Pardo-Roa, C., Riquelme, A., Cai, Y., Renzi, I., Stewart-Jones, G., Chen, B., Medina, R. A., & Alter, G. (2022). Omicron variant Spike-specific antibody binding and Fc activity are preserved in recipients of mRNA or inactivated COVID-19 vaccines. *Science Translational Medicine*, *14*(642), eabn9243. https://doi.org/10.1126/scitranslmed.abn9243

Bates, T. A., McBride, S. K., Winders, B., Schoen, D., Trautmann, L., Curlin, M. E., & Tafesse, F. G. (2022). Antibody Response and Variant Cross-Neutralization After SARS-CoV-2 Breakthrough Infection. *JAMA*, *327*(2), 179–181. https://doi.org/10.1001/jama.2021.22898

Baum, A., Fulton, B. O., Wloga, E., Copin, R., Pascal, K. E., Russo, V., Giordano, S., Lanza, K., Negron, N., Ni, M., Wei, Y., Atwal, G. S., Murphy, A. J., Stahl, N., Yancopoulos, G. D., & Kyratsous, C. A. (2020). Antibody cocktail to SARS-CoV-2 spike protein prevents rapid mutational escape seen with individual antibodies. *Science*, *369*(6506), 1014–1018. https://doi.org/10.1126/science.abd0831

Bermingham, A., Chand, M. A., Brown, C. S., Aarons, E., Tong, C., Langrish, C., Hoschler, K., Brown, K., Galiano, M., Myers, R., Pebody, R. G., Green, H. K., Boddington, N. L., Gopal, R., Price, N., Newsholme, W., Drosten, C., Fouchier, R. A., & Zambon, M. (2012). Severe respiratory illness caused by a novel coronavirus, in a patient transferred to the United Kingdom from the Middle East, September 2012. *Eurosurveillance*, *17*(40). https://doi.org/10.2807/ese.17.40.20290-en

Bosch, B. J., Van Der Zee, R., De Haan, C. A. M., & Rottier, P. J. M. (2003). The Coronavirus Spike Protein Is a Class I Virus Fusion Protein: Structural and Functional Characterization of the Fusion Core Complex. *Journal of Virology*, *77*(16), 8801–8811. https://doi.org/10.1128/JVI.77.16.8801-8811.2003

Bournazos, S., Corti, D., Virgin, H. W., & Ravetch, J. V. (2020). Fc-optimized antibodies elicit CD8 immunity to viral respiratory infection. *Nature*, *588*(7838), 485–490. https://doi.org/10.1038/s41586-020-2838-z

Bowen, J. E., Addetia, A., Dang, H. V., Stewart, C., Brown, J. T., Sharkey, W. K., Sprouse, K. R., Walls, A. C., Mazzitelli, I. G., Logue, J. K., Franko, N. M., Czudnochowski, N., Powell, A. E., Dellota, E., Ahmed, K., Ansari, A. S., Cameroni, E., Gori, A., Bandera, A., … Veesler, D. (2022). Omicron spike function and neutralizing activity elicited by a comprehensive panel of vaccines. *Science*, *377*(6608), 890–894. https://doi.org/10.1126/science.abq0203

Bowen, J. E., Park, Y.-J., Stewart, C., Brown, J. T., Sharkey, W. K., Walls, A. C., Joshi, A., Sprouse, K. R., McCallum, M., Tortorici, M. A., Franko, N. M., Logue, J. K., Mazzitelli, I. G., Nguyen, A. W., Silva, R. P., Huang, Y., Low, J. S., Jerak, J., Tiles, S. W., … Veesler, D. (2022). SARS-CoV-2 spike conformation determines

plasma neutralizing activity elicited by a wide panel of human vaccines. *Science Immunology*, eadf1421. https://doi.org/10.1126/sciimmunol.adf1421
Burton, D. R. (2002). Antibodies, viruses and vaccines. *Nature Reviews Immunology*, *2*(9), 706–713. https://doi.org/10.1038/nri891
Burton, D. R. (2023). Antiviral neutralizing antibodies: From in vitro to in vivo activity. *Nature Reviews Immunology*, *23*(11), 720–734. https://doi.org/10.1038/s41577-023-00858-w
Cai, Y., Zhang, J., Xiao, T., Peng, H., Sterling, S. M., Walsh, R. M., Rawson, S., Rits-Volloch, S., & Chen, B. (2020). Distinct conformational states of SARS-CoV-2 spike protein. *Science (New York, N.Y.)*, *369*(6511), 1586–1592. https://doi.org/10.1126/science.abd4251
Cameroni, E., Bowen, J. E., Rosen, L. E., Saliba, C., Zepeda, S. K., Culap, K., Pinto, D., VanBlargan, L. A., De Marco, A., di Iulio, J., Zatta, F., Kaiser, H., Noack, J., Farhat, N., Czudnochowski, N., Havenar-Daughton, C., Sprouse, K. R., Dillen, J. R., Powell, A. E., … Corti, D. (2022). Broadly neutralizing antibodies overcome SARS-CoV-2 Omicron antigenic shift. *Nature*, *602*(7898), 664–670. https://doi.org/10.1038/s41586-021-04386-2
Cao, Y., Jian, F., Wang, J., Yu, Y., Song, W., Yisimayi, A., Wang, J., An, R., Chen, X., Zhang, N., Wang, Y., Wang, P., Zhao, L., Sun, H., Yu, L., Yang, S., Niu, X., Xiao, T., Gu, Q., … Xie, X. S. (2022). Imprinted SARS-CoV-2 humoral immunity induces convergent Omicron RBD evolution. *Nature*. https://doi.org/10.1038/s41586-022-05644-7
Cao, Y., Yisimayi, A., Jian, F., Song, W., Xiao, T., Wang, L., Du, S., Wang, J., Li, Q., Chen, X., Yu, Y., Wang, P., Zhang, Z., Liu, P., An, R., Hao, X., Wang, Y., Wang, J., Feng, R., … Xie, X. S. (2022). BA.2.12.1, BA.4 and BA.5 escape antibodies elicited by Omicron infection. *Nature*, *608*(7923), 593–602. https://doi.org/10.1038/s41586-022-04980-y
Case, J. B., Bailey, A. L., Kim, A. S., Chen, R. E., & Diamond, M. S. (2020). Growth, detection, quantification, and inactivation of SARS-CoV-2. *Virology*, *548*, 39–48. https://doi.org/10.1016/j.virol.2020.05.015
Case, J. B., Mackin, S., Errico, J. M., Chong, Z., Madden, E. A., Whitener, B., Guarino, B., Schmid, M. A., Rosenthal, K., Ren, K., Dang, H. V., Snell, G., Jung, A., Droit, L., Handley, S. A., Halfmann, P. J., Kawaoka, Y., Crowe, J. E., Fremont, D. H., … Diamond, M. S. (2022). Resilience of S309 and AZD7442 monoclonal antibody treatments against infection by SARS-CoV-2 Omicron lineage strains. *Nature Communications*, *13*(1), 3824. https://doi.org/10.1038/s41467-022-31615-7
Cele, S., Jackson, L., Khoury, D. S., Khan, K., Moyo-Gwete, T., Tegally, H., San, J. E., Cromer, D., Scheepers, C., Amoako, D. G., Karim, F., Bernstein, M., Lustig, G., Archary, D., Smith, M., Ganga, Y., Jule, Z., Reedoy, K., Hwa, S.-H., … Sigal, A. (2022). Omicron extensively but incompletely escapes Pfizer BNT162b2 neutralization. *Nature*, *602*(7898), 654–656. https://doi.org/10.1038/s41586-021-04387-1
Chaikeeratisak, V., Nguyen, K., Khanna, K., Brilot, A. F., Erb, M. L., Coker, J. K. C., Vavilina, A., Newton, G. L., Buschauer, R., Pogliano, K., Villa, E., Agard, D. A., & Pogliano, J. (2017). Assembly of a nucleus-like structure during viral replication

in bacteria. *Science*, *355*(6321), 194–197. https://doi.org/10.1126/science.aal2130

Chalkias, S., McGhee, N., Whatley, J. L., Essink, B., Brosz, A., Tomassini, J. E., Girard, B., Wu, K., Edwards, D. K., Nasir, A., Lee, D., Avena, L. E., Feng, J., Deng, W., Montefiori, D. C., Baden, L. R., Miller, J. M., & Das, R. (2023). *Safety and Immunogenicity of XBB.1.5-Containing mRNA Vaccines* [Preprint]. Infectious Diseases (except HIV/AIDS). https://doi.org/10.1101/2023.08.22.23293434

Chen, J., Yang, X., Si, H., Gong, Q., Que, T., Li, J., Li, Y., Wu, C., Zhang, W., Chen, Y., Luo, Y., Zhu, Y., Li, B., Luo, D., Hu, B., Lin, H., Jiang, R., Jiang, T., Li, Q., … Zhou, P. (2023). A bat MERS-like coronavirus circulates in pangolins and utilizes human DPP4 and host proteases for cell entry. *Cell*, *186*(4), 850-863.e16. https://doi.org/10.1016/j.cell.2023.01.019

Chen, S., McMullan, G., Faruqi, A. R., Murshudov, G. N., Short, J. M., Scheres, S. H. W., & Henderson, R. (2013). High-resolution noise substitution to measure overfitting and validate resolution in 3D structure determination by single particle electron cryomicroscopy. *Ultramicroscopy*, *135*, 24–35. https://doi.org/10.1016/j.ultramic.2013.06.004

Cheng, M. M., Reyes, C., Satram, S., Birch, H., Gibbons, D. C., Drysdale, M., Bell, C. F., Suyundikov, A., Ding, X., Maher, M. C., Yeh, W., Telenti, A., & Corey, L. (2023). Real-World Effectiveness of Sotrovimab for the Early Treatment of COVID-19 During SARS-CoV-2 Delta and Omicron Waves in the USA. *Infectious Diseases and Therapy*, *12*(2), 607–621. https://doi.org/10.1007/s40121-022-00755-0

Cheon, S., Park, U., Park, H., Kim, Y., Nguyen, Y. T. H., Aigerim, A., Rhee, J.-Y., Choi, J.-P., Park, W. B., Park, S. W., Kim, Y., Lim, D.-G., Yang, J.-S., Lee, J.-Y., Kim, Y.-S., & Cho, N.-H. (2022). Longevity of seropositivity and neutralizing antibodies in recovered MERS patients: A 5-year follow-up study. *Clinical Microbiology and Infection*, *28*(2), 292–296. https://doi.org/10.1016/j.cmi.2021.06.009

Cho, A., Muecksch, F., Schaefer-Babajew, D., Wang, Z., Finkin, S., Gaebler, C., Ramos, V., Cipolla, M., Mendoza, P., Agudelo, M., Bednarski, E., DaSilva, J., Shimeliovich, I., Dizon, J., Daga, M., Millard, K. G., Turroja, M., Schmidt, F., Zhang, F., … Nussenzweig, M. C. (2021). Anti-SARS-CoV-2 receptor-binding domain antibody evolution after mRNA vaccination. *Nature*, *600*(7889), 517–522. https://doi.org/10.1038/s41586-021-04060-7

Choe, P. G., Perera, R. a. P. M., Park, W. B., Song, K.-H., Bang, J. H., Kim, E. S., Kim, H. B., Ko, L. W. R., Park, S. W., Kim, N.-J., Lau, E. H. Y., Poon, L. L. M., Peiris, M., & Oh, M.-D. (2017). MERS-CoV Antibody Responses 1 Year after Symptom Onset, South Korea, 2015. *Emerging Infectious Diseases*, *23*(7), 1079–1084. https://doi.org/10.3201/eid2307.170310

Cohen, A. A., Gnanapragasam, P. N. P., Lee, Y. E., Hoffman, P. R., Ou, S., Kakutani, L. M., Keeffe, J. R., Wu, H.-J., Howarth, M., West, A. P., Barnes, C. O., Nussenzweig, M. C., & Bjorkman, P. J. (2021). Mosaic nanoparticles elicit cross-reactive immune responses to zoonotic coronaviruses in mice. *Science (New York, N.Y.)*, *371*(6530), 735–741. https://doi.org/10.1126/science.abf6840

Collier, A.-R. Y., Brown, C. M., McMahan, K. A., Yu, J., Liu, J., Jacob-Dolan, C., Chandrashekar, A., Tierney, D., Ansel, J. L., Rowe, M., Sellers, D., Ahmad, K.,

Aguayo, R., Anioke, T., Gardner, S., Siamatu, M., Bermudez-Rivera, L., Hacker, M. R., Madoff, L. C., & Barouch, D. H. (2022). Characterization of immune responses in fully vaccinated individuals after breakthrough infection with the SARS-CoV-2 delta variant. *Science Translational Medicine*, *14*(641), eabn6150. https://doi.org/10.1126/scitranslmed.abn6150

Corbett, K. S., Edwards, D. K., Leist, S. R., Abiona, O. M., Boyoglu-Barnum, S., Gillespie, R. A., Himansu, S., Schäfer, A., Ziwawo, C. T., DiPiazza, A. T., Dinnon, K. H., Elbashir, S. M., Shaw, C. A., Woods, A., Fritch, E. J., Martinez, D. R., Bock, K. W., Minai, M., Nagata, B. M., … Graham, B. S. (2020). SARS-CoV-2 mRNA vaccine design enabled by prototype pathogen preparedness. *Nature*, *586*(7830), 567–571. https://doi.org/10.1038/s41586-020-2622-0

Corbett, K. S., Nason, M. C., Flach, B., Gagne, M., O'Connell, S., Johnston, T. S., Shah, S. N., Edara, V. V., Floyd, K., Lai, L., McDanal, C., Francica, J. R., Flynn, B., Wu, K., Choi, A., Koch, M., Abiona, O. M., Werner, A. P., Moliva, J. I., … Seder, R. A. (2021). Immune correlates of protection by mRNA-1273 vaccine against SARS-CoV-2 in nonhuman primates. *Science (New York, N.Y.)*, *373*(6561), eabj0299. https://doi.org/10.1126/science.abj0299

Corti, D., Purcell, L. A., Snell, G., & Veesler, D. (2021). Tackling COVID-19 with neutralizing monoclonal antibodies. *Cell*, *184*(12), 3086–3108. https://doi.org/10.1016/j.cell.2021.05.005

Corti, D., Voss, J., Gamblin, S. J., Codoni, G., Macagno, A., Jarrossay, D., Vachieri, S. G., Pinna, D., Minola, A., Vanzetta, F., Silacci, C., Fernandez-Rodriguez, B. M., Agatic, G., Bianchi, S., Giacchetto-Sasselli, I., Calder, L., Sallusto, F., Collins, P., Haire, L. F., … Lanzavecchia, A. (2011). A neutralizing antibody selected from plasma cells that binds to group 1 and group 2 influenza A hemagglutinins. *Science (New York, N.Y.)*, *333*(6044), 850–856. https://doi.org/10.1126/science.1205669

Corti, D., Zhao, J., Pedotti, M., Simonelli, L., Agnihothram, S., Fett, C., Fernandez-Rodriguez, B., Foglierini, M., Agatic, G., Vanzetta, F., Gopal, R., Langrish, C. J., Barrett, N. A., Sallusto, F., Baric, R. S., Varani, L., Zambon, M., Perlman, S., & Lanzavecchia, A. (2015). Prophylactic and postexposure efficacy of a potent human monoclonal antibody against MERS coronavirus. *Proceedings of the National Academy of Sciences*, *112*(33), 10473–10478. https://doi.org/10.1073/pnas.1510199112

Crawford, K. H. D., Eguia, R., Dingens, A. S., Loes, A. N., Malone, K. D., Wolf, C. R., Chu, H. Y., Tortorici, M. A., Veesler, D., Murphy, M., Pettie, D., King, N. P., Balazs, A. B., & Bloom, J. D. (2020). Protocol and Reagents for Pseudotyping Lentiviral Particles with SARS-CoV-2 Spike Protein for Neutralization Assays. *Viruses*, *12*(5), 513. https://doi.org/10.3390/v12050513

Cyster, J. G., & Allen, C. D. C. (2019). B Cell Responses: Cell Interaction Dynamics and Decisions. *Cell*, *177*(3), 524–540. https://doi.org/10.1016/j.cell.2019.03.016

Dan, J. M., Mateus, J., Kato, Y., Hastie, K. M., Yu, E. D., Faliti, C. E., Grifoni, A., Ramirez, S. I., Haupt, S., Frazier, A., Nakao, C., Rayaprolu, V., Rawlings, S. A., Peters, B., Krammer, F., Simon, V., Saphire, E. O., Smith, D. M., Weiskopf, D., … Crotty, S. (2021). Immunological memory to SARS-CoV-2 assessed for up to

8 months after infection. *Science (New York, N.Y.)*, *371*(6529), eabf4063. https://doi.org/10.1126/science.abf4063

Davies, N. G., Abbott, S., Barnard, R. C., Jarvis, C. I., Kucharski, A. J., Munday, J. D., Pearson, C. A. B., Russell, T. W., Tully, D. C., Washburne, A. D., Wenseleers, T., Gimma, A., Waites, W., Wong, K. L. M., Van Zandvoort, K., Silverman, J. D., CMMID COVID-19 Working Group, COVID-19 Genomics UK (COG-UK) Consortium, Diaz-Ordaz, K., … Edmunds, W. J. (2021). Estimated transmissibility and impact of SARS-CoV-2 lineage B.1.1.7 in England. *Science*, *372*(6538), eabg3055. https://doi.org/10.1126/science.abg3055

de Melo, G. D., Lazarini, F., Levallois, S., Hautefort, C., Michel, V., Larrous, F., Verillaud, B., Aparicio, C., Wagner, S., Gheusi, G., Kergoat, L., Kornobis, E., Donati, F., Cokelaer, T., Hervochon, R., Madec, Y., Roze, E., Salmon, D., Bourhy, H., … Lledo, P.-M. (2021). COVID-19-related anosmia is associated with viral persistence and inflammation in human olfactory epithelium and brain infection in hamsters. *Science Translational Medicine*, *13*(596), eabf8396. https://doi.org/10.1126/scitranslmed.abf8396

Dejnirattisai, W., Huo, J., Zhou, D., Zahradník, J., Supasa, P., Liu, C., Duyvesteyn, H. M. E., Ginn, H. M., Mentzer, A. J., Tuekprakhon, A., Nutalai, R., Wang, B., Dijokaite, A., Khan, S., Avinoam, O., Bahar, M., Skelly, D., Adele, S., Johnson, S. A., … Young, P. (2022). SARS-CoV-2 Omicron-B.1.1.529 leads to widespread escape from neutralizing antibody responses. *Cell*, *185*(3), 467-484.e15. https://doi.org/10.1016/j.cell.2021.12.046

Deng, X., Garcia-Knight, M. A., Khalid, M. M., Servellita, V., Wang, C., Morris, M. K., Sotomayor-González, A., Glasner, D. R., Reyes, K. R., Gliwa, A. S., Reddy, N. P., Sanchez San Martin, C., Federman, S., Cheng, J., Balcerek, J., Taylor, J., Streithorst, J. A., Miller, S., Sreekumar, B., … Chiu, C. Y. (2021). Transmission, infectivity, and neutralization of a spike L452R SARS-CoV-2 variant. *Cell*, *184*(13), 3426-3437.e8. https://doi.org/10.1016/j.cell.2021.04.025

Devoto, A. E., Santini, J. M., Olm, M. R., Anantharaman, K., Munk, P., Tung, J., Archie, E. A., Turnbaugh, P. J., Seed, K. D., Blekhman, R., Aarestrup, F. M., Thomas, B. C., & Banfield, J. F. (2019). Megaphages infect Prevotella and variants are widespread in gut microbiomes. *Nature Microbiology*, *4*(4), 693–700. https://doi.org/10.1038/s41564-018-0338-9

Dong, J., Zost, S. J., Greaney, A. J., Starr, T. N., Dingens, A. S., Chen, E. C., Chen, R. E., Case, J. B., Sutton, R. E., Gilchuk, P., Rodriguez, J., Armstrong, E., Gainza, C., Nargi, R. S., Binshtein, E., Xie, X., Zhang, X., Shi, P.-Y., Logue, J., … Crowe, J. E. (2021). Genetic and structural basis for SARS-CoV-2 variant neutralization by a two-antibody cocktail. *Nature Microbiology*, *6*(10), 1233–1244. https://doi.org/10.1038/s41564-021-00972-2

Driouich, J.-S., Bernadin, O., Touret, F., de Lamballerie, X., & Nougairède, A. (2023). Activity of Sotrovimab against BQ.1.1 and XBB.1 Omicron sublineages in a hamster model. *Antiviral Research*, *215*, 105638. https://doi.org/10.1016/j.antiviral.2023.105638

Drosten, C., Günther, S., Preiser, W., Van Der Werf, S., Brodt, H.-R., Becker, S., Rabenau, H., Panning, M., Kolesnikova, L., Fouchier, R. A. M., Berger, A., Burguière, A.-M., Cinatl, J., Eickmann, M., Escriou, N., Grywna, K., Kramme, S.,

Manuguerra, J.-C., Müller, S., … Doerr, H. W. (2003). Identification of a Novel Coronavirus in Patients with Severe Acute Respiratory Syndrome. *New England Journal of Medicine*, *348*(20), 1967–1976. https://doi.org/10.1056/NEJMoa030747

Dudas, G., Carvalho, L. M., Rambaut, A., & Bedford, T. (2018). MERS-CoV spillover at the camel-human interface. *eLife*, *7*, e31257. https://doi.org/10.7554/eLife.31257

Earnest, J. T., Hantak, M. P., Li, K., McCray, P. B., Perlman, S., & Gallagher, T. (2017). The tetraspanin CD9 facilitates MERS-coronavirus entry by scaffolding host cell receptors and proteases. *PLOS Pathogens*, *13*(7), e1006546. https://doi.org/10.1371/journal.ppat.1006546

Ebrahim, S. H., Maher, A. D., Kanagasabai, U., Alfaraj, S. H., Alzahrani, N. A., Alqahtani, S. A., Assiri, A. M., & Memish, Z. A. (2021). MERS-CoV Confirmation among 6,873 suspected persons and relevant Epidemiologic and Clinical Features, Saudi Arabia—2014 to 2019. *eClinicalMedicine*, *41*, 101191. https://doi.org/10.1016/j.eclinm.2021.101191

Edara, V.-V., Pinsky, B. A., Suthar, M. S., Lai, L., Davis-Gardner, M. E., Floyd, K., Flowers, M. W., Wrammert, J., Hussaini, L., Ciric, C. R., Bechnak, S., Stephens, K., Graham, B. S., Bayat Mokhtari, E., Mudvari, P., Boritz, E., Creanga, A., Pegu, A., Derrien-Colemyn, A., … Fabrizio, T. P. (2021). Infection and Vaccine-Induced Neutralizing-Antibody Responses to the SARS-CoV-2 B.1.617 Variants. *New England Journal of Medicine*, *385*(7), 664–666. https://doi.org/10.1056/NEJMc2107799

Emsley, P., Lohkamp, B., Scott, W. G., & Cowtan, K. (2010). Features and development of Coot. *Acta Crystallographica. Section D, Biological Crystallography*, *66*(Pt 4), 486–501. https://doi.org/10.1107/S0907444910007493

Faria, N. R., Mellan, T. A., Whittaker, C., Claro, I. M., Candido, D. D. S., Mishra, S., Crispim, M. A. E., Sales, F. C. S., Hawryluk, I., McCrone, J. T., Hulswit, R. J. G., Franco, L. A. M., Ramundo, M. S., De Jesus, J. G., Andrade, P. S., Coletti, T. M., Ferreira, G. M., Silva, C. A. M., Manuli, E. R., … Sabino, E. C. (2021). Genomics and epidemiology of the P.1 SARS-CoV-2 lineage in Manaus, Brazil. *Science*, *372*(6544), 815–821. https://doi.org/10.1126/science.abh2644

Feng, S., Phillips, D. J., White, T., Sayal, H., Aley, P. K., Bibi, S., Dold, C., Fuskova, M., Gilbert, S. C., Hirsch, I., Humphries, H. E., Jepson, B., Kelly, E. J., Plested, E., Shoemaker, K., Thomas, K. M., Vekemans, J., Villafana, T. L., Lambe, T., … Oxford COVID Vaccine Trial Group. (2021). Correlates of protection against symptomatic and asymptomatic SARS-CoV-2 infection. *Nature Medicine*, *27*(11), 2032–2040. https://doi.org/10.1038/s41591-021-01540-1

Folegatti, P. M., Bittaye, M., Flaxman, A., Lopez, F. R., Bellamy, D., Kupke, A., Mair, C., Makinson, R., Sheridan, J., Rohde, C., Halwe, S., Jeong, Y., Park, Y.-S., Kim, J.-O., Song, M., Boyd, A., Tran, N., Silman, D., Poulton, I., … Gilbert, S. (2020). Safety and immunogenicity of a candidate Middle East respiratory syndrome coronavirus viral-vectored vaccine: A dose-escalation, open-label, non-randomised, uncontrolled, phase 1 trial. *The Lancet. Infectious Diseases*, *20*(7), 816–826. https://doi.org/10.1016/S1473-3099(20)30160-2

Fong, Y., McDermott, A. B., Benkeser, D., Roels, S., Stieh, D. J., Vandebosch, A., Le Gars, M., Van Roey, G. A., Houchens, C. R., Martins, K., Jayashankar, L.,

Castellino, F., Amoa-Awua, O., Basappa, M., Flach, B., Lin, B. C., Moore, C., Naisan, M., Naqvi, M., … and the United States Government (USG)/CoVPN Biostatistics Team. (2022). Immune correlates analysis of the ENSEMBLE single Ad26.COV2.S dose vaccine efficacy clinical trial. *Nature Microbiology*, *7*(12), 1996–2010. https://doi.org/10.1038/s41564-022-01262-1

Frenz, B., Rämisch, S., Borst, A. J., Walls, A. C., Adolf-Bryfogle, J., Schief, W. R., Veesler, D., & DiMaio, F. (2019). Automatically Fixing Errors in Glycoprotein Structures with Rosetta. *Structure*, *27*(1), 134-139.e3. https://doi.org/10.1016/j.str.2018.09.006

Gagne, M., Moliva, J. I., Foulds, K. E., Andrew, S. F., Flynn, B. J., Werner, A. P., Wagner, D. A., Teng, I.-T., Lin, B. C., Moore, C., Jean-Baptiste, N., Carroll, R., Foster, S. L., Patel, M., Ellis, M., Edara, V.-V., Maldonado, N. V., Minai, M., McCormick, L., … Seder, R. A. (2022). mRNA-1273 or mRNA-Omicron boost in vaccinated macaques elicits similar B cell expansion, neutralizing responses, and protection from Omicron. *Cell*, *185*(9), 1556-1571.e18. https://doi.org/10.1016/j.cell.2022.03.038

Garcia-Beltran, W. F., St Denis, K. J., Hoelzemer, A., Lam, E. C., Nitido, A. D., Sheehan, M. L., Berrios, C., Ofoman, O., Chang, C. C., Hauser, B. M., Feldman, J., Roederer, A. L., Gregory, D. J., Poznansky, M. C., Schmidt, A. G., Iafrate, A. J., Naranbhai, V., & Balazs, A. B. (2022). mRNA-based COVID-19 vaccine boosters induce neutralizing immunity against SARS-CoV-2 Omicron variant. *Cell*, *185*(3), 457-466.e4. https://doi.org/10.1016/j.cell.2021.12.033

Gilbert, P. B., Montefiori, D. C., McDermott, A. B., Fong, Y., Benkeser, D., Deng, W., Zhou, H., Houchens, C. R., Martins, K., Jayashankar, L., Castellino, F., Flach, B., Lin, B. C., O'Connell, S., McDanal, C., Eaton, A., Sarzotti-Kelsoe, M., Lu, Y., Yu, C., … United States Government (USG)/CoVPN Biostatistics Team§. (2022). Immune correlates analysis of the mRNA-1273 COVID-19 vaccine efficacy clinical trial. *Science (New York, N.Y.)*, *375*(6576), 43–50. https://doi.org/10.1126/science.abm3425

Goel, R. R., Painter, M. M., Lundgreen, K. A., Apostolidis, S. A., Baxter, A. E., Giles, J. R., Mathew, D., Pattekar, A., Reynaldi, A., Khoury, D. S., Gouma, S., Hicks, P., Dysinger, S., Hicks, A., Sharma, H., Herring, S., Korte, S., Kc, W., Oldridge, D. A., … Wherry, E. J. (2022). Efficient recall of Omicron-reactive B cell memory after a third dose of SARS-CoV-2 mRNA vaccine. *Cell*, *185*(11), 1875-1887.e8. https://doi.org/10.1016/j.cell.2022.04.009

Greaney, A. J., Eguia, R. T., Starr, T. N., Khan, K., Franko, N., Logue, J. K., Lord, S. M., Speake, C., Chu, H. Y., Sigal, A., & Bloom, J. D. (2022). The SARS-CoV-2 Delta variant induces an antibody response largely focused on class 1 and 2 antibody epitopes. *PLOS Pathogens*, *18*(6), e1010592. https://doi.org/10.1371/journal.ppat.1010592

Greaney, A. J., Loes, A. N., Crawford, K. H. D., Starr, T. N., Malone, K. D., Chu, H. Y., & Bloom, J. D. (2021). Comprehensive mapping of mutations in the SARS-CoV-2 receptor-binding domain that affect recognition by polyclonal human plasma antibodies. *Cell Host & Microbe*, *29*(3), 463-476.e6. https://doi.org/10.1016/j.chom.2021.02.003

Greaney, A. J., Loes, A. N., Gentles, L. E., Crawford, K. H. D., Starr, T. N., Malone, K. D., Chu, H. Y., & Bloom, J. D. (2021). Antibodies elicited by mRNA-1273 vaccination bind more broadly to the receptor binding domain than do those from SARS-CoV-2 infection. *Science Translational Medicine*, *13*(600), eabi9915. https://doi.org/10.1126/scitranslmed.abi9915

Greaney, A. J., Starr, T. N., Eguia, R. T., Loes, A. N., Khan, K., Karim, F., Cele, S., Bowen, J. E., Logue, J. K., Corti, D., Veesler, D., Chu, H. Y., Sigal, A., & Bloom, J. D. (2022). A SARS-CoV-2 variant elicits an antibody response with a shifted immunodominance hierarchy. *PLOS Pathogens*, *18*(2), e1010248. https://doi.org/10.1371/journal.ppat.1010248

Gregory, D. A., Trujillo, M., Rushford, C., Flury, A., Kannoly, S., San, K. M., Lyfoung, D. T., Wiseman, R. W., Bromert, K., Zhou, M.-Y., Kesler, E., Bivens, N. J., Hoskins, J., Lin, C.-H., O'Connor, D. H., Wieberg, C., Wenzel, J., Kantor, R. S., Dennehy, J. J., & Johnson, M. C. (2022). Genetic diversity and evolutionary convergence of cryptic SARS- CoV-2 lineages detected via wastewater sequencing. *PLOS Pathogens*, *18*(10), e1010636. https://doi.org/10.1371/journal.ppat.1010636

Grubaugh, N. D., Hodcroft, E. B., Fauver, J. R., Phelan, A. L., & Cevik, M. (2021). Public health actions to control new SARS-CoV-2 variants. *Cell*, *184*(5), 1127–1132. https://doi.org/10.1016/j.cell.2021.01.044

Halfmann, P. J., Frey, S. J., Loeffler, K., Kuroda, M., Maemura, T., Armbrust, T., Yang, J. E., Hou, Y. J., Baric, R., Wright, E. R., Kawaoka, Y., & Kane, R. S. (2022). Multivalent S2-based vaccines provide broad protection against SARS-CoV-2 variants of concern and pangolin coronaviruses. *eBioMedicine*, *86*, 104341. https://doi.org/10.1016/j.ebiom.2022.104341

Hansen, J., Baum, A., Pascal, K. E., Russo, V., Giordano, S., Wloga, E., Fulton, B. O., Yan, Y., Koon, K., Patel, K., Chung, K. M., Hermann, A., Ullman, E., Cruz, J., Rafique, A., Huang, T., Fairhurst, J., Libertiny, C., Malbec, M., … Kyratsous, C. A. (2020). Studies in humanized mice and convalescent humans yield a SARS-CoV-2 antibody cocktail. *Science*, *369*(6506), 1010–1014. https://doi.org/10.1126/science.abd0827

Harman, K., Nash, S. G., Webster, H. H., Groves, N., Hardstaff, J., Bridgen, J., Blomquist, P. B., Hope, R., Ashano, E., Myers, R., Rokadiya, S., Hopkins, S., Brown, C. S., Chand, M., Dabrera, G., & Thelwall, S. (2023). Comparison of the risk of hospitalisation among BA.1 and BA.2 COVID-19 cases treated with sotrovimab in the community in England. *Influenza and Other Respiratory Viruses*, *17*(5), e13150. https://doi.org/10.1111/irv.13150

Hassan, A. O., Feldmann, F., Zhao, H., Curiel, D. T., Okumura, A., Tang-Huau, T.-L., Case, J. B., Meade-White, K., Callison, J., Chen, R. E., Lovaglio, J., Hanley, P. W., Scott, D. P., Fremont, D. H., Feldmann, H., & Diamond, M. S. (2021). A single intranasal dose of chimpanzee adenovirus-vectored vaccine protects against SARS-CoV-2 infection in rhesus macaques. *Cell Reports. Medicine*, *2*(4), 100230. https://doi.org/10.1016/j.xcrm.2021.100230

Hawman, D. W., Meade-White, K., Clancy, C., Archer, J., Hinkley, T., Leventhal, S. S., Rao, D., Stamper, A., Lewis, M., Rosenke, R., Krieger, K., Randall, S., Khandhar, A. P., Hao, L., Hsiang, T.-Y., Greninger, A. L., Gale, M., Berglund, P., Fuller, D. H., … Erasmus, J. H. (2022). Replicating RNA platform enables rapid response

to the SARS-CoV-2 Omicron variant and elicits enhanced protection in naïve hamsters compared to ancestral vaccine. *eBioMedicine*, *83*, 104196. https://doi.org/10.1016/j.ebiom.2022.104196

Hérate, C., Marlin, R., Touret, F., Dereuddre-Bosquet, N., Donati, F., Relouzat, F., Junges, L., Galhaut, M., Dehan, O., Sconosciuti, Q., Nougairède, A., De Lamballerie, X., Van Der Werf, S., & Le Grand, R. (2023). Sotrovimab retains activity against SARS-CoV-2 omicron variant BQ.1.1 in a non-human primate model. *Heliyon*, *9*(6), e16664. https://doi.org/10.1016/j.heliyon.2023.e16664

Hodcroft, E. B., Zuber, M., Nadeau, S., Vaughan, T. G., Crawford, K. H. D., Althaus, C. L., Reichmuth, M. L., Bowen, J. E., Walls, A. C., Corti, D., Bloom, J. D., Veesler, D., Mateo, D., Hernando, A., Comas, I., González-Candelas, F., SeqCOVID-SPAIN consortium, Stadler, T., & Neher, R. A. (2021). Spread of a SARS-CoV-2 variant through Europe in the summer of 2020. *Nature*, *595*(7869), 707–712. https://doi.org/10.1038/s41586-021-03677-y

Hoffman, W., Lakkis, F. G., & Chalasani, G. (2016). B Cells, Antibodies, and More. *Clinical Journal of the American Society of Nephrology: CJASN*, *11*(1), 137–154. https://doi.org/10.2215/CJN.09430915

Hoffmann, M., Kleine-Weber, H., & Pöhlmann, S. (2020). A Multibasic Cleavage Site in the Spike Protein of SARS-CoV-2 Is Essential for Infection of Human Lung Cells. *Molecular Cell*, *78*(4), 779-784.e5. https://doi.org/10.1016/j.molcel.2020.04.022

Hoffmann, M., Kleine-Weber, H., Schroeder, S., Krüger, N., Herrler, T., Erichsen, S., Schiergens, T. S., Herrler, G., Wu, N.-H., Nitsche, A., Müller, M. A., Drosten, C., & Pöhlmann, S. (2020). SARS-CoV-2 Cell Entry Depends on ACE2 and TMPRSS2 and Is Blocked by a Clinically Proven Protease Inhibitor. *Cell*, *181*(2), 271-280.e8. https://doi.org/10.1016/j.cell.2020.02.052

Hong, Q., Han, W., Li, J., Xu, S., Wang, Y., Xu, C., Li, Z., Wang, Y., Zhang, C., Huang, Z., & Cong, Y. (2022). Molecular basis of receptor binding and antibody neutralization of Omicron. *Nature*, *604*(7906), 546–552. https://doi.org/10.1038/s41586-022-04581-9

Hsieh, C.-L., Goldsmith, J. A., Schaub, J. M., DiVenere, A. M., Kuo, H.-C., Javanmardi, K., Le, K. C., Wrapp, D., Lee, A. G., Liu, Y., Chou, C.-W., Byrne, P. O., Hjorth, C. K., Johnson, N. V., Ludes-Meyers, J., Nguyen, A. W., Park, J., Wang, N., Amengor, D., … McLellan, J. S. (2020). Structure-based design of prefusion-stabilized SARS-CoV-2 spikes. *Science*, *369*(6510), 1501–1505. https://doi.org/10.1126/science.abd0826

Hsieh, C.-L., Werner, A. P., Leist, S. R., Stevens, L. J., Falconer, E., Goldsmith, J. A., Chou, C.-W., Abiona, O. M., West, A., Westendorf, K., Muthuraman, K., Fritch, E. J., Dinnon, K. H., Schäfer, A., Denison, M. R., Chappell, J. D., Baric, R. S., Graham, B. S., Corbett, K. S., & McLellan, J. S. (2021). Stabilized coronavirus spike stem elicits a broadly protective antibody. *Cell Reports*, *37*(5), 109929. https://doi.org/10.1016/j.celrep.2021.109929

Huang, A. T., Garcia-Carreras, B., Hitchings, M. D. T., Yang, B., Katzelnick, L. C., Rattigan, S. M., Borgert, B. A., Moreno, C. A., Solomon, B. D., Trimmer-Smith, L., Etienne, V., Rodriguez-Barraquer, I., Lessler, J., Salje, H., Burke, D. S., Wesolowski, A., & Cummings, D. A. T. (2020). A systematic review of antibody mediated immunity to coronaviruses: Kinetics, correlates of protection, and

association with severity. *Nature Communications*, *11*(1), 4704. https://doi.org/10.1038/s41467-020-18450-4

Jang, T.-H., Park, W.-J., Lee, H., Woo, H.-M., Lee, S.-Y., Kim, K.-C., Kim, S. S., Hong, E., Song, J., & Lee, J.-Y. (2022). The structure of a novel antibody against the spike protein inhibits Middle East respiratory syndrome coronavirus infections. *Scientific Reports*, *12*(1), 1260. https://doi.org/10.1038/s41598-022-05318-4

Jette, C. A., Cohen, A. A., Gnanapragasam, P. N. P., Muecksch, F., Lee, Y. E., Huey-Tubman, K. E., Schmidt, F., Hatziioannou, T., Bieniasz, P. D., Nussenzweig, M. C., West, A. P., Keeffe, J. R., Bjorkman, P. J., & Barnes, C. O. (2021). Broad cross-reactivity across sarbecoviruses exhibited by a subset of COVID-19 donor-derived neutralizing antibodies. *Cell Reports*, *37*(12), 110188. https://doi.org/10.1016/j.celrep.2021.110188

Jiang, L., Wang, N., Zuo, T., Shi, X., Poon, K.-M. V., Wu, Y., Gao, F., Li, D., Wang, R., Guo, J., Fu, L., Yuen, K.-Y., Zheng, B.-J., Wang, X., & Zhang, L. (2014). Potent Neutralization of MERS-CoV by Human Neutralizing Monoclonal Antibodies to the Viral Spike Glycoprotein. *Science Translational Medicine*, *6*(234). https://doi.org/10.1126/scitranslmed.3008140

Khoury, D. S., Cromer, D., Reynaldi, A., Schlub, T. E., Wheatley, A. K., Juno, J. A., Subbarao, K., Kent, S. J., Triccas, J. A., & Davenport, M. P. (2021). Neutralizing antibody levels are highly predictive of immune protection from symptomatic SARS-CoV-2 infection. *Nature Medicine*, *27*(7), 1205–1211. https://doi.org/10.1038/s41591-021-01377-8

Kim, Y., Cheon, S., Min, C.-K., Sohn, K. M., Kang, Y. J., Cha, Y.-J., Kang, J.-I., Han, S. K., Ha, N.-Y., Kim, G., Aigerim, A., Shin, H. M., Choi, M.-S., Kim, S., Cho, H.-S., Kim, Y.-S., & Cho, N.-H. (2016). Spread of Mutant Middle East Respiratory Syndrome Coronavirus with Reduced Affinity to Human CD26 during the South Korean Outbreak. *mBio*, *7*(2), e00019-16. https://doi.org/10.1128/mBio.00019-16

Kleine-Weber, H., Elzayat, M. T., Wang, L., Graham, B. S., Müller, M. A., Drosten, C., Pöhlmann, S., & Hoffmann, M. (2019). Mutations in the Spike Protein of Middle East Respiratory Syndrome Coronavirus Transmitted in Korea Increase Resistance to Antibody-Mediated Neutralization. *Journal of Virology*, *93*(2), e01381-18. https://doi.org/10.1128/JVI.01381-18

Knipe, D. M., & Howley, P. M. (2013). *Fields virology* (6th ed). Wolters Kluwer health - Lippincott Williams & Wilkins.

Koch, T., Dahlke, C., Fathi, A., Kupke, A., Krähling, V., Okba, N. M. A., Halwe, S., Rohde, C., Eickmann, M., Volz, A., Hesterkamp, T., Jambrecina, A., Borregaard, S., Ly, M. L., Zinser, M. E., Bartels, E., Poetsch, J. S. H., Neumann, R., Fux, R., … Addo, M. M. (2020). Safety and immunogenicity of a modified vaccinia virus Ankara vector vaccine candidate for Middle East respiratory syndrome: An open-label, phase 1 trial. *The Lancet. Infectious Diseases*, *20*(7), 827–838. https://doi.org/10.1016/S1473-3099(20)30248-6

Kodaka, M., Yang, Z., Nakagawa, K., Maruyama, J., Xu, X., Sarkar, A., Ichimura, A., Nasu, Y., Ozawa, T., Iwasa, H., Ishigami-Yuasa, M., Ito, S., Kagechika, H., & Hata, Y. (2015). A new cell-based assay to evaluate myogenesis in mouse myoblast C2C12 cells. *Experimental Cell Research*, *336*(2), 171–181. https://doi.org/10.1016/j.yexcr.2015.06.015

Kontermann, R. E. (2011). Strategies for extended serum half-life of protein therapeutics. *Current Opinion in Biotechnology*, *22*(6), 868–876. https://doi.org/10.1016/j.copbio.2011.06.012

Kumar, B. V., Connors, T. J., & Farber, D. L. (2018). Human T Cell Development, Localization, and Function throughout Life. *Immunity*, *48*(2), 202–213. https://doi.org/10.1016/j.immuni.2018.01.007

Laffleur, B., Pascal, V., Sirac, C., & Cogné, M. (2012). Production of human or humanized antibodies in mice. *Methods in Molecular Biology (Clifton, N.J.)*, *901*, 149–159. https://doi.org/10.1007/978-1-61779-931-0_9

Lan, J., Ge, J., Yu, J., Shan, S., Zhou, H., Fan, S., Zhang, Q., Shi, X., Wang, Q., Zhang, L., & Wang, X. (2020). Structure of the SARS-CoV-2 spike receptor-binding domain bound to the ACE2 receptor. *Nature*, *581*(7807), 215–220. https://doi.org/10.1038/s41586-020-2180-5

Langel, S. N., Johnson, S., Martinez, C. I., Tedjakusuma, S. N., Peinovich, N., Dora, E. G., Kuehl, P. J., Irshad, H., Barrett, E. G., Werts, A. D., & Tucker, S. N. (2022). Adenovirus type 5 SARS-CoV-2 vaccines delivered orally or intranasally reduced disease severity and transmission in a hamster model. *Science Translational Medicine*, *14*(658), eabn6868. https://doi.org/10.1126/scitranslmed.abn6868

Larson, H. J., Gakidou, E., & Murray, C. J. L. (2022). The Vaccine-Hesitant Moment. *New England Journal of Medicine*, *387*(1), 58–65. https://doi.org/10.1056/NEJMra2106441

Lee, I.-J., Sun, C.-P., Wu, P.-Y., Lan, Y.-H., Wang, I.-H., Liu, W.-C., Yuan, J. P.-Y., Chang, Y.-W., Tseng, S.-C., Tsung, S.-I., Chou, Y.-C., Kumari, M., Lin, Y.-S., Chen, H.-F., Chen, T.-Y., Lin, C.-C., Chiu, C.-W., Hsieh, C.-H., Chuang, C.-Y., … Tao, M.-H. (2022). A booster dose of Delta × Omicron hybrid mRNA vaccine produced broadly neutralizing antibody against Omicron and other SARS-CoV-2 variants. *Journal of Biomedical Science*, *29*(1), 49. https://doi.org/10.1186/s12929-022-00830-1

Lee, J., Stewart, C., Schaefer, A., Leaf, E. M., Park, Y.-J., Asarnow, D., Powers, J. M., Treichel, C., Corti, D., Baric, R., King, N. P., & Veesler, D. (2023). *A broadly generalizable stabilization strategy for sarbecovirus fusion machinery vaccines* [Preprint]. Biochemistry. https://doi.org/10.1101/2023.12.12.571160

Lempp, F. A., Soriaga, L. B., Montiel-Ruiz, M., Benigni, F., Noack, J., Park, Y.-J., Bianchi, S., Walls, A. C., Bowen, J. E., Zhou, J., Kaiser, H., Joshi, A., Agostini, M., Meury, M., Dellota, E., Jaconi, S., Cameroni, E., Martinez-Picado, J., Vergara-Alert, J., … Corti, D. (2021). Lectins enhance SARS-CoV-2 infection and influence neutralizing antibodies. *Nature*, *598*(7880), 342–347. https://doi.org/10.1038/s41586-021-03925-1

Letko, M., Marzi, A., & Munster, V. (2020). Functional assessment of cell entry and receptor usage for SARS-CoV-2 and other lineage B betacoronaviruses. *Nature Microbiology*, *5*(4), 562–569. https://doi.org/10.1038/s41564-020-0688-y

Li, W., Hulswit, R. J. G., Widjaja, I., Raj, V. S., McBride, R., Peng, W., Widagdo, W., Tortorici, M. A., Van Dieren, B., Lang, Y., Van Lent, J. W. M., Paulson, J. C., De Haan, C. A. M., De Groot, R. J., Van Kuppeveld, F. J. M., Haagmans, B. L., & Bosch, B.-J. (2017). Identification of sialic acid-binding function for the Middle East respiratory syndrome coronavirus spike glycoprotein. *Proceedings of the*

National Academy of Sciences, *114*(40). https://doi.org/10.1073/pnas.1712592114
Li, Y., Wan, Y., Liu, P., Zhao, J., Lu, G., Qi, J., Wang, Q., Lu, X., Wu, Y., Liu, W., Zhang, B., Yuen, K.-Y., Perlman, S., Gao, G. F., & Yan, J. (2015). A humanized neutralizing antibody against MERS-CoV targeting the receptor-binding domain of the spike protein. *Cell Research*, *25*(11), 1237–1249. https://doi.org/10.1038/cr.2015.113
Lindenbach, B. D. (2009). Measuring HCV infectivity produced in cell culture and in vivo. *Methods in Molecular Biology (Clifton, N.J.)*, *510*, 329–336. https://doi.org/10.1007/978-1-59745-394-3_24
Liu, C., Ginn, H. M., Dejnirattisai, W., Supasa, P., Wang, B., Tuekprakhon, A., Nutalai, R., Zhou, D., Mentzer, A. J., Zhao, Y., Duyvesteyn, H. M. E., López-Camacho, C., Slon-Campos, J., Walter, T. S., Skelly, D., Johnson, S. A., Ritter, T. G., Mason, C., Costa Clemens, S. A., … Screaton, G. R. (2021). Reduced neutralization of SARS-CoV-2 B.1.617 by vaccine and convalescent serum. *Cell*, *184*(16), 4220-4236.e13. https://doi.org/10.1016/j.cell.2021.06.020
Liu, J., Chandrashekar, A., Sellers, D., Barrett, J., Jacob-Dolan, C., Lifton, M., McMahan, K., Sciacca, M., VanWyk, H., Wu, C., Yu, J., Collier, A.-R. Y., & Barouch, D. H. (2022). Vaccines elicit highly conserved cellular immunity to SARS-CoV-2 Omicron. *Nature*, *603*(7901), 493–496. https://doi.org/10.1038/s41586-022-04465-y
Liu, Y., Liu, J., Johnson, B. A., Xia, H., Ku, Z., Schindewolf, C., Widen, S. G., An, Z., Weaver, S. C., Menachery, V. D., Xie, X., & Shi, P.-Y. (2021). *Delta spike P681R mutation enhances SARS-CoV-2 fitness over Alpha variant* [Preprint]. Microbiology. https://doi.org/10.1101/2021.08.12.456173
Liu, Y., Liu, J., Johnson, B. A., Xia, H., Ku, Z., Schindewolf, C., Widen, S. G., An, Z., Weaver, S. C., Menachery, V. D., Xie, X., & Shi, P.-Y. (2022). Delta spike P681R mutation enhances SARS-CoV-2 fitness over Alpha variant. *Cell Reports*, *39*(7), 110829. https://doi.org/10.1016/j.celrep.2022.110829
Lu, G., Hu, Y., Wang, Q., Qi, J., Gao, F., Li, Y., Zhang, Y., Zhang, W., Yuan, Y., Bao, J., Zhang, B., Shi, Y., Yan, J., & Gao, G. F. (2013). Molecular basis of binding between novel human coronavirus MERS-CoV and its receptor CD26. *Nature*, *500*(7461), 227–231. https://doi.org/10.1038/nature12328
Mackin, S. R., Desai, P., Whitener, B. M., Karl, C. E., Liu, M., Baric, R. S., Edwards, D. K., Chicz, T. M., McNamara, R. P., Alter, G., & Diamond, M. S. (2023). Fc-γR-dependent antibody effector functions are required for vaccine-mediated protection against antigen-shifted variants of SARS-CoV-2. *Nature Microbiology*, *8*(4), 569–580. https://doi.org/10.1038/s41564-023-01359-1
Mao, T., Israelow, B., Peña-Hernández, M. A., Suberi, A., Zhou, L., Luyten, S., Reschke, M., Dong, H., Homer, R. J., Saltzman, W. M., & Iwasaki, A. (2022). Unadjuvanted intranasal spike vaccine elicits protective mucosal immunity against sarbecoviruses. *Science*, *378*(6622), eabo2523. https://doi.org/10.1126/science.abo2523
Martin-Blondel, G., Marcelin, A.-G., Soulié, C., Kaisaridi, S., Lusivika-Nzinga, C., Dorival, C., Nailler, L., Boston, A., Melenotte, C., Cabié, A., Choquet, C., Coustillères, F., Martellosio, J.-P., Gaube, G., Trinh-Duc, A., Ronchetti, A.-M.,

Pourcher, V., Chauveau, M., Lacombe, K., … Yordanov, Y. (2022). Sotrovimab to prevent severe COVID-19 in high-risk patients infected with Omicron BA.2. *The Journal of Infection*, *85*(4), e104–e108. https://doi.org/10.1016/j.jinf.2022.06.033

Martinez, D. R., Schäfer, A., Gobeil, S., Li, D., De la Cruz, G., Parks, R., Lu, X., Barr, M., Stalls, V., Janowska, K., Beaudoin, E., Manne, K., Mansouri, K., Edwards, R. J., Cronin, K., Yount, B., Anasti, K., Montgomery, S. A., Tang, J., … Baric, R. S. (2022). A broadly cross-reactive antibody neutralizes and protects against sarbecovirus challenge in mice. *Science Translational Medicine*, *14*(629), eabj7125. https://doi.org/10.1126/scitranslmed.abj7125

Martinez, D. R., Schäfer, A., Leist, S. R., De la Cruz, G., West, A., Atochina-Vasserman, E. N., Lindesmith, L. C., Pardi, N., Parks, R., Barr, M., Li, D., Yount, B., Saunders, K. O., Weissman, D., Haynes, B. F., Montgomery, S. A., & Baric, R. S. (2021). Chimeric spike mRNA vaccines protect against Sarbecovirus challenge in mice. *Science (New York, N.Y.)*, *373*(6558), 991–998. https://doi.org/10.1126/science.abi4506

Marzi, R., Bassi, J., Silacci-Fregni, C., Bartha, I., Muoio, F., Culap, K., Sprugasci, N., Lombardo, G., Saliba, C., Cameroni, E., Cassotta, A., Low, J. S., Walls, A. C., McCallum, M., Tortorici, M. A., Bowen, J. E., Dellota, E. A., Dillen, J. R., Czudnochowski, N., … Piccoli, L. (2023). Maturation of SARS-CoV-2 Spike-specific memory B cells drives resilience to viral escape. *iScience*, *26*(1), 105726. https://doi.org/10.1016/j.isci.2022.105726

McCallum, M., Bassi, J., De Marco, A., Chen, A., Walls, A. C., Di Iulio, J., Tortorici, M. A., Navarro, M.-J., Silacci-Fregni, C., Saliba, C., Sprouse, K. R., Agostini, M., Pinto, D., Culap, K., Bianchi, S., Jaconi, S., Cameroni, E., Bowen, J. E., Tilles, S. W., … Veesler, D. (2021). SARS-CoV-2 immune evasion by the B.1.427/B.1.429 variant of concern. *Science*, eabi7994. https://doi.org/10.1126/science.abi7994

McCallum, M., Czudnochowski, N., Rosen, L. E., Zepeda, S. K., Bowen, J. E., Walls, A. C., Hauser, K., Joshi, A., Stewart, C., Dillen, J. R., Powell, A. E., Croll, T. I., Nix, J., Virgin, H. W., Corti, D., Snell, G., & Veesler, D. (2022). Structural basis of SARS-CoV-2 Omicron immune evasion and receptor engagement. *Science*, *375*(6583), 864–868. https://doi.org/10.1126/science.abn8652

McCallum, M., De Marco, A., Lempp, F. A., Tortorici, M. A., Pinto, D., Walls, A. C., Beltramello, M., Chen, A., Liu, Z., Zatta, F., Zepeda, S., di Iulio, J., Bowen, J. E., Montiel-Ruiz, M., Zhou, J., Rosen, L. E., Bianchi, S., Guarino, B., Fregni, C. S., … Veesler, D. (2021). N-terminal domain antigenic mapping reveals a site of vulnerability for SARS-CoV-2. *Cell*, *184*(9), 2332-2347.e16. https://doi.org/10.1016/j.cell.2021.03.028

McCallum, M., Walls, A. C., Sprouse, K. R., Bowen, J. E., Rosen, L. E., Dang, H. V., De Marco, A., Franko, N., Tilles, S. W., Logue, J., Miranda, M. C., Ahlrichs, M., Carter, L., Snell, G., Pizzuto, M. S., Chu, H. Y., Van Voorhis, W. C., Corti, D., & Veesler, D. (2021). Molecular basis of immune evasion by the Delta and Kappa SARS-CoV-2 variants. *Science*, *374*(6575), 1621–1626. https://doi.org/10.1126/science.abl8506

McLellan, J. S., Chen, M., Joyce, M. G., Sastry, M., Stewart-Jones, G. B. E., Yang, Y., Zhang, B., Chen, L., Srivatsan, S., Zheng, A., Zhou, T., Graepel, K. W., Kumar,

A., Moin, S., Boyington, J. C., Chuang, G.-Y., Soto, C., Baxa, U., Bakker, A. Q., … Kwong, P. D. (2013). Structure-Based Design of a Fusion Glycoprotein Vaccine for Respiratory Syncytial Virus. *Science*, *342*(6158), 592–598. https://doi.org/10.1126/science.1243283

McMahan, K., Yu, J., Mercado, N. B., Loos, C., Tostanoski, L. H., Chandrashekar, A., Liu, J., Peter, L., Atyeo, C., Zhu, A., Bondzie, E. A., Dagotto, G., Gebre, M. S., Jacob-Dolan, C., Li, Z., Nampanya, F., Patel, S., Pessaint, L., Van Ry, A., … Barouch, D. H. (2021). Correlates of protection against SARS-CoV-2 in rhesus macaques. *Nature*, *590*(7847), 630–634. https://doi.org/10.1038/s41586-020-03041-6

Meng, B., Abdullahi, A., Ferreira, I. A. T. M., Goonawardane, N., Saito, A., Kimura, I., Yamasoba, D., Gerber, P. P., Fatihi, S., Rathore, S., Zepeda, S. K., Papa, G., Kemp, S. A., Ikeda, T., Toyoda, M., Tan, T. S., Kuramochi, J., Mitsunaga, S., Ueno, T., … Gupta, R. K. (2022). Altered TMPRSS2 usage by SARS-CoV-2 Omicron impacts infectivity and fusogenicity. *Nature*, *603*(7902), 706–714. https://doi.org/10.1038/s41586-022-04474-x

Millet, J. K., & Whittaker, G. R. (2014). Host cell entry of Middle East respiratory syndrome coronavirus after two-step, furin-mediated activation of the spike protein. *Proceedings of the National Academy of Sciences*, *111*(42), 15214–15219. https://doi.org/10.1073/pnas.1407087111

Mlcochova, P., Kemp, S. A., Dhar, M. S., Papa, G., Meng, B., Ferreira, I. A. T. M., Datir, R., Collier, D. A., Albecka, A., Singh, S., Pandey, R., Brown, J., Zhou, J., Goonawardane, N., Mishra, S., Whittaker, C., Mellan, T., Marwal, R., Datta, M., … Gupta, R. K. (2021). SARS-CoV-2 B.1.617.2 Delta variant replication and immune evasion. *Nature*, *599*(7883), 114–119. https://doi.org/10.1038/s41586-021-03944-y

Modjarrad, K., Roberts, C. C., Mills, K. T., Castellano, A. R., Paolino, K., Muthumani, K., Reuschel, E. L., Robb, M. L., Racine, T., Oh, M.-D., Lamarre, C., Zaidi, F. I., Boyer, J., Kudchodkar, S. B., Jeong, M., Darden, J. M., Park, Y. K., Scott, P. T., Remigio, C., … Maslow, J. N. (2019). Safety and immunogenicity of an anti-Middle East respiratory syndrome coronavirus DNA vaccine: A phase 1, open-label, single-arm, dose-escalation trial. *The Lancet. Infectious Diseases*, *19*(9), 1013–1022. https://doi.org/10.1016/S1473-3099(19)30266-X

Muecksch, F., Wang, Z., Cho, A., Gaebler, C., Ben Tanfous, T., DaSilva, J., Bednarski, E., Ramos, V., Zong, S., Johnson, B., Raspe, R., Schaefer-Babajew, D., Shimeliovich, I., Daga, M., Yao, K.-H., Schmidt, F., Millard, K. G., Turroja, M., Jankovic, M., … Nussenzweig, M. C. (2022). Increased memory B cell potency and breadth after a SARS-CoV-2 mRNA boost. *Nature*, *607*(7917), 128–134. https://doi.org/10.1038/s41586-022-04778-y

Muecksch, F., Weisblum, Y., Barnes, C. O., Schmidt, F., Schaefer-Babajew, D., Wang, Z., C Lorenzi, J. C., Flyak, A. I., DeLaitsch, A. T., Huey-Tubman, K. E., Hou, S., Schiffer, C. A., Gaebler, C., Da Silva, J., Poston, D., Finkin, S., Cho, A., Cipolla, M., Oliveira, T. Y., … Bieniasz, P. D. (2021). Affinity maturation of SARS-CoV-2 neutralizing antibodies confers potency, breadth, and resilience to viral escape mutations. *Immunity*, *54*(8), 1853-1868.e7. https://doi.org/10.1016/j.immuni.2021.07.008

Murphy, K., & Weaver, C. (2016). *Janeway's immunobiology* (9th edition). Garland Science/Taylor & Francis Group, LLC.

Ng, K. W., Faulkner, N., Finsterbusch, K., Wu, M., Harvey, R., Hussain, S., Greco, M., Liu, Y., Kjaer, S., Swanton, C., Gandhi, S., Beale, R., Gamblin, S. J., Cherepanov, P., McCauley, J., Daniels, R., Howell, M., Arase, H., Wack, A., … Kassiotis, G. (2022). SARS-CoV-2 S2–targeted vaccination elicits broadly neutralizing antibodies. *Science Translational Medicine*, *14*(655), eabn3715. https://doi.org/10.1126/scitranslmed.abn3715

Ngere, I., Hunsperger, E. A., Tong, S., Oyugi, J., Jaoko, W., Harcourt, J. L., Thornburg, N. J., Oyas, H., Muturi, M., Osoro, E. M., Gachohi, J., Ombok, C., Dawa, J., Tao, Y., Zhang, J., Mwasi, L., Ochieng, C., Mwatondo, A., Bodha, B., … Munyua, P. M. (2022). Outbreak of Middle East Respiratory Syndrome Coronavirus in Camels and Probable Spillover Infection to Humans in Kenya. *Viruses*, *14*(8), 1743. https://doi.org/10.3390/v14081743

Nuqui, X., Casalino, L., Zhou, L., Shehata, M., Wang, A., Tse, A. L., Ojha, A. A., Kearns, F. L., Rosenfeld, M. A., Miller, E. H., Acreman, C. M., Ahn, S.-H., Chandran, K., McLellan, J. S., & Amaro, R. E. (2023). *Simulation-Driven Design of Stabilized SARS-CoV-2 Spike S2 Immunogens* [Preprint]. Biophysics. https://doi.org/10.1101/2023.10.24.563841

Oh, J. E., Song, E., Moriyama, M., Wong, P., Zhang, S., Jiang, R., Strohmeier, S., Kleinstein, S. H., Krammer, F., & Iwasaki, A. (2021). Intranasal priming induces local lung-resident B cell populations that secrete protective mucosal antiviral IgA. *Science Immunology*, *6*(66), eabj5129. https://doi.org/10.1126/sciimmunol.abj5129

Oliphant, T., Engle, M., Nybakken, G. E., Doane, C., Johnson, S., Huang, L., Gorlatov, S., Mehlhop, E., Marri, A., Chung, K. M., Ebel, G. D., Kramer, L. D., Fremont, D. H., & Diamond, M. S. (2005). Development of a humanized monoclonal antibody with therapeutic potential against West Nile virus. *Nature Medicine*, *11*(5), 522–530. https://doi.org/10.1038/nm1240

Ou, X., Liu, Y., Lei, X., Li, P., Mi, D., Ren, L., Guo, L., Guo, R., Chen, T., Hu, J., Xiang, Z., Mu, Z., Chen, X., Chen, J., Hu, K., Jin, Q., Wang, J., & Qian, Z. (2020). Characterization of spike glycoprotein of SARS-CoV-2 on virus entry and its immune cross-reactivity with SARS-CoV. *Nature Communications*, *11*(1), 1620. https://doi.org/10.1038/s41467-020-15562-9

Pallesen, J., Wang, N., Corbett, K. S., Wrapp, D., Kirchdoerfer, R. N., Turner, H. L., Cottrell, C. A., Becker, M. M., Wang, L., Shi, W., Kong, W.-P., Andres, E. L., Kettenbach, A. N., Denison, M. R., Chappell, J. D., Graham, B. S., Ward, A. B., & McLellan, J. S. (2017). Immunogenicity and structures of a rationally designed prefusion MERS-CoV spike antigen. *Proceedings of the National Academy of Sciences*, *114*(35). https://doi.org/10.1073/pnas.1707304114

Pang, W., Lu, Y., Zhao, Y.-B., Shen, F., Fan, C.-F., Wang, Q., He, W.-Q., He, X.-Y., Li, Z.-K., Chen, T.-T., Yang, C.-X., Li, Y.-Z., Xiao, S.-X., Zhao, Z.-J., Huang, X.-S., Luo, R.-H., Yang, L.-M., Zhang, M., Dong, X.-Q., … Zheng, Y.-T. (2022). A variant-proof SARS-CoV-2 vaccine targeting HR1 domain in S2 subunit of spike protein. *Cell Research*, *32*(12), 1068–1085. https://doi.org/10.1038/s41422-022-00746-3

Park, J.-E., Li, K., Barlan, A., Fehr, A. R., Perlman, S., McCray, P. B., & Gallagher, T. (2016). Proteolytic processing of Middle East respiratory syndrome coronavirus spikes expands virus tropism. *Proceedings of the National Academy of Sciences*, *113*(43), 12262–12267. https://doi.org/10.1073/pnas.1608147113

Park, W. B., Perera, R. A. P. M., Choe, P. G., Lau, E. H. Y., Choi, S. J., Chun, J. Y., Oh, H. S., Song, K.-H., Bang, J. H., Kim, E. S., Kim, H. B., Park, S. W., Kim, N. J., Man Poon, L. L., Peiris, M., & Oh, M.-D. (2015). Kinetics of Serologic Responses to MERS Coronavirus Infection in Humans, South Korea. *Emerging Infectious Diseases*, *21*(12), 2186–2189. https://doi.org/10.3201/eid2112.151421

Park, Y.-J., De Marco, A., Starr, T. N., Liu, Z., Pinto, D., Walls, A. C., Zatta, F., Zepeda, S. K., Bowen, J. E., Sprouse, K. R., Joshi, A., Giurdanella, M., Guarino, B., Noack, J., Abdelnabi, R., Foo, S.-Y. C., Rosen, L. E., Lempp, F. A., Benigni, F., … Veesler, D. (2022). Antibody-mediated broad sarbecovirus neutralization through ACE2 molecular mimicry. *Science*, *375*(6579), 449–454. https://doi.org/10.1126/science.abm8143

Park, Y.-J., Pinto, D., Walls, A. C., Liu, Z., De Marco, A., Benigni, F., Zatta, F., Silacci-Fregni, C., Bassi, J., Sprouse, K. R., Addetia, A., Bowen, J. E., Stewart, C., Giurdanella, M., Saliba, C., Guarino, B., Schmid, M. A., Franko, N. M., Logue, J. K., … Veesler, D. (2022). Imprinted antibody responses against SARS-CoV-2 Omicron sublineages. *Science*, *378*(6620), 619–627. https://doi.org/10.1126/science.adc9127

Park, Y.-J., Walls, A. C., Wang, Z., Sauer, M. M., Li, W., Tortorici, M. A., Bosch, B.-J., DiMaio, F., & Veesler, D. (2019). Structures of MERS-CoV spike glycoprotein in complex with sialoside attachment receptors. *Nature Structural & Molecular Biology*, *26*(12), 1151–1157. https://doi.org/10.1038/s41594-019-0334-7

Parry, H., Bruton, R., Stephens, C., Bentley, C., Brown, K., Amirthalingam, G., Hallis, B., Otter, A., Zuo, J., & Moss, P. (2022). Extended interval BNT162b2 vaccination enhances peak antibody generation. *NPJ Vaccines*, *7*(1), 14. https://doi.org/10.1038/s41541-022-00432-w

Payne, D. C., Iblan, I., Rha, B., Alqasrawi, S., Haddadin, A., Al Nsour, M., Alsanouri, T., Ali, S. S., Harcourt, J., Miao, C., Tamin, A., Gerber, S. I., Haynes, L. M., & Al Abdallat, M. M. (2016). Persistence of Antibodies against Middle East Respiratory Syndrome Coronavirus. *Emerging Infectious Diseases*, *22*(10), 1824–1826. https://doi.org/10.3201/eid2210.160706

Payne, R. P., Longet, S., Austin, J. A., Skelly, D. T., Dejnirattisai, W., Adele, S., Meardon, N., Faustini, S., Al-Taei, S., Moore, S. C., Tipton, T., Hering, L. M., Angyal, A., Brown, R., Nicols, A. R., Gillson, N., Dobson, S. L., Amini, A., Supasa, P., … PITCH Consortium. (2021). Immunogenicity of standard and extended dosing intervals of BNT162b2 mRNA vaccine. *Cell*, *184*(23), 5699-5714.e11. https://doi.org/10.1016/j.cell.2021.10.011

Peacock, T. P., Brown, J. C., Zhou, J., Thakur, N., Sukhova, K., Newman, J., Kugathasan, R., Yan, A. W. C., Furnon, W., De Lorenzo, G., Cowton, V. M., Reuss, D., Moshe, M., Quantrill, J. L., Platt, O. K., Kaforou, M., Patel, A. H., Palmarini, M., Bailey, D., & Barclay, W. S. (2022). *The altered entry pathway and antigenic distance of the SARS-CoV-2 Omicron variant map to separate domains*

of spike protein [Preprint]. Microbiology. https://doi.org/10.1101/2021.12.31.474653

Peiris, J. S. M., Lai, S. T., Poon, L. L. M., Guan, Y., Yam, L. Y. C., Lim, W., Nicholls, J., Yee, W. K. S., Yan, W. W., Cheung, M. T., Cheng, V. C. C., Chan, K. H., Tsang, D. N. C., Yung, R. W. H., Ng, T. K., Yuen, K. Y., & SARS study group. (2003). Coronavirus as a possible cause of severe acute respiratory syndrome. *Lancet (London, England)*, *361*(9366), 1319–1325. https://doi.org/10.1016/s0140-6736(03)13077-2

Pérez-Then, E., Lucas, C., Monteiro, V. S., Miric, M., Brache, V., Cochon, L., Vogels, C. B. F., Malik, A. A., De la Cruz, E., Jorge, A., De Los Santos, M., Leon, P., Breban, M. I., Billig, K., Yildirim, I., Pearson, C., Downing, R., Gagnon, E., Muyombwe, A., … Iwasaki, A. (2022). Neutralizing antibodies against the SARS-CoV-2 Delta and Omicron variants following heterologous CoronaVac plus BNT162b2 booster vaccination. *Nature Medicine*, *28*(3), 481–485. https://doi.org/10.1038/s41591-022-01705-6

Pettersen, E. F., Goddard, T. D., Huang, C. C., Couch, G. S., Greenblatt, D. M., Meng, E. C., & Ferrin, T. E. (2004). UCSF Chimera—A visualization system for exploratory research and analysis. *Journal of Computational Chemistry*, *25*(13), 1605–1612. https://doi.org/10.1002/jcc.20084

Piccoli, L., Park, Y.-J., Tortorici, M. A., Czudnochowski, N., Walls, A. C., Beltramello, M., Silacci-Fregni, C., Pinto, D., Rosen, L. E., Bowen, J. E., Acton, O. J., Jaconi, S., Guarino, B., Minola, A., Zatta, F., Sprugasci, N., Bassi, J., Peter, A., De Marco, A., … Veesler, D. (2020). Mapping Neutralizing and Immunodominant Sites on the SARS-CoV-2 Spike Receptor-Binding Domain by Structure-Guided High-Resolution Serology. *Cell*, *183*(4), 1024-1042.e21. https://doi.org/10.1016/j.cell.2020.09.037

Pinna, D., Corti, D., Jarrossay, D., Sallusto, F., & Lanzavecchia, A. (2009). Clonal dissection of the human memory B-cell repertoire following infection and vaccination. *European Journal of Immunology*, *39*(5), 1260–1270. https://doi.org/10.1002/eji.200839129

Pinto, D., Park, Y.-J., Beltramello, M., Walls, A. C., Tortorici, M. A., Bianchi, S., Jaconi, S., Culap, K., Zatta, F., De Marco, A., Peter, A., Guarino, B., Spreafico, R., Cameroni, E., Case, J. B., Chen, R. E., Havenar-Daughton, C., Snell, G., Telenti, A., … Corti, D. (2020). Cross-neutralization of SARS-CoV-2 by a human monoclonal SARS-CoV antibody. *Nature*, *583*(7815), 290–295. https://doi.org/10.1038/s41586-020-2349-y

Pinto, D., Sauer, M. M., Czudnochowski, N., Low, J. S., Tortorici, M. A., Housley, M. P., Noack, J., Walls, A. C., Bowen, J. E., Guarino, B., Rosen, L. E., Di Iulio, J., Jerak, J., Kaiser, H., Islam, S., Jaconi, S., Sprugasci, N., Culap, K., Abdelnabi, R., … Veesler, D. (2021). Broad betacoronavirus neutralization by a stem helix–specific human antibody. *Science*, *373*(6559), 1109–1116. https://doi.org/10.1126/science.abj3321

Planas, D., Bruel, T., Staropoli, I., Guivel-Benhassine, F., Porrot, F., Maes, P., Grzelak, L., Prot, M., Mougari, S., Planchais, C., Puech, J., Saliba, M., Sahraoui, R., Fémy, F., Morel, N., Dufloo, J., Sanjuán, R., Mouquet, H., André, E., … Schwartz, O. (2023). Resistance of Omicron subvariants BA.2.75.2, BA.4.6, and

BQ.1.1 to neutralizing antibodies. *Nature Communications*, *14*(1), 824. https://doi.org/10.1038/s41467-023-36561-6

Planas, D., Saunders, N., Maes, P., Guivel-Benhassine, F., Planchais, C., Buchrieser, J., Bolland, W.-H., Porrot, F., Staropoli, I., Lemoine, F., Péré, H., Veyer, D., Puech, J., Rodary, J., Baele, G., Dellicour, S., Raymenants, J., Gorissen, S., Geenen, C., … Schwartz, O. (2022). Considerable escape of SARS-CoV-2 Omicron to antibody neutralization. *Nature*, *602*(7898), 671–675. https://doi.org/10.1038/s41586-021-04389-z

Plante, J. A., Liu, Y., Liu, J., Xia, H., Johnson, B. A., Lokugamage, K. G., Zhang, X., Muruato, A. E., Zou, J., Fontes-Garfias, C. R., Mirchandani, D., Scharton, D., Bilello, J. P., Ku, Z., An, Z., Kalveram, B., Freiberg, A. N., Menachery, V. D., Xie, X., … Shi, P.-Y. (2021). Spike mutation D614G alters SARS-CoV-2 fitness. *Nature*, *592*(7852), 116–121. https://doi.org/10.1038/s41586-020-2895-3

Pollard, A. J., & Bijker, E. M. (2021). A guide to vaccinology: From basic principles to new developments. *Nature Reviews Immunology*, *21*(2), 83–100. https://doi.org/10.1038/s41577-020-00479-7

Premkumar, L., Segovia-Chumbez, B., Jadi, R., Martinez, D. R., Raut, R., Markmann, A. J., Cornaby, C., Bartelt, L., Weiss, S., Park, Y., Edwards, C. E., Weimer, E., Scherer, E. M., Rouphael, N., Edupuganti, S., Weiskopf, D., Tse, L. V., Hou, Y. J., Margolis, D., … De Silva, A. M. (2020). The receptor-binding domain of the viral spike protein is an immunodominant and highly specific target of antibodies in SARS-CoV-2 patients. *Science Immunology*, *5*(48), eabc8413. https://doi.org/10.1126/sciimmunol.abc8413

Punjani, A., Rubinstein, J. L., Fleet, D. J., & Brubaker, M. A. (2017). cryoSPARC: Algorithms for rapid unsupervised cryo-EM structure determination. *Nature Methods*, *14*(3), 290–296. https://doi.org/10.1038/nmeth.4169

Punjani, A., Zhang, H., & Fleet, D. J. (2020). Non-uniform refinement: Adaptive regularization improves single-particle cryo-EM reconstruction. *Nature Methods*, *17*(12), 1214–1221. https://doi.org/10.1038/s41592-020-00990-8

Quandt, J., Muik, A., Salisch, N., Lui, B. G., Lutz, S., Krüger, K., Wallisch, A.-K., Adams-Quack, P., Bacher, M., Finlayson, A., Ozhelvaci, O., Vogler, I., Grikscheit, K., Hoehl, S., Goetsch, U., Ciesek, S., Türeci, Ö., & Sahin, U. (2022). Omicron BA.1 breakthrough infection drives cross-variant neutralization and memory B cell formation against conserved epitopes. *Science Immunology*, *7*(75), eabq2427. https://doi.org/10.1126/sciimmunol.abq2427

Raj, V. S., Mou, H., Smits, S. L., Dekkers, D. H. W., Müller, M. A., Dijkman, R., Muth, D., Demmers, J. A. A., Zaki, A., Fouchier, R. A. M., Thiel, V., Drosten, C., Rottier, P. J. M., Osterhaus, A. D. M. E., Bosch, B. J., & Haagmans, B. L. (2013). Dipeptidyl peptidase 4 is a functional receptor for the emerging human coronavirus-EMC. *Nature*, *495*(7440), 251–254. https://doi.org/10.1038/nature12005

Rambaut, A., Holmes, E. C., O'Toole, Á., Hill, V., McCrone, J. T., Ruis, C., du Plessis, L., & Pybus, O. G. (2020). A dynamic nomenclature proposal for SARS-CoV-2 lineages to assist genomic epidemiology. *Nature Microbiology*, *5*(11), 1403–1407. https://doi.org/10.1038/s41564-020-0770-5

Richardson, S. I., Madzorera, V. S., Spencer, H., Manamela, N. P., van der Mescht, M. A., Lambson, B. E., Oosthuysen, B., Ayres, F., Makhado, Z., Moyo-Gwete, T., Mzindle, N., Motlou, T., Strydom, A., Mendes, A., Tegally, H., de Beer, Z., Roma de Villiers, T., Bodenstein, A., van den Berg, G., … Moore, P. L. (2022). SARS-CoV-2 Omicron triggers cross-reactive neutralization and Fc effector functions in previously vaccinated, but not unvaccinated, individuals. *Cell Host & Microbe*, *30*(6), 880-886.e4. https://doi.org/10.1016/j.chom.2022.03.029

Robbiani, D. F., Gaebler, C., Muecksch, F., Lorenzi, J. C. C., Wang, Z., Cho, A., Agudelo, M., Barnes, C. O., Gazumyan, A., Finkin, S., Hägglöf, T., Oliveira, T. Y., Viant, C., Hurley, A., Hoffmann, H.-H., Millard, K. G., Kost, R. G., Cipolla, M., Gordon, K., … Nussenzweig, M. C. (2020). Convergent antibody responses to SARS-CoV-2 in convalescent individuals. *Nature*, *584*(7821), 437–442. https://doi.org/10.1038/s41586-020-2456-9

Rodriguez-Cousiño, N., Esteban, L. M., & Esteban, R. (1991). Molecular cloning and characterization of W double-stranded RNA, a linear molecule present in Saccharomyces cerevisiae. Identification of its single-stranded RNA form as 20 S RNA. *Journal of Biological Chemistry*, *266*(19), 12772–12778. https://doi.org/10.1016/S0021-9258(18)98966-0

Rosenthal, P. B., & Henderson, R. (2003). Optimal Determination of Particle Orientation, Absolute Hand, and Contrast Loss in Single-particle Electron Cryomicroscopy. *Journal of Molecular Biology*, *333*(4), 721–745. https://doi.org/10.1016/j.jmb.2003.07.013

Rössler, A., Knabl, L., von Laer, D., & Kimpel, J. (2022). Neutralization Profile after Recovery from SARS-CoV-2 Omicron Infection. *The New England Journal of Medicine*, *386*(18), 1764–1766. https://doi.org/10.1056/NEJMc2201607

Russo, C. J., & Passmore, L. A. (2014). Ultrastable gold substrates for electron cryomicroscopy. *Science*, *346*(6215), 1377–1380. https://doi.org/10.1126/science.1259530

Saito, A., Irie, T., Suzuki, R., Maemura, T., Nasser, H., Uriu, K., Kosugi, Y., Shirakawa, K., Sadamasu, K., Kimura, I., Ito, J., Wu, J., Iwatsuki-Horimoto, K., Ito, M., Yamayoshi, S., Loeber, S., Tsuda, M., Wang, L., Ozono, S., … Sato, K. (2022). Enhanced fusogenicity and pathogenicity of SARS-CoV-2 Delta P681R mutation. *Nature*, *602*(7896), 300–306. https://doi.org/10.1038/s41586-021-04266-9

Sauer, M. M., Tortorici, M. A., Park, Y.-J., Walls, A. C., Homad, L., Acton, O. J., Bowen, J. E., Wang, C., Xiong, X., De Van Der Schueren, W., Quispe, J., Hoffstrom, B. G., Bosch, B.-J., McGuire, A. T., & Veesler, D. (2021). Structural basis for broad coronavirus neutralization. *Nature Structural & Molecular Biology*, *28*(6), 478–486. https://doi.org/10.1038/s41594-021-00596-4

Scheaffer, S. M., Lee, D., Whitener, B., Ying, B., Wu, K., Liang, C.-Y., Jani, H., Martin, P., Amato, N. J., Avena, L. E., Berrueta, D. M., Schmidt, S. D., O'Dell, S., Nasir, A., Chuang, G.-Y., Stewart-Jones, G., Koup, R. A., Doria-Rose, N. A., Carfi, A., … Diamond, M. S. (2023). Bivalent SARS-CoV-2 mRNA vaccines increase breadth of neutralization and protect against the BA.5 Omicron variant in mice. *Nature Medicine*, *29*(1), 247–257. https://doi.org/10.1038/s41591-022-02092-8

Scheres, S. H. W. (2012). RELION: Implementation of a Bayesian approach to cryo-EM structure determination. *Journal of Structural Biology*, *180*(3), 519–530. https://doi.org/10.1016/j.jsb.2012.09.006

Schmidt, F., Muecksch, F., Weisblum, Y., Da Silva, J., Bednarski, E., Cho, A., Wang, Z., Gaebler, C., Caskey, M., Nussenzweig, M. C., Hatziioannou, T., & Bieniasz, P. D. (2022). Plasma Neutralization of the SARS-CoV-2 Omicron Variant. *The New England Journal of Medicine*, *386*(6), 599–601. https://doi.org/10.1056/NEJMc2119641

Silva, R. P., Huang, Y., Nguyen, A. W., Hsieh, C.-L., Olaluwoye, O. S., Kaoud, T. S., Wilen, R. E., Qerqez, A. N., Park, J.-G., Khalil, A. M., Azouz, L. R., Le, K. C., Bohanon, A. L., DiVenere, A. M., Liu, Y., Lee, A. G., Amengor, D. A., Shoemaker, S. R., Costello, S. M., … Maynard, J. A. (2023). Identification of a conserved S2 epitope present on spike proteins from all highly pathogenic coronaviruses. *eLife*, *12*, e83710. https://doi.org/10.7554/eLife.83710

Simões, E. A. F., Center, K. J., Tita, A. T. N., Swanson, K. A., Radley, D., Houghton, J., McGrory, S. B., Gomme, E., Anderson, M., Roberts, J. P., Scott, D. A., Jansen, K. U., Gruber, W. C., Dormitzer, P. R., & Gurtman, A. C. (2022). Prefusion F Protein–Based Respiratory Syncytial Virus Immunization in Pregnancy. *New England Journal of Medicine*, *386*(17), 1615–1626. https://doi.org/10.1056/NEJMoa2106062

Stalls, V., Lindenberger, J., Gobeil, S. M.-C., Henderson, R., Parks, R., Barr, M., Deyton, M., Martin, M., Janowska, K., Huang, X., May, A., Speakman, M., Beaudoin, E., Kraft, B., Lu, X., Edwards, R. J., Eaton, A., Montefiori, D. C., Williams, W. B., … Acharya, P. (2022). Cryo-EM structures of SARS-CoV-2 Omicron BA.2 spike. *Cell Reports*, *39*(13), 111009. https://doi.org/10.1016/j.celrep.2022.111009

Stamatatos, L., Czartoski, J., Wan, Y.-H., Homad, L. J., Rubin, V., Glantz, H., Neradilek, M., Seydoux, E., Jennewein, M. F., MacCamy, A. J., Feng, J., Mize, G., De Rosa, S. C., Finzi, A., Lemos, M. P., Cohen, K. W., Moodie, Z., McElrath, M. J., & McGuire, A. T. (2021). mRNA vaccination boosts cross-variant neutralizing antibodies elicited by SARS-CoV-2 infection. *Science*, *372*(6549), 1413–1418. https://doi.org/10.1126/science.abg9175

Starr, T. N., Czudnochowski, N., Liu, Z., Zatta, F., Park, Y.-J., Addetia, A., Pinto, D., Beltramello, M., Hernandez, P., Greaney, A. J., Marzi, R., Glass, W. G., Zhang, I., Dingens, A. S., Bowen, J. E., Tortorici, M. A., Walls, A. C., Wojcechowskyj, J. A., De Marco, A., … Snell, G. (2021). SARS-CoV-2 RBD antibodies that maximize breadth and resistance to escape. *Nature*. https://doi.org/10.1038/s41586-021-03807-6

Starr, T. N., Greaney, A. J., Addetia, A., Hannon, W. W., Choudhary, M. C., Dingens, A. S., Li, J. Z., & Bloom, J. D. (2021). Prospective mapping of viral mutations that escape antibodies used to treat COVID-19. *Science*, *371*(6531), 850–854. https://doi.org/10.1126/science.abf9302

Starr, T. N., Greaney, A. J., Hannon, W. W., Loes, A. N., Hauser, K., Dillen, J. R., Ferri, E., Farrell, A. G., Dadonaite, B., McCallum, M., Matreyek, K. A., Corti, D., Veesler, D., Snell, G., & Bloom, J. D. (2022). *Shifting mutational constraints in*

the SARS-CoV-2 receptor-binding domain during viral evolution [Preprint]. Microbiology. https://doi.org/10.1101/2022.02.24.481899

Starr, T. N., Greaney, A. J., Hilton, S. K., Ellis, D., Crawford, K. H. D., Dingens, A. S., Navarro, M. J., Bowen, J. E., Tortorici, M. A., Walls, A. C., King, N. P., Veesler, D., & Bloom, J. D. (2020). Deep Mutational Scanning of SARS-CoV-2 Receptor Binding Domain Reveals Constraints on Folding and ACE2 Binding. *Cell*, *182*(5), 1295-1310.e20. https://doi.org/10.1016/j.cell.2020.08.012

Starr, T. N., Greaney, A. J., Stewart, C. M., Walls, A. C., Hannon, W. W., Veesler, D., & Bloom, J. D. (2022). Deep mutational scans for ACE2 binding, RBD expression, and antibody escape in the SARS-CoV-2 Omicron BA.1 and BA.2 receptor-binding domains. *PLoS Pathogens*, *18*(11), e1010951. https://doi.org/10.1371/journal.ppat.1010951

Starr, T. N., Zepeda, S. K., Walls, A. C., Greaney, A. J., Alkhovsky, S., Veesler, D., & Bloom, J. D. (2022). ACE2 binding is an ancestral and evolvable trait of sarbecoviruses. *Nature*, *603*(7903), 913–918. https://doi.org/10.1038/s41586-022-04464-z

Stiasny, K., Medits, I., Springer, D., Graninger, M., Camp, J., Höltl, E., Aberle, S., Traugott, M., Hoepler, W., Deutsch, J., Lammel, O., Borsodi, C., Elisabeth Puchhammer-St&#x00F6, Zoufaly, A., Weseslindtner, L., & Aberle, J. (2022). *Human primary Omicron BA.1 and BA.2 infections result in sub-lineage-specific neutralization* [Preprint]. In Review. https://doi.org/10.21203/rs.3.rs-1536794/v1

Suloway, C., Pulokas, J., Fellmann, D., Cheng, A., Guerra, F., Quispe, J., Stagg, S., Potter, C. S., & Carragher, B. (2005). Automated molecular microscopy: The new Leginon system. *Journal of Structural Biology*, *151*(1), 41–60. https://doi.org/10.1016/j.jsb.2005.03.010

Sun, X., Yi, C., Zhu, Y., Ding, L., Xia, S., Chen, X., Liu, M., Gu, C., Lu, X., Fu, Y., Chen, S., Zhang, T., Zhang, Y., Yang, Z., Ma, L., Gu, W., Hu, G., Du, S., Yan, R., … Sun, B. (2022). Neutralization mechanism of a human antibody with pan-coronavirus reactivity including SARS-CoV-2. *Nature Microbiology*, *7*(7), 1063–1074. https://doi.org/10.1038/s41564-022-01155-3

Suzuki, R., Yamasoba, D., Kimura, I., Wang, L., Kishimoto, M., Ito, J., Morioka, Y., Nao, N., Nasser, H., Uriu, K., Kosugi, Y., Tsuda, M., Orba, Y., Sasaki, M., Shimizu, R., Kawabata, R., Yoshimatsu, K., Asakura, H., Nagashima, M., … Sato, K. (2022). Attenuated fusogenicity and pathogenicity of SARS-CoV-2 Omicron variant. *Nature*, *603*(7902), 700–705. https://doi.org/10.1038/s41586-022-04462-1

Tai, W., Wang, Y., Fett, C. A., Zhao, G., Li, F., Perlman, S., Jiang, S., Zhou, Y., & Du, L. (2017). Recombinant Receptor-Binding Domains of Multiple Middle East Respiratory Syndrome Coronaviruses (MERS-CoVs) Induce Cross-Neutralizing Antibodies against Divergent Human and Camel MERS-CoVs and Antibody Escape Mutants. *Journal of Virology*, *91*(1), e01651-16. https://doi.org/10.1128/JVI.01651-16

Tang, X.-C., Agnihothram, S. S., Jiao, Y., Stanhope, J., Graham, R. L., Peterson, E. C., Avnir, Y., Tallarico, A. St. C., Sheehan, J., Zhu, Q., Baric, R. S., & Marasco, W. A. (2014). Identification of human neutralizing antibodies against MERS-CoV and their role in virus adaptive evolution. *Proceedings of the National Academy of Sciences*, *111*(19). https://doi.org/10.1073/pnas.1402074111

Tarke, A., Coelho, C. H., Zhang, Z., Dan, J. M., Yu, E. D., Methot, N., Bloom, N. I., Goodwin, B., Phillips, E., Mallal, S., Sidney, J., Filaci, G., Weiskopf, D., da Silva Antunes, R., Crotty, S., Grifoni, A., & Sette, A. (2022). SARS-CoV-2 vaccination induces immunological T cell memory able to cross-recognize variants from Alpha to Omicron. *Cell*, *185*(5), 847-859.e11. https://doi.org/10.1016/j.cell.2022.01.015

Tegally, H., Wilkinson, E., Giovanetti, M., Iranzadeh, A., Fonseca, V., Giandhari, J., Doolabh, D., Pillay, S., San, E. J., Msomi, N., Mlisana, K., Von Gottberg, A., Walaza, S., Allam, M., Ismail, A., Mohale, T., Glass, A. J., Engelbrecht, S., Van Zyl, G., … De Oliveira, T. (2021). Detection of a SARS-CoV-2 variant of concern in South Africa. *Nature*, *592*(7854), 438–443. https://doi.org/10.1038/s41586-021-03402-9

Tegunov, D., & Cramer, P. (2019). Real-time cryo-electron microscopy data preprocessing with Warp. *Nature Methods*, *16*(11), 1146–1152. https://doi.org/10.1038/s41592-019-0580-y

The CITIID-NIHR BioResource COVID-19 Collaboration, The COVID-19 Genomics UK (COG-UK) Consortium, Collier, D. A., De Marco, A., Ferreira, I. A. T. M., Meng, B., Datir, R. P., Walls, A. C., Kemp, S. A., Bassi, J., Pinto, D., Silacci-Fregni, C., Bianchi, S., Tortorici, M. A., Bowen, J., Culap, K., Jaconi, S., Cameroni, E., Snell, G., … Gupta, R. K. (2021). Sensitivity of SARS-CoV-2 B.1.1.7 to mRNA vaccine-elicited antibodies. *Nature*, *593*(7857), 136–141. https://doi.org/10.1038/s41586-021-03412-7

Thomson, E. C., Rosen, L. E., Shepherd, J. G., Spreafico, R., Da Silva Filipe, A., Wojcechowskyj, J. A., Davis, C., Piccoli, L., Pascall, D. J., Dillen, J., Lytras, S., Czudnochowski, N., Shah, R., Meury, M., Jesudason, N., De Marco, A., Li, K., Bassi, J., O'Toole, A., … Snell, G. (2021). Circulating SARS-CoV-2 spike N439K variants maintain fitness while evading antibody-mediated immunity. *Cell*, *184*(5), 1171-1187.e20. https://doi.org/10.1016/j.cell.2021.01.037

Tortorici, M. A., Addetia, A., Seo, A. J., Brown, J., Sprouse, K. R., Logue, J., Clark, E., Franko, N., Chu, H., & Veesler, D. (2023). *Persistent immune imprinting after XBB.1.5 COVID vaccination in humans* [Preprint]. Immunology. https://doi.org/10.1101/2023.11.28.569129

Tortorici, M. A., Beltramello, M., Lempp, F. A., Pinto, D., Dang, H. V., Rosen, L. E., McCallum, M., Bowen, J., Minola, A., Jaconi, S., Zatta, F., De Marco, A., Guarino, B., Bianchi, S., Lauron, E. J., Tucker, H., Zhou, J., Peter, A., Havenar-Daughton, C., … Veesler, D. (2020). Ultrapotent human antibodies protect against SARS-CoV-2 challenge via multiple mechanisms. *Science*, *370*(6519), 950–957. https://doi.org/10.1126/science.abe3354

Tortorici, M. A., Czudnochowski, N., Starr, T. N., Marzi, R., Walls, A. C., Zatta, F., Bowen, J. E., Jaconi, S., Di Iulio, J., Wang, Z., De Marco, A., Zepeda, S. K., Pinto, D., Liu, Z., Beltramello, M., Bartha, I., Housley, M. P., Lempp, F. A., Rosen, L. E., … Pizzuto, M. S. (2021). Broad sarbecovirus neutralization by a human monoclonal antibody. *Nature*, *597*(7874), 103–108. https://doi.org/10.1038/s41586-021-03817-4

Tortorici, M. A., & Veesler, D. (2019). Structural insights into coronavirus entry. *Advances in Virus Research*, *105*, 93–116. https://doi.org/10.1016/bs.aivir.2019.08.002

Tse, L. V., Hou, Y. J., McFadden, E., Lee, R. E., Scobey, T. D., Leist, S. R., Martinez, D. R., Meganck, R. M., Schäfer, A., Yount, B. L., Mascenik, T., Powers, J. M., Randell, S. H., Zhang, Y., Wang, L., Mascola, J., McLellan, J. S., & Baric, R. S. (2023). A MERS-CoV antibody neutralizes a pre-emerging group 2c bat coronavirus. *Science Translational Medicine*, *15*(715), eadg5567. https://doi.org/10.1126/scitranslmed.adg5567

Turner, J. S., O'Halloran, J. A., Kalaidina, E., Kim, W., Schmitz, A. J., Zhou, J. Q., Lei, T., Thapa, M., Chen, R. E., Case, J. B., Amanat, F., Rauseo, A. M., Haile, A., Xie, X., Klebert, M. K., Suessen, T., Middleton, W. D., Shi, P.-Y., Krammer, F., … Ellebedy, A. H. (2021). SARS-CoV-2 mRNA vaccines induce persistent human germinal centre responses. *Nature*, *596*(7870), 109–113. https://doi.org/10.1038/s41586-021-03738-2

Viana, R., Moyo, S., Amoako, D. G., Tegally, H., Scheepers, C., Althaus, C. L., Anyaneji, U. J., Bester, P. A., Boni, M. F., Chand, M., Choga, W. T., Colquhoun, R., Davids, M., Deforche, K., Doolabh, D., du Plessis, L., Engelbrecht, S., Everatt, J., Giandhari, J., … de Oliveira, T. (2022). Rapid epidemic expansion of the SARS-CoV-2 Omicron variant in southern Africa. *Nature*, *603*(7902), 679–686. https://doi.org/10.1038/s41586-022-04411-y

Virology: Coronaviruses. (1968). *Nature*, *220*(5168), 650–650. https://doi.org/10.1038/220650b0

V'kovski, P., Kratzel, A., Steiner, S., Stalder, H., & Thiel, V. (2021). Coronavirus biology and replication: Implications for SARS-CoV-2. *Nature Reviews Microbiology*, *19*(3), 155–170. https://doi.org/10.1038/s41579-020-00468-6

Voysey, M., Costa Clemens, S. A., Madhi, S. A., Weckx, L. Y., Folegatti, P. M., Aley, P. K., Angus, B., Baillie, V. L., Barnabas, S. L., Bhorat, Q. E., Bibi, S., Briner, C., Cicconi, P., Clutterbuck, E. A., Collins, A. M., Cutland, C. L., Darton, T. C., Dheda, K., Dold, C., … Oxford COVID Vaccine Trial Group. (2021). Single-dose administration and the influence of the timing of the booster dose on immunogenicity and efficacy of ChAdOx1 nCoV-19 (AZD1222) vaccine: A pooled analysis of four randomised trials. *Lancet (London, England)*, *397*(10277), 881–891. https://doi.org/10.1016/S0140-6736(21)00432-3

Vu, M. N., Alvarado, R. E., Morris, D. R., Lokugamage, K. G., Zhou, Y., Morgan, A. L., Estes, L. K., McLeland, A. M., Schindewolf, C., Plante, J. A., Ahearn, Y. P., Meyers, W. M., Murray, J. T., Crocquet-Valdes, P. A., Weaver, S. C., Walker, D. H., Russell, W. K., Routh, A. L., Plante, K. S., & Menachery, V. (2023). *Loss-of-function mutation in Omicron variants reduces spike protein expression and attenuates SARS-CoV-2 infection* [Preprint]. Microbiology. https://doi.org/10.1101/2023.04.17.536926

Walls, A. C., Fiala, B., Schäfer, A., Wrenn, S., Pham, M. N., Murphy, M., Tse, L. V., Shehata, L., O'Connor, M. A., Chen, C., Navarro, M. J., Miranda, M. C., Pettie, D., Ravichandran, R., Kraft, J. C., Ogohara, C., Palser, A., Chalk, S., Lee, E.-C., … King, N. P. (2020). Elicitation of Potent Neutralizing Antibody Responses by

Designed Protein Nanoparticle Vaccines for SARS-CoV-2. *Cell*, *183*(5), 1367-1382.e17. https://doi.org/10.1016/j.cell.2020.10.043

Walls, A. C., Miranda, M. C., Schäfer, A., Pham, M. N., Greaney, A., Arunachalam, P. S., Navarro, M.-J., Tortorici, M. A., Rogers, K., O'Connor, M. A., Shirreff, L., Ferrell, D. E., Bowen, J., Brunette, N., Kepl, E., Zepeda, S. K., Starr, T., Hsieh, C.-L., Fiala, B., … Veesler, D. (2021). Elicitation of broadly protective sarbecovirus immunity by receptor-binding domain nanoparticle vaccines. *Cell*, *184*(21), 5432-5447.e16. https://doi.org/10.1016/j.cell.2021.09.015

Walls, A. C., Park, Y.-J., Tortorici, M. A., Wall, A., McGuire, A. T., & Veesler, D. (2020). Structure, Function, and Antigenicity of the SARS-CoV-2 Spike Glycoprotein. *Cell*, *181*(2), 281-292.e6. https://doi.org/10.1016/j.cell.2020.02.058

Walls, A. C., Sprouse, K. R., Bowen, J. E., Joshi, A., Franko, N., Navarro, M. J., Stewart, C., Cameroni, E., McCallum, M., Goecker, E. A., Degli-Angeli, E. J., Logue, J., Greninger, A., Corti, D., Chu, H. Y., & Veesler, D. (2022). SARS-CoV-2 breakthrough infections elicit potent, broad, and durable neutralizing antibody responses. *Cell*, *185*(5), 872-880.e3. https://doi.org/10.1016/j.cell.2022.01.011

Walls, A. C., Tortorici, M. A., Snijder, J., Xiong, X., Bosch, B.-J., Rey, F. A., & Veesler, D. (2017). Tectonic conformational changes of a coronavirus spike glycoprotein promote membrane fusion. *Proceedings of the National Academy of Sciences*, *114*(42), 11157–11162. https://doi.org/10.1073/pnas.1708727114

Walls, A. C., Xiong, X., Park, Y.-J., Tortorici, M. A., Snijder, J., Quispe, J., Cameroni, E., Gopal, R., Dai, M., Lanzavecchia, A., Zambon, M., Rey, F. A., Corti, D., & Veesler, D. (2019). Unexpected Receptor Functional Mimicry Elucidates Activation of Coronavirus Fusion. *Cell*, *176*(5), 1026-1039.e15. https://doi.org/10.1016/j.cell.2018.12.028

Walsh, E. E., Frenck, R. W., Falsey, A. R., Kitchin, N., Absalon, J., Gurtman, A., Lockhart, S., Neuzil, K., Mulligan, M. J., Bailey, R., Swanson, K. A., Li, P., Koury, K., Kalina, W., Cooper, D., Fontes-Garfias, C., Shi, P.-Y., Türeci, Ö., Tompkins, K. R., … Gruber, W. C. (2020). Safety and Immunogenicity of Two RNA-Based Covid-19 Vaccine Candidates. *New England Journal of Medicine*, *383*(25), 2439–2450. https://doi.org/10.1056/NEJMoa2027906

Wang, L., Shi, W., Joyce, M. G., Modjarrad, K., Zhang, Y., Leung, K., Lees, C. R., Zhou, T., Yassine, H. M., Kanekiyo, M., Yang, Z., Chen, X., Becker, M. M., Freeman, M., Vogel, L., Johnson, J. C., Olinger, G., Todd, J. P., Bagci, U., … Graham, B. S. (2015). Evaluation of candidate vaccine approaches for MERS-CoV. *Nature Communications*, *6*(1), 7712. https://doi.org/10.1038/ncomms8712

Wang, N., Rosen, O., Wang, L., Turner, H. L., Stevens, L. J., Corbett, K. S., Bowman, C. A., Pallesen, J., Shi, W., Zhang, Y., Leung, K., Kirchdoerfer, R. N., Becker, M. M., Denison, M. R., Chappell, J. D., Ward, A. B., Graham, B. S., & McLellan, J. S. (2019). Structural Definition of a Neutralization-Sensitive Epitope on the MERS-CoV S1-NTD. *Cell Reports*, *28*(13), 3395-3405.e6. https://doi.org/10.1016/j.celrep.2019.08.052

Wang, N., Shi, X., Jiang, L., Zhang, S., Wang, D., Tong, P., Guo, D., Fu, L., Cui, Y., Liu, X., Arledge, K. C., Chen, Y.-H., Zhang, L., & Wang, X. (2013). Structure of MERS-CoV spike receptor-binding domain complexed with human receptor DPP4. *Cell Research*, *23*(8), 986–993. https://doi.org/10.1038/cr.2013.92

Wang, Q., Iketani, S., Li, Z., Liu, L., Guo, Y., Huang, Y., Bowen, A. D., Liu, M., Wang, M., Yu, J., Valdez, R., Lauring, A. S., Sheng, Z., Wang, H. H., Gordon, A., Liu, L., & Ho, D. D. (2023). Alarming antibody evasion properties of rising SARS-CoV-2 BQ and XBB subvariants. *Cell*, *186*(2), 279-286.e8. https://doi.org/10.1016/j.cell.2022.12.018

Wang, R. Y.-R., Song, Y., Barad, B. A., Cheng, Y., Fraser, J. S., & DiMaio, F. (2016). Automated structure refinement of macromolecular assemblies from cryo-EM maps using Rosetta. *eLife*, *5*, e17219. https://doi.org/10.7554/eLife.17219

Wang, Z., Muecksch, F., Schaefer-Babajew, D., Finkin, S., Viant, C., Gaebler, C., Hoffmann, H.-H., Barnes, C. O., Cipolla, M., Ramos, V., Oliveira, T. Y., Cho, A., Schmidt, F., Da Silva, J., Bednarski, E., Aguado, L., Yee, J., Daga, M., Turroja, M., … Nussenzweig, M. C. (2021). Naturally enhanced neutralizing breadth against SARS-CoV-2 one year after infection. *Nature*, *595*(7867), 426–431. https://doi.org/10.1038/s41586-021-03696-9

Westendorf, K., Žentelis, S., Wang, L., Foster, D., Vaillancourt, P., Wiggin, M., Lovett, E., Van Der Lee, R., Hendle, J., Pustilnik, A., Sauder, J. M., Kraft, L., Hwang, Y., Siegel, R. W., Chen, J., Heinz, B. A., Higgs, R. E., Kallewaard, N. L., Jepson, K., … Barnhart, B. C. (2022). LY-CoV1404 (bebtelovimab) potently neutralizes SARS-CoV-2 variants. *Cell Reports*, *39*(7), 110812. https://doi.org/10.1016/j.celrep.2022.110812

Wibmer, C. K., Ayres, F., Hermanus, T., Madzivhandila, M., Kgagudi, P., Oosthuysen, B., Lambson, B. E., de Oliveira, T., Vermeulen, M., van der Berg, K., Rossouw, T., Boswell, M., Ueckermann, V., Meiring, S., von Gottberg, A., Cohen, C., Morris, L., Bhiman, J. N., & Moore, P. L. (2021). SARS-CoV-2 501Y.V2 escapes neutralization by South African COVID-19 donor plasma. *Nature Medicine*, *27*(4), 622–625. https://doi.org/10.1038/s41591-021-01285-x

Widjaja, I., Wang, C., Van Haperen, R., Gutiérrez-Álvarez, J., Van Dieren, B., Okba, N. M. A., Raj, V. S., Li, W., Fernandez-Delgado, R., Grosveld, F., Van Kuppeveld, F. J. M., Haagmans, B. L., Enjuanes, L., Drabek, D., & Bosch, B.-J. (2019). Towards a solution to MERS: Protective human monoclonal antibodies targeting different domains and functions of the MERS-coronavirus spike glycoprotein. *Emerging Microbes & Infections*, *8*(1), 516–530. https://doi.org/10.1080/22221751.2019.1597644

Wilhelm, A., Widera, M., Grikscheit, K., Toptan, T., Schenk, B., Pallas, C., Metzler, M., Kohmer, N., Hoehl, S., Marschalek, R., Herrmann, E., Helfritz, F. A., Wolf, T., Goetsch, U., & Ciesek, S. (2022). Limited neutralisation of the SARS-CoV-2 Omicron subvariants BA.1 and BA.2 by convalescent and vaccine serum and monoclonal antibodies. *eBioMedicine*, *82*, 104158. https://doi.org/10.1016/j.ebiom.2022.104158

Willett, B. J., Grove, J., MacLean, O. A., Wilkie, C., De Lorenzo, G., Furnon, W., Cantoni, D., Scott, S., Logan, N., Ashraf, S., Manali, M., Szemiel, A., Cowton, V., Vink, E., Harvey, W. T., Davis, C., Asamaphan, P., Smollett, K., Tong, L., … Thomson, E. C. (2022). SARS-CoV-2 Omicron is an immune escape variant with an altered cell entry pathway. *Nature Microbiology*, *7*(8), 1161–1179. https://doi.org/10.1038/s41564-022-01143-7

Wong, L.-Y. R., Zheng, J., Sariol, A., Lowery, S., Meyerholz, D. K., Gallagher, T., & Perlman, S. (2021). Middle East respiratory syndrome coronavirus Spike protein variants exhibit geographic differences in virulence. *Proceedings of the National Academy of Sciences*, *118*(24), e2102983118. https://doi.org/10.1073/pnas.2102983118

Wrammert, J., Koutsonanos, D., Li, G.-M., Edupuganti, S., Sui, J., Morrissey, M., McCausland, M., Skountzou, I., Hornig, M., Lipkin, W. I., Mehta, A., Razavi, B., Del Rio, C., Zheng, N.-Y., Lee, J.-H., Huang, M., Ali, Z., Kaur, K., Andrews, S., … Wilson, P. C. (2011). Broadly cross-reactive antibodies dominate the human B cell response against 2009 pandemic H1N1 influenza virus infection. *The Journal of Experimental Medicine*, *208*(1), 181–193. https://doi.org/10.1084/jem.20101352

Wrapp, D., Wang, N., Corbett, K. S., Goldsmith, J. A., Hsieh, C.-L., Abiona, O., Graham, B. S., & McLellan, J. S. (2020). Cryo-EM structure of the 2019-nCoV spike in the prefusion conformation. *Science (New York, N.Y.)*, *367*(6483), 1260–1263. https://doi.org/10.1126/science.abb2507

Wrobel, A. G., Benton, D. J., Xu, P., Roustan, C., Martin, S. R., Rosenthal, P. B., Skehel, J. J., & Gamblin, S. J. (2020). SARS-CoV-2 and bat RaTG13 spike glycoprotein structures inform on virus evolution and furin-cleavage effects. *Nature Structural & Molecular Biology*, *27*(8), 763–767. https://doi.org/10.1038/s41594-020-0468-7

Wu, K., Werner, A. P., Koch, M., Choi, A., Narayanan, E., Stewart-Jones, G. B. E., Colpitts, T., Bennett, H., Boyoglu-Barnum, S., Shi, W., Moliva, J. I., Sullivan, N. J., Graham, B. S., Carfi, A., Corbett, K. S., Seder, R. A., & Edwards, D. K. (2021). Serum Neutralizing Activity Elicited by mRNA-1273 Vaccine. *The New England Journal of Medicine*, *384*(15), 1468–1470. https://doi.org/10.1056/NEJMc2102179

Xiong, Q., Cao, L., Ma, C., Tortorici, M. A., Liu, C., Si, J., Liu, P., Gu, M., Walls, A. C., Wang, C., Shi, L., Tong, F., Huang, M., Li, J., Zhao, C., Shen, C., Chen, Y., Zhao, H., Lan, K., … Yan, H. (2022). Close relatives of MERS-CoV in bats use ACE2 as their functional receptors. *Nature*, *612*(7941), 748–757. https://doi.org/10.1038/s41586-022-05513-3

Yamasoba, D., Kimura, I., Nasser, H., Morioka, Y., Nao, N., Ito, J., Uriu, K., Tsuda, M., Zahradnik, J., Shirakawa, K., Suzuki, R., Kishimoto, M., Kosugi, Y., Kobiyama, K., Hara, T., Toyoda, M., Tanaka, Y. L., Butlertanaka, E. P., Shimizu, R., … Sato, K. (2022). Virological characteristics of the SARS-CoV-2 Omicron BA.2 spike. *Cell*, *185*(12), 2103-2115.e19. https://doi.org/10.1016/j.cell.2022.04.035

Ying, B., Scheaffer, S. M., Whitener, B., Liang, C.-Y., Dmytrenko, O., Mackin, S., Wu, K., Lee, D., Avena, L. E., Chong, Z., Case, J. B., Ma, L., Kim, T. T. M., Sein, C. E., Woods, A., Berrueta, D. M., Chang, G.-Y., Stewart-Jones, G., Renzi, I., … Diamond, M. S. (2022). Boosting with variant-matched or historical mRNA vaccines protects against Omicron infection in mice. *Cell*, *185*(9), 1572-1587.e11. https://doi.org/10.1016/j.cell.2022.03.037

Yue, C., Song, W., Wang, L., Jian, F., Chen, X., Gao, F., Shen, Z., Wang, Y., Wang, X., & Cao, Y. (2023). ACE2 binding and antibody evasion in enhanced

transmissibility of XBB.1.5. *The Lancet Infectious Diseases*, *23*(3), 278–280. https://doi.org/10.1016/S1473-3099(23)00010-5

Zaki, A. M., Van Boheemen, S., Bestebroer, T. M., Osterhaus, A. D. M. E., & Fouchier, R. A. M. (2012). Isolation of a Novel Coronavirus from a Man with Pneumonia in Saudi Arabia. *New England Journal of Medicine*, *367*(19), 1814–1820. https://doi.org/10.1056/NEJMoa1211721

Zhang, S., Jia, W., Zeng, J., Li, M., Wang, Z., Zhou, H., Zhang, L., & Wang, X. (2022). Cryoelectron microscopy structures of a human neutralizing antibody bound to MERS-CoV spike glycoprotein. *Frontiers in Microbiology*, *13*, 988298. https://doi.org/10.3389/fmicb.2022.988298

Zhang, S., Zhou, P., Wang, P., Li, Y., Jiang, L., Jia, W., Wang, H., Fan, A., Wang, D., Shi, X., Fang, X., Hammel, M., Wang, S., Wang, X., & Zhang, L. (2018). Structural Definition of a Unique Neutralization Epitope on the Receptor-Binding Domain of MERS-CoV Spike Glycoprotein. *Cell Reports*, *24*(2), 441–452. https://doi.org/10.1016/j.celrep.2018.06.041

Zhang, Z., Mateus, J., Coelho, C. H., Dan, J. M., Moderbacher, C. R., Gálvez, R. I., Cortes, F. H., Grifoni, A., Tarke, A., Chang, J., Escarrega, E. A., Kim, C., Goodwin, B., Bloom, N. I., Frazier, A., Weiskopf, D., Sette, A., & Crotty, S. (2022). Humoral and cellular immune memory to four COVID-19 vaccines. *Cell*, *185*(14), 2434-2451.e17. https://doi.org/10.1016/j.cell.2022.05.022

Zhao, J., Alshukairi, A. N., Baharoon, S. A., Ahmed, W. A., Bokhari, A. A., Nehdi, A. M., Layqah, L. A., Alghamdi, M. G., Al Gethamy, M. M., Dada, A. M., Khalid, I., Boujelal, M., Al Johani, S. M., Vogel, L., Subbarao, K., Mangalam, A., Wu, C., Ten Eyck, P., Perlman, S., & Zhao, J. (2017). Recovery from the Middle East respiratory syndrome is associated with antibody and T cell responses. *Science Immunology*, *2*(14), eaan5393. https://doi.org/10.1126/sciimmunol.aan5393

Zhou, H., Chen, Y., Zhang, S., Niu, P., Qin, K., Jia, W., Huang, B., Zhang, S., Lan, J., Zhang, L., Tan, W., & Wang, X. (2019). Structural definition of a neutralization epitope on the N-terminal domain of MERS-CoV spike glycoprotein. *Nature Communications*, *10*(1), 3068. https://doi.org/10.1038/s41467-019-10897-4

Zhou, P., Song, G., Liu, H., Yuan, M., He, W., Beutler, N., Zhu, X., Tse, L. V., Martinez, D. R., Schäfer, A., Anzanello, F., Yong, P., Peng, L., Dueker, K., Musharrafieh, R., Callaghan, S., Capozzola, T., Limbo, O., Parren, M., … Andrabi, R. (2023). Broadly neutralizing anti-S2 antibodies protect against all three human betacoronaviruses that cause deadly disease. *Immunity*, *56*(3), 669-686.e7. https://doi.org/10.1016/j.immuni.2023.02.005

Zhou, P., Yang, X.-L., Wang, X.-G., Hu, B., Zhang, L., Zhang, W., Si, H.-R., Zhu, Y., Li, B., Huang, C.-L., Chen, H.-D., Chen, J., Luo, Y., Guo, H., Jiang, R.-D., Liu, M.-Q., Chen, Y., Shen, X.-R., Wang, X., … Shi, Z.-L. (2020). A pneumonia outbreak associated with a new coronavirus of probable bat origin. *Nature*, *579*(7798), 270–273. https://doi.org/10.1038/s41586-020-2012-7

Zhu, N., Zhang, D., Wang, W., Li, X., Yang, B., Song, J., Zhao, X., Huang, B., Shi, W., Lu, R., Niu, P., Zhan, F., Ma, X., Wang, D., Xu, W., Wu, G., Gao, G. F., & Tan, W. (2020). A Novel Coronavirus from Patients with Pneumonia in China, 2019. *New England Journal of Medicine*, *382*(8), 727–733. https://doi.org/10.1056/NEJMoa2001017

Zivanov, J., Nakane, T., Forsberg, B. O., Kimanius, D., Hagen, W. J., Lindahl, E., & Scheres, S. H. (2018). New tools for automated high-resolution cryo-EM structure determination in RELION-3. *eLife*, *7*, e42166. https://doi.org/10.7554/eLife.42166

Zivanov, J., Nakane, T., & Scheres, S. H. W. (2019). A Bayesian approach to beam-induced motion correction in cryo-EM single-particle analysis. *IUCrJ*, *6*(1), 5–17. https://doi.org/10.1107/S205225251801463X